Aerosol and cloud radiative properties over India and adjoining Seas

A thesis submitted during 2021 to the University of Hyderabad in partial
fulfilment of the degree of a PhD degree in
Centre for Earth, Ocean and Atmospheric Sciences

by

Abin Thomas

Centre for Earth, Ocean and Atmospheric Sciences
School of Physics

University of Hyderabad
(P.O.) Central University, Gachibowli,
Hyderabad-500 046
Telangana
India

CERTIFICATE

This is to certify that the thesis entitled "**Aerosol and cloud radiative properties over India and adjoining Seas**", submitted by **Abin Thomas** bearing Reg. No. **17ESPE01,** in partial fulfilment of the requirements for the award of the degree of Doctor of Philosophy in **Earth Sciences,** is a bonafide record of the work that has been carried out by him under my supervision and guidance.

This thesis has not been submitted previously in part or in full to this or any other University or Institution for the award of any degree or diploma.

Dr Vijay P. Kanawade

Supervisor

Dr. Vijay P. Kanawade
UGC-Assistant Professor
Centre for Earth, Ocean & Atmospheric Sciences
University of Hyderabad
Hyderabad-500 046, Telangana, INDIA.

08.11.2021

Head

Centre for Earth Ocean and Atmospheric Sciences

Head
Centre for Earth, Ocean &
Atmospheric Sciences
University of Hyderabad
Hyderabad-500 046, INDIA.

Dean

School of Physics

DEAN
School of Physics
University of Hyderabad
derabad-500 046, INDI

UNIVERSITY OF HYDERABAD
सा विद्या या विमुक्तये

CERTIFICATE

This is to certify that the thesis entitled "**Aerosol and cloud radiative properties over India and adjoining Seas**" submitted by **Abin Thomas** bearing registration number **17ESPE01** in partial fulfilment of the requirements for the award of **Doctor of Philosophy** in **Earth Sciences** is a bona fide research work carried out by her under my supervision and guidance.

The thesis is free from plagiarism and has not been submitted previously, either in part or in full, for the award of any academic degree or diploma to this or any other university or institution.

Further, the student has the following publication(s) before submission of the thesis for adjudication and has produced evidence for the same in the form of acceptance letter or the reprint in the relevant area of his research:

1. **Thomas, A.,** V. P. Kanawade, C. Sarangi & A. K. Srivastava. Effect of COVID-19 shutdown on aerosol direct radiative forcing over the Indo-Gangetic Plain outflow region of the Bay of Bengal. *Science of the Total Environment,* 2021.
   This publication appears in **Chapter - 4** of the dissertation
2. **Thomas, A**., V. P. Kanawade, K. Chakravarty & A. K. Srivastava, Characterization of raindrop size distributions and its response to cloud microphysical properties. *Atmospheric Research,* 2021.
   This publication appears in **Chapter - 6** of the dissertation
3. **Thomas, A.**, C. Sarangi & V. P. Kanawade. Recent increase in winter hazy days over Central India and the Arabian Sea. *Scientific Reports,* 2019.
   This publication appears in **Chapter - 3** of the dissertation

and has made presentation in the following conferences:

1. **<u>Thomas, A.,</u>** V.P. Kanawade, C. Sarangi & A.K. Srivastava., *'Aerosol direct radiative forcing over the outflow region of Indo-Gangetic Plains: A case study during the COVID-19 lockdown.'* International Conference on Clouds and Precipitation at Indian Institute of Tropical Meteorology, Pune on 2 - 6 August 2021 (Poster Presentation)
2. **<u>Thomas, A.</u>,** C. Sarangi & V. P. Kanawade, *'Increasing trend of Aerosol Direct Radiative Forcing over Indian region and adjoining Seas.'* Fifth International Skynet Workshop 2019 at Indian Meteorological Department, New Delhi on 13-15 February 2019. (Oral Presentation)
3. **Thomas, A.,** C. Sarangi & V. P. Kanawade, *'Recent increase in winter hazy days over central India and the Arabian sea.'* Fourth Atmospheric Composition and Asian Monsoon workshop at Universiti Kebangsaan Malaysia, Bangi, Malaysia on 25 -28 June 2019. (Poster Presentation)

Further, the student has passed the following courses towards the fulfilment of the coursework required for a Ph.D.

Course code	**Course**	**Credit**	**Pass/Fail**
ES801	Earth System Sciences	4	Pass
ES805	Research Methodology	3	Pass
ES806	Mathematics for Earth Sciences	4	Pass
ES807	Interdisciplinary Course	3	Pass
AP811-830	Special paper on specific research topic	2	Pass
	Total	16	

Dr Vijay P. Kanawade

Supervisor

Dr. Vijay P. Kanawade
UGC-Assistant Professor
Centre for Earth, Ocean & Atmospheric Sciences
University of Hyderabad
Hyderabad-500 046, Telangana, INDIA.

08.11.2021

Head

Centre for Earth Ocean and Atmospheric Sciences

Head
Centre for Earth, Ocean &
Atmospheric Sciences
University of Hyderabad
Hyderabad-500 046, INDIA.

Dean

School of Physics

DEAN
School of Physics
University of Hyderabad
Hyderabad-500 046, INDIA

DECLARATION

I, **Abin Thomas,** hereby declare that the thesis entitled "**Aerosol and cloud radiative properties over India and adjoining Seas**" submitted by me under the guidance and supervision of **Dr Vijay P. Kanawade** is a bonafide research work. I also declare that it has not been submitted previously in part or in full to this University or any other University or institution to award any degree or diploma.

Date:10/11/2021

Abin Thomas
Reg. No. 17ESPE01

Dedicated to

My Parents and all my teachers,
who have shone the light in my path to the quest for knowledge

Acknowledgements

I would like to thank my supervisor Dr Vijay P Kanawade, for giving me an opportunity to pursue my doctoral research work under his guidance. He has been an ideal teacher, mentor, and guide, offering advice and encouragement right when I needed them. I’m proud of and grateful for my time as his student.

I wish to express my gratitude to my doctoral committee members, Prof K. Ashok and Prof V Chakravarthi, who gave their insights in every step of the work. Their suggestions and encouragement along the way have helped me improve my work further. I thank Dr S. Srilakshmi and Dr Syed Maqbool Ahmed for their support and appreciation.

I am grateful to Prof. K. S. Krishna, Head, Centre for Earth, Ocean and Atmospheric Sciences, and former Head, Prof. M. Jayananda, for providing all the facilities and support in the centre.

My sincere appreciation goes out to Dr Chandan Sarangi, who has helped me with his ideas and insights throughout the thesis work. I would like to thank Dr Atul K. Srivastava for giving me a chance to work on various research problems and helping me with his suggestions. I also wish to thank Dr Kaustav Chakravarty for providing data and collaborating with a part of my thesis work.

I would like to acknowledge University Grants Commission-Junior Research Fellowship for providing financial support throughout my tenure.

I would like to thank the various science teams and data producers at NASA, NOAA and ECMWF for making the wide variety of satellite and ground observations available freely, without which this research work would not have been possible.

I wish to thank my friends Mathew, Arun, Feba, Charan, Vikas and Reshma for their company, support and fruitful scientific discussions. Last but not least; I am deeply indebted to my parents and my brother, who have always stood by me and inspired me

Abin Thomas

Contents

List of Figures

Page No.

Chapter - 1

Chapter - 3

Chapter - 4

Chapter - 5

Chapter - 6

List of Tables

Chapter - 2 **Page No.**

Chapter - 3

Chapter - 4

Chapter - 5

Chapter - 6

Abbreviations

AAOD	Absorbing Aerosol Optical Depth
AOD	Aerosol Optical Depth
AS	Arabian Sea
ADRF	Aerosol Direct Radiative Forcing
BC	Black Carbon
BoB	Bay of Bengal
CCN	Cloud Condensation Nuclei
CDNC	Cloud Droplet Number Concentration
CERES	Clouds and the Earth's Radiant Energy System
CI	Central India
CRF	Cloud Radiative Forcing
DMS	Dimethyl Sulphide
DSD	Raindrop Size Distribution
ECMWF	European Centre for Medium-Range Weather Forecasts
EOS	Earth Orbiting Satellite
ERA-5	ECMWF Reanalysis, Version5
ERBE	Earth Radiation Budget Experiment
GDAS	Global Data Assimilation System
GFS	Global Forecasting System
IGP	Indo-Gangetic Plain
IPCC	Intergovernmental Panel for Climate Change
LTS	Lower Tropospheric Stability
LWP	Liquid Water Path
MERRA-2	Modern-Era Retrospective analysis for Research and Applications, Version 2
MODIS	Moderate Resolution Imaging Spectroradiometer
OMI	Ozone Measuring Instrument
OC	Organic Carbon
UTLS	Upper Troposphere and Lower Stratosphere
UV-AI	Ultra Violet - Aerosol Index
VOC	Volatile Organic Compound

List of publications/conferences

Publications from the thesis

1. **Thomas, A.,** V. P. Kanawade, C. Sarangi & A. K. Srivastava. Effect of COVID-19 shutdown on aerosol direct radiative forcing over the Indo-Gangetic Plain outflow region of the Bay of Bengal. *Science of the Total Environment*, 2021. (IF: 7.963)
2. **Thomas, A**., V. P. Kanawade, K. Chakravarty & A. K. Srivastava, Characterization of raindrop size distributions and its response to cloud microphysical properties. *Atmospheric Research*, 2021. (IF: 5.695)
3. **Thomas, A**., C. Sarangi & V. P. Kanawade. Recent increase in winter hazy days over Central India and the Arabian Sea. *Scientific Reports,* 2019. (IF: 5.133)

Publications related to the thesis work

1. Srivastava, A. K., **A. Thomas**, R. K. Hooda, V. P. Kanawade, A.P. Hyvärinen, V. Singh, D. S. Bisht & S. Tiwari. How secondary inorganic aerosols from Delhi influence aerosol optical and radiative properties at a downwind sub-urban site over Indo-Gangetic Basin? *Atmospheric Environment,* 2021. (IF: 5.402)
2. Srivastava, A. K., P. Bhoyar, V. Kanawade, D. Panuganti, **A. Thomas** & V. K. Soni. Improved air quality at an urban megacity over the Indo-Gangetic Basin: From stringent to relaxed lockdown phases. *Urban Climate*, 2021. (IF: 5.731)
3. Nair, A., S. S. Das, **A. Thomas**, C. Sarangi, V. P. Kanawade. Role of Cyclone "Ockhi" in the re-distribution of aerosols and its impact on the precipitation over the Arabian Sea. *Atmospheric Research*, 2019. (IF: 5.695)
4. Sarangi, C. V. P. Kanawade, S.N. Tripathi, **A. Thomas** & D. Ganguly. Aerosol-induced intensification of cooling effect of clouds during Indian summer monsoon. *Nature Communications,* 2018. (IF: 12.121)

National Conferences/Symposiums

1. **Thomas, A.,** V. P. Kanawade, K. Chakravarty & A. K. Srivastava., '*Characterization of raindrop size distributions and its response to cloud microphysical properties.'* Virtual National Symposium on Weather and Climate Services over Mountainous Regions at NESAC, Umiam, Meghalaya on 14 - 17 December 2020. (Oral Presentation)

International Conferences/ workshops

1. **Thomas, A.,** V.P. Kanawade, C. Sarangi & A.K. Srivastava., *‘Aerosol direct radiative forcing over the outflow region of Indo-Gangetic Plains: A case study during the COVID-19 lockdown.'* International Conference on Clouds and Precipitation at Indian Institute of Tropical Meteorology, Pune on 2 - 6 August 2021 (Poster Presentation)
2. **Thomas, A.,** C. Sarangi & V. P. Kanawade, *'Increasing trend of Aerosol Direct Radiative Forcing over Indian region and adjoining Seas.'* Fifth International Skynet Workshop 2019 at Indian Meteorological Department, New Delhi on 13 - 15 February 2019. (Oral Presentation)
3. **Thomas, A.,** C. Sarangi & V. P. Kanawade, *'Recent increase in winter hazy days over central India and the Arabian sea.'* Fourth Atmospheric Composition and Asian Monsoon workshop at Universiti Kebangsaan Malaysia, Bangi, Malaysia on 25 -28 June 2019. (Poster Presentation)
4. International Workshop on Cloud Dynamics, Microphysics, and Small-Scale Simulation at Indian Institute of Tropical Meteorology, Pune on 13 -17 August 2018.

International summer/training school

1. Third Atmospheric Composition and Asian Monsoon training school at Universiti Kebangsaan Malaysia, Bangi, Malaysia on 23 - 24 June 2019.

Abstract

Aerosols are ubiquitous in the atmosphere and significantly impact air quality, human health, weather and climate. Due to rapid industrialisation and urbanisation, India is a global hotspot of aerosols, particularly Indo-Gangetic Plain (IGP). Multivariate and multidimensional information from various sensors (ground and space) and models have extensively been integrated over the last two decades to characterise aerosols. But the uncertainties in the aerosol climatic effects remain significant owing to nonuniform spatial and temporal sampling and coverage and considerable heterogeneity in aerosol sources. Here, we analyse the aerosol and cloud variables from space-borne sensors and model reanalysis products to delineate how to investigate atmospheric aerosol properties and impact on regional climate under the reduced anthropogenic emissions radiative effects of aerosol and clouds over Indian continental adjoining marine areas. Numerous investigators reported the increasing trend in anthropogenic aerosols over India, particularly over IGP. In recent years, the rising trend in aerosols has been higher over Central India (CI) than IGP. The enhanced lower tropospheric stability over CI due to aerosol-induced positive forcing on the atmosphere and negative forcing at the surface created a positive feedback mechanism that could further favour the accumulation of aerosols near the surface. The continental aerosol outflow onto the Bay of Bengal (BoB) during the pre-monsoon (March through May) is a year-round phenomenon, which constitutes a mixture of mineral dust and anthropogenic aerosols. A drastic reduction in anthropogenic emissions due to the pandemic outbreak of novel coronavirus (COVID-19) imposed lockdown in 2020 provided a unique and rare opportunity to estimate the anthropogenic contribution to aerosol forcing over the outflow region of the BoB. A 10–25% reduction in aerosol loading over the IGP resulted in a 20-25% reduction in aerosol direct radiative forcing over the outflow region of the BoB. Using satellite-derived cloud droplet number concentration, we found that aerosol-induced changes in cloud properties show different signals over the Arabian Sea and the BoB during the monsoon season (June through September). The difference in the aerosol-cloud interaction could be attributed to the changes in the cloud microstructure. The analyses using in-situ raindrop size distribution measurements and satellite-derived cloud properties revealed a distinct instantaneous response of raindrop size distribution to different rain regimes (convective and stratiform). Overall, the satellite and model reanalysis datasets offered an improved outlook of aerosol and cloud radiative effects over the Indian region. The processes, interactions and feedback mechanisms can be further delineated by isolating the impact of aerosols, clouds and dynamical conditions.

Chapter 1

Introduction

> **"*We have in this fine dust (referring to aerosols) a most beautiful illustration of how the little things in the world work great effects by virtue of their numbers*" - John Aitken, 1880**

1.1 Fundamentals of atmospheric aerosols

1.1.1 Atmospheric aerosols

Atmospheric aerosols are suspended solid/ liquid particles in a gaseous dispersion medium, i.e., the atmosphere, and must have a minimum atmospheric lifetime of one hour (Junge, 1964; Jaenicke, 1980a). They are generated from natural and anthropogenic sources through two major processes: disintegration and dispersion of bulk matter or gas to particle conversion of gaseous emissions in the atmosphere (Jaenicke, 1980b). Aerosols exist in a broad spectrum of sizes, as small as ~ 1 nanometer (nm) to few tens of micrometres (µm). The lifetime of aerosols also varies widely and mainly depends on their size and location; larger aerosols settle down faster due to gravity than smaller aerosols (less than 1 µm). The size of the aerosol particle determines the properties of the aerosols and how they interact with the environment (Hinds, 1982).

Aerosols from the atmosphere are removed through deposition, i.e., aerosols get collected or deposited on surfaces. Deposition processes can be dry or wet. Dry deposition happens via gravitational sedimentation, impaction on larger surfaces or Brownian diffusion. (Chamberlain, 1953; Tomasi and Lupi, 2017). Particle size and wind velocity determine the dry deposition velocity. For sub-micron particles, the deposition is controlled by Brownian motion, and deposition velocity increases with a decrease in size. But gravitational settling dominates for particles larger than 1 µm diameter, and the deposition velocity increases with particle size. Particles in the nucleation range are removed through coagulation which is determined by mobility and concentration of aerosols. For accumulation mode, removal is primarily through wet deposition processes, giving them a longer residence time (Jaenicke, 1980a). Wet deposition is the scavenging of aerosols by atmospheric hydrometeors (Tomasi and Lupi, 2017). The aerosols may act as cloud condensation nuclei and get incorporated into the cloud droplet or get impacted into a cloud droplet. This is known as in-cloud scavenging. The aerosols can also get scavenged by falling raindrops or snow, known as below-cloud scavenging.

1.1.2 Aerosols classification

Aerosols can be classified based on their atmospheric location, geographical location, source, composition, formation mechanism, and characteristic property. Tropospheric aerosols are generally confined to the boundary layer and are generated from localized sources, and exist for a few days in the atmosphere (Coakley et al., 1983). Aerosols are also injected into the stratosphere during volcanic eruptions and exist as a distinct layer between 12-25 km altitude known as the stratospheric aerosol layer (Junge et al., 1961). During the Asian summer monsoon, the anti-cyclone also transports surface aerosols into the upper troposphere and lower stratosphere (UTLS) (Pan et al., 2016; Yu et al., 2017).

The aerosol sources can be grouped as primary and secondary based on their formation mechanism. Primary aerosols are emitted directly into the atmosphere as particles and are mostly of natural origin. Natural sources make up ~89% of emissions and are distributed globally (Hinds, 1982; Satheesh and Krishna Moorthy, 2005). Wind-borne dust, sea salt spray, volcanic emission, pollen, forest fire emissions are natural sources. The secondary aerosols are formed by the gas-to-particle conversion of natural and anthropogenic precursor gases. The natural secondary aerosols originate from SO_2 from volcanoes, DMS from marine planktons, H_2S from bacteria, biogenic VOCs, etc. Since the beginning of the industrial age, fossil fuel combustion has led to higher emission of precursor gases like SO_2 and NO_x (Seinfeld and Pandis, 2016). The secondary sources make up a majority of the sub-micron aerosols.

The major aerosol species considered in this thesis are black carbon, organic carbon, sulfate, mineral dust, and sea salt spray. Sea salt aerosols are produced by the dynamic interaction of winds with the sea surface. The wave breaking at the surface of the Sea produces bubbles which is a function of surface wind speed (greater than 3-4 m s^{-1}). The surface free energy of the breaking bubble converts into kinetic energy, which ejects particles away from the sea surface (Warneck, 2000). Mineral dust aerosols are the second most dominant aerosol, and they originate from wind dispersal of surface materials from deserts, semi-arid regions, and regions altered by anthropogenic activities. The dispersion of dust aerosols depends on the size of the particles and wind velocity (Warneck, 2000). The central and south Asian regions are a consistent source of dust aerosols. The dust mobility is mainly modulated by natural sources (Prospero et al., 2002), but Tegen and Fung (1995) estimated that 30-50% of dust originate from disturbed soil surfaces that are mainly considered to be anthropogenic. Sulphate aerosols are emitted from biota, volcanoes, marshes, and anthropogenic combustion processes. The DMS, H_2S, COS emissions from various natural sources oxidise to more stable sulphuric dioxide (SO_2). SO_2 is emitted directly into the atmosphere from volcanoes, fossil fuel combustion and biomass burning. SO_2 is further gets converted into sulphuric acid (H_2SO_4), and sulphuric acid particles form sulphate aerosols. The conversion of SO_2 to H_2SO_4 in the atmosphere takes up to 24 days. The Black carbon aerosols are produced as primary particles from incomplete combustion of biomass or fossil fuels. Hence, they are generally anthropogenic in origin. Historically, North America and Europe were significant emitters of BC, but after the 1950s, developing countries in the south-east Asian region (India and China) are leading in emissions (Novakov et al., 2003; Bond et al., 2007). Organic Carbon (OC) aerosols are produced as primary aerosols from anthropogenic or natural sources and as secondary aerosols via oxidation of VOCs (Ramachandran, 2018).

Depending on the size of aerosols, they are segregated into Aitken nuclei (10^{-3} to 10^{-1} µm), accumulation (10^{-1} to 1 µm), and coarse particles (1 to 10^{2} µm) (Junge, 1958). The Aitken nuclei are ultrafine particles produced in the atmosphere due to gas to particle conversion of vapours and gaseous species or through the primary combustion process (Junge, 1964). The nuclei mode particles grow by coagulation or condensation of vapour onto existing particles and form an accumulation mode. The coarse mode particles are formed by mechanical processes like wind-blown dust, pollen, sea salt spray, etc.

The various sources and atmospheric processes that are characteristic of each geographic location can alter the aerosol composition. Therefore, based on geographic locations, aerosols can be characterised as urban, marine, rural continental, remote continental, polar and desert aerosols (Seinfeld and Pandis, 2016). Urban aerosols consist of particulate emissions from power plants, industries, construction and natural sources. Most of the particles will be smaller than 0.1 µm, and they vary in concentration depending on the distance from the source. Marine aerosols consist primarily of sea-spray aerosols formed from the bursting of air bubbles at the sea surface, followed by secondary aerosols from Biogenic volatile organic compounds and their oxidation products (O'Dowd and de Leeuw, 2007). Rural aerosols are a mixture of natural aerosols with a moderate amount of anthropogenic aerosols. Remote continental aerosols have primary particles like dust and pollen and secondary oxidation products. The emissions from northern midlatitudes are transported to the Arctic to form the Polar aerosols. It consists of sea salt mixed with ammonium, nitrate, dust, and organic matter. Desert aerosols smaller than 10 µm are transported across continents by winds from its source regions.

1.1.3. Spatio-temporal variation

The spatio-temporal variation of aerosols adds to the uncertainty in modelling the aerosol-climate interaction (Mishchenko et al., 2007; Carslaw et al., 2013). Natural aerosols like dust and sea salt vary with the wind speed (Junge, 1958; Jaenicke, 1980b) as they are lifted and transported by winds from its origin. The short residence time of various aerosols also adds to the high variability of aerosol concentration. The wet deposition due to rainfall removes most of the aerosol loading over a region (Seinfeld and Pandis, 2016). The variation in planetary boundary layer height can prevent the dispersion of aerosols and increase their concentration near the surface (Nair et al., 2007; Li et al., 2017). The ground-based measurements of aerosol loading have shown significant diurnal variation in aerosol concentration (Smirnov et al., 2002; Moorthy et al., 2016). Spatially, the aerosol loading can vary from very polluted areas like East Asia and India to very clean regions like Australia (Remer et al., 2008). The dust aerosols are persistent over North Africa, the Middle East, south and central Asia (Prospero et al., 2002). The biomass burning and forest fires around Africa, Brazilian Amazon, equatorial Asia, Boreal forest and northern Australia make them major emitters of black carbon aerosols (Andreae and Merlet, 2001; van der Werf et al., 2010; Andreae, 2019).

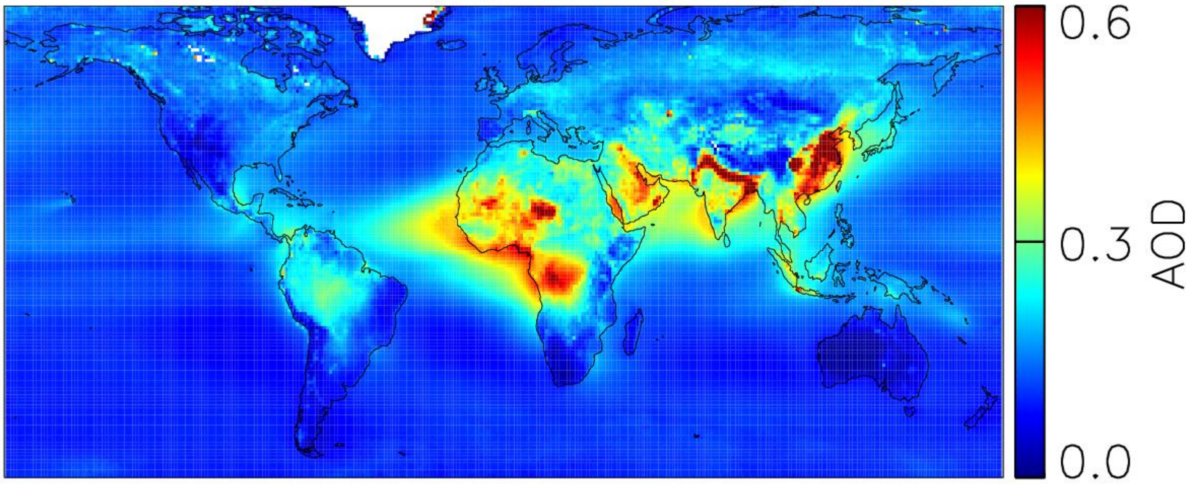

Figure 1.1 Mean MODIS AQUA retrieved AOD from 2002-2019.

1.1.4 Characteristics of atmospheric aerosols

i) Physical properties

The size of aerosols spans over five orders of magnitude from 10^{-3} to 10^{2} µm, and all the effects of aerosols are size-dependent. Therefore, it is essential to define the aerosol size distribution that can account for the size of each particle. Hence, the size range of aerosols are divided into discrete size intervals, and corresponding number concentrations are represented in a simple histogram (Fig. 1.2). The loss of information may occur from a change in width of the size range in the bin of the discrete distribution. Hence, the continuous size distribution function, $n(D_p)$ is defined where n is the number of particles of diameter D_p and dD_p is the infinitesimally slight increase in diameter. The total number of particles per cm^3 can be defined as (Seinfeld and Pandis, 2016)

$$N_t = \int_0^\infty n(D_p) dD_p \tag{1.1}$$

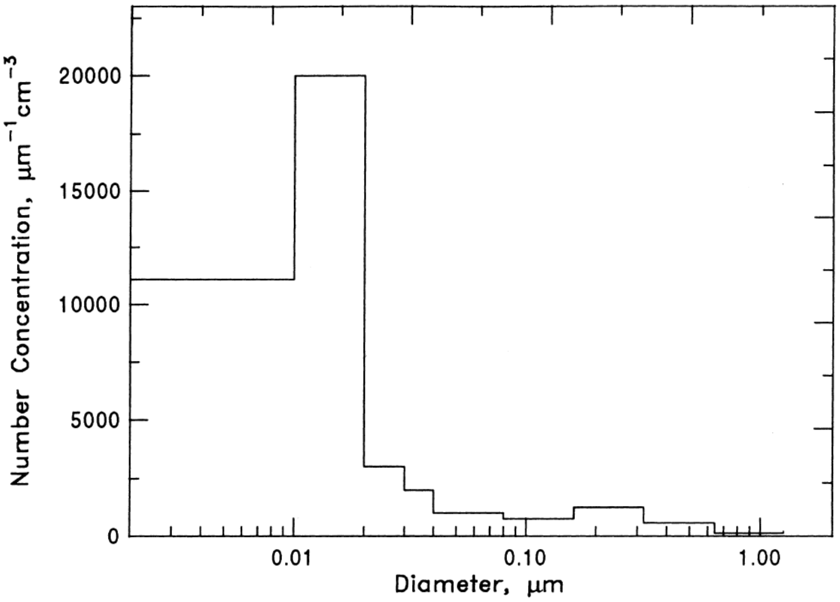

Figure 1.2 Aerosol number concentration normalised by the width of the size range. Taken from *Seinfeld and Pandis (2016).*

Due to the vast diameter range of the aerosols, logarithmic scales are used to illustrate the size distribution. Junge (1958) proposed a power-law distribution as given below

$$\frac{dn(D_p)}{dlogD_p} = c{D_p}^{-\nu} \tag{1.2}$$

where c and ν are positive constants. *c* depends on the number of aerosols per cm$^{-3,}$ and ν shows the slope of the curve.

Lognormal distributions are used to represent multi-modal aerosol distributions (Hinds, 1982; D'Almeida et al., 1991)

$$n(lnD_p) = \frac{N_t}{(2\pi)^{1/2} ln\sigma_g} exp\left(\frac{\left(lnD_p - ln\overline{D_{pg}}\right)^2}{2ln^2\sigma_g}\right) \tag{1.3}$$

where σ_g signifies the width of the distribution, and D_{pg} is the median diameter.

ii) Optical properties

Aerosols interact with incoming solar radiation in UV and visible wavelengths and affect the transmission of said radiation to the Earth's surface (Erlick and Frederick, 1998). Aerosols can scatter the radiation depending on the size of the particle via Rayleigh scattering or Mie scattering. If the particle is smaller than the wavelength of the light, then it is Rayleigh scattering, where an equal amount of light is scattered both forward and backward in the direction of incidence. In the case of Mie scattering, the diameter of the particles will be a larger or comparable size to the wavelength of the incident light. The Mie scattering is asymmetrical and more radiation is scattered in the forward direction. Some particles can absorb the incident radiation and add to the extinction of radiation by aerosols.

From Beer-Lambert's law, the attenuation of solar radiation intensity (I) through a column of atmosphere with optical depth (τ) for a given wavelength λ can be given as

$$I(\lambda) = I_0(\lambda)e^{-\tau(\lambda)} \tag{1.4}$$

Aerosol optical depth (AOD), in particular, describes the attenuation of light by a column of aerosol with unit cross-section. AOD can be defined as the column integration of extinction coefficient (β_{ext}).

$$\tau = \int_{z1}^{z2} \beta_{ext}(z)dz \tag{1.5}$$

The effectiveness of scattering over absorption by aerosols is given by single scattering albedo (ω). It is defined as the ratio of scattering coefficient to extinction coefficient (McClatchey et al., 1972)

$$\omega = \frac{\beta_{sca}}{\beta_{ext}} \tag{1.6}$$

The asymmetry parameter (g) describes how much the forward or backward scattering dominates. It is defined as the average cosine of the scattering angle (Zege and Kokhanovsky, 1994; Marshall et al., 1995). The value of g ranges from -1 to 1, with a positive value for forward scattering and a negative value for backscattering.

$$g = \langle \cos\theta \rangle \tag{1.7}$$

iii) Chemical properties

The chemical composition of aerosols is complex and varies with its sources. Tropospheric aerosols generally consist of black carbon, organic compounds, sulfate, nitrate, sodium chloride, heavy metals, crustal elements, and water (Pandis et al., 1995). Aerosols are produced from mechanical processes, like mineral dust contains, Ca, Fe, Si, Al, etc. (Turner and Colbeck, 2008). Black carbon aerosols are emitted into the atmosphere from combustion processes. Organic carbon aerosols are formed from volatile organic compounds in the atmosphere. Sulfate aerosols are produced from sulphur dioxide gas precursors in the atmosphere from anthropogenic sources, volcanoes or oceanic dimethyl sulfide.(Saltzman et al., 1983; Boucher et al., 2003) The aerosol chemical composition influences hygroscopicity, radiative effects, reactivity and its general impact on the environment (Gilardoni and Fuzzi, 2017). The hygroscopic aerosols like sea salt and sulfate aerosols grow in volume and result in changes in the refractive index (Hess et al., 1998). The growth of such aerosols alters the radiative forcing, and the difference in the growth of various chemical species adds to the uncertainty in estimating the radiative forcing (Pilinis et al., 1995).

iv) Dynamical properties

The atmospheric aerosols undergo many transport and transformation processes that alter their number concentration, size and composition. The nucleation process produces new particles from gaseous chemical species when supersaturation is attained (Pandis et al., 1995). The pre-existing particles can grow by condensational growth or coagulation (Brock and Suck, 1982). The turbulent motions in the atmosphere aid in the collision of particles and lead to coagulation into a single particle. The coagulation can occur among similar size particles to form a larger particle or between disparate sized particles. The smaller particles coagulating onto larger particles do not modify the size of the particle but change the number concentration of smaller particles (Wexler et al., 1994). The existing aerosols can evaporate and undergo a reduction in size. Therefore, condensation, evaporation, and nucleation are generally the transformation processes that influence aerosol distribution (Pandis et al., 1995). The external processes like diffusion, gravitational settling, charge polarity can remove the particle from a population.

1.2 Radiative effects of atmospheric aerosols

The response of climate strongly depends on how the atmosphere solar radiation is absorbed or scattered in the atmosphere (Chylek and Wong, 1995). The IPCC AR-5 predicted a doubling of CO_2 concentration in this century from the pre-industrial levels (IPCC, 2013). But the recent observational studies show that changes in the aerosol loading have masked one-third of the warming by greenhouse gases (Storelvmo et al., 2016). Therefore, studies to assess the impact of aerosol radiative effect are carried out extensively. The third assessment report of IPCC categorised aerosol radiative forcing into direct and indirect forcing (Forster et al., 2007).

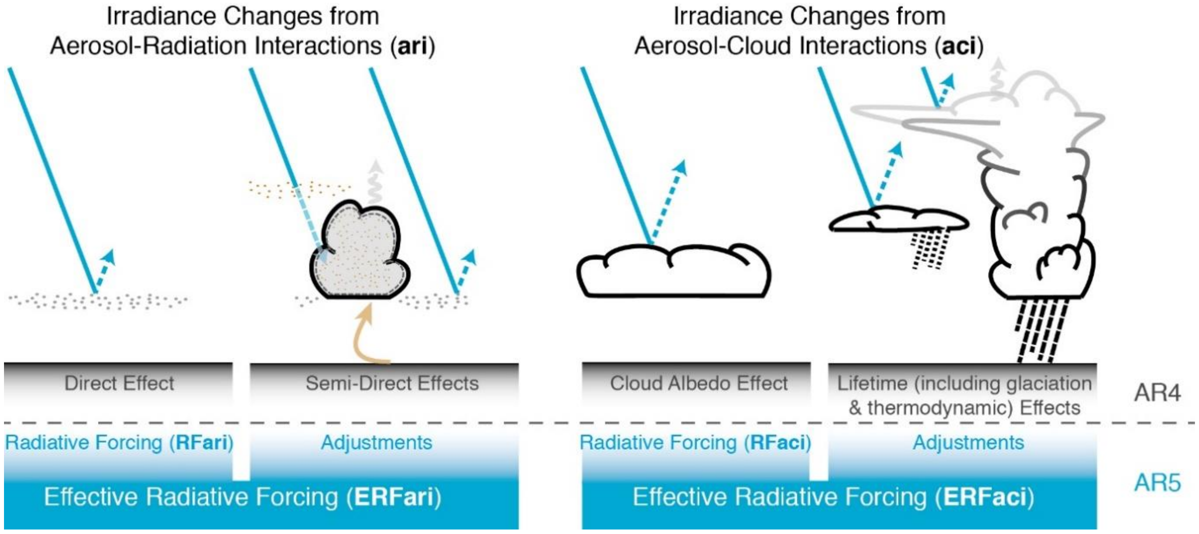

Figure 1.3 Radiative effects of aerosols and clouds. Taken from *IPCC (2013).*

1.2.1 Direct radiative effects

The alteration of the Earth's radiation budget through scattering and absorption of shortwave and longwave radiation is called aerosol direct effect (Forster et al., 2007). The aerosols generally scatter the incoming radiation and cause a cooling effect at the surface of the Earth (Charlson et al., 1992). Absorbing aerosols cause a cooling effect at the top of the atmosphere over dark surfaces like oceans or forests and a warming effect if over high albedo surfaces like desert, snow or clouds (Chylek and Wong, 1995). The forcing at the top of the atmosphere and at the surface of the Earth are considered separately as the surface forcing might be stronger in the presence of absorbing aerosols (Ramanathan et al., 2001b). Aerosol direct radiative can change with the spatio-temporal distribution of aerosols, atmospheric humidity and wavelength of radiation (Haywood and Boucher, 2000). The direct radiative forcing can be determined using the optical properties of aerosols such as AOD, SSA, asymmetry parameter, etc. (Hess et al., 1998).

1.2.2 Indirect radiative effects

The ability of a fraction of aerosols to act as cloud condensation nuclei (CCN) and ice nuclei (IN) can impact the cloud microphysical properties and thus the cloud radiative forcing. The increase in CCN at a limited amount of moisture can enhance the number of cloud droplets and reduce the size of the droplet. The reduced size of cloud droplets leads to an increase in cloud albedo and causes a negative forcing known as the Twomey effect (Twomey, 1977) or first indirect effect (Ramaswamy et al., 2001) or cloud albedo effect (Lohmann and Feichter, 2005). The smaller cloud droplets lead to decreased precipitation efficiency, which means that the clouds require more time to grow up to precipitable size. This increases the lifetime of the cloud, adding to the cooling effect known as the Albrecht effect (Albrecht, 1989) or the second indirect effect. IPCC (2013) regards aerosol-induced changes in cloud radiative forcing as the largest uncertainty in estimating the climate forcing. The uncertainty in the aerosol indirect effect arises from the spatio-temporal variation of aerosols, clouds, and changes in the dynamical feedbacks (Lohmann and Feichter, 2005).

1.2.3 Semi-direct effects

The absorbing aerosols can affect the cloud cover without acting as CCN. These aerosols heat the air surrounding them, facilitating the evaporation of existing clouds and thereby decreasing the cloud cover. The warming effect of absorbing aerosols at an altitude can stabilize the atmosphere and reduce convection. This combined effect of absorbing aerosols in reducing cloud cover is called the semi-direct effect (Hansen et al., 1997; Ackerman et al., 2000). The uncertainty in this effect arises from the vertical distribution of absorbing aerosol (Bond et al., 2007).

1.3. Observations of aerosol impacts

1.3.1 Observations of aerosol-radiation-climate interactions

The estimates of aerosol direct radiative forcing have improved over the last two decades due to improvements in observations and modelling efforts (IPCC, 2013). The models have evolved from including sulphate aerosols for direct forcing measurements (Charlson et al., 1991) to multi-model ensembles with multi aerosol microphysical schemes (Myhre et al., 2017; Xian et al., 2019; Gliß et al., 2021). The uncertainties in estimating aerosol direct radiative forcing came from the complexities in aerosol mixing, understanding the species-wise contribution to forcing and vertical distribution of aerosols (Quinn and Bates, 2005; Buchard et al., 2016). The development in the model physics was complemented by a large array of datasets that measured aerosol optical properties. Observational campaigns (Quinn and Bates, 2005; Tripathi et al., 2006; Moorthy et al., 2016) and long-term remote sensing from the ground (Holben et al., 1998; Takamura and Nakajima, 2004; Moorthy et al., 2013) have provided detailed datasets to improve our understanding of aerosols. The lack of continuity and spatial extent from the ground-based measurements were overcome by the satellite-borne measurements (Remer et al., 2005; Levy et al., 2013; Torres et al., 2013).

The Aerosol Robotic Network (AERONET) has been providing ground-based AOD measurements for the last 25 years (Giles et al., 2019). The quality controlled, cloud screened data from Cimel Electronique Sun–sky radiometers which are globally distributed, have lesser uncertainties as they have minimal assumptions, reliable calibration, and weak dependency on trace gases (Holben et al., 1998). The AERONET AOD measurements are used to validate the satellite-borne measurements and provided more accurate ground truth data. The Advanced Very-High-Resolution Radiometer (AVHRR) instrument onboard NOAA satellites have been providing continuous radiance data since 1980 (Holben et al., 1992). Total Ozone Mapping Spectrometer (TOMS) has also provided AOD measurements since 1979 (Prospero et al., 2002). The advent of Earth Orbiting Satellite (EOS) mounted radiometers have provided much more frequent laboratory quality datasets (Kaufman and Tanré, 1996). The development of more accurate retrieval algorithms over land and ocean has added to the knowledge of aerosol loading. The global climatology from Moderate Resolution Imaging Spectroradiometer (MODIS) onboard EOS-TERRA and AQUA satellites has given a picture of regional variation in aerosol loading. The Multi-angle Imaging SpectroRadiometer (MISR) is another instrument onboard EOS-TERRA that provides spectral AOD measurements (Diner et al., 1998). The east Asia and Indian regions were seen as the most polluted area (Remer et al., 2008). The comparative study using both MODIS and MISR long-term measurements of aerosols have shown that the rise in aerosol loading has coincided with the centres of increasing industrialization, population, and urbanization, i.e., the South East Asian region (Mehta et al., 2016).

The Indian region has been a hotspot for aerosol research since the 1960s. Mani and colleagues studied solar attenuation due to dust aerosols during the pre-monsoon season (Mani et al., 1969; Mani et al., 1973). The Indian Ocean Experiment (INDOEX) in 1999 studied the climate impact and optical properties of anthropogenic aerosols over the northern Indian Ocean (Moorthy et al., 2001; Ramanathan et al., 2001b). Several measurement campaigns were conducted over the Indian region by the Geosphere-Biosphere Program of ISRO (Moorthy et al., 2005a; Tripathi et al., 2006; Nair et al., 2007) to study the aerosol direct radiative effects. The Integrated Campaign on Aerosol and Radiation Budget (ICARB) was a multi-platform campaign over India and surrounding seas to study the vertical distribution and radiative impact of aerosols (Beegum et al., 2008; Moorthy et al., 2008; Moorthy et al., 2009). A strong latitudinal and longitudinal gradient in aerosol properties and radiative forcing was observed over the marine regions around India during the pre-monsoon season using data from ICARB, satellites and model estimates (Nair et al., 2013a). The Aerosol Radiative Forcing over India project of ISRO has a long-term observation from a network of stations scattered all over India (Babu et al., 2013; Manoj et al., 2019).

1.3.2 Observations of aerosol-cloud-radiation-climate interactions

The cloud adjustments due to aerosols and the changes in cloud properties like cloud fraction, liquid water path and cloud droplet number concentration remain uncertain in estimating the radiative forcing from aerosol-cloud interactions (Bellouin et al., 2020; Gryspeerdt et al., 2020). Even though many studies have made progress in understanding the processes involved in warm marine clouds, the aerosol interactions in the mixed-phase clouds remain highly uncertain due to the complexity of microphysical pathways (Lohmann, 2017). The uncertainties in the aerosol-cloud interactions arise from meteorological influence on clouds, surface feedbacks, changes in microphysical feedbacks, and spatio-temporal variations in aerosols and clouds (Fan et al., 2016). The uncertainties in modelling aerosol indirect effects can come from parameterisations of aerosol and cloud processes and biases in the observations (Christensen et al., 2017; Gryspeerdt et al., 2019). In-situ ground-based and airborne measurements were conducted to quantify the aerosol indirect effect (Andreae, 2009; Prabha et al., 2011; Rosenfeld et al., 2014).

The satellite-based studies of aerosol-cloud interaction tend to underestimate compared to models due to uncertainties in the retrieval. The aerosols grow hygroscopically in the presence of clouds, and AOD cannot be retrieved in cloudy pixels (Rosenfeld et al., 2014). Therefore, the poor association of AOD to CCN makes it challenging to estimate the aerosol-cloud interactions effectively (Gryspeerdt et al., 2016; Gryspeerdt et al., 2019). In order to accurately measure the CCN ingested by the clouds and their association, cloud droplet number concentration is used from satellite retrieved cloud effective radius and cloud optical thickness (Bennartz and Rausch, 2017; Zhu et al., 2018). This approach helped to isolate the environmental and meteorological impact on clouds and estimate the modifications due to aerosols on low marine clouds (Rosenfeld et al., 2019).

The presence of high aerosol loading and monsoon cloudiness makes the Indian region an ideal area for observing aerosol-cloud interactions. Only a fraction of the aerosols act as CCN, depending on its size and chemical composition (Chang et al., 2017). INDOEX campaign measured the CCN along with aerosol properties over the northern Indian ocean and found that the outflow influenced the CCN concentration (Cantrell et al., 2000). Cloud-Aerosol Interaction Precipitation Enhancement Experiment (CAIPEEX) began in 2009 and has continued phase-wise, making airborne and ground-based measurements of aerosols, cloud microphysical properties and CCN concentrations (Prabha et al., 2011; Kulkarni et al., 2012). The CCN efficiency of aerosols in the northern Indian Ocean during winter was size-dependent and increased with supersaturation (Nair et al., 2020).

The cloud radiative forcing estimates over the Indian region was estimated using Earth Radiation Budget Experiment (ERBE) data by Rajeevan and Srinivasan (2000) and found a negative net forcing ~30 W m^{-2} during the monsoon season. The previous observation over the tropical convective clouds showed a zero net forcing due to near cancellation of shortwave and longwave cloud radiative forcing (Kiehl and Ramanathan, 1990). A strong imbalance between shortwave cloud radiative forcing and longwave cloud radiative forcing was found over the Indian region, which resulted in the negative forcing. This was attributed to the high clouds with large optical depth that dominated the area in this season (Rajeevan and Srinivasan, 2000). Later, Thampi and Roca (2014) used Clouds and Earth’s Radiant Energy System (CERES) data to concur the high negative NETCRF over the Indian monsoon region and the changes in the atmospheric water vapour was found to influence the NETCRF. The vertical distribution of cloud properties (cloud optical depth and cloud water content) retrieved from CloudSat also influenced the NETCRF over the region (Ravi Kiran et al., 2015). The climatological study of CRF over the Indian region using 13-year data from CERES and MODIS showed that the variability in NETCRF can be explained by the changes in the cloud properties like cloud fraction, cloud optical depth and cloud top pressure (Saud et al., 2016). The aerosol-induced cloud invigoration was observed during the Indian monsoon leading to enhanced cooling due to the enhanced formation of thicker stratiform anvil clouds (Sarangi et al., 2018). A semi-direct effect was observed for cumulus clouds over the Arabian Sea and the Bay of Bengal in all seasons except post-monsoon (Rao and Dey, 2020). The variation in aerosol indirect effect was observed with the change in LWP over the outflow regions of the Indian peninsula, i.e., the cloud effective radius increased with aerosol loading when the clouds had low LWP and vice versa during the winter season (Jose et al., 2020).

1.3.3 Observations of aerosol-cloud-radiation-rainfall-climate interactions

The aerosol-induced changes in the cloud microphysics not only causes radiative budget impact but also weaken the hydrological cycle (Ramanathan et al., 2001a). The increase in aerosol loading increases the number of cloud droplets concentration and decreases the radius of the cloud droplets (Twomey, 1977). The narrowing of the droplet size distribution reduces the chances of collision-coalescence processes and thus delays the precipitation (Albrecht, 1989). Later it was found that the initial suppression of rainfall due to aerosol indirect effects can then initiate feedback mechanisms within convective clouds to form deeper invigorated clouds (Andreae et al., 2004; Koren et al., 2005). The decrease in the size of cloud droplets improves the mobility and gets carried higher up due to updrafts in the convective clouds resulting in taller clouds (Koren et al., 2005; Fan et al., 2009; Koren et al., 2010). The ice formation above the freezing level results in the release of latent heat, which further invigorates the vertical extent of the cloud. This aerosol-induced cloud invigoration mechanism was initially observed over North Atlantic Ocean and Amazon during forest fires. The aerosol-cloud invigoration results in opposing cloud radiative effects. The increased vertical extent of the cloud reflects more incoming solar radiation and the cold tops of the large vertical clouds emit less longwave radiation back to space, thereby warming the atmosphere. But, the reflection of shortwave radiation masks the longwave warming due to invigoration (Koren et al., 2014). Sarangi et al.

(2017) observed a similar positive association between aerosol loading and rainfall during the Indian summer monsoon season, indicating the role of aerosols in deepening the cloud system.

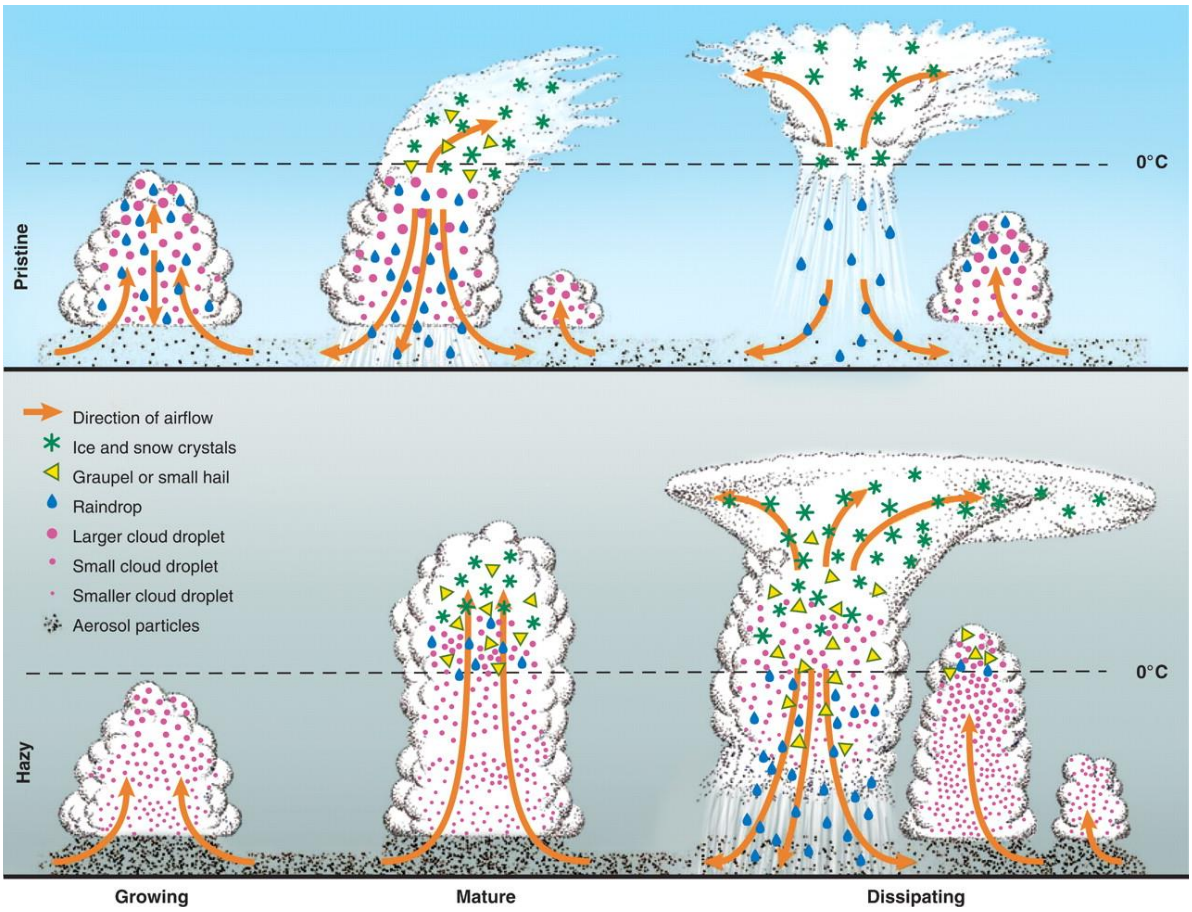

Figure 1.4 Schematic showing the aerosol-induced effect on cloud macro- and micro-physical properties in pristine (top) and polluted (bottom) atmosphere. Taken from Rosenfeld et al. (2008).

The anthropogenic aerosol forcing over the south Asian monsoon region was observed to slow down the overturning circulation and weaken the monsoon (Bollasina et al., 2011). The increased anthropogenic emissions over the south Asian region have increased the atmospheric stability and reduced monsoon rainfall (Ramanathan et al., 2005). The dust layer over the Indian region during the pre-monsoon is known to strengthen the monsoon circulation and bring forward the monsoon onset by elevated heat pump mechanism (Lau and Kim, 2006; Lau and Kim, 2010; Sarangi et al., 2016), but the recent analysis has shown a reduction in the dust layer which leads to weakening of monsoon circulation (Pandey et al., 2017). The dust aerosols over the north African and Arabian peninsula can modulate the monsoonal moisture flow towards India by heating the atmosphere (Vinoj et al., 2014). Another study over south Asia found short-term intra-seasonal suppression of rainfall due to aerosol forcing, which can elongate the break spells (Dave et al., 2017). Aerosol and cloud microphysical associations were found to alter diametrically with monsoon abundant or deficit years (Patil et al., 2017).

1.4 Research Gaps and significance of the study

The climate type of India is a tropical monsoon climate because of the manifestation of the resulting circulation and rainfall in response to seasonal variation in incoming solar radiation. India also experiences strong spatio-temporal heterogeneity in aerosol loading resulting from diverse sources, varying transport pathways, complex aerosol mixing, elevated aerosol layers. This forms complexity in understanding aerosol-related changes in clouds, radiation, rainfall, and climate. The Indo-Gangetic Plain (IGP) is a highly polluted region in the Indian landmass. This is due to its geographical location, regional meteorology, the influx of long-transported natural dust aerosols, and high emission rates due to its high emissions to high population density, industrial and agricultural activities. Several researchers have shown the increasing trend in aerosol loading over the Indian region, with the highest trend value over IGP. Moreover, the high aerosol loading is not only an urban problem due to increased urbanisation and population but also is just as harmful in rural areas as in urban areas in India (Ravishankara et al., 2020). Further, the high aerosol loading is not just limited to continental regions, but it can also be transported to long distances here onto adjoining seas (the Bay of Bengal and the Arabian Sea). Thus, the anthropogenic aerosols transported onto outflow marine regions can impact aerosol loading and associated changes over marine regions. The complex mixture of natural and anthropogenic aerosols further aids the complexity in understanding radiative properties over continental and marine regions to derive climatic impacts. Overall, aerosols are highly variable in size, composition and sources and the associated strong spatio-temporal variability make it extremely hard to quantify aerosols impact on climate. Unlike greenhouse gases, the impact is precise and certain. The following are some of the major gaps in aerosol research, particularly over the Indian region and adjoining seas; 1) spatio-temporal heterogeneity in aerosol sources leading to varying aerosol change from one location to another, 2) the contribution of long-range transported natural and anthropogenic aerosol onto outflow regions of the Bay of Bengal and the Arabain Sea, 3) aerosol-related changes in clouds, radiation, and rainfall, and thus hydrological cycle and climate, 4) the meteorological and cloud-mediated influence on rain properties, 5) aerosol impact on warm and cold rain initiation processes

1.5 Objectives of the study

Despite extensive research using multiple approaches (ground, aircraft, satellite and modelling) over more than two decades in India, the current understanding of aerosol-related changes to cloud, radiation, rainfall and climate remain elusive. This led to large uncertainties in estimating aerosols direct and indirect effects on climate. Thus, it is crucial to develop a better process-level understanding of aerosol processes and feedback mechanisms to accurately estimate the mean global radiative forcing under the warming anthropogenic future scenario. With this motivation, the objectives addressed in this thesis are:

1. to investigate spatio-temporal variability in aerosol loading over India and adjoining seas.
2. to examine aerosol-related changes in radiation and clouds over the Indian region and adjoining Seas.
3. to examine the response of rain properties to cloud properties and meteorological conditions.

1.6 Outline of the thesis work

The thesis consists of a total of seven chapters, including Introduction Chapter 1.

Chapter-2 presents the datasets (satellite, model reanalysis, and ground-based) and analysis tools used in the thesis.

Chapter-3 presents objective #1 to investigate the trend in aerosol loading over India and the adjoining Sea in recent years and illustrates the associated source and feedback mechanism (Thomas et al., 2019).

Chapter-4 presents objective #2 to examine the contribution of anthropogenic aerosols on the direct radiative forcing over outflow regions of the Bay of Bengal (Thomas et al., 2021b).

Chapter-5 presents objective #2 to study aerosol related changes in cloud properties and associated cloud radiative forcing over the Arabian Sea and the Bay of Bengal (Thomas et al., under preparation, 2021)

Chapter-6 presents objective #3 to investigate the influence of cloud properties on different rain regimes (Thomas et al., 2021a).

Chapter-7 summarises the overall conclusions of the thesis and presents the scope for future work.

Chapter 2

Data and Methods

2.1 Executive Summary

The lack of long-term observations has been a significant setback in understanding aerosol direct and indirect forcing and its feedbacks on the climate. The advancements in satellites, complex models, and reanalysis datasets have contributed to closing the knowledge gap in understanding the aerosol variability, primarily due to their global coverage and continuous operation. The finer resolution, better retrieval algorithms, and validation studies using ground-based observations and in-situ aircraft measurement have improved satellite measurements' reliability over the years. Reanalysis is the method of harmonizing available observations from various sources and ingesting them using a data assimilation scheme and atmospheric model, which gives a dynamically consistent estimate of recent climate. The rise in computational power and better representation of physics in atmospheric models, combined with the increase in frequency and coverage o observations, have made model reanalysis products a staple in the research community. The chapter describes various datasets, models, and techniques used in the study.

2.2 Satellite

2.2.1 MODIS

The Moderate-resolution imaging spectroradiometer sensor (MODIS) is onboard two of NASA's Earth Observing System (EOS), TERRA, and AQUA launched in May 2002 and December 1999, respectively. TERRA satellite is part of NASA's morning constellation satellites (AM-constellation) and crosses the equator at 10:30 AM local time. AQUA is part of the afternoon constellation or A-train that crosses the equator at 1:30 PM local time. With a swath width of 2330 km, MODIS covers the entire globe in 1-2 days. It measures the radiances in wavelengths ranging from 0.41–14.4 µm divided into 36 channels (Remer et al., 2005). The uncertainties from surface reflectance were reduced by employing three different algorithms; the Dark Target for land, Dark Target for the ocean and Deep Blue for the land surface. The spectrometer radiances provide aerosol and cloud properties at various processing levels. In this study, level-2 and level-3 data from collection 6.1 were used. Level-2 cloud products from TERRA and AQUA (MOD06L2 and MYD06L2) use reflectance infrared to the visible range to derive the cloud properties at 1 or 5 km resolution (Platnick et al., 2017). MYD08_D3 product provides daily level-3 aerosol and cloud products at $1^\circ \times 1^\circ$ resolution. AOD at 0.55 μm using the Dark Target and Deep Blue combined retrieval algorithm is used in the study (Hsu et al., 2013; Levy et al., 2013; Sayer et al., 2014). MODIS is used as a primary source of data for the study as it is extensively validated using ground-based measurements (Levy et al., 2010; He et al., 2017). The Deep Blue and Dark Target algorithms are evaluated extensively, both regionally and globally (Remer et al., 2008; Levy et al., 2010; Sayer et al., 2014; Bilal and Nichol, 2015; Mhawish et al., 2017). Both the algorithms were found to overestimate AOD over IGP region by 14-25%, with varying accuracy among the algorithms for various aerosol size range. The combined algorithm derived AOD performed better than individual Dark Target and Deep Blue algorithms over the IGP (Mhawish et al., 2017). The MODIS also measures thermal anomalies in the infrared wavelengths to determine active fire locations across the globe (Giglio et al., 2003). The collection-6 active fire location product originally at 1km resolution is regridded to $1^\circ \times 1^\circ$ and used in the chapter-3 analysis. MODIS data is publicly available at Level-1 and Atmosphere Archive & Distribution System (LAADS) Distributed Active Archive Center (DAAC) website (https://ladsweb.modaps.eosdis.nasa.gov/search/).

2.2.2 CERES

Clouds and Earth's Radiant Energy System (CERES) are a collection of broadband scanning radiometers launched on multiple polar-orbiting satellites (TRMM, Terra, Aqua, S-NPP, NOAA-20) with a mission to make long-term measurements of the Earth's radiation budget. The field of vision for the CERES instruments are narrow (10-24 km) with higher spatial resolution and measures radiances in three channels, namely shortwave (0.3 -5 µm), total-wave broadband (0.3 - 200 µm), and a narrowband water vapour window (8-12 µm) region (Wielicki et al., 1996). The instrument was calibrated pre-launch and spectral response functions were updated (Shankar et al., 2010). The accuracy of the sensors was tested post-launch and corrected (Thomas et al., 2010; Su et al., 2015; Loeb et al., 2016). The global monthly mean bias on TOA flux had an uncertainty of less than 0.2 W m^{-2} in the shortwave and 0.2– 0.4 W

m^{-2} in the longwave. The uncertainties were also high on snow/ice surfaces (Loeb et al., 2007). The new angular distribution model that converts radiances to flux measurements have improved the uncertainties on TOA fluxes from the previous version (Su et al., 2015). This study used the synoptic SYN1deg (Edition 4.1) product, which is gridded globally at 1° × 1° spatial resolution. This product uses fluxes from geostationary satellites to incorporate the diurnal variation between the observations of AQUA and TERRA satellites (Doelling et al., 2016). CERES data products are freely available at https://ceres.larc.nasa.gov/data/.

2.2.3 OMI

The Ozone Measuring Instrument is a nadir viewing spectrometer onboard NASA's EOS-AURA satellite. It measures solar backscatter radiation in the UV-visible range (264-504 nm) to estimate total ozone, aerosols, and other pollutants (SO_2, NO_2, BrO, formaldehyde, and Chlorine dioxide). In this study, we have used level-3 aerosol optical depth, absorption aerosol optical depth (AAOD), and UV aerosol index (UV-AI) from OMAERUVd (version-3) product which provides daily observations at 1° × 1° resolution (Torres et al., 2007). UV-AI and AAOD indicate the presence of absorbing aerosols like smoke and dust. The OMAERUV retrieval algorithm uses 354 and 388 nm reflectance to derive aerosol absorption optical depth (AAOD) at 388 nm (Torres et al., 2007; Curier et al., 2008; Torres et al., 2013). The tropospheric column NO_2 measurements at level-3 processing were also used in the study at a resolution of 0.25° × 0.25°. The retrieval algorithm of the tropospheric column NO_2 is described by Bucsela et al. (2013). The observed wavelength shifts were calibrated in-flight using a high-resolution solar reference spectrum (Voors et al., 2006; Dirksen et al., 2017). Jethva and Torres (2011) improved the OMI derived AOD by updating the OMAERUV algorithm and using the near UV measurements. The over estimation of AOD over the biomass burning sited was reduced and could reproduce the ground-based AOD over central Africa and northern India. The OMI data products are downloaded from the NASA Goddard Earth Sciences, Data and Information Services Center website (http://disc.sci.gsfc.nasa.gov)

2.3 Model reanalysis

2.3.1 MERRA-2

The Modern-Era Retrospective Analysis for Research and Application version 2 (MERRA-2) is the reanalysis dataset released by NASA's Global Modeling and Assimilation Office

(GMAO) (Gelaro et al., 2017). MERRA-2 takes advantage of the data availability of the satellite era and uses the updated version of the Goddard Earth Observing System-5 (GEOS-5) atmospheric general circulation model for climate analysis (Molod et al., 2015). It has advanced assimilation of aerosol observations and improvements in the representation of hydrosphere processes. The aerosol observations are assimilated, and the species-wise aerosol properties and radiative fluxes are generated using the Goddard Global Ozone Chemistry Aerosol Radiation and Transport model (GOCART) coupled with the GEOS-5 climate model (Randles et al., 2017). Multiple satellite AOD (MODIS, AVHRR, and MISR) inputs and ground-based (AERONET) AOD data are assimilated after careful cloud screening and homogenization. The GOCART aerosol module simulates the AOD and aerosol mixing ratio profile of 5 species; BC, OC, Sulphate, Dust, and Sea salt (Randles et al., 2017). The radiative fluxes data from MERRA-2 was evaluated against independent datasets and is able to capture the global trends and variability (Hinkelman, 2019). The dataset is available at a horizontal resolution of 0.5° × 0.625° and 72 pressure levels from the surface to 0.01 hPa.

The data is regridded to a grid resolution of 1° longitude × 1° latitude and was downloaded from NASA Goddard Earth Sciences (GES) Data and Information Services Center (DISC) https://disc.gsfc.nasa.gov/. The details of the variables used, products, and their resolutions are given in Table 2.1.

Table 2.1 MERRA-2 products and variables used in the study.

Product	Variables	Temporal resolution	Horizontal resolution
M2I3NXGAS	Aerosol Optical Depth at 550nm	3-hourly	1° × 1°
M2T1NXRAD	Longwave and shortwave radiation fluxes at TOA and surface; clear-sky with aerosol and clear-sky without aerosols	hourly	1° × 1°
M2I3NVAER	Aerosol mixing ratio at 72 model levels for five aerosol species (BC, OC,	3-hourly	1° × 1°

	Sulphate, Dust and Sea Salt)		
M2T1NXAER	Aerosol Optical Depth at 550nm for five aerosol species	hourly	1° × 1°
M2I3NVASM	Meteorological data at 72 model levels	3-hourly	1° × 1°

The clear-sky aerosol direct radiative forcing (ADRF) is calculated from the radiative fluxes (shortwave and longwave) by taking the difference between the fluxes in clear-sky conditions with aerosols and without aerosol. The hourly variables; SWGNTCLR (surface net downward shortwave flux assuming clear-sky), SWGNTCLRCLN (surface net downward shortwave flux assuming clear-sky and no aerosol), LWGNTCLR (surface net downward longwave flux assuming clear sky), and LWGNTCLRCLN (surface net downward longwave flux assuming clear-sky and no aerosol) is used to calculate ADRF at the surface ($ADRF_{SURF}$). Concurrently, ADRF at the top of the atmosphere ($ADRF_{TOA}$) is computed from hourly variables, SWTNTCLR (TOA net downward shortwave flux assuming clear sky), SWTNTCLRCLN (TOA net downward shortwave flux assuming clear-sky and no aerosol), LWTUPCLR (upwelling longwave flux at TOA assuming clear-sky) and LWTUPCLRCLN (upwelling longwave flux at TOA assuming clear-sky and no aerosol).

$$ADRF_{SUR} = (SWGNTCLR + LWGNTCLR) - (SWGNTCLRCLN + LWGNTCLRCLN) \tag{2.1}$$

$$ADRF_{TOA} = (SWTNTCLR + LWTUPCLR) - (SWTNTCLRCLN + LWTUPCLRCLN) \tag{2.2}$$

The ADRF on the atmosphere ($ADRF_{ATM}$), which indicates the energy trapped by all aerosols in the atmosphere, is calculated by taking the difference between $ADRF_{TOA}$ and $ADRF_{SURF}$.

2.3.2 ERA-5

ERA5 is the replacement for ERA-interim climate reanalysis product from the European Centre for Medium-Range Weather Forecasts (ECMWF) (Dee et al., 2011; Hersbach and Dee, 2016; Hersbach et al., 2020). It is produced using the Integrated Forecast System (IFS) Cycle 41r2 4D-Var assimilation system, and data is available from 1950 to the present in near real-time.

The atmospheric data is available at 37 model pressure levels (from surface to 1hPa), along with 2-dimensional or surface-level variables at a resolution of 0.25° longitude × 0.25° latitude. The data is freely available to download from the climate data store (CDS) website (https://cds.climate.copernicus.eu/cdsapp#!/home). The cross-validation of data against other reanalysis products like MERRA-2 and APHRODITE has shown agreeable comparison (Hoffmann et al., 2019; Baudouin et al., 2020). Vertical profiles of wind speed and convective available potential energy were used from ERA5 for analysis in Chapter-6. Wind shear was calculated from wind profile data, which is the difference in average wind speed at 700 hPa and 300 hPa.

2.4 In-situ measurements

2.4.1 Joss-Waldvogel disdrometer

Disdrometer is an instrument that measures the size distribution and velocity of hydrometeors. Joss Waldvogel disdrometer is a classic instrument used for analyzing raindrop size distribution and rainfall characteristics. It is an impact type disdrometer that has an electromechanical sensor that can measure the moment of raindrops falling on it (Joss and Waldvogel, 1967). The sampling interval was 30 seconds with a sensor area of 0.005 m^2. The size distribution is measure in 20 size bins within a size range of 0.3 to 5.3 mm. The rain rate can be derived from the equation given below

$$R = \frac{\pi \times 3.6}{6 \times 10^3} \times \frac{1}{F \times t} \sum_{i=1}^{n} (n_i \times D_i^3) \tag{2.3}$$

where *i* is the raindrop size bin, t is the time interval (30 seconds), F is the size of the sensor surface (0.005 m^2), n_i is the number of rain droplets measured in the raindrop size bin *i* and D_i is the size of the raindrop.

The impact sensor in the JW disdrometer has uncertainties due to the intrinsic noises and underestimates smaller raindrops in heavy rainfall. That is, the impact due to larger drops causes smaller drops to be unaccounted for in the measurement as the sensor needs time to recover from the initial impact. The delay in sensing due to impact by larger droplets has been accounted for and is known as deadtime correction. The drawbacks arising from the sensor mechanism have been discussed in previous studies. Tokay and Short (1996) has suggested removing samples of less than the total drop count of 10 and derived rain rate less than 0.1mm hr^{-1} to constraint the sampling errors. Following this path, in the analysis, we have eliminated samples with a drop count less than 10 or derived rain rate less than 0.5 mm hr^{-1}. Also, the 20th channel in the DSD measurement has been removed due to an unrealistically high droplet count. Therefore, only 19 channels (0.3 to 4.86 mm) have been used. In order to characterize raindrop size distribution, the gamma model distribution as described by Ulbrich (1983) is used in this analysis;

$$N(D) = N_0 \exp(-\Lambda \mathrm{D}) * D^{\mu} \tag{2.4}$$

where N(D) (m^{-3} mm^{-1}) is the number of raindrops with diameter D (mm), μ (unitless), and Λ (mm^{-1}) are shape and slope parameters, respectively. N_0 (m^{-3} mm$^{-1-\mu}$) is the intercept parameter. The shape parameter represents the breadth of the curve, and the positive value indicates that the curve is concave downwards. The slope parameter denotes the extension of the curve towards the broader diameter spectrum.

2.5 HYSPLIT trajectory model

The Hybrid Single Particle Lagrangian Integrated Trajectory (HYSPLIT) Model is used to compute air parcel trajectories and transport of pollutants along with it (Stein et al., 2016; Rolph et al., 2017). The model was developed by the NOAA air resources laboratory to track and forecast pollutants. The forward trajectories simulated by the model is used for analysis in chapter-4 to determine the outflow of contaminants into the Bay of Bengal. The Global Data assimilation system (GDAS) 1° × 1° meteorology data is used as an input in the PC -based version of the model. The GDAS assimilation data is used by the GFS model to normalise the observations into a gridded model space. A wide range of input data, from surface observations and balloon data to satellite observations, are used in GDAS assimilation (Kanamitsu, 1989). The coarse resolution of the GDAS data into the HYSPLIT model could have uncertainties related to the terrain closer to the surface. Hence, the trajectory calculations are used at a minimum origin height of 500 m from ground level to avoid such uncertainties.

Chapter 3

Recent trends in winter-time aerosol loading and radiative forcing

3.1 Executive summary

In this chapter, the trends in aerosol loading in recent years over India and the adjoining Sea and attributed radiative forcing and feedback mechanisms are examined using long-term (2002-2017) datasets from space-borne sensors and model reanalysis datasets. Several researchers showed an increasing trend in aerosols over India using ground-based and satellite observations. But the changes in aerosol loading during the recent decade compared to the previous decade were not quantified. With this intriguing question, we attempt to estimate trends in aerosol loading over different regions of the Indian region in recent years during the winter season. The major finding is that the trend in aerosol loading was higher over central India than much polluted Indo-Gangetic plains. The Arabian Sea is in the downwind direction of central India, also had a higher increment in aerosol loading as compared to the Bay of Bengal. The calm meteorological conditions in the winter season are known for their higher concentration of anthropogenic aerosols. The increase in the absorbing aerosols was found to correlate temporally and spatially with the rise in the fire counts associated with biomass burning. The aerosol induced atmospheric warming was found to be higher in recent years over central India as compared to other regions. Enhanced lower-tropospheric stability was observed over central India and the Arabian Sea in recent years. A stable atmosphere would favour the accumulation of aerosols in the lower troposphere and further increase the aerosol loading. Thus, creating a positive feedback mechanism.

3.2 Literature review

The long-term measurements of aerosols have shown that the rise in aerosol loading has coincided with the centres of increasing industrialization, population, and urbanization, i.e., the South East Asian region (Mehta et al., 2016). A decrease in aerosol loading has been observed over Europe and American continents by both satellite and ground-based measurements, and the decrease has been attributed to a reduction in anthropogenic emissions in the region (Smith et al., 2011; Hsu et al., 2012; Yoon et al., 2012; Mao et al., 2014; Mehta et al., 2016; Yang et al., 2020). The Indian landmass and surrounding marine regions experience a tropical and sub-tropical climate and the seasonal reversal of winds due to the monsoon circulation. The changes in the wind pattern between the season modulate the transport and ventilation of aerosols in the region. Throughout the year, the Indo-Gangetic Plains (IGP) has high aerosol loading due to anthropogenic activities related to high population density (urbanization, industrialization, biomass, and fossil fuel burning) and transport of mineral dust aerosols (Dey et al., 2004; Dey and Di Girolamo, 2010; Srivastava et al., 2012b). The seasonal variation in aerosol composition, complex mixing of aerosol species, regional variations, and the high emissions makes the Indian region and its outflow marine regions a focus of aerosol studies in the last two decades. Several observational campaigns and field studies like the Indian Space Research Organization-Geosphere Biosphere Programme (ISRO-GBP), Arabian Sea Monsoon Experiment (ARMEX), Indian Ocean Experiment (INDOEX), Winter Fog Experiment (WIFEX), have been conducted to study the aerosol composition, properties and its radiative effect over the region. The first land campaign under the ISRO-GBP was conducted over the peninsular region during the dry winter season (February - March 2004) and observed high fine mode aerosol concentration over coastal urban regions compared to the semi-arid interior region (Moorthy et al., 2005b). The second campaign was conducted over three sites spread out over the IGP (Delhi, IIT Kanpur, and IIT Kharagpur) during December 2004 and found high aerosol concentration with 75% total mass contributed by fine aerosols (Tripathi et al., 2006). INDOEX was conducted over the north Indian Ocean and studied the composition of aerosols and radiative forcing due to the outflow from the Indian region during the dry winter months. The north-south gradient in the aerosol concentration with a higher concentration of accumulation mode particles towards the north was observed, which becomes shallower with increased wind speed. They found that the anthropogenic haze that extends over the north Indian ocean affects the clouds through the first indirect effect. The absorbing nature of the aerosol particles resulted in a decrease in surface solar radiation and an increase in atmospheric warming in the lower troposphere, affecting the hydrological cycle (Ramanathan et al., 2001b). ARMEX was conducted during March 2003 under the Indian Climate Research Programme and observed the increase in AOD and BC concentration with change in wind trajectories

(Moorthy et al., 2005a; Rao, 2005). The WIFEX was organized to characterize the heavy winter fog events over the IGP region during the winter season (Ghude et al., 2017).

The aerosol loading over the Indian region and its influence on air quality, human health, crop yield, radiation forcing, hydrological cycle, and regional climate has been studied extensively in the last few decades (Satheesh et al., 2008; Lawrence and Lelieveld, 2010; Bollasina et al., 2011; Burney and Ramanathan, 2014; Vinoj et al., 2014; Latha et al., 2017; Sarangi et al., 2018). The strong seasonality in the aerosol composition, with a strong influence of anthropogenic aerosols in the post-monsoon and winter seasons, followed by strong modulation due to natural dust aerosols in the pre-monsoon and monsoon season, adds to the complexity in understanding the impacts of aerosols and their trend in the region (Ramanathan and Ramana, 2005; Srivastava et al., 2012b). The low temperature, wind speed, and shallow boundary layer lead to the accumulation of aerosols near the surface and reduce the chance of ventilation. The lack of precipitation leads to lesser removal of aerosols by wet removal processes, which further adds to the worsening of air quality (Moorthy et al., 2005b; Pan et al., 2015; Ghude et al., 2017; Bharali et al., 2019; Kanawade et al., 2020). The weak winds lessen the natural dust aerosol loading, and the aerosol composition during this season is predominantly of anthropogenic origin (Nair et al., 2007; Safai et al., 2008; Ghude et al., 2017).

Several studies have shown the increase in the aerosol loading over the Indian region using long-term satellite and ground-based measurements (Dey and Di Girolamo, 2010; Dey et al., 2012; Kaskaoutis et al., 2012; Babu et al., 2013; Moorthy et al., 2013; Srivastava, 2017; Kumar et al., 2018). A significant increase in aerosol loading was observed by Dey and Di Girolamo (2011), where the AOD was seen to increase in the range of 0.01-0.04 year^{-1} using MISR AOD data from 2000-2010. Aerosol Robotic Network (AERONET) ground-based AOD observations from Kanpur (located in Central IGP) also showed an increasing trend in AOD of 0.0062 year^{-1} (Kaskaoutis et al., 2012). The rise in AOD (0,0053 year^{-1}) was also observed over northern India and surrounding seas using SeaWiFS measurement from 1997 to 2010 during the dry winter and post-monsoon seasons when the outflow from IGP is active (Hsu et al., 2012). Ramachandran et al. (2012) used Level-2 MODIS data from the last decade (2000-2009) and found an increase in AOD over all major cities due to urbanization. The increase in aerosol loading over New Delhi is attributed to anthropogenic emissions, and the Northeast Indian region has seen an increase in forest fires which increased AOD over the region. The long-term ground-based observations from ARFINET (Aerosol Radiative Forcing over India) spread across the country has shown a statistically significant increasing trend in aerosol loading over India during winter season (Babu et al., 2013). The average rate of increase in AOD over the Indian region is 2.3% as compared to the 1985 value, and the trend has become steeper in the last decade (Moorthy et al., 2013). The MODIS AOD and Ångström exponent trends (2001-2014) have shown an increase in fine aerosols over the Indian region on all seasons, and more than 70% of the Indian region shows a high increase in AOD during winter and post-monsoon seasons (Srivastava, 2017). A similar study by Kumar et al. (2018) has shown a relatively high aerosol loading over IGP loading with a dominance of fine mode aerosols during the dry winter season. Previous studies have highlighted the trend and high pollution over IGP and its outflow over BoB due to anthropogenic emissions.

The recent global trends in the aerosol direct radiative forcing have shown a decreasing trend at the top of the atmosphere and at the surface except for South Asia, Africa, and the middle east region, where a significant increase in atmospheric warming is observed (Subba et al., 2020). The improvements in the observational and modelling capacities in the last decades have reduced the uncertainties regarding the climatic impact of aerosols (IPCC, 2013). But the heterogeneity in aerosol sources and the spatio-temporal variability of aerosols and their effect on the regional circulation leads to complexity and low confidence in understanding the aerosol feedback in the climate. We used 15 years of satellite and model reanalysis datasets in tandem to analyze the recent trends in composite and species-wise aerosol loading and examine the region-wise increase in hazy days during the dry winter season (November-February). A day with high aerosol loading (AOD greater than 66th percentile) is considered as a hazy day, and the analysis is carried out during the dry winter season since the anthropogenic aerosols dominate the aerosol loading.

3.3 Data analysis methodology

The study region is bounded by a box 7°-38°N and 66°-94°E. The region is subdivided into four; Indo-Gangetic Plain (IGP), Central India (CI), Bay of Bengal (BoB), and Arabian Sea (AS), all of them of comparable areas as shown in Fig. 3.1. Level-3 AOD from MODIS onboard the AQUA satellite is used in this study for a time period of 2003-2017. MODIS active fire locations product is also used, which helps identify large-scale biomass burning in the area. The UV-AI from OMI onboard AURA satellite is used along with MODIS AOD to understand the changes in absorbing aerosols in the region. The species-wise AOD (sulfate, BC, OC, sea salt, and dust) and the estimated radiative fluxes are obtained from the MERRA-2 products. The methodology for calculating ADRF from the radiative fluxes is explained in Chapter-2. The wind and potential temperature (θ) profile are taken from GDAS, and Lower Tropospheric stability is calculated from the potential temperature as LTS = θ_{700}-$\theta_{surface}$, where θ_{700} is the potential temperature at 700 hPa (free troposphere) and $\theta_{surface}$ is the potential temperature at the surface.

Table 3.1 shows the variables, products, and their resolution in which they are used in the study. The detailed description, retrieval algorithm, and validation of the data products are already explained in Chapter-2. Fog is a common phenomenon over the IGP during the winter season (Ghude et al., 2017; Hingmire et al., 2019). Hence, to avoid the AOD retrievals being contaminated by fog/cloud, AOD > 1.0 has been eliminated from the data. The winter fog becomes dense overnight and starts to dissipate after dawn due to effective ventilation. The AQUA instrument has an overpass at about 1:30 PM local time, when the fog would have thinned out, thereby decreasing the chances of fog influencing the measurements.

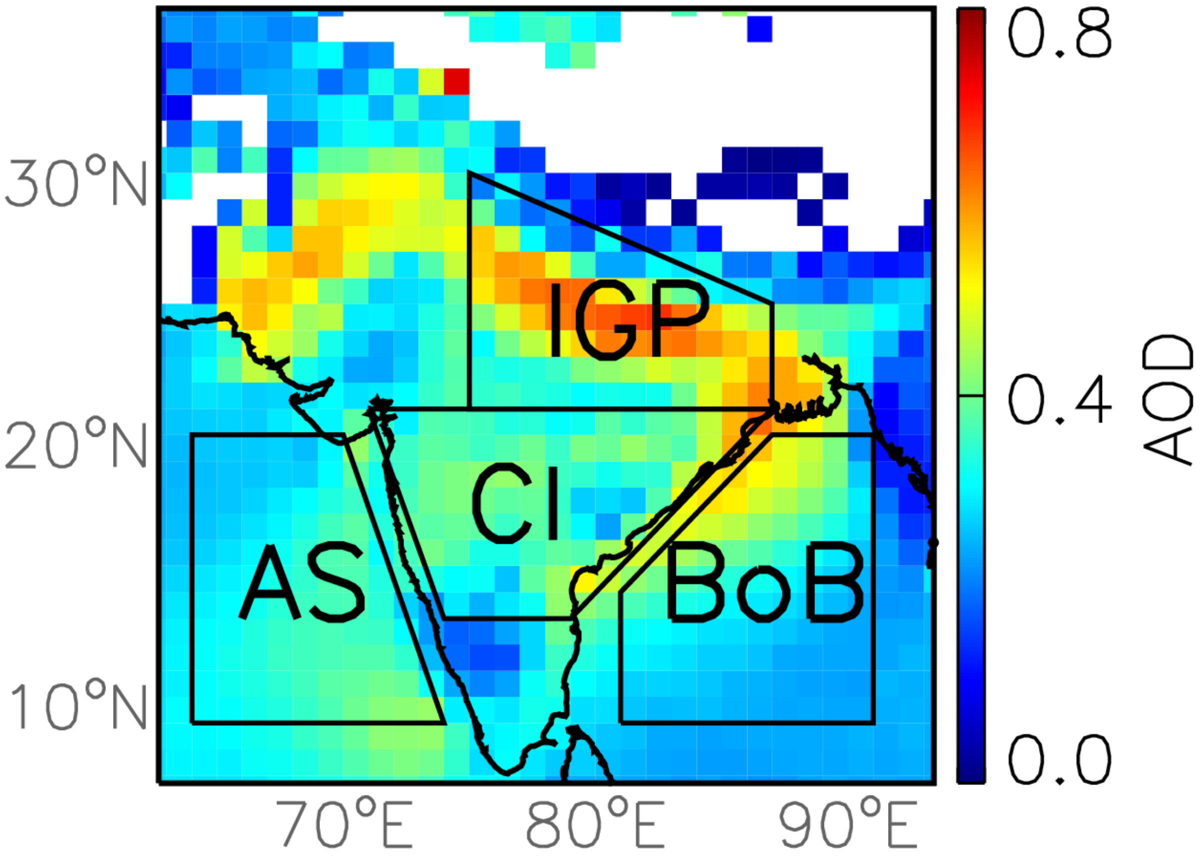

Figure 3.1 Averaged spatial distribution of MODIS AOD for November through February over the time period 2003-2007 (past years). The study regions are bounded by the solid black line. IGP: Indo-Gangetic Plain, AS: Arabian Sea, CI: Central India and BoB: Bay of Bengal.

Table 3.1 Summary of the satellite and model reanalysis datasets used in this study.

Data Source and Version	**Parameter**	**Temporal resolution**	**Spatial resolution**
MODIS, AQUAL3, C6.1	AOD	Daily,13:30	1°×1°
AURA OMI, V3	Absorption AOD	Daily,13:30	1°×1°
MODIS, AQUA L2, C6.1	Fire counts	Daily,13:30	1 km×1 km
MERRA-2	AOD and SW fluxes	Hourly, 11:00-14:00	0.5°×0.625°
NOAA-NCEP GDAS	Wind fields and Temp.	6-hourly, 11:30	1°×1°

The aerosol loading is highly variable over the Indian region, both spatially and temporally, and in order to normalize this variation, the percentile bin approach is used. The daily AOD is segregated into three percentile bins; less than 33rd, between 33rd and 66th, and greater than 66th, over each 1° × 1° grid based on the AOD values from November to February of 2003. The three bins are named as three distinct aerosol regimes; low (<33rd percentiles), medium (33rd – 66th percentiles), and high or hazy (>66th percentiles).

3.4 Trends in winter-time aerosol loading over India and adjoining seas

The spatial distribution of MODIS AOD and OMI UV-AI during the past and recent years is given in Fig. 3.2. The high aerosol loading over the IGP can be seen in the average plots (Fig. 3.2a, b, d, and e), as reported by previous studies (Dey and Di Girolamo, 2010; Hsu et al., 2012). The increase in aerosol loading, especially the absorbing species, is clearly evident in recent years, but the difference in aerosol loading over IGP is less magnitude over the years (Fig. 3.2c and f). The increment of aerosol loading between past and recent years varies regionally due to differences in the sources and meteorological conditions (Babu et al., 2013; Moorthy et al., 2013). The increase in AOD and UV-AI over central India denotes a distinctive enhancement of absorbing particles like soot/smoke and mineral dust over the region. The calm winds during the dry winter season reduce the chance of mineral dust influence, along with the decrease in average windspeed over the region (Fig. 3.3) in recent years makes it more unlikely. The reduction in the wind speed poses a question on the potential sources of the absorbing aerosols over the CI region.

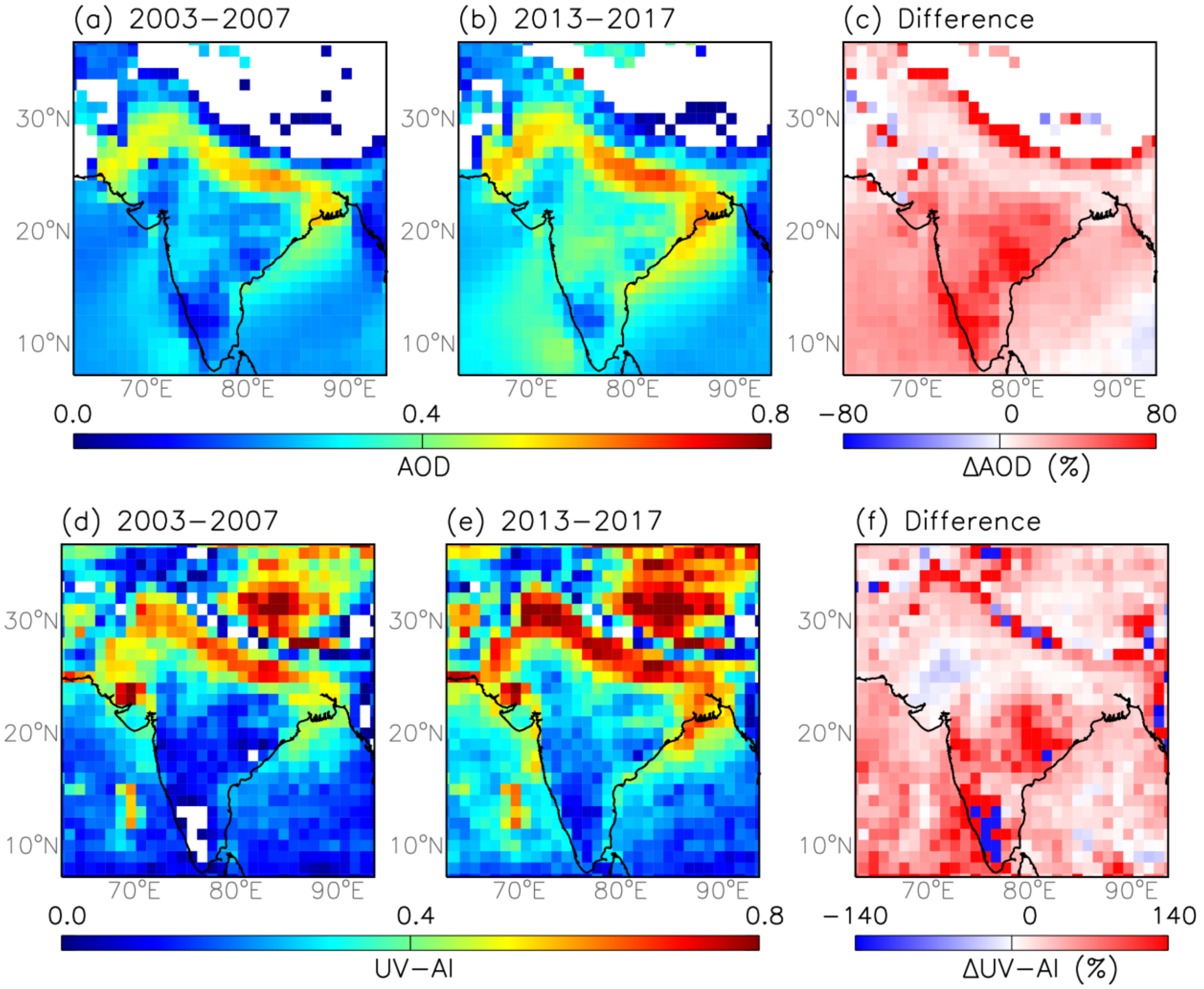

Figure 3.2 Averaged spatial distribution of MODIS AOD for November through February over the time periods (a) 2003-2007 (past years), (b) 2013-2017 (recent years) and (c) the percentage difference between the recent and the past years. Averaged spatial distribution of OMI UV-AI for November through February over the time periods (d) 2003-2007, (e) 2013-2017 and (f) the percentage difference between the recent and the past years.

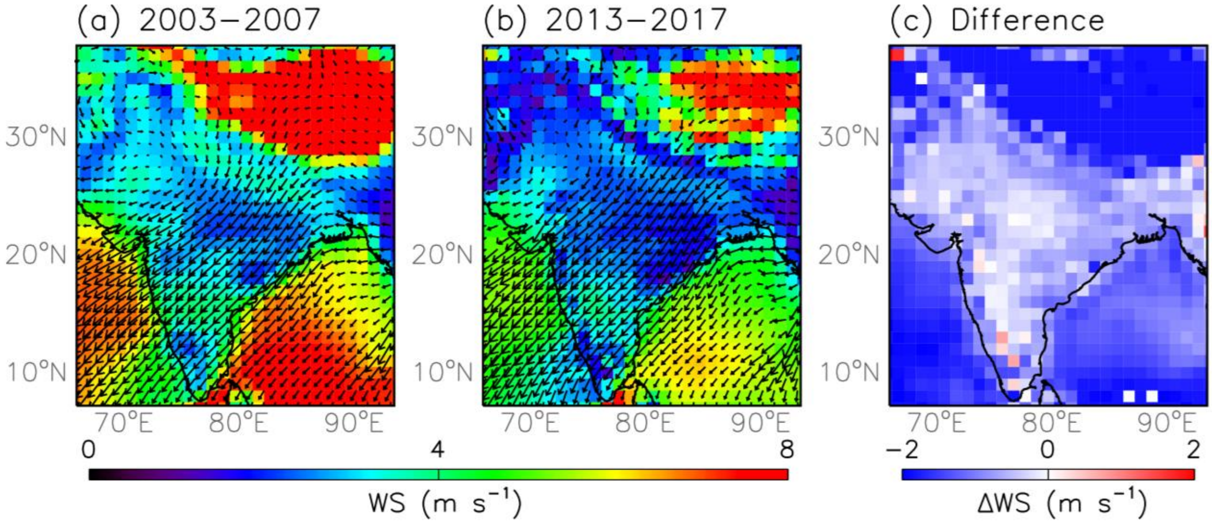

Figure 3.3 The wind speed and vectors at 950hPa level during the past (a) and the recent (b) time periods. (c) The difference in wind speed between the recent and the past years.

3.5 Trends in the number of hazy days

In order to compare the change in the low to high aerosol loading days between the past and the recent years, the daily AOD observations are segregated into three percentile bins (low, medium, and high), as explained in Section 3.2. The number of days in each bin is counted for the past (Fig. 3.4a) and recent (Fig. 3.4b) years in each 1°×1° grid point. The high polluted days have increased all over the study region with a rapid increase over CI and AS. The significant positive trend over the CI and AS in the number of days (Fig. 3.4c) also concurs with the observed increase in hazy days, as seen in Fig. 3 4b. The trend in the low to medium aerosol loading days was negative over India and adjoining Seas.

The increment is more significant over CI (~2.6 days/season) than the polluted IGP (~1.8 days/season). Similarly, the rate is higher over the AS (~1.9 days/season) than over the BoB (~1.1 days/season), where the BoB is known to be much more polluted than AS due to its outflow from IGP (Hsu et al., 2012; Srivastava, 2017). The number of days with high aerosol loading (hazy days) has increased two-fold in all four regions in the year 2017 compared to 2003 (Fig. 3.5), indicating the shift towards much higher aerosol loading in recent years. Previous studies have reported the increase in aerosol loading over the Indian region due to anthropogenic emissions (Dey et al., 2012; Ramachandran et al., 2012; Babu et al., 2013; Moorthy et al., 2013; Srivastava, 2017), but our results highlight the pronounced positive trend over CI and AS. Moorthy et al. (2013) used ground-based AOD observations from ARFINET and found that during 2000-2011 the rate of AOD increment was much more rapid than in the previous decade. The study also found a higher increasing trend over central peninsular (3.63%/year) India than southern and northern India during the winter season. Kumar et al. (2018) showed a less significant trend over the IGP in the last decade. Long-term near-surface measurements combined with satellite observations show that even though there is an increase in columnar AOD, the surface BC over the Indian region shows a decreasing trend during 2007-2016 (Manoj et al., 2019).

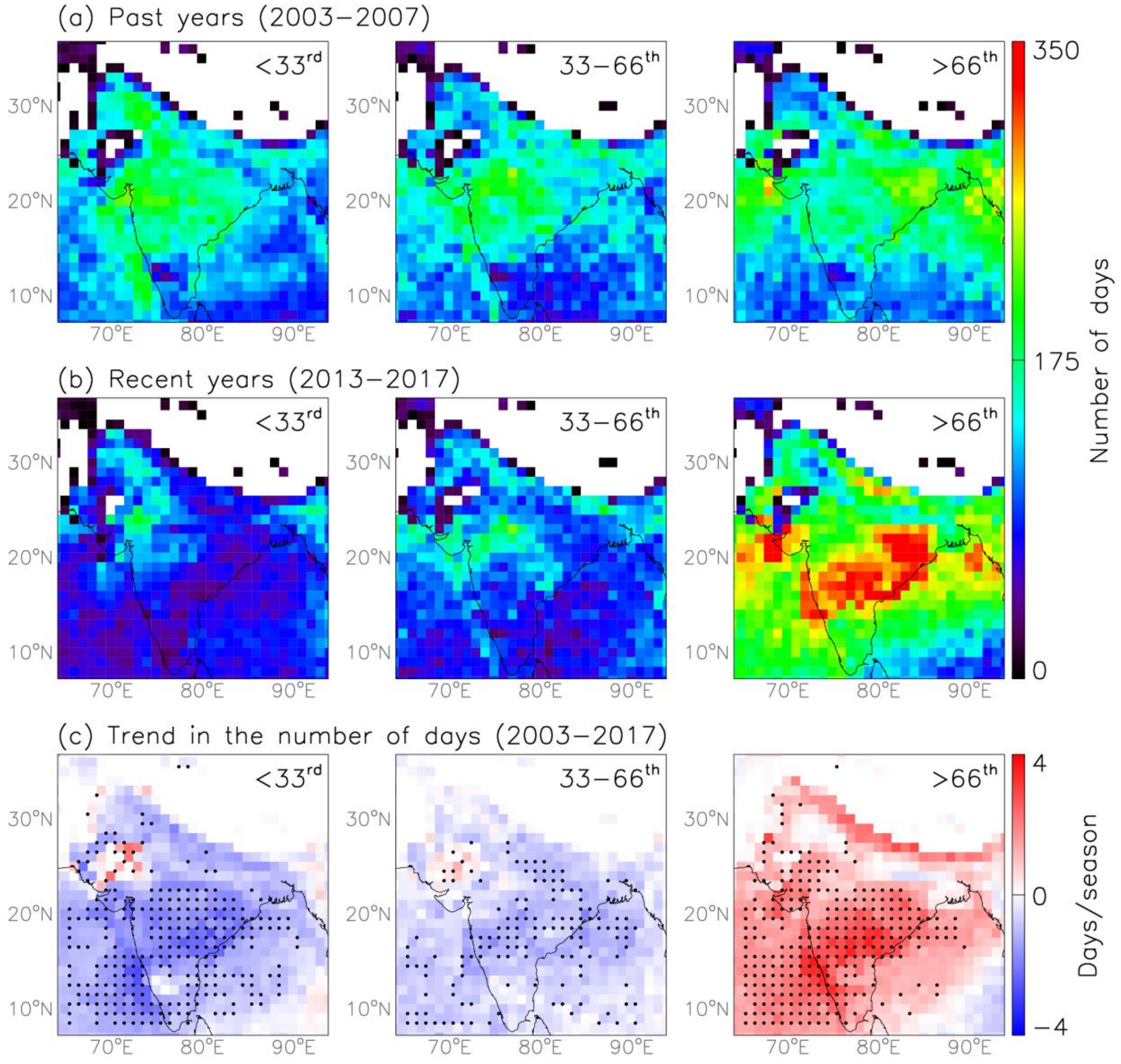

Figure 3.4 The trend in the number of days with aerosol loading from low to high regimes. (a) The number of days with low (< 33rd percentile value of AOD), medium (33-66th), and high

(>66th) aerosol loading for November-February of 2003-2007 (b) same as (a) except that for 2013-2017. (c) The trend in the number of days with <33rd, 33-66th, and >66th percentile values of AOD for November -February of 2003-2017. Black dots indicate statistical significance using the Student's t-test at a confidence interval of 95%.

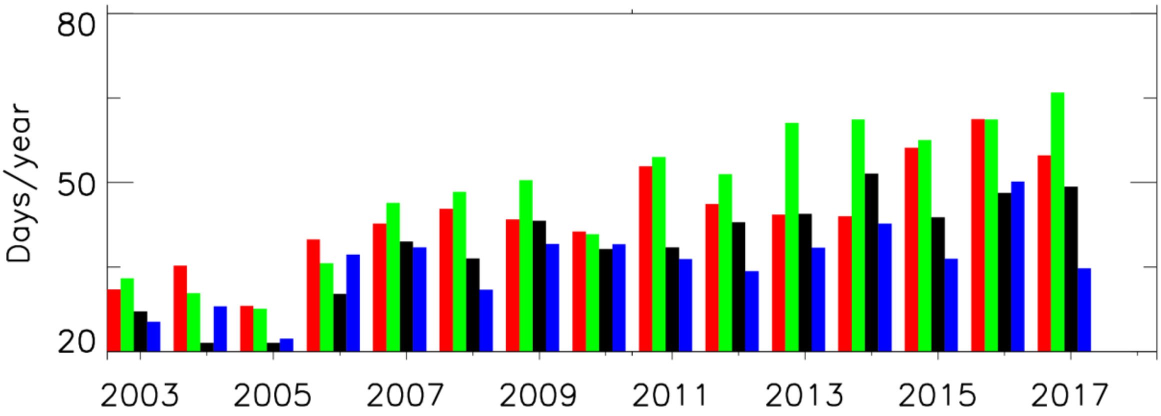

Figure 3.5 Timeseries of the average number of days with AOD greater than 66th percentile value from 2003-2017 for all study regions.

The percentage frequency distribution of MODIS AOD is seen to be skewed towards the higher AOD when the difference between the past and the recent years is calculated (Fig. 6a). The frequency of low aerosol loading (AOD < 0.1) is decreasing, whereas the frequency of medium to high aerosol loading (AOD > 0.4) is increasing over all the regions. The AOD from the MERRA-2 reanalysis product also concurred with this result (Fig. 3.6b). The difference in the percentage frequency distribution for MERRA-2 species-wise AOD was calculated. The carbonaceous aerosols (BC+OC; Fig. 3.6c) and sulfate aerosols (Fig. 6d) show a significant difference similar to that of MODIS AOD (Fig. 3.6a) and MERRA-2 composite AOD (Fig. 3.6b). The BC and OC AOD are combined since they are co-emitted from their sources, i.e., anthropogenic emissions and biomass burning. Natural aerosols like SS and dust are generally transported onto the IGP and CI by strong winds, which are generally absent in the season (Fig. 3.4). The changes in the natural aerosols (Fig. 3.6e and f) are negligible compared to anthropogenic aerosols (Fig. 3.6c and 3.6d). The variation in the intensity-frequency of composite AOD and anthropogenic AODs (Fig. 3.6a-d) is much more visible in AS and CI regions than in IGP. This leads to the question of sources of such emissions in these regions. The difference in the vertical profile of aerosol mixing ratio of various species shows a significant enhancement of carbonaceous aerosols from surface to 700 hPa (~3.1km) in recent years, which implies a near-surface source. The interesting observation is that the enhancement of BC and OC is much higher over CI than IGP.

Over the marine regions, the changes in the AOD are more prominent over AS than BoB. Also, the difference in the anthropogenic species is three times higher than in sea salt and dust (Fig. 3.6). This means that the aerosol composition over the marine regions is modulated by the outflow from the continental regions, which is predominantly anthropogenic emissions. The mean wind circulation pattern over the region confirms the fact (Fig. 3.3), and AS is located in the downwind region of CI. Therefore, the BC, OC, and sulfate aerosols were transported over from the local emission sources from CI over to the AS. The higher percentage change over the AS compared to BoB, even though BoB is known to have much higher aerosol loading than AS. Previous studies have shown that the contribution from anthropogenic outflow is much higher over the BoB during winter due to the IGP outflow (Lawrence and Lelieveld, 2010; Kaskaoutis et al., 2011).

Interestingly, the intensity-frequency changes in AOD observed over the AS region are more prominent compared to the BoB region. In addition, the anthropogenic species over the AS, particularly BC, OC, and sulfate, are found to be three times higher than sea salt aerosols during the winter season (Fig. 3.6). The mean wind circulation clearly illustrates predominant northeasterly flow over the continental region, mostly flowing into the AS, i.e., the AS is located in the downwind regions of CI (Fig. 3.3). Thus, the BC, OC, and sulfate aerosols over the AS are probably transported from local emissions over CI. This also explains the high percentage change in aerosol loading over the AS than the BoB in recent years (Fig. 3.6). This suggests that the increase in continental aerosol emissions has a profound impact on the aerosol loading over the adjacent marine regions. This finding is different from previous investigators as those studies indicated that the aerosol loading over the BoB is higher than over the AS and that the relative contribution of anthropogenic aerosol mass tends to be higher over the BoB (Ramachandran and Jayaraman, 2003; Lawrence and Lelieveld, 2010; Kaskaoutis et al., 2011; Sanwlani et al., 2011). It could be noted that most of these studies used data before the year 2012, except the recent study by Srivastava (2017), further highlighting the significance of our finding on aerosol perturbations in the recent five years (2013-2017).

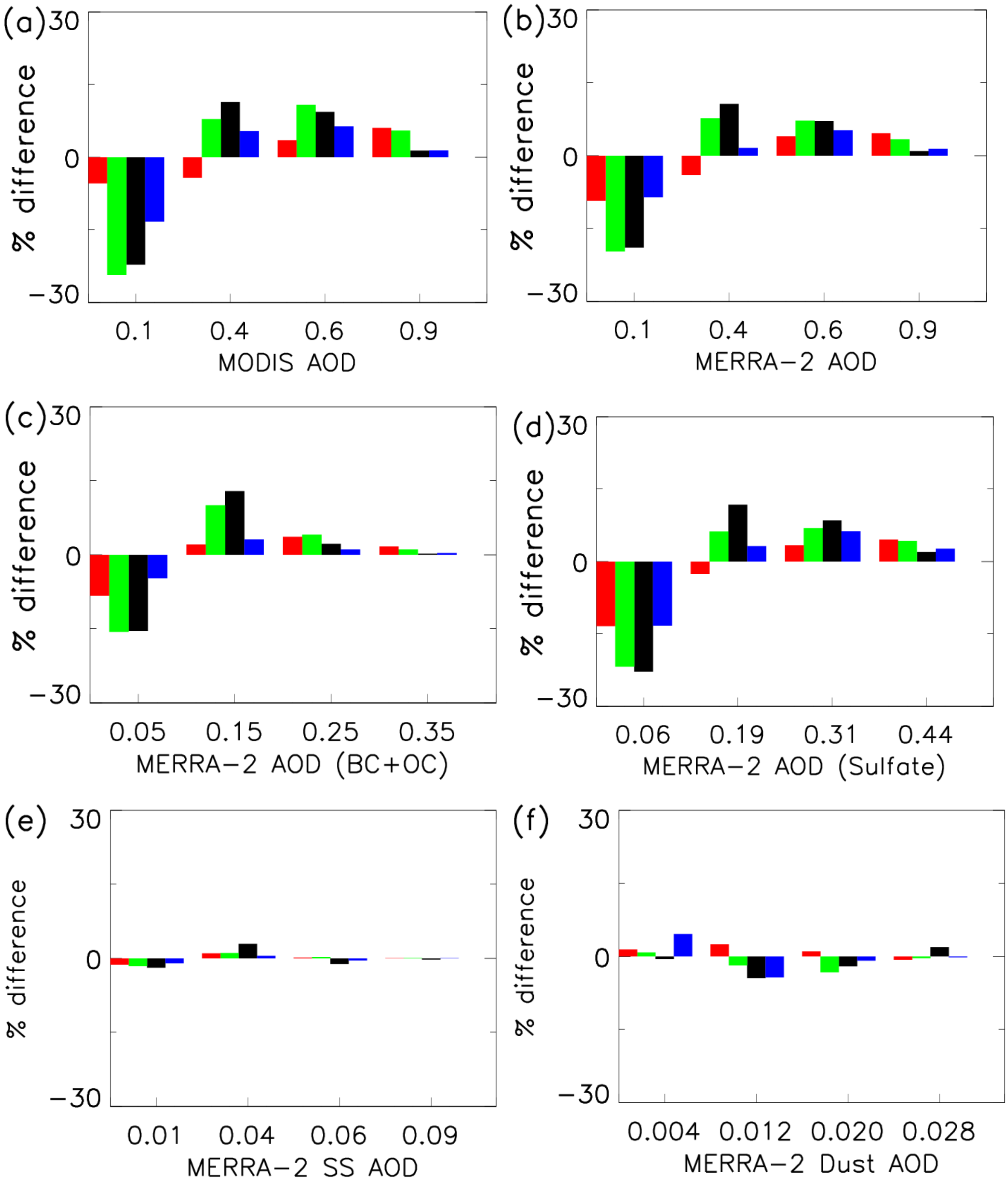

Figure 3.6 The percentage difference in the frequency distribution of (a) MODIS AOD, (b) MERRA-2 AOD, (c) MERRA-2 (BC+OC) AOD and (d) MERRA-2 sulfate AOD between the past and the recent years over different study regions.

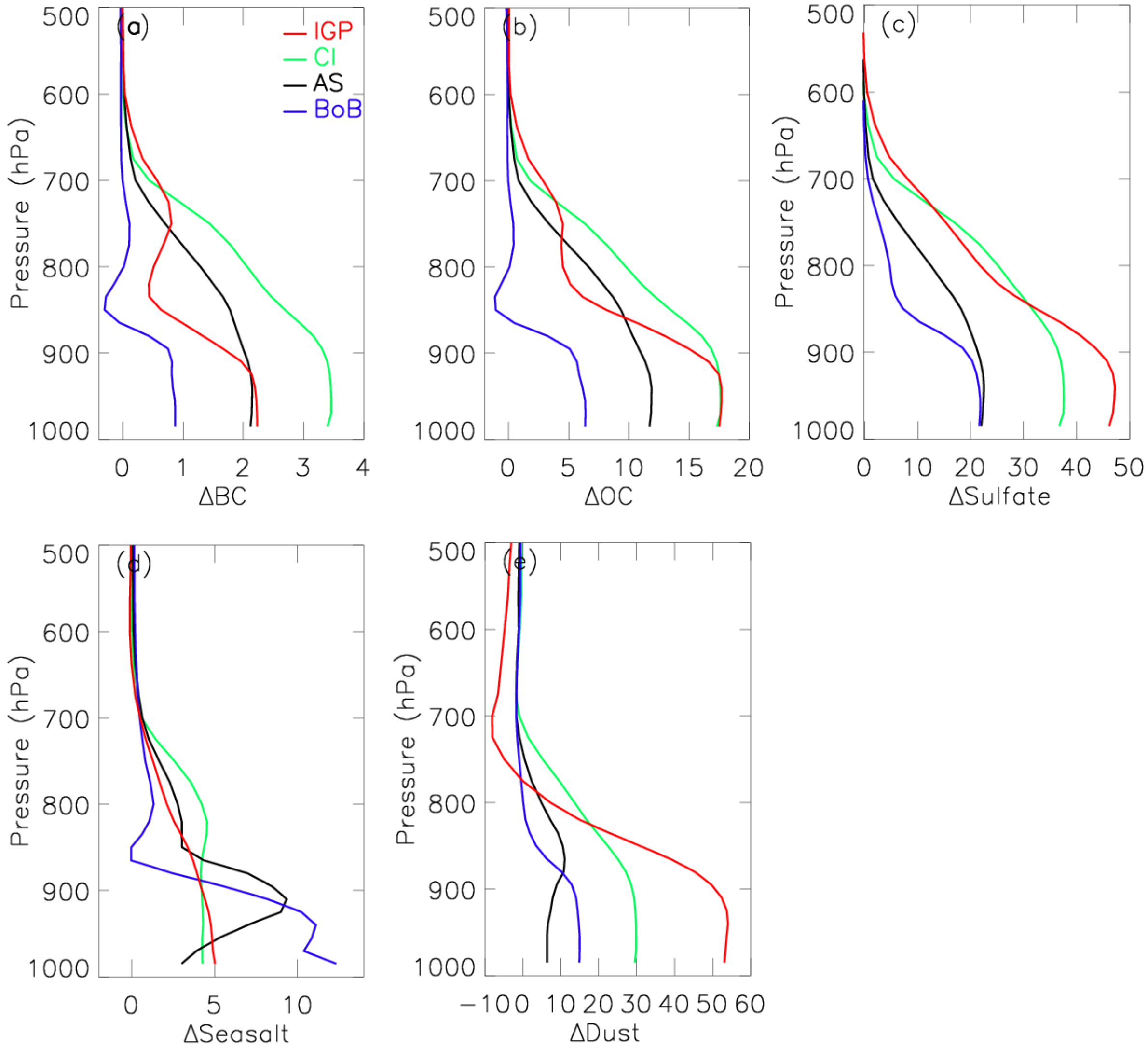

Figure 3.7 The difference in MERRA-2 mixing ratio profile (in 10^{-10} kg kg^{-1}) over various regions of (a) BC, (b) OC, (c) sulfate, (d) sea salt and (e) and Dust aerosols between the past and the recent years during November-February, 2003-2017.

3.6 Changes in fire counts from biomass burning

Aerosol loading has been rising in developing countries like India due to rapid urbanization (Mehta et al., 2016; Han et al., 2018; Haque and Patel, 2018). In India, out of the ten most populated metropolitan cities which are known for rapid development in the last decade are located within the CI region (Mumbai, Pune, Hyderabad, Bangalore, and Nagpur) and are showing changes in the land use and land cover (Rathee, 2014). Forests, shrubs, and croplands cover a significant fraction of the CI, and hence, biomass burning is common, especially in two states, Madhya Pradesh and Maharashtra. The fires from these two states account for about

36% of total fire counts in India (Sahu et al., 2015). The shifting cultivation practices along the eastern Ghats region make it an active fire hotspot. The deciduous forest in this area is cleared through burning during the late winter season to make way for agriculture (Prasad et al., 2008; Vadrevu et al., 2015). Therefore biomass burning is a major contributor to the carbonaceous aerosols in the region (Venkataraman et al., 2005) and explains the recent increase in aerosol loading.

The fire counts retrieved from MODIS reflectances were regridded into 1° × 1° total fire counts and are plotted in Fig. 3.8. The accumulated fire counts in during the winter of past and recent years are shown in Fig. 3.8a and 3.8b. The difference between the fire counts in the two periods is shown in Fig. 3.8c, and it spatially correlates with the anomalous increase in aerosol loading over CI (Fig. 3.2c and f). Thus, the recent increase in aerosol loading can be attributed to the increase in fire activities in the region. To further elucidate the argument, the monthly fire count difference (Fig. 3.9) is compared with the monthly trend in high aerosol loading days (Fig. 3.10). The high aerosol loading days match with the areas of high fire counts. The fire activities are also high on the western IGP near Punjab and Haryana in this season. But when we calculated the percentage contribution of fire counts between IGP and CI (Fig. 3.8d), a significant increase in the fire counts over CI was observed. The fire counts have increased by about 55% from 2003 to 2017. The number of gridded pixels (n=75) is equal in the sub-regions we have considered so that the comparison will be valid. The biomass burning over the northwestern IGP has been studied extensively and is related to severe air pollution over the IGP region (Andreae and Merlet, 2001; Cusworth et al., 2018; Liu et al., 2018; Andreae, 2019; Kanawade et al., 2020). Transport model studies have attributed 7-78% of fine mode aerosol mass over New Delhi to the biomass burning from Punjab and Haryana during the dry winter season (Cusworth et al., 2018). The aerosols from the biomass burning in the northwest states are transported to CI as well as northern BoB (Kaskaoutis et al., 2011; Sarkar et al., 2018). Therefore, the observed enhancement in the high pollution days over the CI can be attributed to the long-range aerosol transport from the northwestern IGP and the increased local biomass burning.

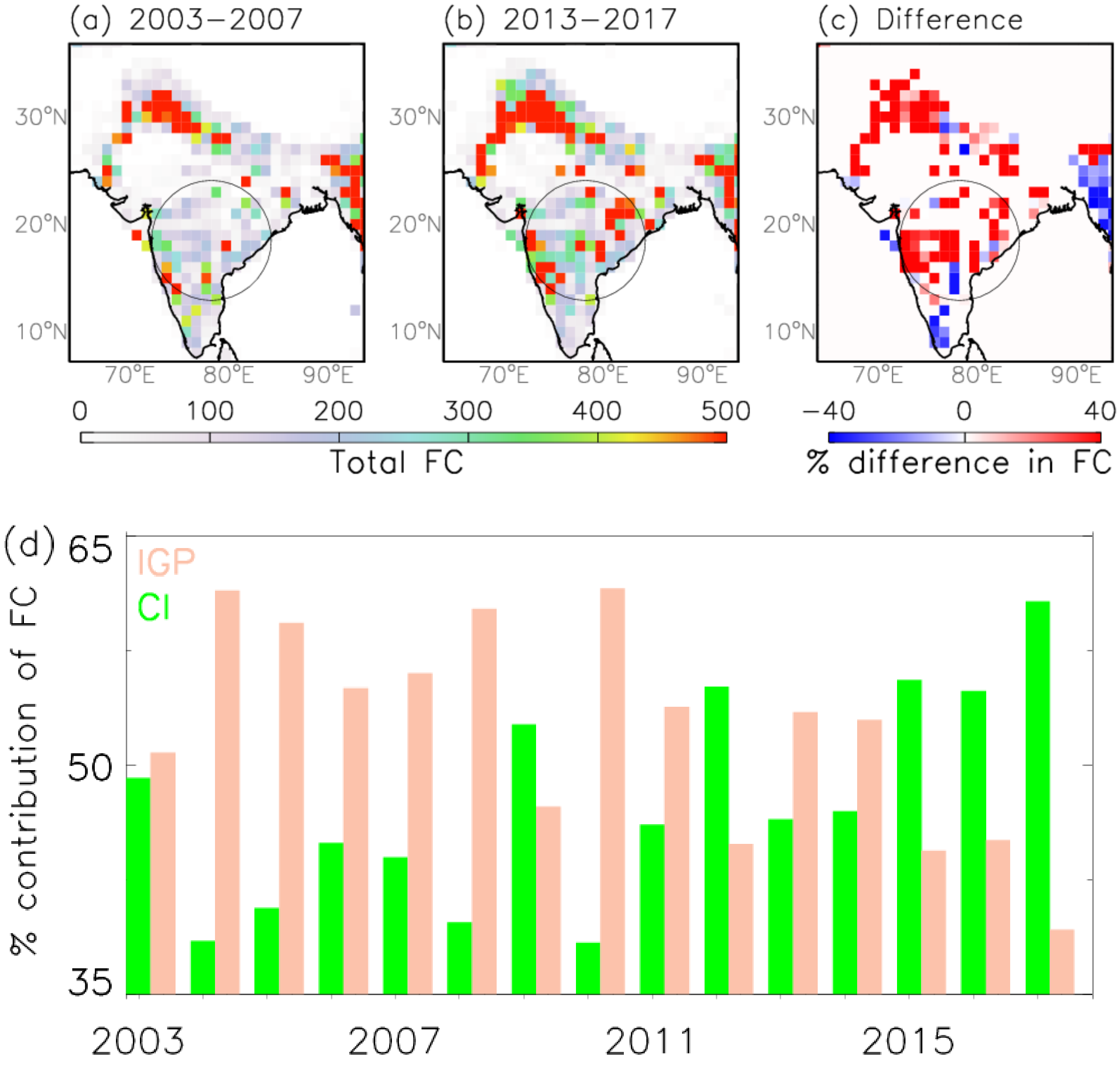

Figure 3.8 (a) Spatial map of 1°×1° gridded total fire counts (FC) for November-February of 2003-2007 (past years). (b) Same as (a) except that for 2013-2017 (recent years). (c) The difference between the past and the recent years. (d) The change in percentage contribution of fire counts over CI and IGP for November-February of 2003 to 2017.

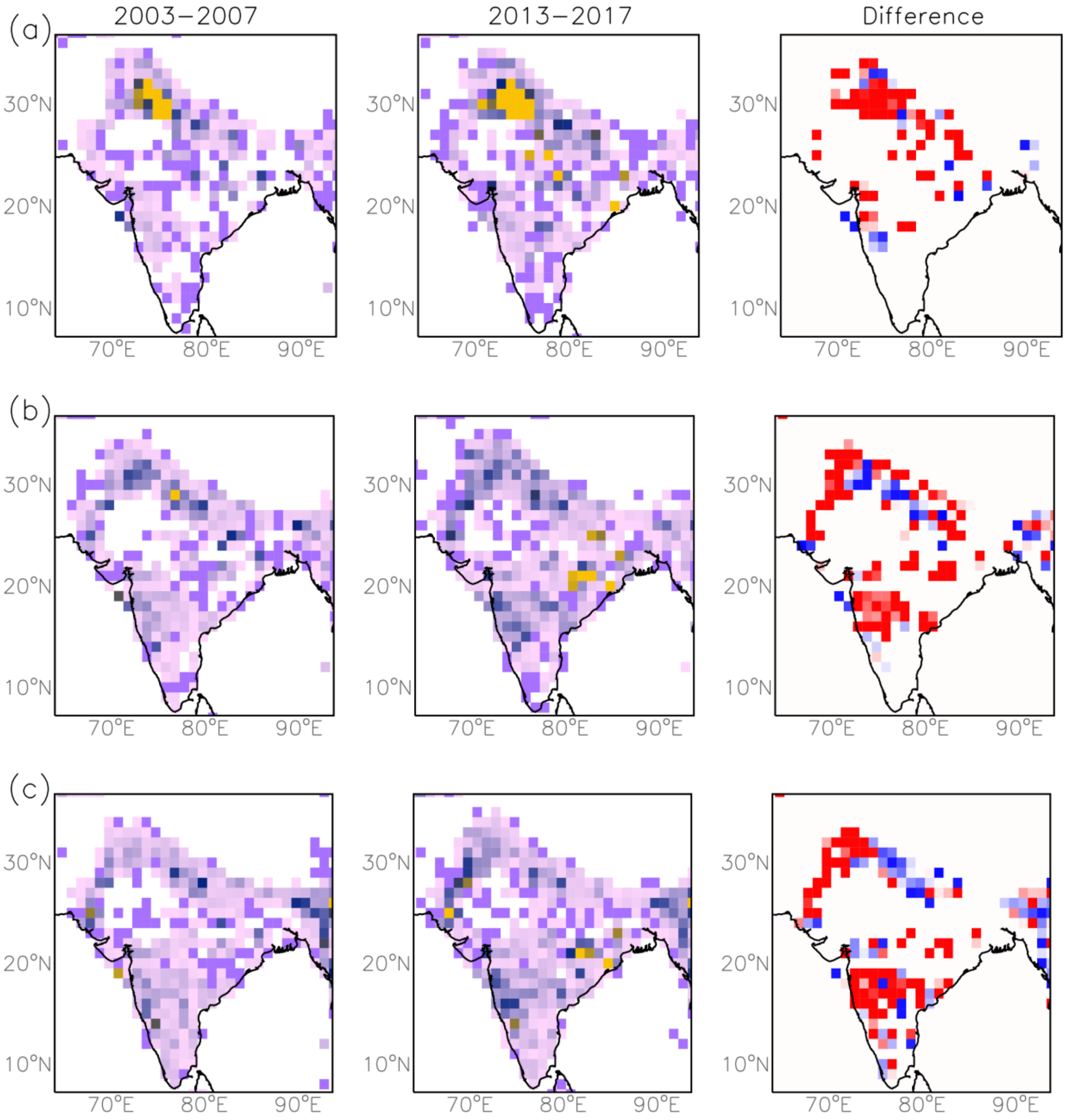
(a)
2003−2007
2013−2017
Difference
(b)
(c)
30°N
20°N
10°N
70°E
80°E
90°E

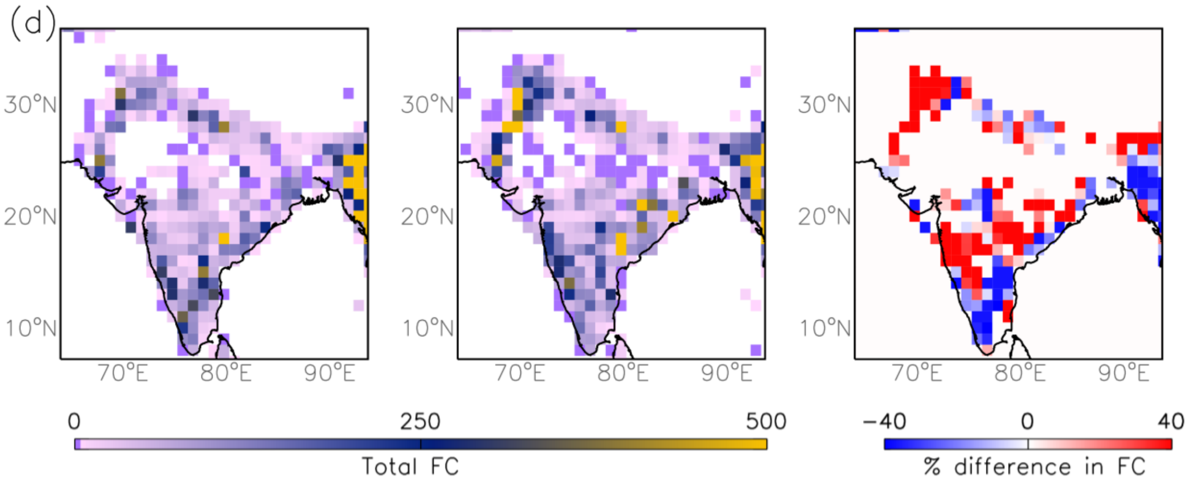

Figure 3.9 Monthly 1°×1° gridded total fire counts (FC) for the past years (2003-2007), the recent years (2013-2017) and the difference between the past and the recent years for the month of (a) November, (b) December, (c) January and (d) February.

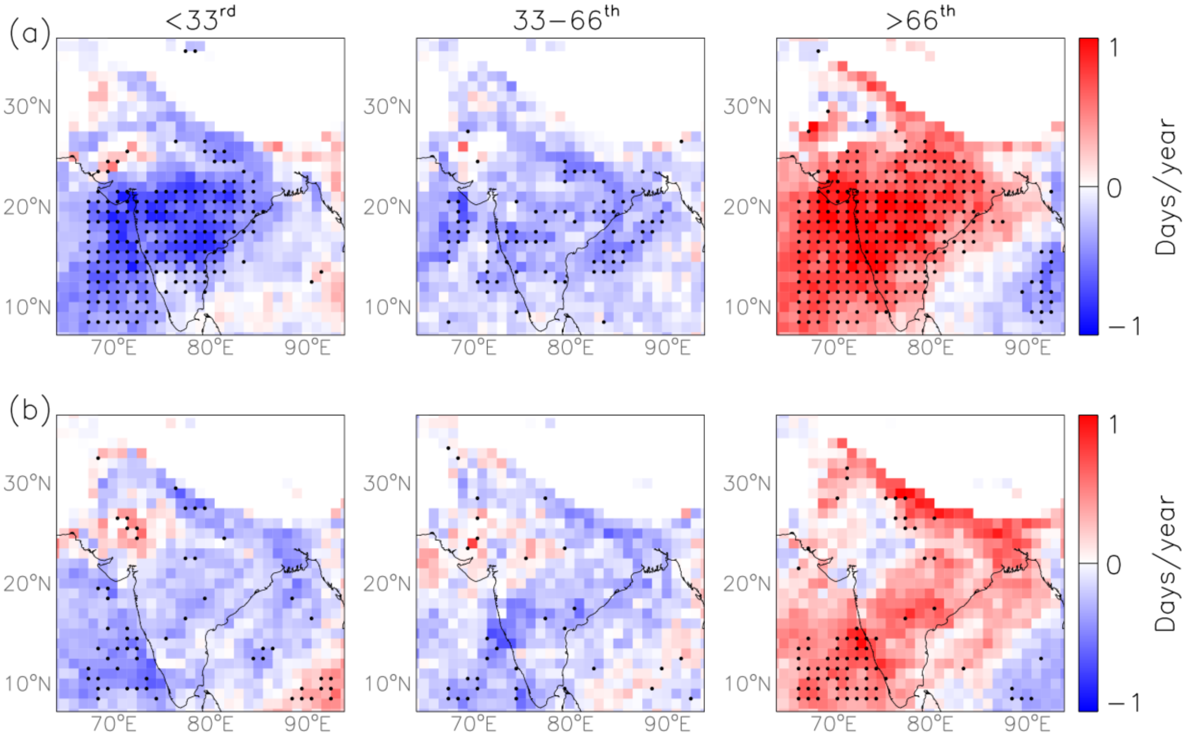

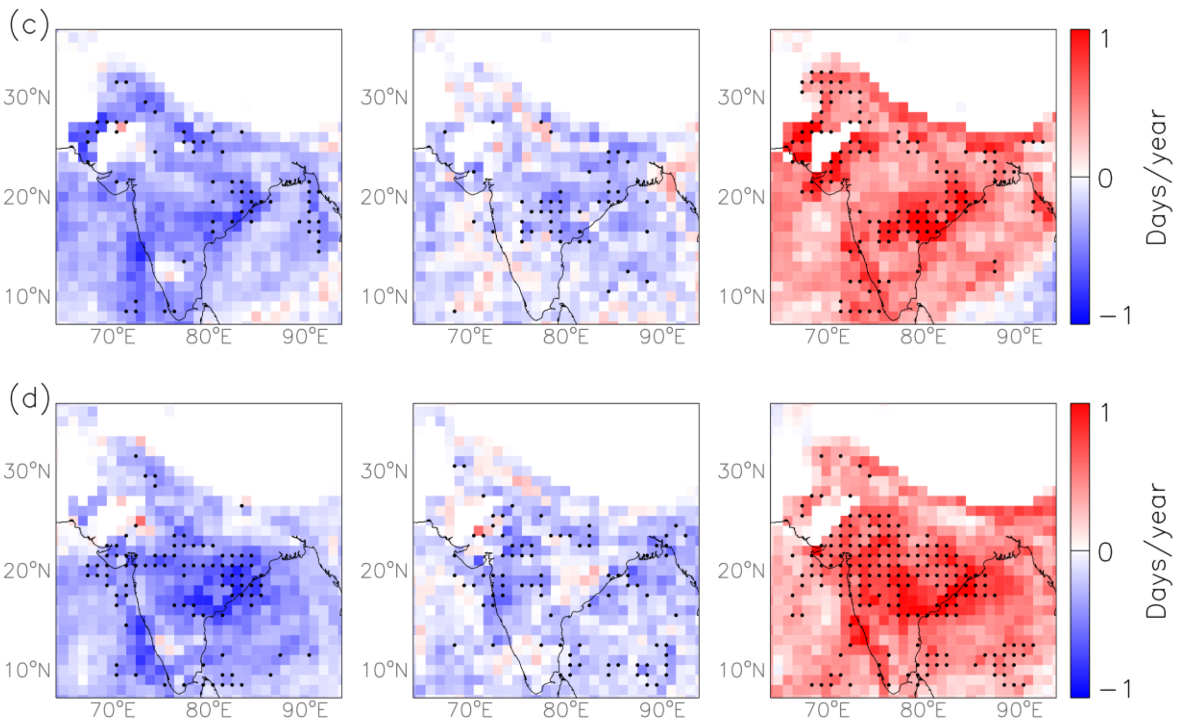

Figure 3.10 Monthly trend in the number of days with <33rd, 33-66th and >66th percentile values of AOD for 2003-2017 for the month of (a) November, (b) December, (c) January and (d) February. Black dots indicate statistical significance using the Student's t-test at a confidence interval of 95%.

3.7 Changes in aerosol direct radiative forcing

Anthropogenic aerosols are known to contribute substantially to radiative forcing, which is comparable enough to counteract greenhouse gas warming (Charlson et al., 1992; Wild et al., 2005; Storelvmo et al., 2016). The high temporal and spatial variability of aerosol loading affects the aerosol direct forcing as well, making it difficult to estimate the impact on the climate (IPCC, 2013). High aerosol loading over the Indian region and surrounding regions due to the presence of dust, soot, and other aerosols makes it a region of high aerosol forcing. The BC aerosol in soot absorbs solar radiation and warms the atmosphere, and is considered as the second strongest contributor to global warming (Ramanathan and Carmichael, 2008). The ADRF at the top of the atmosphere, on the atmosphere and at the surface is estimated using the flux data from MERRA-2, and the detailed calculation is explained in Chapter-2. The spatial mean of ADRF in the past and recent years and the difference between the two periods are given in Fig. 3.11-3.13. The average ADRF peaks over regions with high aerosol loading, and Nair et al. (2017) the ADRF at TOA is mainly modulated by the anthropogenic aerosols over the Indian region. The average ADRF over BoB (31 W m^{-2}) was observed to be much less than the AS region (18 W m^{-2}) by (Moorthy et al., 2009) due to significantly higher anthropogenic aerosol loading transported from IGP during the winter season (Kaskaoutis et al., 2011). But here, we find that the overall increment in ADRF is higher over the AS when compared to BoB. From Fig. 3.11-3.13, it is clear that the cooling at TOA and surface and warming in the atmosphere have increased in recent years owing to the increase in aerosol loading (Fig. 3.2).

The regional changes in ADRF with response to the aerosol loading are visualized in Fig. 3.14. The overall surface and atmospheric forcing are higher in magnitude over the IGP than the CI during both past and recent years. But, the difference between these two periods (Table 3.2) is more apparent over the CI, with atmospheric warming of 4.50 Wm^{-2} as opposed to 2.01 W m^{-2} over IGP. Similarly, the difference in atmospheric forcing over the BoB (0.48 W m^{-2}) is lesser than AS (3.67 W m^{-2}). This means that the increase in the aerosol loading has led to seven times more increment in aerosol forcing over the AS than the BoB. These observations imply that the increment in biomass burning has led to an alteration in forcing over the downwind AS region.

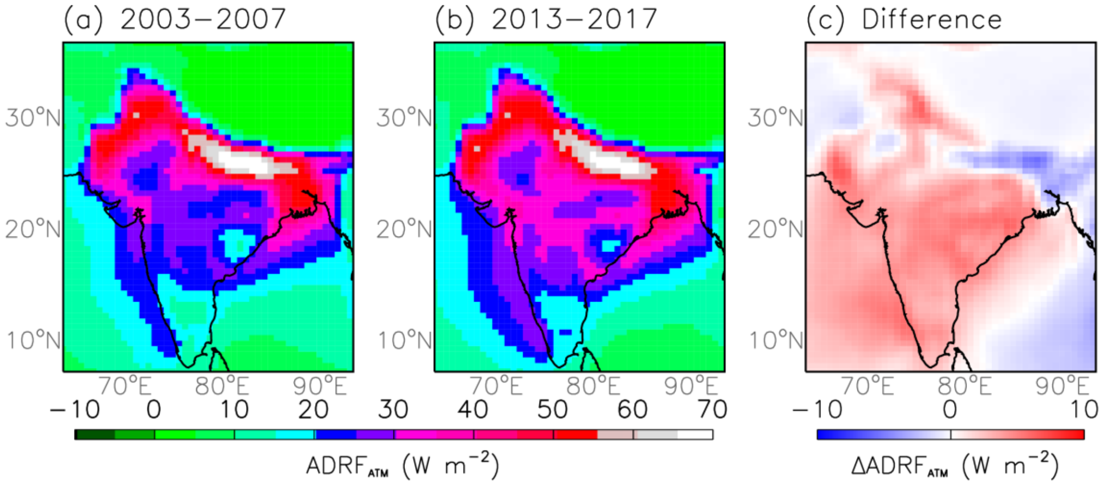

Figure 3.11 Averaged ADRF at the top of the atmosphere during (a) past (2003-2007), (b) recent (2013-17) and its (c) difference using MERRA-2 reanalysis

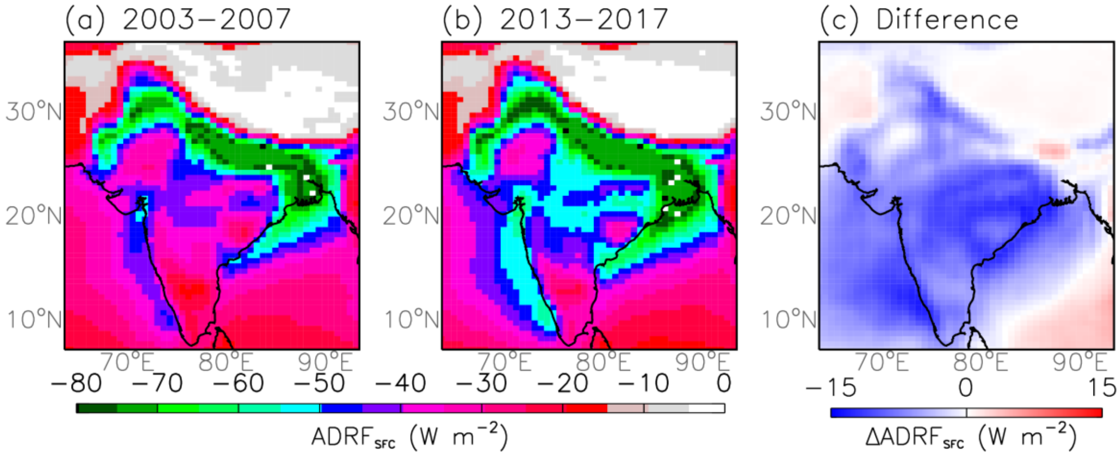

Figure 3.12 Same as Figure 3.11, but for ADRF on the surface.

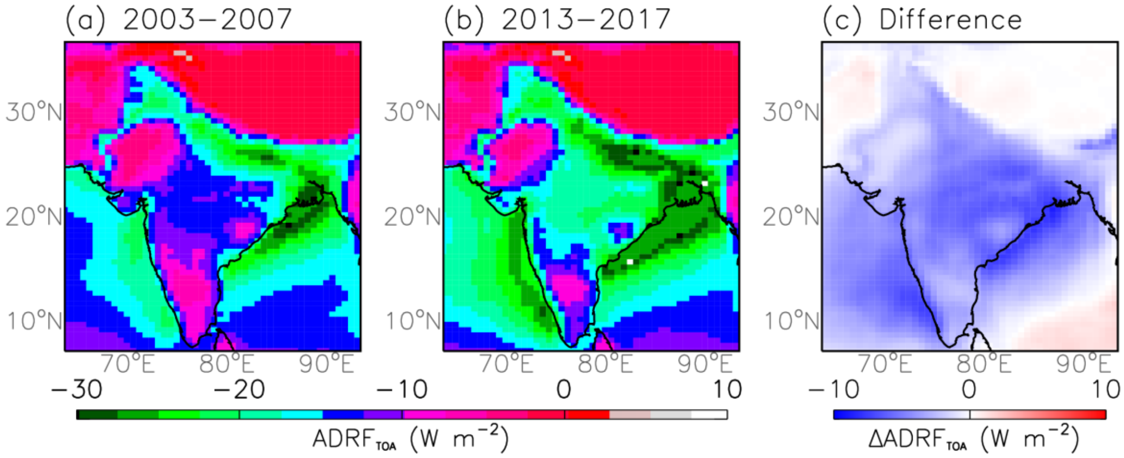

Figure 3.13 Same as Figure 3.11, but for ADRF on the TOA.

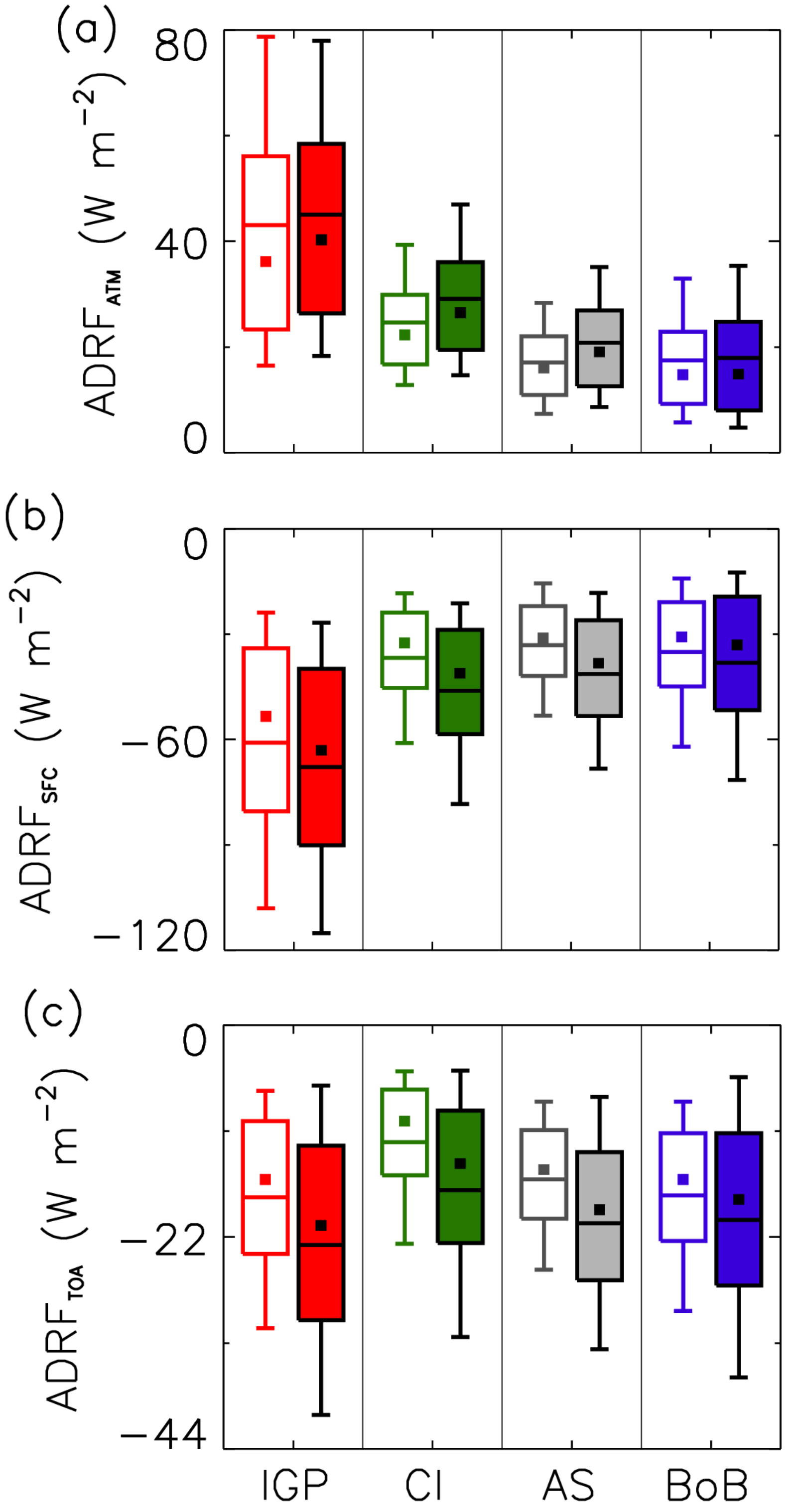

Figure 3.14 The aerosol direct radiative forcing (W m^{-2}) for the past (hollow box) and recent (filled box) years over the four regions was calculated from MERRA-2. The horizontal solid line indicates the mean, the small square box indicates the median, the upper and lower

boundary of the box indicates 25th and 75th percentile values and the whiskers indicate 10th and 90th percentile values.

Table 3.2 Mean difference in ADRF (W m^{-2}) between the recent and the past years over study regions.

	IGP	**CI**	**AS**	**BoB**
SWDRF$_{ATM}$	2.01	4.50	3.67	0.48
SWDRF$_{SFC}$	-6.96	-9.44	-8.24	-3.08
SWDRF$_{TOA}$	-4.95	-4.94	-4.57	-2.60

3.8 Feedback mechanism and implications

The increase in atmospheric warming and surface cooling over the CI and the AS can lead to an increase in the stability of the atmosphere. The stable atmosphere could favour lesser ventilation of aerosols causing more accumulation near the surface. The surface cooling due to aerosols is known to decrease the height of the atmospheric boundary layer by ~200 m over the IGP, and this further increases the aerosol loading near the surface by 3-30 µg m^{-3} (Bharali et al., 2019). The enhanced accumulation of aerosols near the surface can further accelerate the frequency of haze days. Fig. 3.15 shows an increase in lower tropospheric stability (LTS) over the CI and the AS regions. LTS is calculated using the potential temperature profile from GDAS, and the method of calculation is explained in Section 3.2. Sarangi et al. (2016) has illustrated that the increase in LTS can be influenced by the rise in atmospheric warming due to aerosols. Thus, the aerosol forcing-LTS coupling can induce a positive feedback cycle on accumulation within the boundary layer, thereby enhancing the aerosol loading over the CI and the AS regions. Further, the increase in stability can also enhance the low-level cloud fraction over the marine region, leading to negative feedback on the warming climate system.

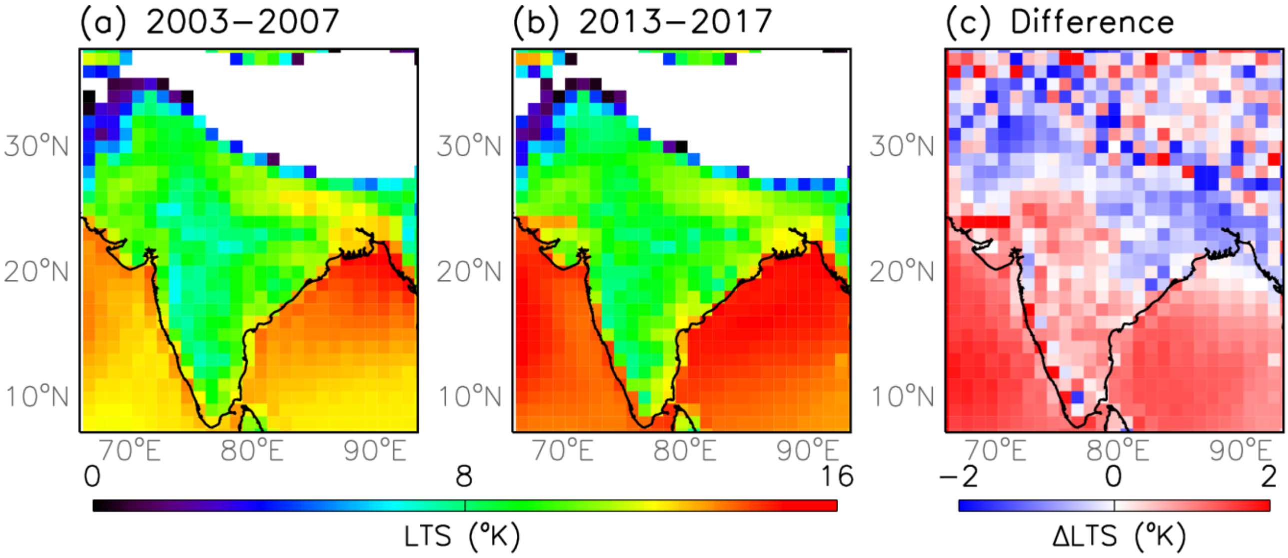

Figure 3.15 Lower tropospheric stability of (a) past, (b) recent and (c) difference between recent and past years using GDAS temperature data.

3.9 Conclusions

India and its surrounding regions are known for their aerosol loading due to rapid urbanization. The low wind speed, low temperature, and shallow boundary layer height make the winter season more prone to hazy conditions, especially over the land-locked and highly polluted IGP region. The outflow from the IGP influences the aerosol composition over the northern BoB, and the BoB is generally known to be more polluted than the AS. But our investigation using the satellite and reanalysis datasets of 15 years (2003-2017) has shown an enhanced increment in the aerosol loading over less polluted CI and the AS regions in the recent years (2013-17). All over the Indian region, the number of hazy days is increasing at the rate of about 2 days/season, but the rate over the CI (~2.6 days/season) is much higher than that of the IGP (~1.7 days/season). The AS region (~1.9 days/season) being downwind from CI has led to a similar enhancement in aerosol loading as compared to the BoB (~1.1 days/season). UV-AI shows a collocated increase along with AOD over the CI region than IGP, suggesting a dominance of absorbing aerosols over the CI region in recent years. The species-wise aerosol optical depth shows a rise in carbonaceous and sulfate aerosols, which are primarily anthropogenic in origin. Natural aerosols, like dust and sea salt, showed less changes over the years. The increase in the anthropogenic aerosol loading has been attributed to the local biomass burning over the CI region, which was evident from the increase in accumulated fire counts during the same period. The increase in absorbing aerosols has led to an increase in atmospheric warming and surface cooling over the Indian region. The increment in forcing is much higher over CI than in other regions, and the enhancement in atmospheric warming is twice that of IGP. Similarly, the increment in atmospheric forcing is seven times higher over CI than the BoB. The changes in the forcing have led to an increase in LTS over the CI and the AS, which can lead to an increased accumulation of aerosols near the surface, creating a positive feedback loop.

Chapter 4

Quantifying aerosol radiative effect over the Bay of Bengal outflow region

4.1 Executive Summary

The pre-monsoon aerosol loading over the IGP is a complex mixture of long-range transported natural mineral dust and local anthropogenic emission of aerosols. The prevailing wind direction is conducive (south-easterly) for the transport of continental aerosols onto the Bay of Bengal (BoB) and thereby alters the properties and radiative forcing of aerosols over the BoB. In this chapter, the airmass forward trajectory analysis using the HYSPLIT model was employed to segregate the days when the aerosol loading over the BoB is directly influenced by upwind continental outflow. The reduced emissions of anthropogenic aerosols over the Indo-Gangetic Plain (IGP) during the COVID-19 lockdown helped in quantifying the contribution of long-range transported aerosols from the IGP to total aerosol loading over the BoB. The main finding is that the continental outflow onto the BoB accounted for about 20-25% of the total ADRF over the BoB (Thomas et al., 2021b).

4.2 Literature review

The IGP is a densely populated and highly polluted region, a global air pollution hotspot(Dey et al., 2004; Srivastava et al., 2012a; Kumar et al., 2018; Brooks et al., 2019; Kanawade et al., 2020; Srivastava et al., 2021b). The high aerosol loading in the region affects the air quality, radiation budget, hydrological cycle, and regional climate (Nigam and Bollasina, 2010; Bollasina et al., 2011; Sarangi et al., 2016; Sarangi et al., 2018; Tiwari et al., 2018). The anthropogenic emissions are on a rising trend over the region in recent decades due to an increase in industrial, agricultural and economic activities (Babu et al., 2013; Moorthy et al., 2013; Srivastava, 2017; Thomas et al., 2019). The aerosol loading generally remains high throughout the season, but the composition of aerosols shows high seasonality (Gautam et al., 2011; Babu et al., 2013; Brooks et al., 2019). The pre-monsoon season (March to May) was accompanied by an increase in the coarse mode aerosols over the IGP region due to the advection of mineral dust by the westerly winds (Beegum et al., 2008; Srivastava et al., 2014). The regional variation in aerosol composition is also observed over IGP during this season since the western IGP is influenced more by the dust and the central to eastern IGP has anthropogenic aerosol dominance due to the thermal power plants, agricultural activities and vehicular emissions (Gautam et al., 2011; Gogoi et al., 2020). The multiple natural and anthropogenic aerosol sources give rise to a complex mixture, including absorbing aerosols and secondary aerosol formation (Srivastava et al., 2021b). The complex mixing processes in the region adds to the uncertainty in estimating aerosol properties and the resulting direct radiative forcing (Thamban et al., 2017; Kompalli et al., 2020; Srivastava et al., 2020). The vertical composition of aerosol shows two distinct aerosol layers, where in addition to the surface layer, an elevated dust layer with mixed anthropogenic aerosols is found at an altitude between 1.5 km to 5.5 km (Sarangi et al., 2016; Brooks et al., 2019). The elevated aerosol layer can alter the monsoon meridional circulation via the ‘elevated heat pump’ mechanism leading to an earlier monsoon onset (Menon et al., 2002; Lau and Kim, 2006; Nigam and Bollasina, 2010).

The westerly winds during the pre-monsoon transport the aerosols from the IGP over to the BoB (Srinivas and Sarin, 2014; Srinivas et al., 2015; Banerjee et al., 2019). The outflow from IGP is known to affect the aerosol loading and composition over the BoB and thus the radiative forcing. The anthropogenic aerosols are found to be transported up to southern BoB, creating a strong north-south gradient of aerosol radiative forcing and atmospheric heating rate (Satheesh et al., 2006; Kedia et al., 2010; Nair et al., 2013a). The outflow can influence the warm clouds over the northern Indian ocean with a low liquid water path (LWP), causing a warming effect (Jose et al., 2020). The influx of aerosols is a known source of nutrients over the marine regions and influences the primary production (Nair et al., 2013b; Srinivas et al., 2015). The dust transported from the sub-continent makes up 22% of the total aerosol extinction over BoB, but the long-term trend of satellite retrieved vertical profiles shows a decreasing trend of dust aerosols over the region (Lakshmi et al., 2017). Significant radiative forcing is caused by the anthropogenic aerosols over the BoB, but quantifying the anthropogenic aerosol impact is difficult due to the complex mixing processes with natural dust (Babu et al., 2008; Beegum et al., 2008).

The COVID-19 pandemic and the following lockdown around the world have led to a dramatic reduction in anthropogenic activities. The decline in traffic and industrial production decreased the emission of greenhouse gases and aerosols and has improved the air quality around the globe (Chauhan and Singh, 2020; Muhammad et al., 2020; Singh and Chauhan, 2020). The lockdown in India was implemented in four phases starting from 24 March till 31 May 2020 (Srivastava et al., 2021a). Phase 1 and 2 of the lockdown had brought the country to an almost standstill, where only the essential services were allowed. Sharma et al. (2020) report a ~ 43% decline in the $PM_{2.5}$ concentration from the measurement sites across India during phases 1 and 2. A sudden change in the air quality index was observed in the major cities across the country on the first week of the lockdown in March 2020 (Singh and Chauhan, 2020). Similarly, a reduction in PM by ~50% was observed during the lockdown period (24 March – 31 May) over Delhi against the pre-lockdown period (1-23 March). The satellite retrieved AOD and absorption AOD showed a reduction of ~30% over the polluted IGP, and the in-situ measurements of pollutants like of PM_{10}, $PM_{2.5}$, NO, NO_2 and CO decreased by about 58%, 47%, 76%, 68% and 58%, respectively ,over Delhi (Srivastava et al., 2021a). The COVID-19 lockdown and the resulting reduction in anthropogenic aerosol loading has provided a unique opportunity to study the change in the aerosol direct radiative forcing (ADRF) over the BoB outflow region. In this chapter, an attempt is made to examine the contribution of anthropogenic aerosols on the ADRF over the BoB during pre-monsoon season.

4.3 Data analysis methodology

The study region, IGP and the outflow region over the BoB is highlighted in Fig. 4.1. The satellite retrievals from MODIS and OMI are used in conjunction with MERRA-2 reanalysis data sets. The products and variables used in this study are listed in Table 1. In order to understand the anthropogenic influence on the ADRF over BoB from the IGP outflow, the forward trajectories from two locations (Kolkata; 22.57°N, 88.42°E and Kanpur; 26.28°N, 80.21°E) over IGP are analysed. The locations are chosen such that they represent the central and eastern IGP. The forward trajectories that originate from these locations are calculated using the HYSPLIT model. A detailed description of the model is given in Chapter 2. The trajectories are calculated daily at 05:30 hours local time starting at two altitudes, 500 m and 1500 m. The model run from Kanpur was used to understand the general wind flow pattern over the IGP region. The model run from Kolkata was used to segregate the days when the forward trajectories are flowing directly onto the BoB. The five-year mean aerosol loading and ADRF from 2015-2019 of the pre-monsoon season were compared with the days when forward from Kolkata were flowing directly onto the BoB.

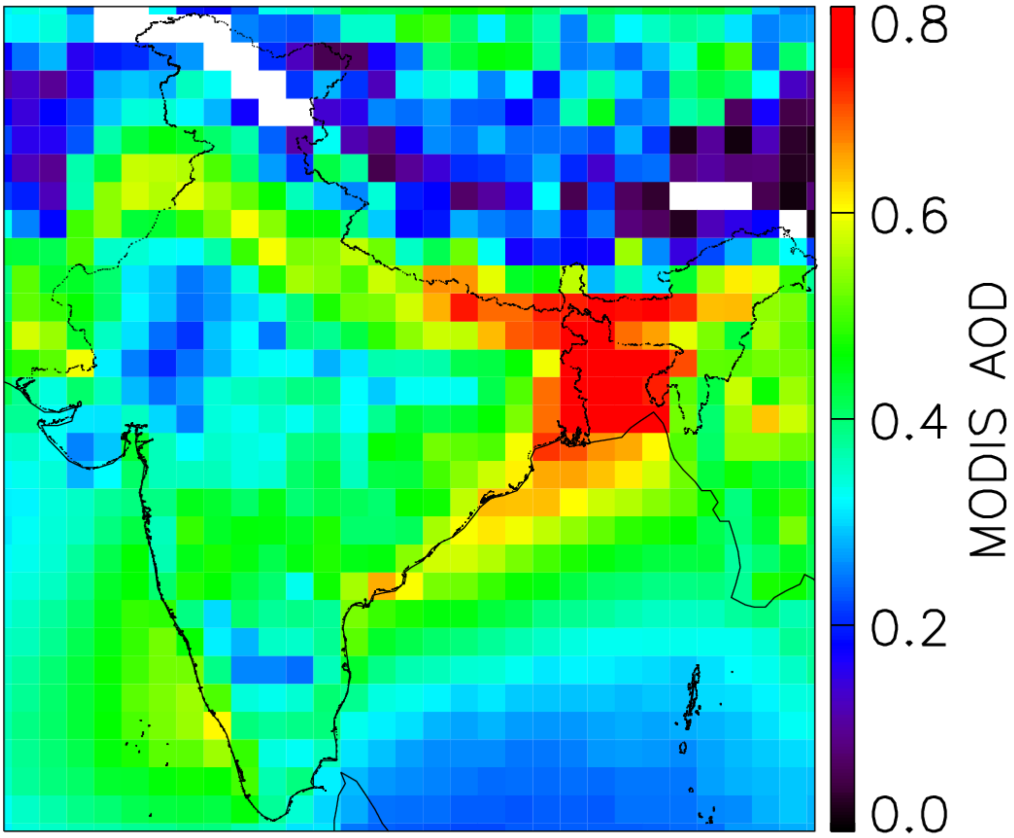

Figure 4.1 Averaged MODIS AOD over pre-monsoon (24 March through 31 May) of 2015-2019. The solid triangle and circle indicate the city of Kanpur and Kolkata.

Table 4.1 Summary of the satellite and model reanalysis datasets used in this study.

Data Source and Version	**Parameter**	**Temporal resolution**	**Spatial resolution**
MODIS, AQUA L3, C6.1	AOD	Daily,13:30	1°×1°
AURA OMI, V3	Absorption AOD	Daily,13:30	1°×1°
AURA OMI, V3	tropospheric column NO_2	Daily,13:30	0.25° × 0.25°
MERRA-2	AOD and SW fluxes	Hourly, 11:00-14:00	1°×1°

4.4 Climatological mean AOD over Indo-Gangetic plain and the Bay of Bengal

The average of MODIS AOD, MERRA-2 AOD, OMI AAOD, and OMI tropospheric NO_2 column concentration for the pre-monsoon season during the years 2015-19 is shown in Fig. 4.1. The AOD observed by MODIS and MERRA-2 compares well spatially and has a higher value across the IGP region, especially towards the eastern side (Fig. 4.2a and b). The OMI-AAOD also follows a higher value over the IGP and northern BoB, as shown in Fig. 4.2c. The tropospheric NO_2 column concentration shows the regions with high anthropogenic emissions, and it highlights the IGP region (Fig. 4.2d). Over IGP, the pre-monsoon season has the highest aerosol loading due to the combined effect of high local anthropogenic emissions and dust transport from Desert regions to the west. The western IGP is dominated by the presence of natural aerosols, and central to eastern IGP is influenced by anthropogenic aerosols (Gogoi et al., 2020). This is substantiated by the high column NO_2 concentration over the region. The increase in population, industrialisation and economic growth has led to the increasing aerosol loading over the region, especially during the winter season due to prevailing weather conditions (Babu et al., 2013; Moorthy et al., 2013; Thomas et al., 2019). But the trend of total aerosol loading over the IGP region during the pre-monsoon season is insignificant due to mineral dust transport (Babu et al., 2013). The dust influx has a dominant influence over the region such that it can mask the diurnal changes in the local anthropogenic emissions and increase the aerosol loading by ~50% (Dey et al., 2004). A recent study has shown a 10-20% reduction in the pre-monsoon dust influx due to weakening circulation patterns and an increase in the pre-monsoon rainfall, which leads to wet scavenging of aerosols (Pandey et al., 2017).

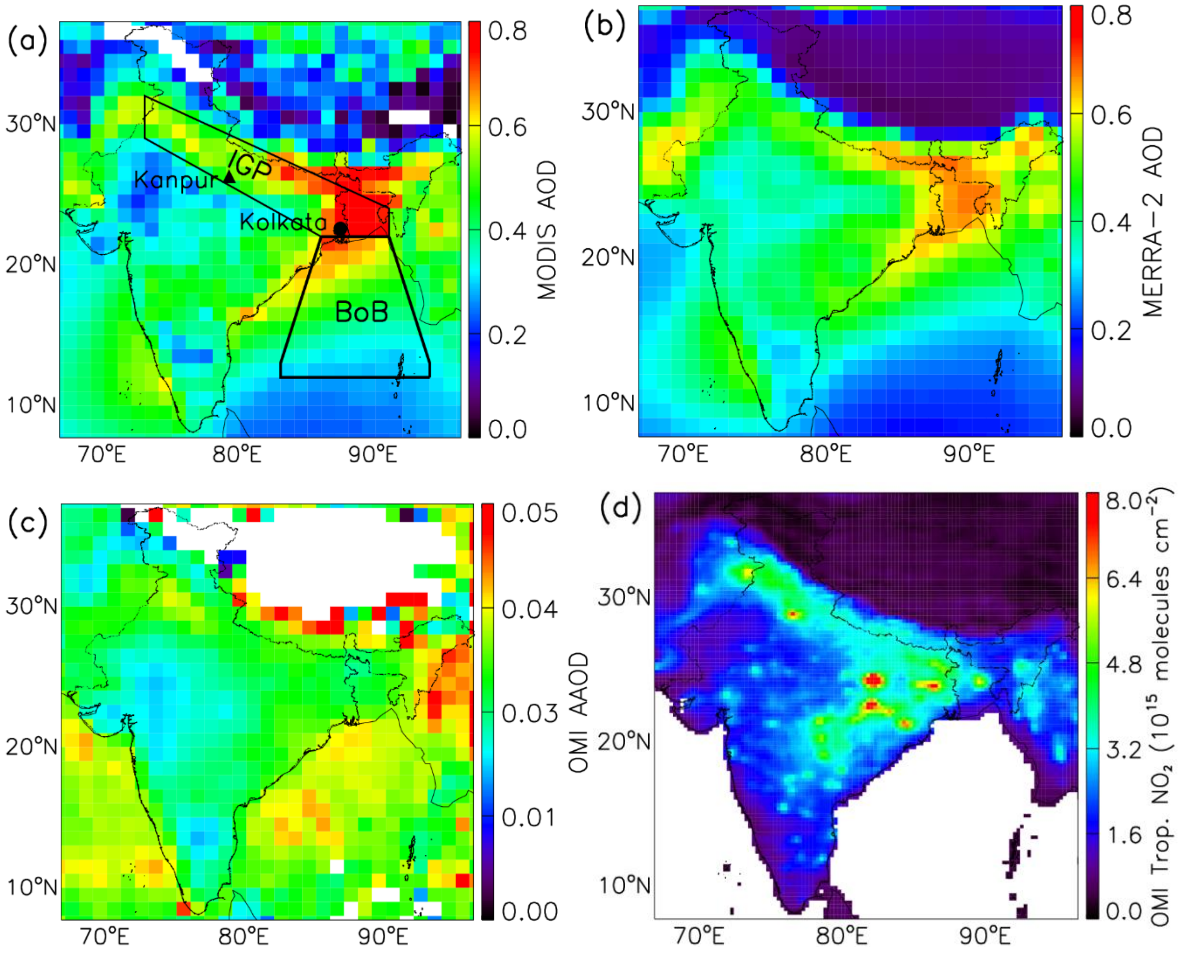

Figure 4.2 Averaged (a) MODIS AOD, (b) MERRA-2 AOD, (c) OMI AAOD and (d) OMI tropospheric NO_2 column for the pre-monsoon season (24 March through 31 May) of 2015-19.

4.5 Airmass trajectory analysis

The wind direction is predominantly westerly over the IGP region during the pre-monsoon, and the winds pick up speed as the season progresses from March to May (Satheesh, 2002; Beegum et al., 2008). The increase in cyclone frequency and mid-tropospheric moisture are characteristic over the Bay of Bengal during this season (Li et al., 2013; Wang et al., 2013; Balaguru et al., 2016) which is a precursor for the monsoon onset (Fosu and Wang, 2015). The westerly wind flow across the region during this period carries pollution from the Indian east coast to the Bay of Bengal (Niranjan et al., 2007; Satheesh et al., 2010).

The HYSPLIT model forward trajectories originating from Kolkata and Kanpur are used to map the wind pattern across the Indo-Gangetic plains. The forward trajectories are calculated at two different origin heights, 500 m and 1500 m, over both the locations in order to account for the surface and elevated layers of aerosol over the Indo-Gangetic plains during the pre-monsoon season (Sarangi et al., 2016; Brooks et al., 2019). The near-surface layers (<1.5km) have a higher concentration of absorbing aerosols, and an elevated layer containing dust and other scattering aerosols are observed over IGP during this season (Brooks et al., 2019). The majority of the forward trajectories from both the altitudes and locations are flowing towards the east, with about 17% trajectories onto the BoB (Fig. 4.3). The trajectories calculated from Kolkata is used in the further analysis since it is located on the eastern edge of the Indo-Gangetic plains and the trajectories flow directly onto the Bay of Bengal. Approximately 16% of the total trajectories at 500 m origin height from Kolkata flows directly over the Bay of Bengal and maintain an altitude below 2 km (Fig. 4.4). The majority of these southeastward trajectories flow over the eastern boundary of the Bay of Bengal, thereby influencing the aerosol loading over the region (Fig. 4.4).

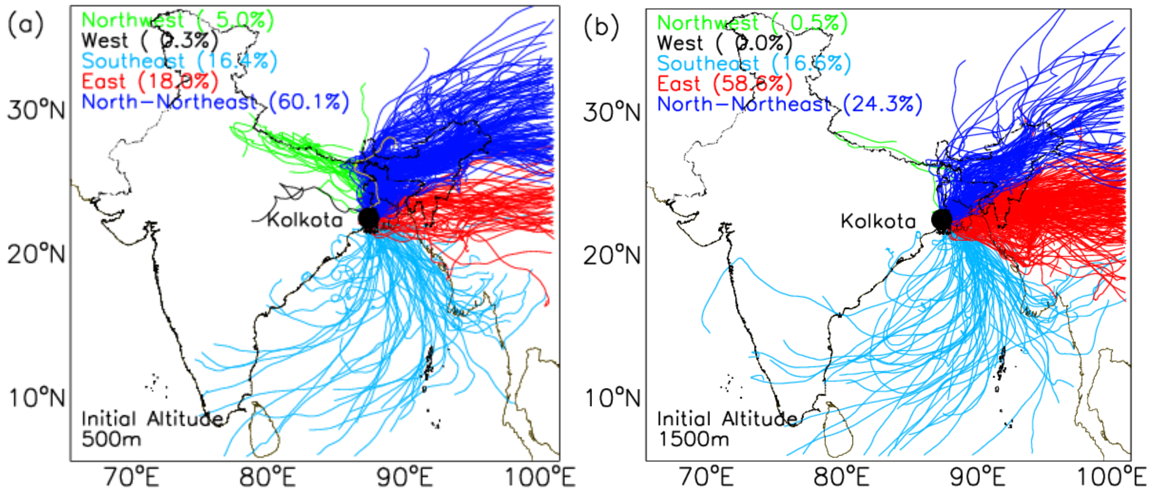

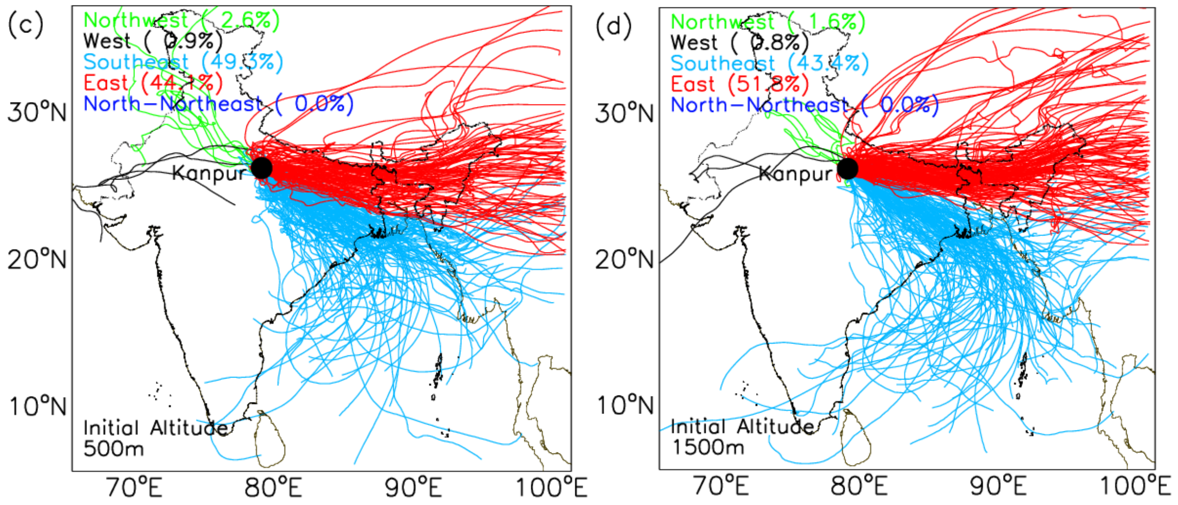

Figure 4.3 (a) 5-days forward trajectory clusters from Kolkata during pre-monsoon of 2015-19 with the model start height 500m above ground level. (b) Same as (a) with model start height 1500m above ground level. (c) same as (a) with the model start at Kanpur (d) same as (b) with the model start at Kanpur

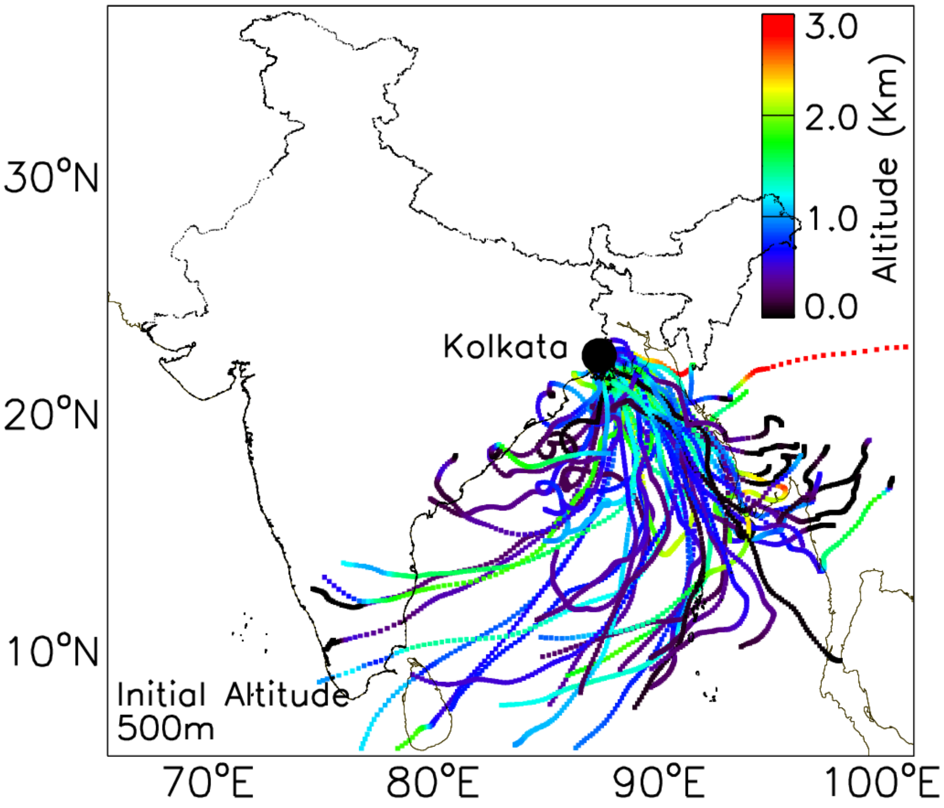

Figure 4.4 Five-day forward southeastward trajectories from Kolkata during pre-monsoon of 2015-19 with the model start height 500m above ground level. The colour bar indicates the altitude of the trajectory.

4.6 Aerosol forcing over Indo-Gangetic Plain and Bay of Bengal

Here, the averaged aerosol direct radiative forcing over the Indo Gangetic Plains (IGP_{ALL}) and the Bay of Bengal (BoB_{ALL}) is compared against the ADRF over the Bay of Bengal when the trajectories are flowing directly from IGP. The days when the transport is directly from the IGP is marked as BOB_{SE}. Fig. 4.5 shows the mean ADRF at the surface, top of the atmosphere, and in the atmosphere. Over IGP, the five-year average (2015-19) of pre-monsoon ADRF was 56.2 ± 5.8 W m^{-2} (surface), -20.1 ± 3.7 W m^{-2} (TOA) and 35.9 ± 2.9 W m^{-2} (atmosphere) and over BoB it was -46.3 ± 7.1 W m^{-2} (surface), -24.9 ± 4.0 W m^{-2} (TOA) and 20.6 ± 3.2 W m^{-2} (atmosphere). The mean ADRF of the BoB_{SE} days was observed as -54.2 ± 6.4 W m^{-2} (surface), -26.9 ± 3.4 W m^{-2} (TOA) and 27.0 ± 3.1 W m^{-2} (atmosphere), which was higher than ADRF of BoB_{ALL}. The prominent difference in atmospheric ADRF (-27.6 ± 6.8%) between BoB_{ALL} and BoB_{SE} than the surface (-14.8 ± 5.2%) or the top of the atmosphere (-5.7 ± 4.6%) indicates the presence of absorbing aerosols over BoB due to the lower-level transport from IGP.A net surface forcing of -27 W m^{-2} and top of the atmosphere forcing of -4 W m^{-2} was reported by Satheesh (2002) over the BoB during the pre-monsoon of 2001. Later in the pre-monsoon of 2006, Kedia et al. (2010) observed the average ADRF to be -22.4 W m^{-2}, -12.0 W m^{-2}, and 10.4 W m^{-2} at the surface, top of the atmosphere, and in the atmosphere, respectively. Comparing our ADRF estimates over the BoB to those reported previously indicates a doubling of radiative forcing over the last decade.

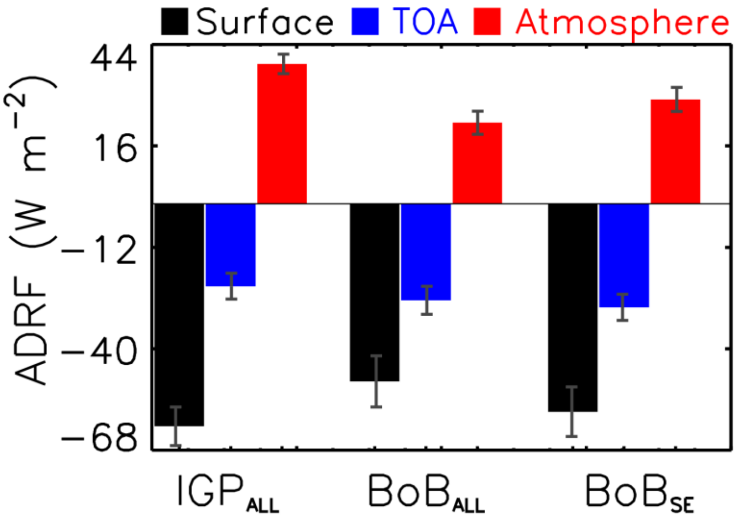

Figure 4.5 Mean ADRF at the surface, top of the atmosphere and in the atmosphere over IGP, BoB during pre-monsoon of 2015-2019 and ADRF over the BoB when the southeastward forward trajectories from Kolkata are flowing into the BoB.

4.7 Aerosol forcing over Indo-Gangetic plain and Bay of Bengal under cleaner conditions

The COVID-19 lockdown and resulting reduction in the anthropogenic activities, which led to a cleaner atmospheric condition, has been widely reported in the literature (Chauhan and Singh, 2020; Muhammad et al., 2020; Sharma et al., 2020; Venter et al., 2020; Srivastava et al., 2021a). The datasets used in the current analysis have also shown such reductions over India. Fig. 4.6 shows the difference in MODIS AOD, MERRA-2 AOD, OMI - AAOD and OMI tropospheric column NO_2 between the pre-monsoon season of 2020 and the average of the same season of 2015-19. A reduction of 17.9 ± 8.5 % and 19.1 ± 6.6 % is observed over IGP and the BoB for MODIS-AOD (Fig. 4.6a). An increase in AOD observed over central India is due to the frequent dust transport from the Thar desert (Sikka, 1997; Badarinath et al., 2007; Verma et al., 2013; Sarkar et al., 2019). MERRA-2 reanalysis data has also captured the reduction in AOD during the lockdown (Fig. 4.6b). A higher magnitude of reduction is observed over the IGP (35.8 ± 11.3%) from the OMI-AAOD, indicating the decline in the absorbing aerosol concentration in Fig. 4.6c. The OMI tropospheric NO_2 (Fig. 4.6d) also concurs with the reduction in aerosol loading, with a decrease of 8.7 ± 10.2% observed over the IGP region. The reduction in OMI tropospheric NO_2 indicates the reduction in anthropogenic emissions over the Indian landmass during the lockdown period, due to its short lifetime and inability to transport long distances.,

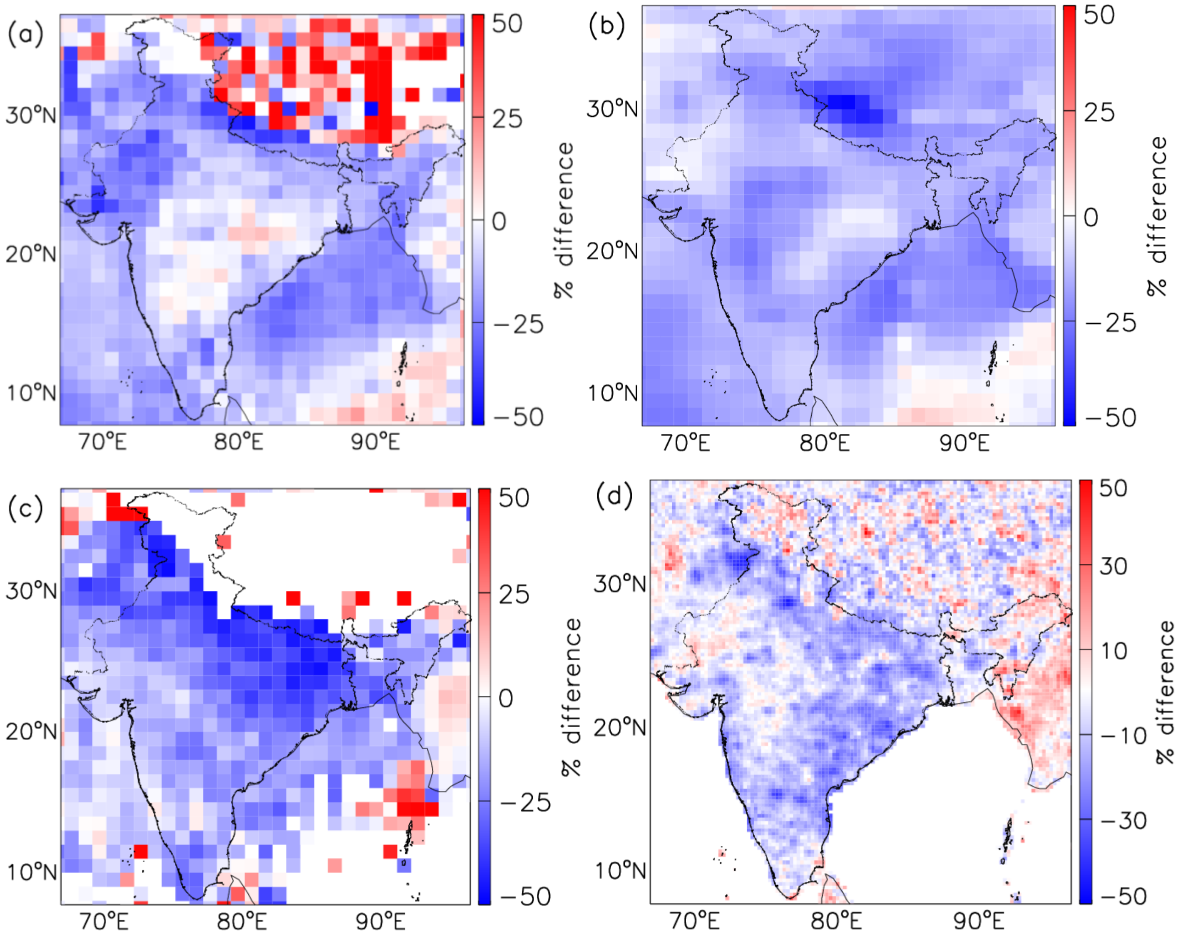

Figure 4.6 Percentage difference in (a) MODIS AOD, (b) MERRA-2 AOD, (c) OMI AAOD and (d) OMI tropospheric column NO_2 between pre-monsoon of 2020 and the five-year average (2015-19).

The reduction in the aerosol loading during the lockdown has led to a decrease in ADRF. The difference in the ADRF in 2020 and the average of the previous five years (2015-19) at the surface, TOA and in the atmosphere is given in Fig. 7. Over IGP, a reduction of 17.4 ± 4.9%, 17.2 ± 4.8% and 17.4 ± 5.5% (IGP_{ALL}: surface, TOA and atmosphere, respectively) were observed. The BoB showed a decrease of 19.7 ± 5.3%, 20.9 ± 5.6% and 18.3 ± 5.5% (BoB_{ALL}) due to lockdown. Comparing the days when the trajectories were from IGP (BoB_{SE}), the reduction was seen to be 22.0 ± 3.1%, 20.9 ± 3.4% and 23.2 ± 3.3%. The magnitude of the reduction in ADRF over BoB is higher during BoB_{SE} than BoB_{ALL}, especially in the atmospheric ADRF (~20-25%), highlights the contribution of absorbing aerosols due to transport from IGP. The ~20-25% reduction in the atmospheric ADRF over BoB can be directly attributed to the ~10-25 % reduction in total AOD and ~24-45% reduction in AAOD over IGP since the trajectories originated from IGP. The reduction in ADRF is much less over IGP as compared to the BoB due to the dust influx during pre-monsoon, which possibly diluted the reduction of anthropogenic aerosols.

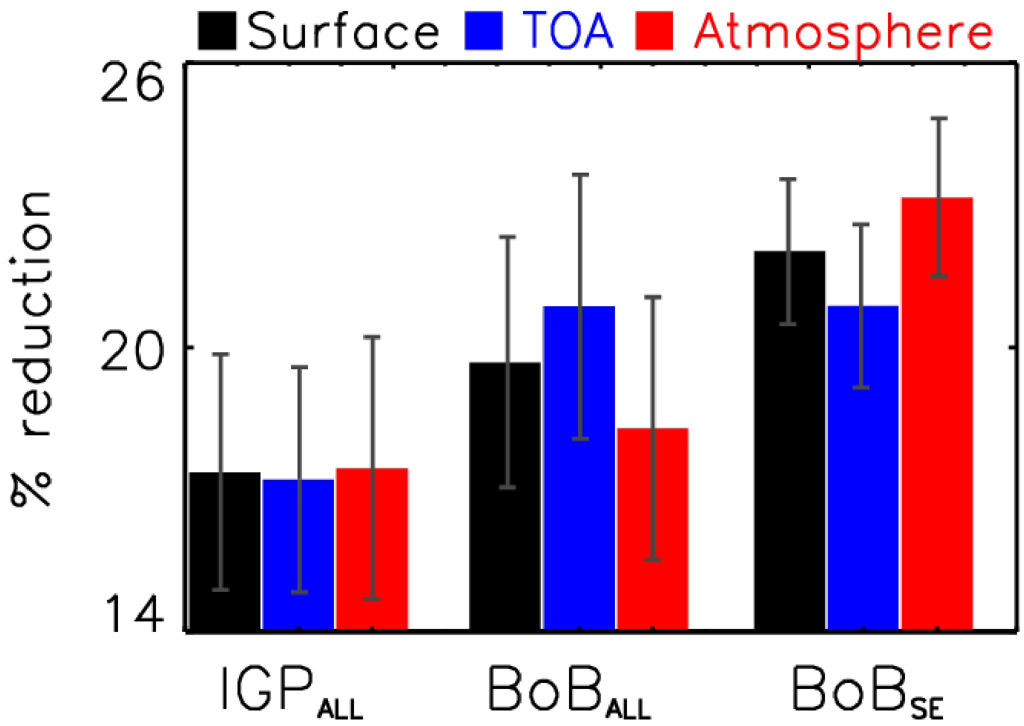

Figure 4.7 Percentage difference of mean ADRF at the surface, top of the atmosphere and in the atmosphere for the pre-monsoon season of 2020 to the five-year average (2015-2019) over the Indo Gangetic plain and the Bay of Bengal. BoB_{SE} indicates the days when Southeast forward trajectories from Kolkata reaching onto the BoB.

4.8 Conclusion

The prevailing wind pattern during the pre-monsoon season influences the aerosol composition and the ADRF over the BoB due to the outflow from IGP. The mean ADRF estimated from the MERRA-2 radiation fluxes over the IGP was -56.2 ± 5.8 W m^{-2}, -20.1 ± 3.7 W m^{-2} and 35.9 ± 2.9 W m^{-2}, respectively, at the surface, top of the atmosphere and in the atmosphere. The seasonal average of ADRF over the BoB is much less than the days when the wind trajectories are flowing directly from IGP, denoting the influence of the aerosol transported from the IGP. The reduction in the emissions from power plants, industries and the transport sector during the lockdown has led to a reduction of ~10-25% in AOD and 24-45% in AAOD over the IGP region. This reduction in anthropogenic aerosols over the IGP has helped in analysing its contribution in ADRF over the outflow region. A reduction of ~20-25% in ADRF was observed over the BoB during the lockdown, and this reduction is higher when the winds originate from the IGP. This implies the robustness of the relation of ADRF over the BoB to the emissions from IGP during the pre-monsoon season. The ADRF change over the BoB can alter the meridional circulation through thermodynamic feedbacks in the atmosphere. The changes in cloud properties and the storms due to the reduced aerosol loading could have a much stronger alteration in the forcing over this region. Our findings warrant more detailed observational and modelling studies to quantify this association as the variability in ADRF over the BoB could influence the monsoon circulation and cyclone genesis by perturbing the land-sea thermal gradients.

Chapter 5

Aerosol-cloud-radiation interactions over the Arabian Sea and the Bay of Bengal

5.1 Executive summary

Aerosol-induced changes in cloud properties are studied extensively over the Indian region (Achuthan, 2001; Prabha et al., 2011; Hazra et al., 2013; Gayatri et al., 2017). The satellite-derived studies were able to understand the seasonal and long-term aerosol-cloud interaction over the region using AOD as a proxy for aerosol concentration (Patil et al., 2017; Sarangi et al., 2017; Sarangi et al., 2018; Kant et al., 2019). The satellite-derived cloud droplet number concentration (CDNC) can be a better proxy for cloud condensation nuclei (CCN) to study aerosol-cloud-radiation interactions, which are otherwise hampered by the larger uncertainties in the association between the aerosol optical depth (aerosol loading) and cloud properties. The aerosol-cloud interaction is different over the Arabian Sea (AS) and the Bay of Bengal (BoB) due to differences in aerosol loading, cloud microstructure and meteorological conditions during the monsoon season. The atmospheric condition over AS supports the dominance of low cloud cover, and BoB has abundant high and deep clouds. The aerosol-induced changes in the cloud radiative forcing (CRF) due to low clouds are less over the BoB than the AS. The meteorological feedbacks have varying impacts on the aerosol sensitivity to shortwave forcing due to low clouds.

5.2 Literature review

Clouds interact with the Earth's radiation budget by reflecting the incoming shortwave radiation and absorbing the outgoing terrestrial radiation (Ramanathan et al., 1989). The competing warming and cooling effects of the clouds change with their macro and microphysical properties (Liu et al., 2011). The changes in CRF through aerosol mediated changes in the cloud properties is called aerosol indirect effect (Twomey, 1977; Albrecht, 1989). Aerosol-induced changes on the cloud radiative forcing remain the largest uncertainty in estimating climate forcing (IPCC, 2013). The uncertainty arises from the strong spatio-temporal heterogeneity in aerosols, cloud types, and dynamical feedbacks at various spatial and temporal scales (Stevens and Feingold, 2009; Fan et al., 2016). The 67 % of the Earth's surface is covered by clouds at any given time and the fact that low clouds cover most of the Earth's surface and reflect the incoming solar radiation, leading to the cloud cooling effect (King et al., 2013; Rosenfeld et al., 2019). The tropical deep convective clouds were found to have near cancellation of longwave and shortwave effects over the equatorial Indian Ocean region near Indonesia (Kiehl and Ramanathan, 1990; Kiehl, 1994), but the high clouds with large optical thickness have a net cooling effect over the Indian region during monsoon (Rajeevan and Srinivasan, 2000; Ravi Kiran et al., 2015).

The flight observations on the monsoon clouds over Indo – Gangetic plains observed a reduction in the cloud mean radius and cloud droplet spectral width in polluted clouds as compared to clean clouds (Prabha et al., 2011). The impact of aerosols on the transition of intraseasonal oscillations was demonstrated using a high-resolution model, and the invigoration of precipitation by aerosols was observed when the break in the monsoon was followed by an active phase (Hazra et al., 2013). The monsoon clouds over the rain shadow region showed that the cloud with high CCN concentration had broader size distribution spectra compared to that of low CCN clouds (Gayatri et al., 2017).

The aerosol-cloud interaction over the marine regions surrounding the Indian region is elusive due to the changes in aerosol loading due to long-range transport from continents onto marine regions. The warm clouds over the outflow region of the Indian region were found to increase cloud effective radius with an increase in aerosol loading at low liquid path conditions (Jose et al., 2020). A decrease in the liquid water path with an increase in aerosol index indicated the aerosol semi-direct effect over the AS and the BoB (Rao and Dey, 2020). Another study highlighted that the aerosol-induced cloud invigoration is dominant over the Indian Summer Monsoon region during the monsoon season (Sarangi et al., 2017). Aerosol-induced invigoration of mixed-phase clouds over the Indian summer monsoon region resulted in taller, thicker mesoscale clouds which had stratiform anvils clouds branching out as they grow up to the tropopause and/or advected out by tropical easterly jet, which increased the net cooling due to clouds over the region (Sarangi et al., 2018). The long-term (2000-17) satellite observation of aerosol-cloud interaction over the Indian region had shown the evidence of anti-Twomey effect during monsoon season due to the wind pattern, meteorology and presence of absorbing aerosols (Kant et al., 2019). The variation in aerosol particle size has demonstrated variation in aerosol-cloud interaction pre-monsoon and monsoon season over the Indo-Gangetic Plain. The smaller sizes aerosols were found to favour the Twomey effect, and larger size particles tend to show an increase in cloud effect radius with an increase in aerosol loading (Jose et al., 2021).

The initial estimates for CRF using satellites were from the Earth Radiation Budget Experiment (ERBE) satellite (Ramanathan et al., 1989; Rajeevan and Srinivasan, 2000). The dominance of deep convective clouds over the BoB during July was observed by Roca and Ramanathan (2000). The low clouds over the Indian Ocean region were studied by Bony et al. (2000) using geostationary INSAT satellite and found the predominance of cumulus clouds over the AS and the BoB during the winter monsoon (November-January). Strong negative NETCRF over the BoB, western Ghats, and coastal Myanmar during the monsoon season was observed using CERES radiation flux data (Thampi and Roca, 2014). A long-term satellite climatology of NETCRF and cloud properties over the Indian region revealed the largest negative forcing when the clouds grew above 400 hPa level (Saud et al., 2016). The dominance of low-level clouds over the AS and tall deep clouds over the BoB was reported by (Sathiyamoorthy et al., 2013). The low clouds were found to have a cooling of -55 W m^{-2} over the region.

Jia et al. (2019) showed the possibility that satellite retrieval bias can amplify the AOD-CER relation over land and ocean. Cloud vertical structure, along with microphysical properties, can affect aerosol-cloud interactions making it essential to analyze various cloud types and their interactions at different environmental conditions (Jia et al., 2021). . The atmospheric conditions can govern the strength of aerosol-cloud radiative forcing through liquid water responses in the marine warm clouds (Chen et al., 2014). The poor relation of AOD/AI with the CCN poses another bias in understanding the aerosol-cloud interaction (Rosenfeld et al., 2019). Rosenfeld et al. (2019) further showed that three-fourth of the cloud radiative effect could be explained using changes in CCN in the low marine clouds. The study used cloud droplet number concentration (Zhu et al., 2018) as a better proxy for CCN to find the association of cloud properties and also to isolate the meteorological impacts. Therefore, the cloud droplet number concentration estimated from the MODIS cloud product (Bennartz and

Rausch, 2017) was used to examine the association of cloud properties and CRF of low clouds during the monsoon season over the AS and BoB.

5.3 Data analysis methodology

The study regions, the AS and the BoB, are depicted by boxes in Fig. 5.1a. MODIS level 3 retrieved aerosol and cloud data during monsoon season (15 June- 30 September) of 2002-2019 is used in this study. The meteorological parameters are obtained from the ERA5 reanalysis product for the same period. Shortwave and longwave fluxes in all-sky and clear-sky conditions are taken from CERES. The details of the variables and datasets used in this study are summarised in Table 5.1. The detailed description, retrieval algorithm, and validation of the data products are already explained in Chapter 2.

Table 5.1 Summary of the satellite and model reanalysis datasets used in this study.

Data Source and Version	Parameter	Temporal resolution	Spatial resolution
MODIS, AQUAL3, C6.1	AOD, CF, CTP, CER-liq, COT-liq	Daily	1º×1º
CERES	LW fluxes, SW fluxes, All - sky albedo, clear sky albedo	3-hourly	1º×1º
ERA 5	Relative humidity and Temperature	hourly	1º×1º

The cloud radiative forcing is calculated from CERES retrieved fluxes at the TOA using the relation from Ramanathan (1987),

$$SWCRF = SW_{CLEAR} - SW_{ALL\text{-}SKY} \tag{5.1}$$

$$LWCRF = LW_{CLEAR} - LW_{ALL\text{-}SKY} \tag{5.2}$$

where, $\mathrm{LW}_{\mathrm{CLEAR}}$ and $\mathrm{SW}_{\mathrm{CLEAR}}$ are longwave and shortwave clear sky flux; similarly, $\mathrm{LW}_{\mathrm{ALL\text{-}SKY}}$ and $\mathrm{SW}_{\mathrm{ALL\text{-}SKY}}$ is long wave and short wave all-sky flux, respectively. NETCRF is the sum of LWCRF and SWCRF.

5.3.1 CDNC estimation

The cloud droplet number concentration can be calculated from MODIS retrieved cloud optical thickness (τ) and cloud effective radius (r_e) using the relation described by (Zhu et al., 2018)

$$\mathrm{N_d} = \mathrm{c}^{\frac{1}{2}}\, \tau^{\frac{1}{2}} \left(\frac{\mathrm{r_e}}{\mathrm{k}}\right)^{\frac{-5}{2}} \tag{5.3}$$

$c = \frac{5.A}{3.\pi.Q_{ext}}$, $A = \frac{C_w}{\frac{4}{3}.\pi.\rho_w}$ and k = 1.08 (Szczodrak et al., 2001; Freud et al., 2011). Mie scattering efficiency, $Q_{ext} = 2$ and moist condensate coefficient, $C_w = 2.1 \times 10^{-11}$ are assumed as given by Zhu et al. (2018) and references within. In this study, we have used MODIS level 3 cloud products as input with constraints for low warm clouds, i.e., only clouds with cloud top pressure greater than 500 hPa are considered in the analysis. Following Nakajima and King (1990), $\mathrm{CER}_{\mathrm{LIQ}}$ less than 4 µm and $\mathrm{COT}_{\mathrm{LIQ}}$ less than 4 is discarded in order to reduce the ambiguity related to the retrieval of $\mathrm{COT}_{\mathrm{LIQ}}$ and $\mathrm{CER}_{\mathrm{LIQ}}$ in the liquid clouds. Taking the $\mathrm{CER}_{\mathrm{LIQ}}$ at 3.7 µm wavelength channel is used in the calculation to reduce said ambiguity and also to reduce the penetration depth in clouds. Also, liquid clouds are more absorptive to 3.7 µm wavelength than 2.1 µm, retrieval from a less absorptive channel will result in a higher CER value (Seethala and Horváth, 2010).

5.3.2 Aerosol radiative effect

In order to estimate the change in cloud radiative forcing with CDNC (Chen et al., 2014), the derivative of SWCRF with respect to CDNC is obtained as,

$$\frac{dSWCRF_{TOA}}{dln(CDNC)} = \left[\overline{Cm}\left\{\frac{dA_{CLR}}{dln(CDNC)} - \frac{dA_{CLD}}{dln(CDNC)}\right\} + (A_{CLR} - A_{CLD})\,\frac{dCF}{dln(CDNC)}\right]\overline{F_{\downarrow}} \tag{5.4}$$

where $\overline{Cm}$ is low cloud coverage, $\mathrm{A}_{\mathrm{CLR}}$ is clear sky albedo $\mathrm{A}_{\mathrm{CLD}}$ is cloud sky albedo, CF is cloud fraction of warm clouds. $\overline{F_{\downarrow}}$ is mean incoming solar radiation. The first term on the righthand side of the equation shows the effect of changes in cloud microphysics due to aerosol loading on SW flux at TOA (intrinsic radiative effect), and the second term denotes the effect of changes in cloud cover due to aerosol loading on SW flux at TOA (extrinsic radiative effect) (Chen et al., 2014). The cloud-sky albedo (A_{CLD}) is calculated from CERES all-sky albedo (A_{ALL}), clear sky albedo and MODIS cloud fraction using relation (Chen et al., 2014).

$$A_{CLD} = [A_{ALL} - (1 - CF)\, A_{CLR}]/CF \qquad (5.5)$$

5.4 Aerosol and Cloud climatology over the Arabian Sea and the Bay of Bengal

The average AOD over the AS and the BoB during the monsoon season from 2002-2019 is given in Fig. 5.1a. These regions show high seasonality in aerosol loading as the wind direction changes with monsoon circulation reverses (Dey and Di Girolamo, 2010; Babu et al., 2013; Moorthy et al., 2013). The aerosol loading over the AS and the BoB is predominantly anthropogenic and are transported from the adjoining Indian continent during the post-monsoon and winter season. In contrast, during pre-monsoon and monsoon, the aerosols are more of marine aerosols or mineral dust transported from middle-east and North Africa (Dey and Di Girolamo, 2010). The aerosol loading over the AS is much higher than BoB due to the predominant transport of mineral dust from north Africa and West Asia across the Arabian Sea on to Indian continent during monsoon (Manoj et al., 2011; Vinoj et al., 2014; Chen et al., 2019; Zhang et al., 2020). Dust is a good CCN, and because of its size, a large fraction of dust aerosols can be activated as CCN. Therefore the high aerosol loading is almost directly proportional to the high CDNC over the northern AS (Fig. 5.1b). Large cloud fraction (CF) is a characteristic of the monsoon season, and the CF over the BoB is much larger than the AS (Fig. 5.1c). Also, the clouds over the BoB are predominantly high and deep clouds during this season as compared to the AS (Rajeevan and Srinivasan, 2000; Saud et al., 2016). Fig. 5.2 shows the International Satellite Cloud Climatology Project (ISCCP) cloud classification over the AS and the BoB. Cirrus and cirrostratus clouds dominate the BoB region making up ~60% of the cloud cover during the period of study (Table 5.1). Low and thin clouds make up more than 50% of occurrence over the AS.

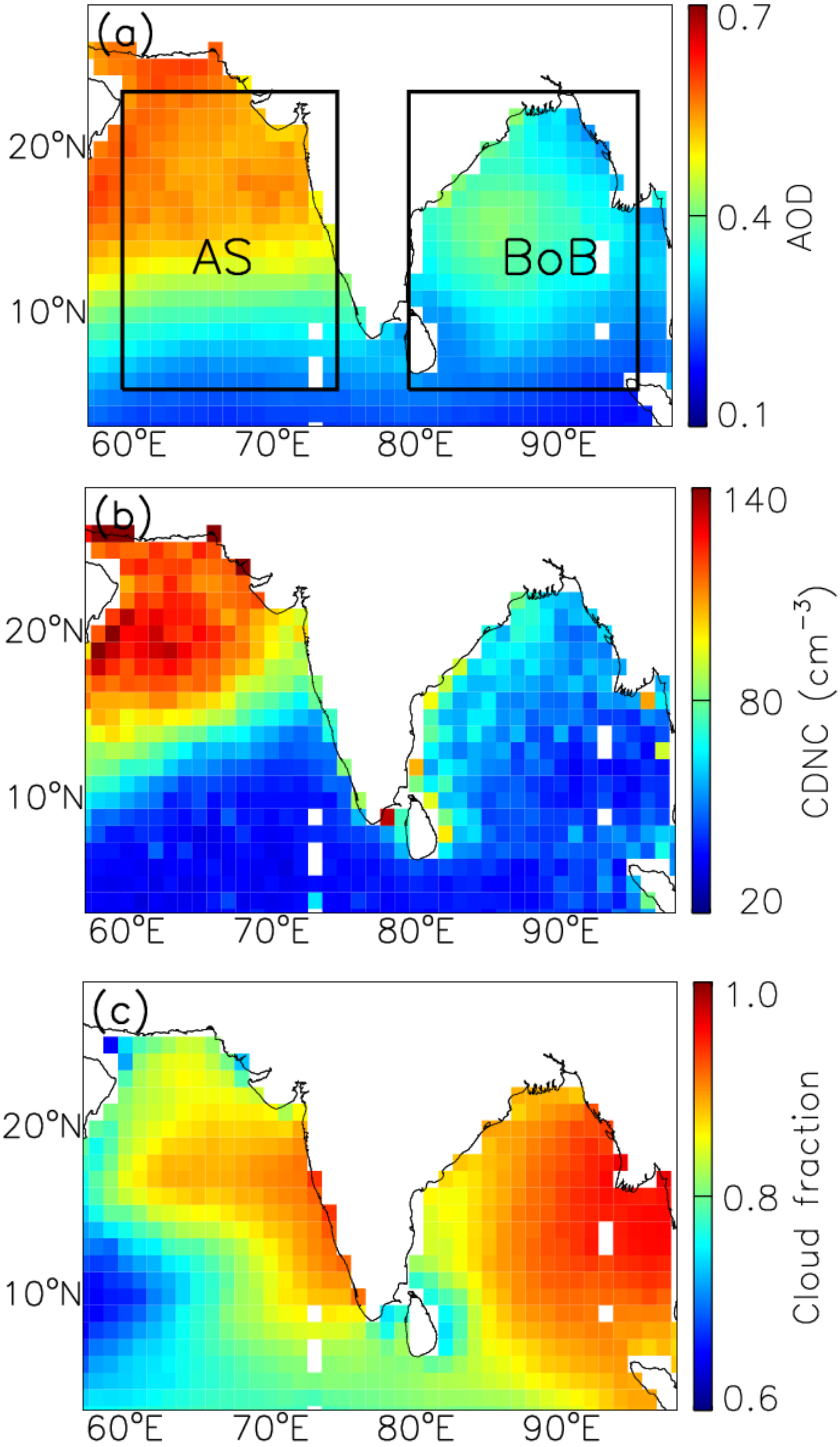

Figure 5.1: Average (a) AOD, (b) CDNC and (c) cloud fraction during 15 June - 30 September of 2002-2019 over the marine regions surrounding the Indian region.

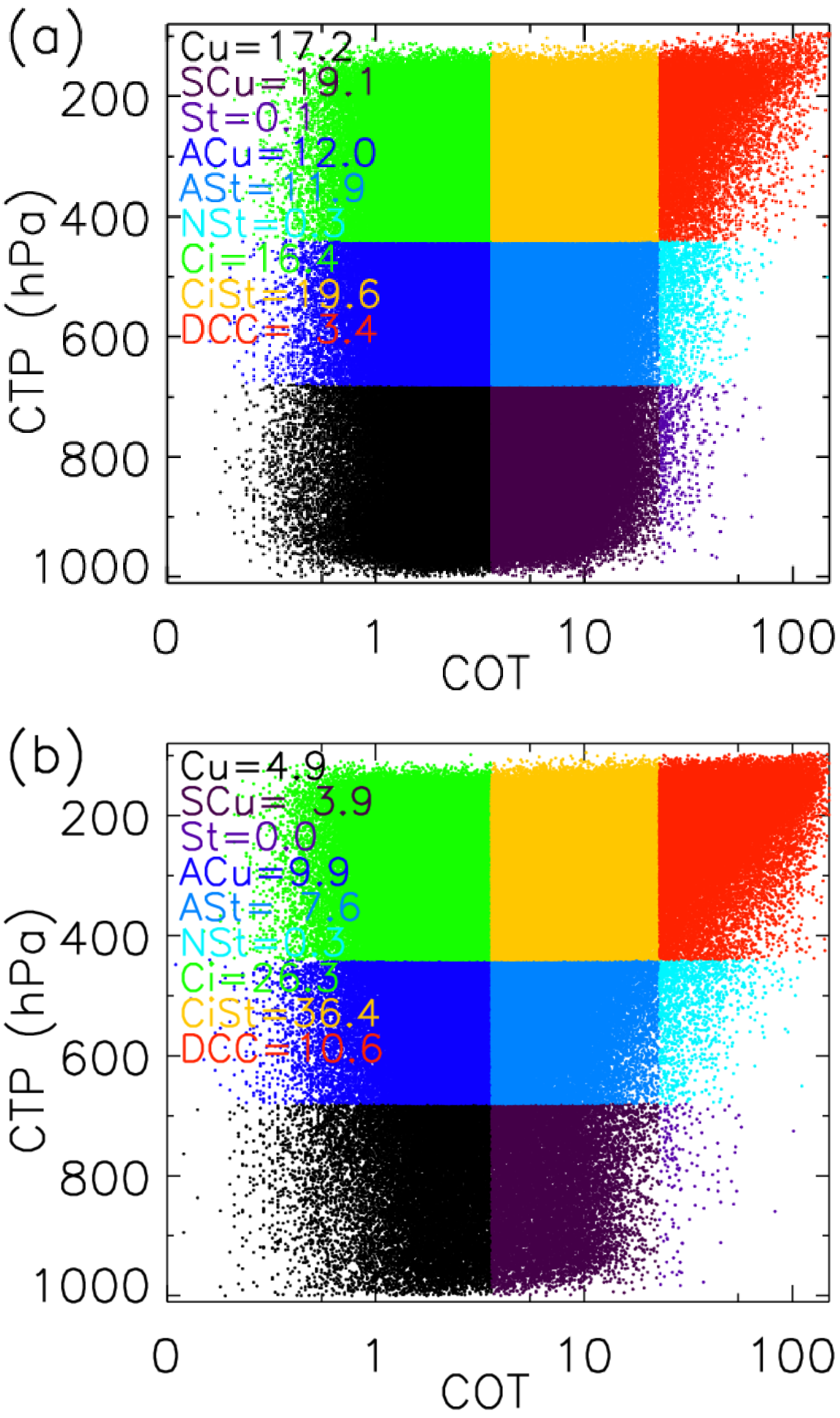

Figure 5.2 ISCCP cloud type distribution during 15 June – 30 September of 2002-2019 over (a) the Arabian Sea and (b) the Bay of Bengal.

Table 5.2 Percentage distribution of cloud types based on ISCCP cloud classification

Cloud type	Arabian Sea	Bay of Bengal
Cumulus	17.2	4.9
Stratocumulus	19.1	3.9
Stratus	0.1	0.0
Altocumulus	12.0	9.9
Altostratus	11.9	7.6
Nimbostratus	0.3	0.3
Cirrus	16.4	26.3
Cirrostratus	19.6	36.4
Deep Convection	3.4	10.6

The abundance of low clouds over the AS is seasonal and are found to peak during the monsoon season during August. The low clouds are present more on the western AS, where the exiting part of the monsoon low-level jet (LLJ) exist. The LLJ decelerates in this region, and decelerating horizontal winds imply a higher horizontal convergence bringing in more moisture (Sathiyamoorthy et al., 2013). The higher moisture content results in the parcel uplifting leading to cloud formation. The presence of thermal inversion coinciding with the region of convergence suppresses the development of clouds into deep convection (Narayanan et al., 2004). Over the BoB, weaker stability and mid-tropospheric wind shear promotes the development of clouds and thus results in deeper/taller clouds (Saikranthi et al., 2019). The difference in the cloud types and aerosol loading in both regions can result in varying aerosol-cloud-radiation interactions.

5.5. Association between cloud droplet number concentration and cloud microphysical properties

The cloud droplet number concentration (CDNC) is directly related to available CCN, cloud albedo, lifetime and cloud cover (Wood, 2012; Zhu et al., 2018). Previous studies investigating aerosol-cloud interactions relied on AOD as a proxy for CCN, but AOD is poorly related to CCN (Stier, 2016; Rosenfeld et al., 2019). The association of AOD with CDNC over the AS and the BoB regions was found to be similar (Fig. 5.3). The CDNC has a better association with AOD over AS than BoB due to the abundance of low clouds over AS. The large AOD values over northern AS were spatially collocated with large CDNC due to the dust transport over the region(Fig. 5.1 a and b).

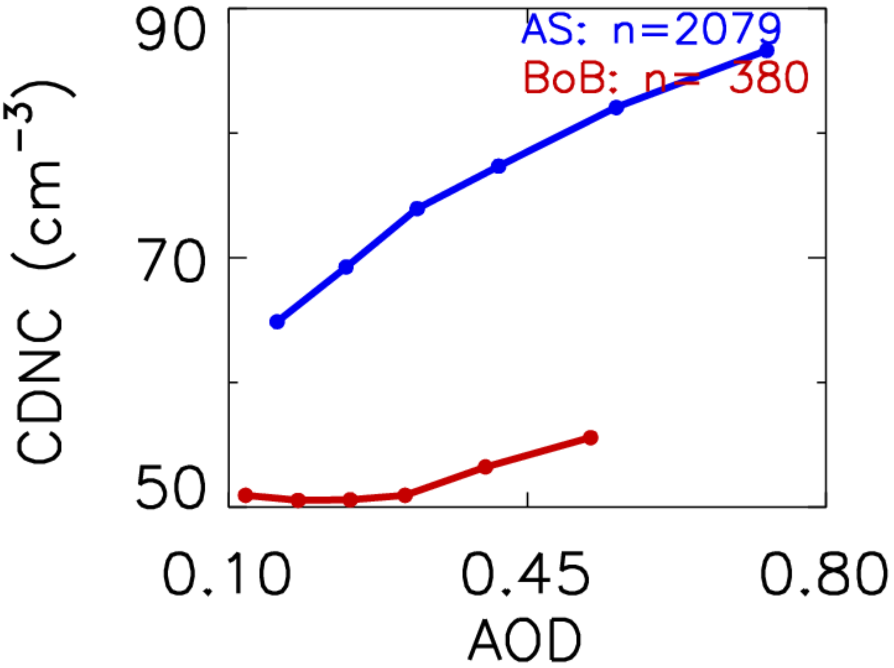

Figure 5.3 The association of AOD and cloud droplet number concentration (CDNC) during 15 June - 30 September of 2002-2019 over the AS and the BoB.

The association of low cloud CF with CDNC is positive in both regions (Fig. 5.4a), but the CER$_{LIQ}$ had an inverse association with CDNC (Fig. 5.4b). The increase of cloud albedo with CDNC also concurs with the decrease in the size of cloud droplets (Fig. 5.4d). But the change in LWP is contrasting among the regions (Fig. 5.4c), pointing to the difference in the aerosol-cloud interaction effects. The increase in LWP with CDNC, as observed over the BoB, could be explained by an initial suppression of rainfall as the precipitation efficiency decreases (Albrecht, 1989). The increase of CDNC in supersaturated polluted clouds, as in the case of the BoB, can increase the LWP of clouds. The vertical extent of clouds further increases due to latent heat release causing invigoration of clouds leading to a positive association of LWP with CDNC (Koren et al., 2014). The aerosol-induced cloud invigoration effect was also found dominant over the Indian summer monsoon region (Sarangi et al., 2018). The inverse association of LWP against CDNC over AS can be explained by the evaporation-entrainment feedback (Small et al., 2009) in the low clouds due to high dust amount. The thermal inversion present in the AS region suppresses the development of deep convective clouds (Sathiyamoorthy et al., 2013). The high atmospheric stability over the region due to the thermal inversion along with the presence of dust aerosols above the clouds can result in a burnout effect, which is in competition with the aerosol indirect effect. Rao and Dey (2020) have demonstrated that the second indirect effect was common over both AS and BoB, where the CER decreased with AOD. Also, a reduction in LWP was observed with an increase in AOD, indicating the semi-direct effect over both regions. The impact of relative humidity was shown to obscure the AOD-CF relation (Quaas et al., 2010), and the necessity to use CDNC as a mediator variable to isolate such influence is explained by Gryspeerdt et al. (2016).

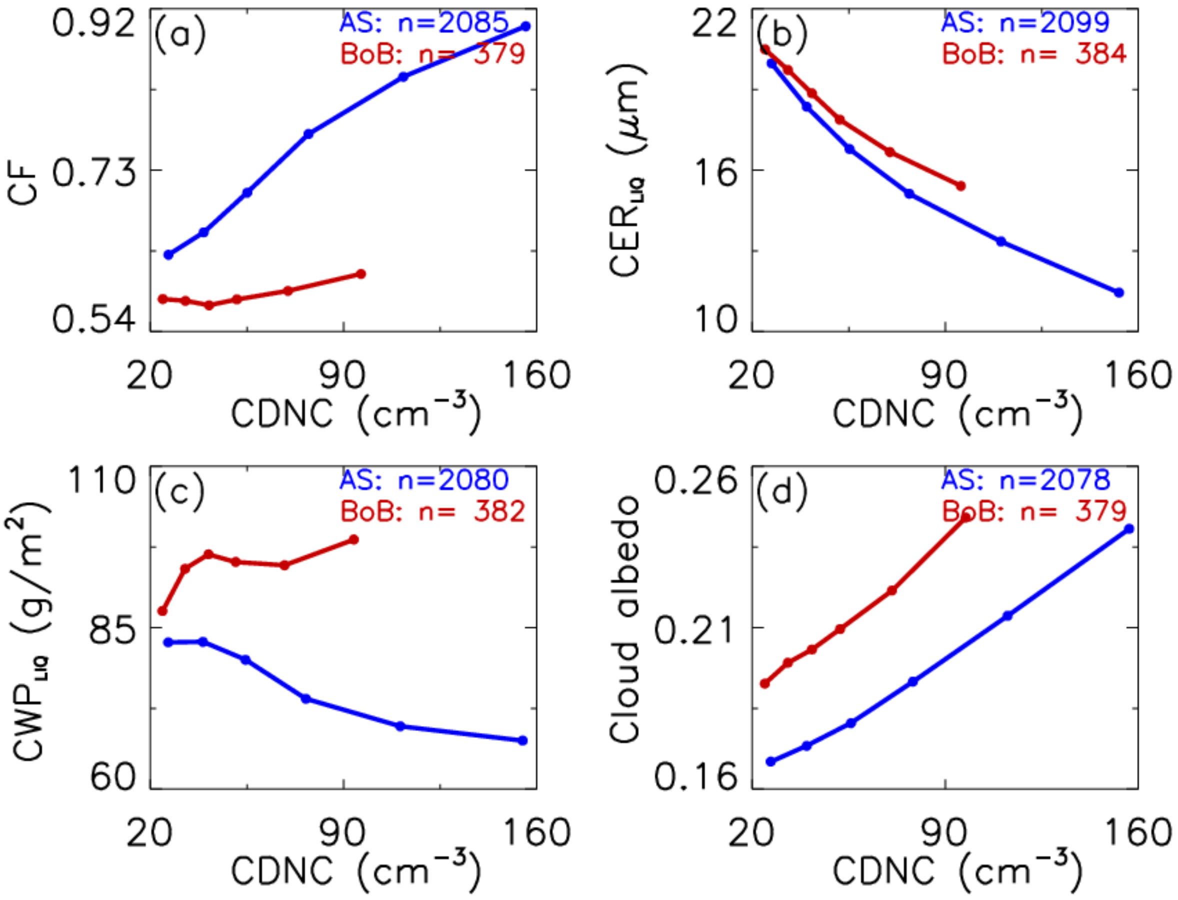

Figure 5.4 (a-d) The association of cloud droplet number concentration (CDNC) and cloud properties during 15 June - 30 September of 2002-2019 over the Arabian Sea and the Bay of Bengal.

5.6 Association between cloud droplet number concentration and cloud radiative forcing

The CRF has been studied over the Indian region in the previous studies, and an overall negative forcing is observed in all seasons, with enhanced cooling during the monsoon season (Rajeevan and Srinivasan, 2000; Saud et al., 2016; Sarangi et al., 2018). Thampi and Roca (2014) have shown that strong negative CRF during monsoon season exists over the BoB and near western Ghats owing to high-level clouds and higher precipitable water content. The low-level clouds were found to have less influence over these regions of high negative CRF. The CDNC - SWCRF association shows a larger sensitivity over the AS than the BoB and has larger negative SWCRF demonstrating that low clouds have limited influence over the BoB. The increase in LWCRF with CDNC in the BoB further reduces the NETCRF. Ravi Kiran et al. (2015) explain that the 50% variance in CRF can be attributed to the vertical distribution of cloud microphysical properties. Over the AS, the SWCRF overpowers LWCRF resulting in a stronger negative NETCRF due to low clouds. The trend analysis of cloud cover over marine regions showed a large decrease over the years, which resulted in a decrease in SWCRF (Saud et al., 2016).

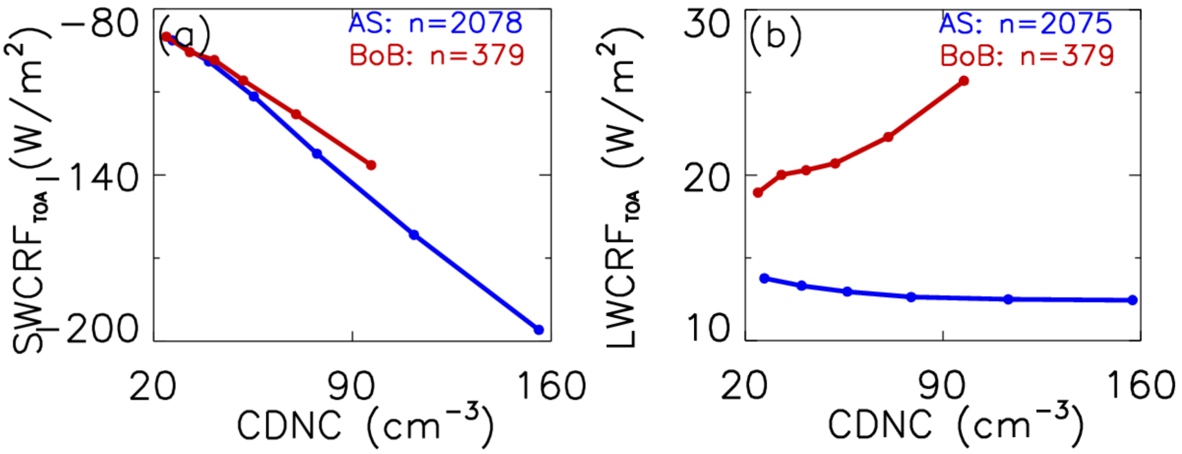

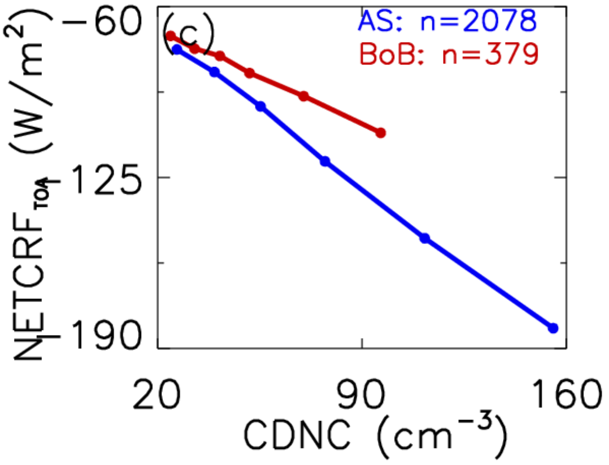

Figure 5.5 The association of cloud droplet number concentration (CDNC) and short wave cloud radiative forcing at the surface during 15th June - 30th September of 2002-2019 over AS and BoB

5.7 Meteorological influence on aerosol-cloud- radiative interactions

The aerosol-cloud interaction and CRF due to low clouds are different in both regions during the monsoon season. The dominance of different cloud types is attributed to the atmospheric conditions over the AS and the BoB (Sathiyamoorthy et al., 2013). To understand the sensitivity of SWCRF to CDNC in various atmospheric conditions, four atmospheric conditions are segregated based on free tropospheric humidity (FTH) and lower-tropospheric stability (LTS), as shown in Fig. 5.6. Dry and wet conditions were segregated based on free tropospheric humidity below or above 40%. Stable and unstable conditions are defined by lower-tropospheric stability being above or below 17° K. The thermal inversion over the AS, along with the moisture convergence and abundance of dust aerosols, make it an ideal place to examine the aerosol-induced CRF changes in low clouds. The aerosol-induced changes to CRF comprise the intrinsic and extrinsic effects (Chen et al., 2014). The intrinsic effect is due to the changes in cloud albedo due to aerosols, and the extrinsic effect shows the changes in cloud cover due to aerosols affect the forcing.

Most cooling over the BoB due to SWCRF occurs in wet-unstable conditions, but over the AS, the forcing remains high in all four conditions. The magnitude of the sensitivity is higher for intrinsic forcing than extrinsic in both regions, but the impact of the intrinsic effect is most pronounced over the AS. The change in warm cloud cover (extrinsic) doesn’t cause much variation in the SW forcing over the BoB. The microphysical impact on the clouds may not be enough to explain the variation in CRF due to low clouds over the AS. The presence of aerosol layers over the low clouds in the AS region can alter the extrinsic radiative forcing. The predominance of wet/stable conditions due to thermal stability and moisture convergence over the AS (Sathiyamoorthy et al., 2013) can also impact the CRF over the region.

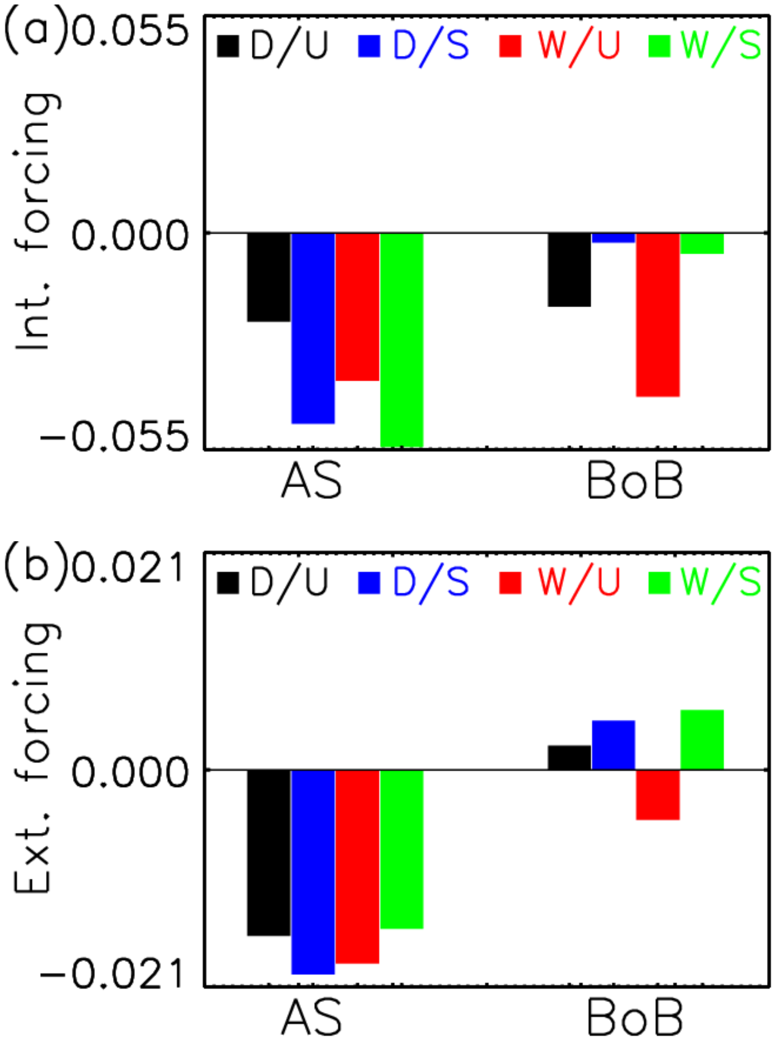

Figure 5.6 (a) Intrinsic and (b) extrinsic aerosol-cloud radiative forcing in various atmospheric conditions using CDNC surface during 15 June - 30 September of 2002-2019 over Arabian Sea and Bay of Bengal. Dry unstable, Dry stable, Wet unstable and Wet stable are segregated based on Lower tropospheric stability and Free tropospheric humidity.

5.8 Conclusions

The predominant cloud types are different in marine regions on either side of the Indian Ocean during the monsoon season. The thermodynamic and convergence conditions over the AS region make it conducive for low cloud formation. The lower stability and lower wind shear conditions over the BoB helps in the development of clouds to deep convective systems. The south-westerly winds during the monsoon season carry mineral dust aerosols from the dust from north Africa and West Asia towards the Indian continent. The proximity to the dust source regions results in higher aerosol loading over the AS than the BoB (Dey and Di Girolamo, 2010). The difference in aerosol-cloud interaction across the regions is evident from the association of CDNC against cloud properties (Fig. 5.4). The previous studies have reported a stronger negative forcing over BoB due to the presence of high and deep clouds (Rajeevan and Srinivasan, 2000; Thampi and Roca, 2014; Saud et al., 2016). The sensitivity of CRF to CDNC is higher over the AS than the BoB, demonstrating that low clouds have limited influence over the CRF over BoB (Fig. 5.5). The difference in the aerosol-cloud interaction in both regions can be influenced by meteorological conditions. The sensitivity of intrinsic and extrinsic forcing shows that the higher impact of aerosols on CRF due to low clouds is observed over AS (Fig. .5. 6). Isolating the aerosol impact on cloud properties using a mediating variable like CDNC and understanding aerosol perturbations on the cloud radiative forcing and its regional variation can reduce the uncertainties regarding aerosol effects.

Chapter 6

Raindrop size distribution response to cloud microphysics and meteorology

6.1. Executive Summary

The response of cloud microphysical properties and meteorological conditions to the surface rainfall properties in different rain regimes are analysed. Joss – Waldvogel disdrometer was used to measure the raindrop size distribution (DSD) at a tropical site, Pune. The characterisation of the measured DSD illustrated the microphysical processes involved in the rain formation. The derived rainfall rate was segregated into two rain regimes as stratiform and convective rain. The analyses showed that the response of cloud microphysical and meteorological properties was contrasting for the two rain regimes. The difference in the instantaneous responses and understanding the mechanisms of rain formation associated could aid in the short-term forecasting of heavy rainfall events, becoming more common in a warming climate scenario. (Thomas et al., 2021a).

6.2 Literature review

The DSD gives information about the rain forming processes (Rosenfeld and Ulbrich, 2003). The changes in microphysical processes within the cloud systems, along with meteorological conditions and dynamical conditions during its descent from the cloud base, determines the shape of the DSD (Atlas and Ulbrich, 2000; Kollias et al., 2001). The characterisation of DSD is important to reduce current uncertainties in the microphysical parameterisation of rainfall in regional to global models, estimating the precipitation from radar reflectivity and studies related to soil erosion and runoff (Bringi et al., 1984; Rosewell, 1986; Zhang et al., 2006; Tapiador et al., 2014). The DSD can vary dramatically with geographical location, season to season or rainfall type within a season (Tokay and Short, 1996; Chakravarty and Raj, 2013; Chakravarty et al., 2013; Konwar et al., 2014; Seela et al., 2018). Sauvageot and Lacaux (1995) found that the mean geometric raindrop is larger in the equatorial sites as compared to the midlatitudes. The influence of orography can also reflect on the DSD (Konwar et al., 2014). Several studies have highlighted the difference in DSD between stratiform and convective rainfall regimes due to the difference in cloud microphysics and dynamical processes in the rain formation processes (Bringi et al., 2003; Rosenfeld and Ulbrich, 2003; Ulbrich and Atlas, 2007). It is observed that the DSD can change within a rainfall event as convective rainfall gives way for stratiform rain. The frequency of stratiform rain is much higher than convective rain, but the accumulated rainfall amount is higher in convective rain. In order to find a good approximation for the DSD, various distribution models have been used in the literature, viz., exponential distribution (Sato et al., 1990), Gaussian distribution (Maguire II and Avery, 1994), three-parameter gamma distribution (Ulbrich, 1983). Among the above mentioned, three-parameter gamma distribution has widely been used to estimate the variation in DSD as it can account for rapid changes in the droplet concentrations and accurately describe rainfall parameters (Ulbrich, 1983).

The DSD studies over the Indian region have been mainly focused on the inter-seasonal or regional variation. Kirankumar et al. (2008) showed the vertical variability in the gamma parameters of convective rain regime over Gadanki station using a dual-frequency (UHF and VHF) wind profiler. The variability of the DSD within the convective rain was attributed to the evaporation and breakup of droplets. The inter-seasonal changes in the DSD between pre-monsoon and monsoon seasons over Kolkata showed a dominance of smaller rain droplets during monsoon (Chakravarty et al., 2013). Another study over Pune reported the concentration of large-sized raindrops in the post-monsoon to be higher as compared to small-medium sized raindrops in the monsoon season (Chakravarty and Raj, 2013). Both studies attribute the changes in the DSD to the changes in cloud and aerosol conditions between the seasons. Konwar et al. (2014) showed the dominance of collision-coalescence processes in the stratiform clouds over the windward side of Western Ghats and the breakup of larger droplets to be observed on the leeward side. Another long-term study over the windward side of the Western Ghats (Braemore) showed that the monsoon has short and less intense rainfall with small-sized raindrops (Sreekanth et al., 2019).

The previous studies over Pune (Chakravarty and Raj, 2013; Konwar et al., 2014) have compared the DSD and its parameters with seasonal changes in cloud properties and variation in geographical location. The cloud and meteorological conditions can change significantly between seasons and thus the DSD. Here, the instantaneous response of cloud properties and meteorological conditions on the DSD is studied by harmonising ground-based DSD, satellite-derived cloud properties, and meteorological reanalysis data during monsoon season to highlight some insights into cloud microphysics and dynamics in the rain formation processes.

6.3 Data analysis methodology

6.3.1 Measurement site

The DSD measurements were conducted over a tropical sub-urban site at the Indian Institute of Tropical Meteorology (IITM), Pune (18.53°N, 73.85°E, 560 m above mean sea level), which is located ~80 km away on the leeward side of the Western Ghats (Fig. 6.1). It is surrounded by 500-700 m high mountains on three sides, and the nearest coast is 200 km to the west (Arabian Sea). The south-westerly winds during the monsoon season bring in moisture and rainfall, and during winter, the winds are easterly or north-easterly. The monsoon trough (climatological mean) passes over this region on 15 June and 15 October during onset and withdrawal phases, respectively (Singh and Ranade, 2010). Therefore, the ground-based, satellite, and model reanalysis datasets considered for this study are during the time period from 15 June to 15 October (2013-2015). The summer monsoon rainfall brings in most of the rainfall for the region, and the annual rainfall averages at 722 mm (Chakravarty and Raj, 2013).

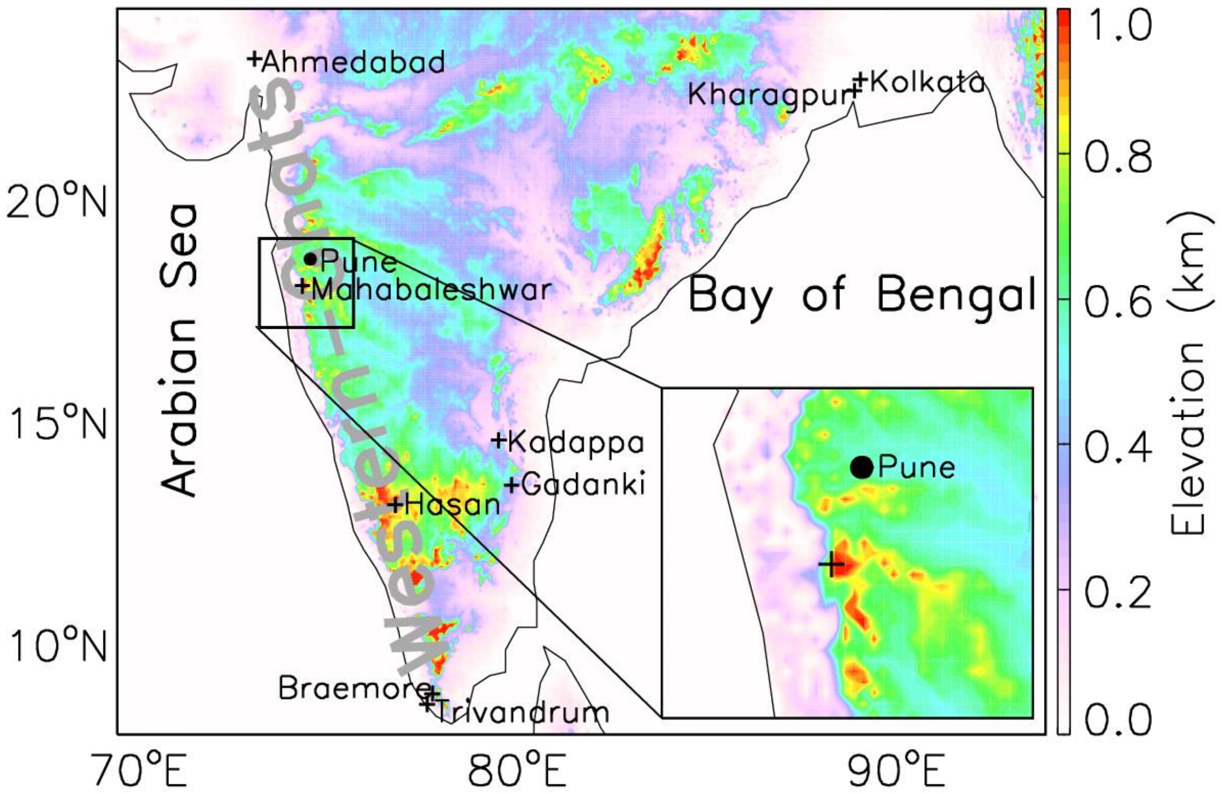

Figure 6.1 Indian peninsular map showing the location of the measurement site (Pune, black dot) and other sites (plus sign) from where DSD observations have been reported from tropical Peninsular India in the literature. The filled contour shows the surface elevation.

6.3.2 Joss Waldvogel disdrometer

The Joss Waldvogel disdrometer is an impact type disdrometer used to measure the raindrop size distribution (Joss and Waldvogel, 1967). It has a 0.005 m^2 sensor surface that records the number of raindrops at a sampling interval of 30 seconds. The raindrop size distribution was recorded in a size range from 0.3 to 5.3 mm divided into 20 size channels. The rain rate can be estimated from the size distribution using the equation:

$$R = \frac{\pi\times 3.6}{6\times 10^3}\times\frac{1}{F\times t}\sum_{i=1}^{n}(n_i\times D_i^3) \tag{6.1}$$

where i is the raindrop size bin, t is the time interval (30 seconds), F is the size of the sensor surface (0.005 m^2), n_i is the number of rain droplets measured in the raindrop size bin i and D_i is the size of the raindrop size bin i. The major drawback of an impact type disdrometer is the uncertainties due to surrounding noise and deadtime of the instrument due to large droplets during heavy rainfall (Tokay and Short, 1996). In order to avoid the deadtime problem, the samples with a total raindrop count less than 10 or derived rain rate less than 0.5 mm hr^{-1} were discarded. The 20th channel in the DSD measurement has been removed from the data due to an unrealistically high droplet count. Therefore, only 19 channels (0.3 to 4.86 mm) have been used in this analysis.

The three-parameter gamma model, as described by Ulbrich (1983) is used to characterise the DSD.

$$N(D) = N_0 \exp(-\Lambda \mathrm{D}) * D^{\mu} \tag{6.2}$$

where N(D) (m^{-3} mm^{-1}) is the number of raindrops with diameter D (mm), μ (unitless), and Λ (mm^{-1}) are shape and slope parameters, respectively. N_0 (m^{-3} mm^{-1}) is the intercept parameter. The shape parameter represents the breadth of the curve, and the positive value indicates that the curve is concave downwards. The slope parameter denotes the extension of the curve towards the broader diameter spectrum

The gamma parameters are calculated from moments of central tendency given by the nth moment of the distribution given by the equation (6.3);

$$M_n = \sum_{i=1}^{n} N(D_i) D_i^n dD_i \tag{6.3}$$

Then, the mass-weighted mean diameter (mm) is given as,

$$\mathrm{D_m} = \frac{M_4}{M_3} \tag{6.4}$$

M_3 and M_4 are the third and fourth moments of central tendency calculated from Eq. (6.3).

$$\mu = \frac{3M_4M_2 - 4M_3^2}{M_3^2 - M_4M_2} \tag{6.5}$$

$$\Lambda = \frac{\mu + 4}{D_m} \tag{6.6}$$

The normalised DSD scaling parameter (N_w) helps in comparing the shape of two DSDs with different LWC and D_m and is given by Eq.(6.7);

$$N_W = \frac{4^4}{\pi \rho_w}\left[\frac{10^6 LWC}{D_m^4}\right] \tag{6.7}$$

The liquid water content (LWC in g m^{-3}) was calculated from the rain DSD data using Eq. 8.

$$\mathrm{L}WC = \frac{\pi \times \rho_w \times 10^{-6}}{6} \sum_{i=1}^{n} D_i^3 N(D_i) dD_i \tag{6.8}$$

where, ρ_w is the density of water (10^3 kg m^{-3}).

6.3.3 Estimation of Cloud droplet number concentration

In order to understand the aerosol feedback to DSD, we have derived CDNC as described by Zhu et al. (2018), based on cloud microphysical properties, using Eq. (8);

$$\mathrm{N_d} = \mathrm{c}^{\frac{1}{2}}\, \tau^{\frac{1}{2}} \left(\frac{\mathrm{r_e}}{\mathrm{k}}\right)^{\frac{-5}{2}} \tag{6.9}$$

where r_e is liquid cloud effective radius (CER_{liq}) and τ is liquid cloud optical depth (COT_{liq}). $c = \frac{5.A}{3.\pi.Q_{ext}}$, $A = \frac{C_w}{\frac{4}{3}.\pi.\rho_w}$ (Szczodrak et al., 2001), and k=1.08 (Freud et al., 2011). Mie scattering efficiency, $Q_{ext} = 2$ and moist condensate coefficient, $C_w = 2.1 \times 10^{-11}$ are assumed as given by (Zhu et al., 2018).MODIS cloud properties and derived CDNC were collocated with the corresponding DSD by taking an average of the DSD within a 2-hour bracket of TERRA and AQUA satellites ascending overpasses during the daytime. TERRA and AQUA have ascending crossing times over India at 10:30 AM local time and 1:30 PM local time, respectively. The mean DSD was calculated between 10:30 AM and 2:30 PM local time to match with satellite-derived CDNC and microphysical cloud properties.

6.3.4 Segregating rainfall regimes

The type of rain is usually classified into convective rain and stratiform rain based on its intensity, horizontal homogeneity and different rain growth mechanisms (Anagnostou and Kummerow, 1997; Yang et al., 2013). Here, we classified the type of rain using the disdrometer derived rain rate based on the method established by Bringi et al. (2003). The method uses the standard deviation of rain rate (1.5 mm hr^{-1}) as the threshold to classify into convective and stratiform rain. The rain type was identified as convective if the DSD samples for consecutive 10 minutes have a mean rain rate greater than 5 mm hr^{-1} and a standard deviation greater than 1.5 mm hr^{-1}. The rain type was identified as the stratiform if the mean rain rate was greater than 0.5 mm hr^{-1} and a standard deviation of less than 1.5 mm hr^{-1}. This method has been adopted in several previous studies (Marzano et al., 2010; Chen et al., 2013; Seela et al., 2018).

6.4 Characteristics of raindrop size distribution

Out of the 30153 samples taken for analysis, 10360 and 4260 samples were segregated for stratiform rain and convective rain, respectively. The estimated rain rate varied from 0.5 to 95 mm hr^{-1}, with a mean and standard deviation of 3.94 ± 8.62 mm hr^{-1}. The stratiform rain rate ranged from 0.5 to 8.5 mm hr^{-1}, with a mean and standard deviation of 2.1 ± 1.2 mm hr^{-1}, whereas the convective rain rate was from 0.5 to 95 mm hr^{-1}, with a mean and standard deviation of 13.1 ± 14.5 mm hr^{-1}. The frequency of stratiform rain was much higher than convective over Pune (34% and 14%, respectively). Previous studies have shown that the DSD varies with rain rate (Chakravarty and Raj, 2013; Konwar et al., 2014; Das et al., 2017; Sreekanth et al., 2019). Here we look into how the DSD changes with each percentile bin of rain rate for both rain regimes. Fig. 6.2 shows the average DSD during the study period for stratiform and convective rain regimes. It can be observed that the DSD is distinct for both the rain regimes.

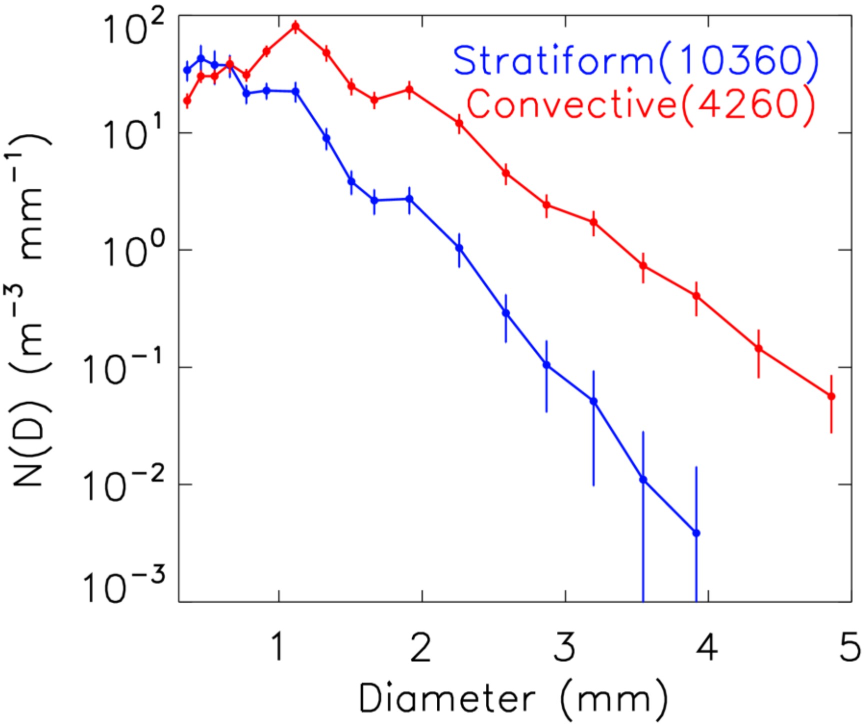

Figure 6.2 The averaged raindrop size distribution for stratiform and convective rain over the study period. The error bars indicate the standard deviation across each size bin. The numbers in the legend parenthesis indicate the total number of samples used to calculate mean raindrop size distribution for each rain type.

6.5 Rain rate and rainfall regimes

Table 6.1 summarises percentile bins considered in the analysis and corresponding stratiform and convective rain rate ranges for each percentile bin (rain rate class). The stratiform and convective rainfall is further segregated based on percentile values of estimated rain rate to illustrate the variation of DSD with rain rate. Fig. 6.3a and b show the average DSD for each rain rate class for stratiform rain and convective rain regimes. The rain rate ranges of convective rain are two orders higher than stratiform rain; hence it is not feasible to compare them in identical rain rate classes. The dominance of small raindrops (<1 mm) is seen throughout the stratiform rain rate classes. In the case of convective rain, the shift in the mode diameter of raindrops towards larger size is observed with an increase in the rain rate. Also, the concentration of smaller raindrops decreases with the rain rate for convective rain.

Table 6.1 Averaged values of mass-weighted mean diameter (D_m), rain rate (RR), and normalised intercept parameter ($\log_{10}N_w$) for stratiform rain (SR) and convective rain (CR) for each rain rate class.

RR class	Quartile range	Stratiform rain				Convective rain			
		RR (mm hr^{-1})	# Samples	D_m (mm)	$\log_{10}N_w$ (m^{-3} mm^{-1})	RR (mm hr^{-1})	# Samples	D_m (mm)	$\log_{10}N_w$ (m^{-3} mm^{-1})
1	0 - 20	0.5 - 1.0	2072	1.1	2.59	0.5 - 4.4	852	1.28	2.84
2	20 - 40	1.0 - 1.5	2072	1.23	2.63	4.4 - 6.9	852	1.47	3.00
3	40 - 60	1.5 - 2.2	2072	1.34	2.66	6.9 - 10.0	852	1.58	3.06
4	60 - 80	2.2 - 3.1	2072	1.47	2.68	10.0 - 17.6	852	1.76	3.09
5	80 - 90	3.1 - 3.9	1036	1.58	2.70	17.6 - 30.1	426	2.16	3.02
6	90 - 95	3.9 - 4.6	518	1.65	2.72	30.1 - 44.2	213	2.48	3.01
7	95 - 98	4.6 - 5.3	311	1.69	2.75	44.2 - 62.1	128	2.64	3.08
8	98 - 100	5.3 - 8.5	206	1.74	2.79	62.1 - 143.3	84	2.80	3.15

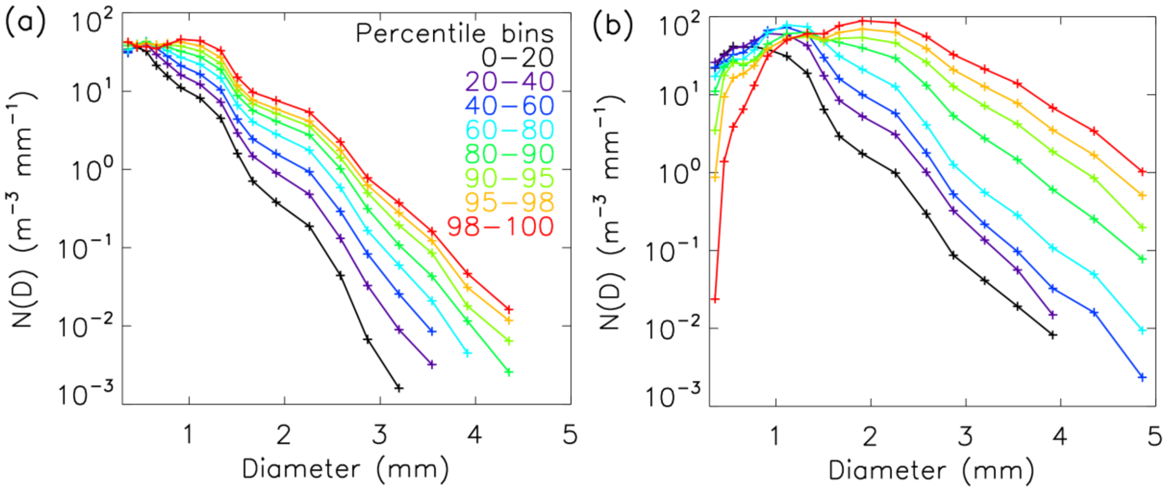

Figure 6.3 (a) averaged DSD for stratiform rain for chosen rain rate classes (refer to Table 6.1) and (b) same as (a), but for convective rain.

The mass-weighted mean diameter is 1.5 times larger in convective rain as compared to stratiform rain in higher rain rate classes (Table 6.1). The increase in $\log_{10}N_w$ with the rain rate indicates the increase in the number of raindrops. The association between the rain rate classes and estimated gamma parameters is given in Fig. 6.4. The higher D_m and $\log_{10}N_w$ values for convective rain compared to stratiform in all rain rate classes show that the convective rain has higher concentrations of medium (1-3 mm) to large (>3 mm) size raindrops (Fig. 6.4a-b). The positive value of μ for both stratiform and convective rain indicates the concave downwards shape of the DSD in the monsoon season (Fig. 6.3c). The skew of convective DSDs towards larger drops is shown by the higher values of μ. The breadth of the DSD is demonstrated by the Λ, i.e., a smaller value of Λ indicates a broader DSD. The comparison between Λ values of both rain regimes shows that convective DSD extends towards larger diameter drops (Fig. 6.4d). The shape and slope parameters across the rain rate classes implies a wider raindrop size spectrum for convective rain than stratiform rain.

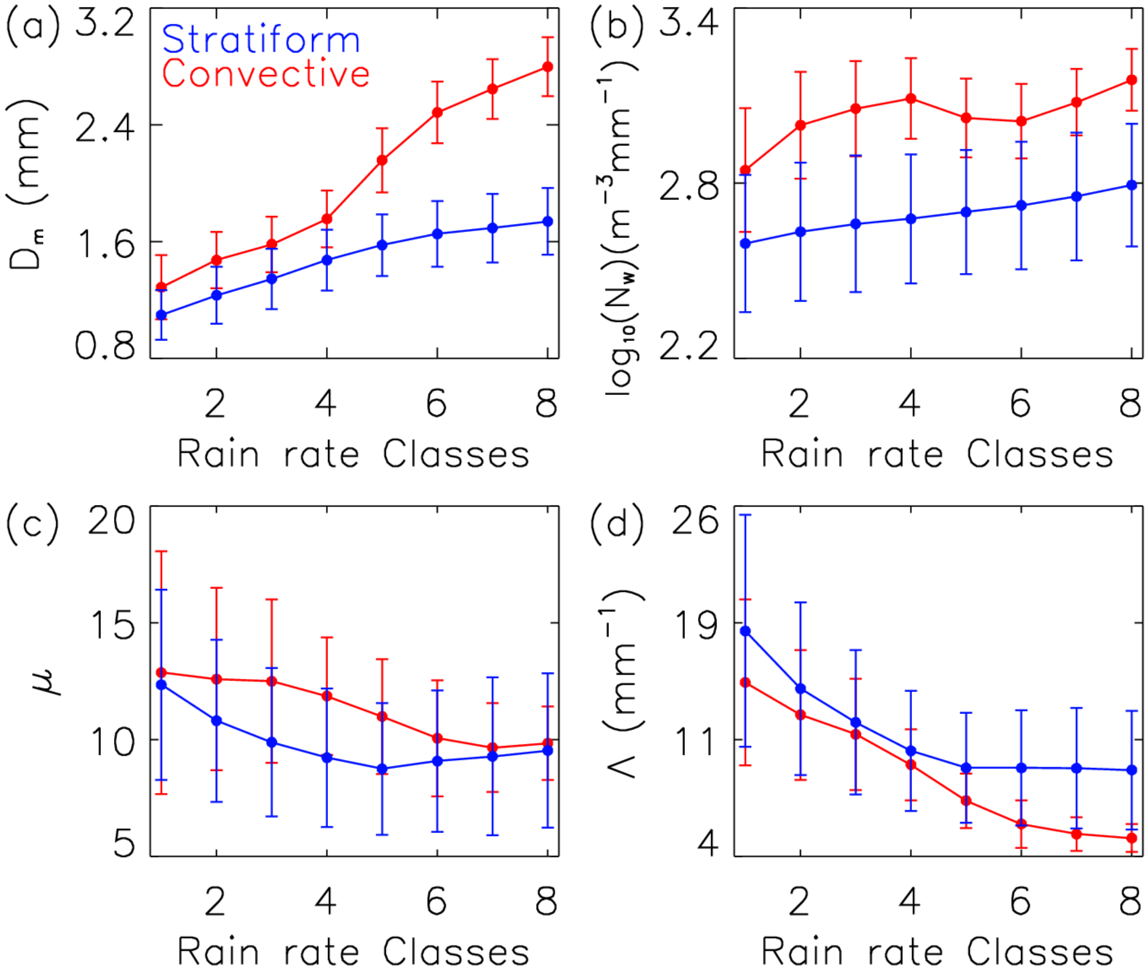

Figure 6.4 Association between rain rate classes and calculated gamma parameters from the DSD. (a) mass-weighted mean diameter, (b) normalised DSD scaling parameter, (c) shape parameter and (d) slope parameter.

The association between D_m and $\log_{10}N_w$ for stratiform and convective rain at Pune and previous studies over other locations is illustrated in Fig. 6.5. The clustering of points on the D_m - $\log_{10}N_w$ space is distinctive for stratiform and convective rain. Bringi et al. (2003) demonstrated the clustering of the points into maritime and continental rain in the D_m - $\log_{10}N_w$ space based on disdrometer measurements from various sites. The DSD measurement from Nanjing, China, during the East Asian monsoon (June-August) season of 2009-2011, and 2014-2015, was reported by Chen et al. (2013) and Wen et al. (2016), respectively. The long-term (2005-2014) summer rainfall disdrometer measurements from Taiwan were reported by Seela et al. (2018). The convective rainfall points from the coastal sites, Nanjing and Taiwan, were clustered around the maritime convective box of Bringi et al. (2003) since they are influenced by the maritime clouds originating from South China sea. The points from Mahabaleswar during the Indian summer monsoon season of 2012-2015 (Das et al., 2017) stands out in the space as the site is located at a high altitude on the Western Ghats, where the DSD is known to be influenced by the orography (Konwar et al., 2014). The averaged $\log_{10}N_w$ and D_m from the coastal site of Thumba, Trivandrum during the monsoon season of 2007-2015 is lying between the values from other coastal stratiform and convective values in terms of D_m and have similar $\log_{10}N_w$. The D_m value over Pune in this study is comparable to all the studies mentioned above the $\log_{10}N_w$ value is smaller. Pune and Mahabaleswar are located on the leeward and windward sides of the Western Ghats, respectively. But the difference in the $\log_{10}N_w$ can be explained by the influence of orography, even though both site experience similar air mass during the monsoon season.

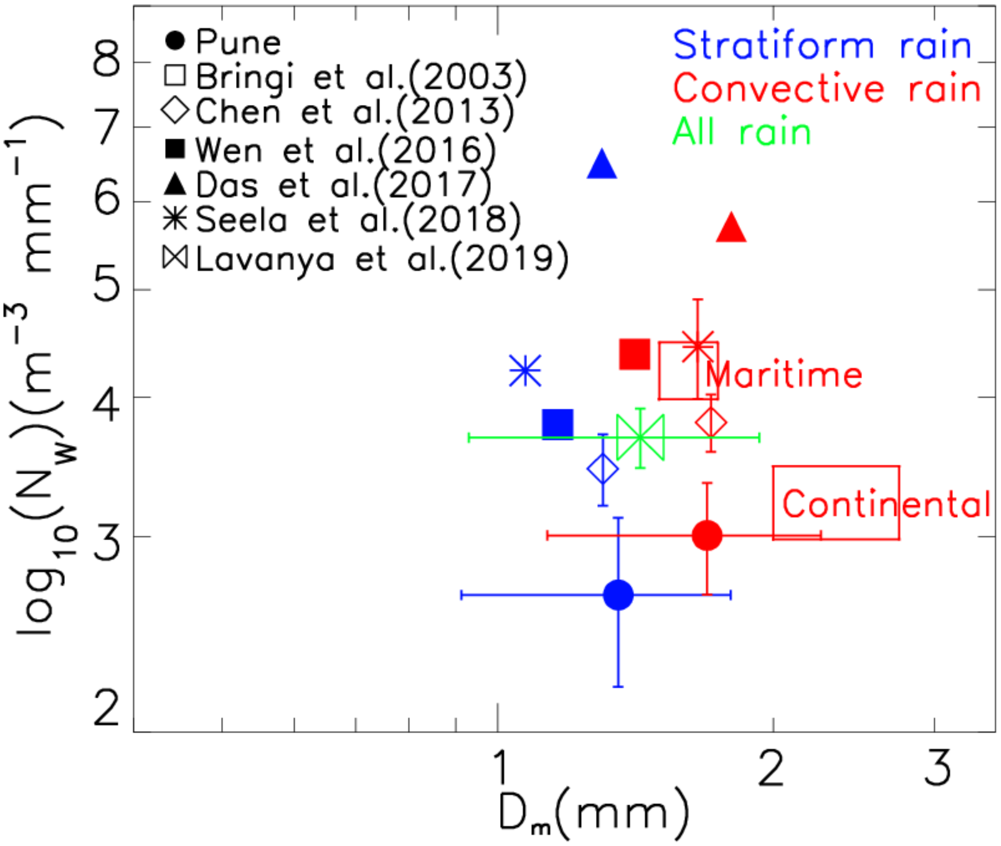

Figure 6.5 The normalised DSD scaling parameter ($\log_{10}N_w$) versus mass-weighted mean diameter (D_m) for stratiform rain (blue colour), convective rain (red colour) and all rain (green colour) regimes for this study (solid dot) and previous studies such as Bringi et al. (2003) (open square box), Chen et al. (2013) (open diamond), Wen et al. (2016) (filled square), Das et al. (2017) (filled upward triangle), Seela et al. (2018) (asterisk) and Lavanya et al. (2019) (open bowtie).

6.6 Cloud microphysical and meteorological variables

Previous studies have attributed the seasonal variation in the DSD to the seasonal changes in the cloud properties (Chakravarty and Raj, 2013; Chakravarty et al., 2013; Lavanya et al., 2019). Within a season, the difference in rainfall regimes and corresponding rain forming processes could vary the DSD. Hence, it is important to segregate and understand the instantaneous response of DSD to the varying cloud and meteorological conditions within the season. Table 6.2 summarises the low and high percentile values of CER, CDNC, CAPE and vertical wind shear (WS) for stratiform and convective rain regimes. The response of DSD is different in stratiform and convective rain regimes to the CER. Low CER resulted in a narrower

DSD (thin blue line connected by plus symbols) with a higher number concentration of small-sized raindrops (<1 mm) compared to high CER DSD (thick blue solid line) for the stratiform rain. The high CER condition resulted in a higher concentration of medium-sized raindrops (1 - 3 mm) than low CER DSD in the stratiform rain. In the case of convective rain, the response of the DSD between low and high CER is opposite and only visible for large diameter droplets (>3 mm). The variation in the DSD at low and high CDNC also showed similar responses to that of CER. The low CDNC condition resulted in a higher concentration of medium and large-sized droplets in the convective DSD compared to high CDNC.

The stratiform DSD response for low and high CAPE values was insignificant throughout the drop size spectrum except for a slight increase in small drops concentration during low CAPE. The variation in the DSD is more prominent for the convective DSD, where high CAPE resulted in an increased concentration of larger raindrops (Fig. 6.6c). The low WS resulted in a higher concentration of medium and large droplets in both rain regimes. This impact is more visible in convective rain regimes (Fig. 6.6d).

Table 6.2 Summary of cloud microphysical properties and meteorological parameters at low and high percentiles for the stratiform and convective rain. Low and high values indicate 33rd and 66th percentile values, respectively.

	Stratiform		**Convective**	
	Low	High	Low	High
CER (μm)	21.79	28.92	20.93	25.77
CDNC (cm^{-3})	45.18	68.93	41.65	73.62
CAPE ($J\ kg^{-1}$)	28.49	116.52	18.49	213.26
Wind Shear (s^{-1})	1.90	8.09	3.04	9.50

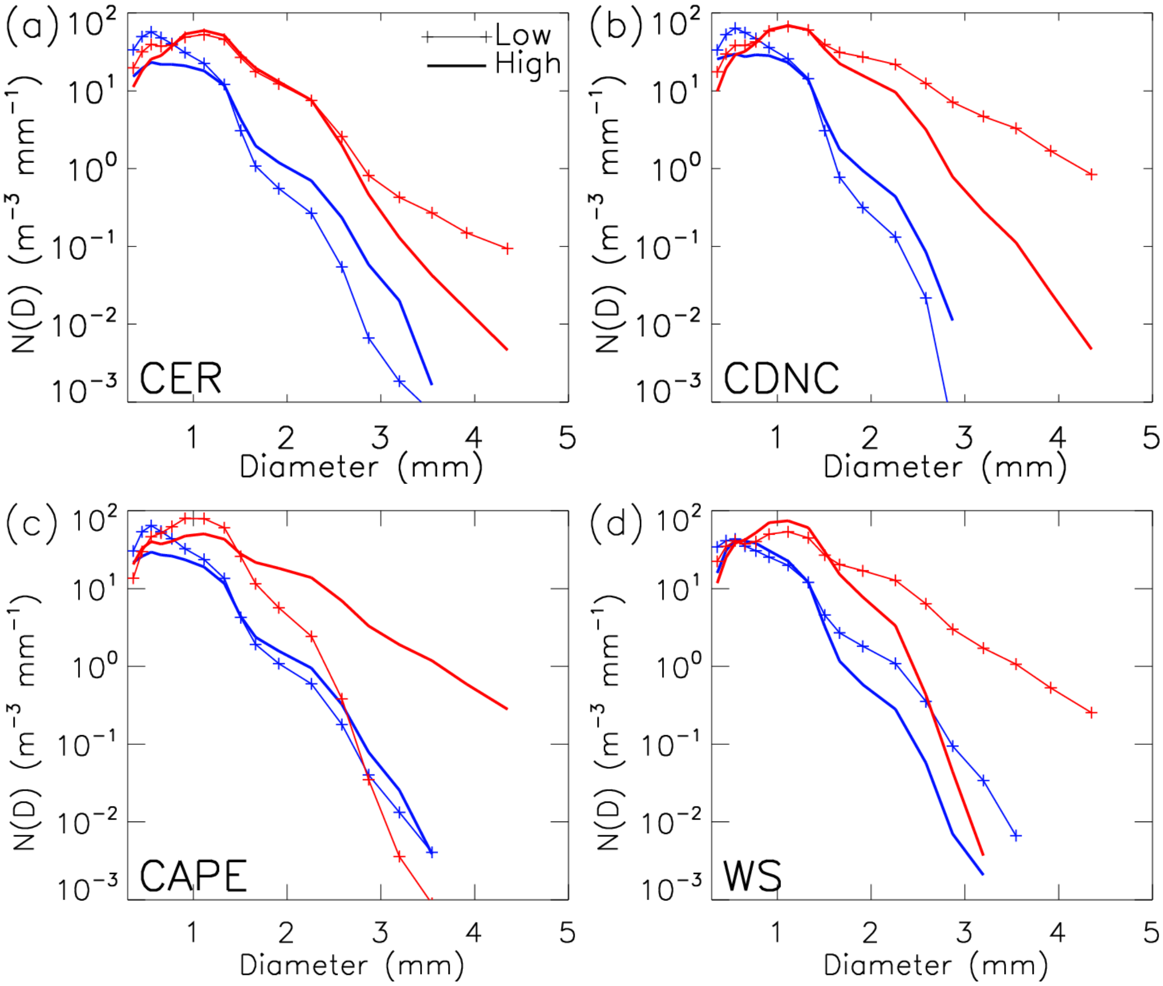

Figure 6.6 The variation in the stratiform rain (blue colour) and convective rain (red colour) DSD with respect to low and high quartile values of (a) cloud effective radius, (b) cloud droplet number concentration, (c) convective available potential energy and (d) wind shear

6.7 Discussion and conclusions

Previous studies analysed the DSD and gamma parameters by segregating them based on absolute rain rates (Chakravarty and Raj, 2013; Chakravarty et al., 2013; Seela et al., 2018; Lavanya et al., 2019). When comparing different rain regimes, seasons and locations, the rain rate classes based on absolute values will result in different numbers of samples in each class bin. Hence, taking equivalent percentile bin size will yield an equal number of samples in each bin (Table 6.1). An equal number of samples in rain rate classes can help in deriving the robust association between rain rate and corresponding gamma parameters in the stratiform and convective regimes. The DSD in the stratiform rain showed an increase in raindrop concentration in all sizes with an increase in rain rate. Whereas the concentration of larger drops increases and the smaller drops decreases for the convective rain (Fig. 6.3a-b). The gamma parameters are averaged for each rain rate class characterise the variation in the DSD with rain rate. The overall high values of D_m and $\log_{10}N_w$ in the convective rain throughout the rain rate classes highlight the larger average raindrop size and the higher number concentration of drops as compared to the stratiform. The lower values of Λ and higher values of μ in the convective rain show that the DSD is broader and skewed towards a larger drop size. The difference in the rain forming mechanism of stratiform and convective rain is reflected in the variation in gamma parameters. Convective rain is formed within active cumulus/cumulonimbus clouds, and stratiform rain is produced in nimbostratus clouds (Houze, 2014). The difference in the updraft velocities causes variation in the raindrop growth. The convectively active clouds have higher updrafts, helping them to grow to a medium-large size before falling to the ground.

The inter-seasonal variation of the DSD has been widely studied over the Indian region, and the variation in DSD was linked to the seasonal average of cloud and dynamical properties (Chakravarty and Raj, 2013; Chakravarty et al., 2013; Das et al., 2017; Lavanya et al., 2019). The D_m value reported over the location of the study is comparable to previous studies in India and abroad (Fig. 6.5). In contrast, the $\log_{10}N_w$ values are lesser for both rain regimes over the study location compared to other studies. Mahabaleswar is located on the windward side of the Western Ghats, and 89% of the rain received was shallow-convective with a high $\log_{10}N_w$ value (Das et al., 2017). Pune, being on the leeward side of the Western Ghats, explains the dominance of smaller to medium-sized raindrops. Konwar et al. (2014) demonstrated that the breakup and collision-coalescence processes of large raindrops amplify the number concentration of medium-sized raindrops over Pune. The orographic forcing over Mahabaleswar triggered collision-coalescence processes which triggered the collision-coalescence processes leading to larger drops (Konwar et al., 2014).

The previous studies which compared the DSD between seasons showed that the monsoon season has a higher number of smaller-sized droplets as compared to pre-monsoon and post-monsoons season, and a higher CER value is observed during the monsoon season (Chakravarty and Raj, 2013; Chakravarty et al., 2013). A similar result is attained when the convective DSD is compared for low and high CER conditions (Fig. 6.6a), a narrower DSD with a higher concentration of smaller drops is observed when the CER is high. The aerosol-induced cloud invigoration effect can explain the high CER during the monsoon season (Koren and Feingold, 2011; Sarangi et al., 2017; Sarangi et al., 2018). Konwar et al. (2014) have shown that the breakup of large raindrops leads to an increase in the concentration of medium size raindrops over Pune. The observations made at Gadanki (Southeastern peninsular India) also showed a prevalence of smaller raindrops in the monsoon season (Rao et al., 2009). The aerosols can increase the number of cloud droplets and decrease the droplet size for a given cloud water content (Albrecht, 1989). But the increased moisture in the monsoon season aids in the growth of cloud drops (Chakravarty and Raj, 2013). The cloud droplet number concentrations were derived to understand the aerosol impact on the cloud and thus on the raindrop spectrum. The higher cloud droplet number concentration resulted in a broader DSD in the stratiform rain regime and the opposite for the convective rain regime. The higher moisture and stronger ascent in the monsoon season help in the growth of raindrops even at high cloud droplet number concentrations.

The strong convection, indicated by the higher CAPE values, results in stronger updrafts which can keep the raindrops aloft for a longer time. The raindrops grow via collision and coalescence up to the limit when their fall velocities are greater than the updraft, therefore only larger drops reach the ground (Kollias et al., 2001). The advection drops above the freezing levels, increases the efficiency of riming and forms larger ice hydrometeors, which eventually melt and fall as large raindrops (Andreae et al., 2004; Rosenfeld et al., 2008; Sarangi et al., 2017). Strong vertical wind shear is a characteristic of monsoon circulation (Joseph and Sijikumar, 2004). The presence of a low-level jet stream results in enhanced convection which alters the DSD during monsoon season (Joshi et al., 2006; Ruchith et al., 2016). Lower wind shear and higher convective available potential energy further promoted the concentration of larger droplets in convective rain due to stronger updrafts in such conditions. Our findings suggest that the improved understanding of such instantaneous responses, especially on the convective rain DSD, could help in the short-term prediction of heavy rainfall events that are becoming frequent in the warming anthropogenic scenario.

Chapter 7

Conclusions and Future Scope

7.1 Conclusions

Despite extensive studies of atmospheric aerosols over the last more than three decades, the impact of the aerosols on human health, air quality, weather, and climate is not well understood. This is mainly due to high spatio-temporal heterogeneity in aerosol number, mass, size and composition and inadequate process-level understanding of aerosol-related changes in the cloud, particularly. The uncertainties are hampered by our limited understanding of diverse aerosol sources and their transformation in the atmosphere. The comprehensive and rigorous data analyses of satellite and reanalysis datasets have provided new insights to our current understanding of spatio-temporal variability of aerosol loading over India and adjoining marine regions. Our investigations showed that aerosol loading over central India is increasing at a much faster rate than the aerosol loading over Indo-Gangetic Plain in recent years. However, the absolute aerosol concentration is higher over Indo-Gangetic Plain than over Central India during the dry winter season. The increase in aerosol loading is corroborated by the enhanced biomass burning (absorbing aerosols) over Central India, which is one of the potential reasons. This resulted in higher aerosol loading over the Arabian Sea than the Bay of Bengal in recent years during the dry winter season. The increase in aerosol loading in recent years has caused enhanced aerosol-induced atmospheric warming and surface cooling. This has led to an increase in lower tropospheric stability, which can cause a positive feedback cycle which further leads to the accumulation of aerosols near the surface (Thomas et al., 2019)

To further quantify the long-range transport of aerosols onto the outflow region of the Bay of Bengal, the COVID-19 forced lockdown natural clean scenario during pre-monsoon 2020 was used and compared with business-as-usual time periods (2015-2019). The westerly winds during the pre-monsoon are stronger, and the mixing of anthropogenic aerosols with mineral dust aerosols in this season makes it difficult to estimate the anthropogenic impact on aerosol loading over the Bay of Bengal. Thus, the COVID-19 enforced lockdown created a natural low concentration scenario to investigate the anthropogenic influence of aerosols onto the outflow region of the Bay of Bengal. We found a 10-25% reduction in anthropogenic aerosol loading over the Indo-Gangetic Plain during the COVID-19 enforced lockdown, which has led to a 20-25% decrease of aerosol direct radiative forcing over outflow region of the Bay of Bengal (Thomas et al., 2021b).

Thomas et al. (2019) and Thomas et al. (2021b) showed significant transport of anthropogenic aerosols onto outflow regions of the Arabian Sea in the dry winter season and the Bay of Bengal in the pre-monsoon season, respectively. We further investigate aerosol-related changes in cloud properties over the Arabian Sea and the Bay of Bengal during the monsoon season, where the influx of dust aerosols is prominent. The aerosol-cloud interaction over the Arabian Sea and the Bay of Bengal during the monsoon season was found to be different owing to the difference in aerosol loading and cloud structure across the basins. The south-westerlies during the monsoon season bring in dust from the middle east and north African region over to the Indian summer monsoon region. The dominance of low clouds in the Arabian Sea and deep clouds in the Bay of Bengal results in different cloud radiative effects. Therefore, an attempt is made to understand the forcing of low clouds on both basins under various meteorological conditions. The difference in meteorological feedbacks impacted the aerosol sensitivity to the shortwave forcing due to low clouds in both regions.

The processes, interaction, and feedback mechanisms related to aerosol-cloud interaction impacts rainfall and thereby influence the hydrological cycle and climate. As a case study, we utilise raindrop size distribution measurements from a tropical site, Pune, to understand the response of cloud properties and meteorological parameters on raindrop size distribution for stratiform and convective rain regimes. The raindrop formation in clouds is influenced by the various cloud, meteorological and dynamical conditions, and it varies for different rainfall regimes. We found that the response of the cloud microphysical properties to the surface raindrop size distribution are different for stratiform and convective rainfall regimes during the monsoon season. The high cloud effective radius conditions resulted in a raindrop size distribution that was skewed towards larger drops in the stratiform rain. However, the cloud effective radius conditions resulted in a narrower raindrop size distribution with the dominance of smaller raindrops for convective rain. The distinctive response of raindrop size distribution to various rain regimes shows the need to parameterise the instantaneous cloud responses to rainfall in order to understand the cloud microphysical effects in rainfall (Thomas et al., 2021a).

7.2. Future scope

IPCC (2021) has shown an improvement in scientific understanding and estimation of aerosol radiative forcing. The forcing attributed to sulphate aerosols has increased from AR5, and that of black carbon has reduced. The uncertainty associated with black carbon radiative forcing has also decreased in the current assessment report. The AR6 concludes with high confidence that human drivers, including aerosols, have affected the global water cycle. Even though CMIP6 models have included more aerosol-cloud interaction processes, the radiative forcing from aerosol-cloud interactions remains at medium confidence. Therefore, the following knowledge gaps are yet largely open in the context of aerosols impact on weather and climate.

1. The spatio-temporal heterogeneity of aerosol concentration and the lack of observations still remains a challenge. The mixing of natural and anthropogenic aerosols and distinguishing their effects on clouds and hydrological cycles is difficult.

2. The space-borne instruments provide a long-term continuous global record of aerosol, cloud, radiation and rainfall datasets to study their impacts on weather and climate but are associated with inherent inaccuracies and drawbacks of space-borne polar-orbiting satellites. A network of high spatio-temporal collocated aerosol and cloud measurements is a way forward to study aerosol-cloud-radiation-rainfall-climate interactions

3. While instantaneous aerosol perturbation leads to suppression of rainfall (Rosenfeld, 1999, 2000; van den Heever et al., 2011; Grabowski, 2015), aerosol-induced invigoration in convective clouds has shown enhanced rainfall intensities (Koren et al., 2005; Fan et al., 2013; Khain et al., 2015; Sarangi et al., 2017). The major question is how aerosol impacts on initiation of warm rain as the amount and intensity of rain is more dictated by dynamics and atmospheric moisture availability.

4. Investigating spatio-temporal changes aerosol-cloud interactions owing to instantaneous changes in the environmental and meteorological conditions.

A high spatio-temporally resolved network of aerosol, cloud, rainfall and meteorological conditions aided with modelling efforts to interpret field observations will help to reduce current uncertainties in radiative forcing due to aerosol-induced cloud adjustments.

Bibliography

Achuthan, J., 2001. Aerosol radiation cloud interactions over the tropical Indian Ocean prior to the onset of the summer monsoon, *Curr. Sci.* **81**

Ackerman, A.S. et al., 2000. Reduction of Tropical Cloudiness by Soot, *Science* **288**, pp. 1042-1047. https://doi.org/10.1126/science.288.5468.1042

Albrecht, B.A., 1989. Aerosols, Cloud Microphysics, and Fractional Cloudiness, *Science* **245**, pp. 1227-1230. https://doi.org/10.1126/science.245.4923.1227

Andreae, M.O., 2009. Correlation between cloud condensation nuclei concentration and aerosol optical thickness in remote and polluted regions, *Atmos. Chem. Phys.*. **9**, pp. 543-556. https://doi.org/10.5194/acp-9-543-2009

Andreae, M.O., 2019. Emission of trace gases and aerosols from biomass burning – an updated assessment, *Atmos. Chem. Phys.* **19**, pp. 8523-8546. https://doi.org/10.5194/acp-19-8523-2019

Andreae, M.O., Merlet, P., 2001. Emission of trace gases and aerosols from biomass burning, *Global Geochem. Cycles* **15**, pp. 955-966. https://doi.org/10.1029/2000GB001382

Andreae, M.O. et al., 2004. Smoking Rain Clouds over the Amazon, *Science* **303**, pp. 1337-1342. https://doi.org/10.1126/science.1092779

Atlas, D., Ulbrich, C.W., 2000. An Observationally Based Conceptual Model of Warm Oceanic Convective Rain in the Tropics, *J. Appl. Meteorol. Climatol.* **39**, pp. 2165-2181. https://doi.org/10.1175/1520-0450(2001)040<2165:Aobcmo>2.0.Co;2

Babu, S.S. et al., 2013. Trends in aerosol optical depth over Indian region: Potential causes and impact indicators, *J. Geophys. Res. Atmos*. **118**, pp. 11,794-711,806. https://doi.org/10.1002/2013JD020507

Babu, S.S. et al., 2008. Aircraft measurements of aerosol black carbon from a coastal location in the north-east part of peninsular India during ICARB, *J. Earth Syst. Sci.***117**, pp. 263-271. https://doi.org 10.1007/s12040-008-0030-1

Badarinath, K.V.S., Kharol, S.K., Kaskaoutis, D.G., Kambezidis, H.D., 2007. Case study of a dust storm over Hyderabad area, India: Its impact on solar radiation using satellite data and ground measurements, *Sci. Total Environ.* **384**, pp. 316-332. https://doi.org/10.1016/j.scitotenv.2007.05.031

Balaguru, K., Leung, L.R., Lu, J., Foltz, G.R., 2016. A meridional dipole in premonsoon Bay of Bengal tropical cyclone activity induced by ENSO, *J. Geophys. Res. Atmos*. **121**, pp. 6954-6968. https://doi.org/10.1002/2016jd024936

Banerjee, P., Satheesh, S.K., Moorthy, K.K., Nanjundiah, R.S., Nair, V.S., 2019. Long-Range Transport of Mineral Dust to the Northeast Indian Ocean: Regional versus Remote Sources and the Implications, *J. Clim.* **32**, pp. 1525-1549. https://doi.org/10.1175/JCLI-D-18-0403.1 %J

Baudouin, J.P., Herzog, M., Petrie, C.A., 2020. Cross-validating precipitation datasets in the Indus River basin, *Hydrol. Earth Syst. Sci.* **24**, pp. 427-450. https://doi.org/10.5194/hess-24-427-2020

Beegum, S.N. et al., 2008. Characteristics of spectral aerosol optical depths over India during ICARB, *J. Earth Syst. Sci.* **117**, pp. 303-313. https://doi.org/10.1007/s12040-008-0033-y

Bellouin, N. et al., 2020. Bounding Global Aerosol Radiative Forcing of Climate Change, *Rev. Geophys* **58**, p. e2019RG000660. https://doi.org/10.1029/2019rg000660

Bennartz, R., Rausch, J., 2017. Global and regional estimates of warm cloud droplet number concentration based on 13 years of AQUA-MODIS observations, *Atmos. Chem. Phys*. **17**, pp. 9815-9836. https://doi.org/10.5194/acp-17-9815-2017

Bharali, C., Nair, V.S., Chutia, L., Babu, S.S., 2019. Modeling of the Effects of Wintertime Aerosols on Boundary Layer Properties Over the Indo Gangetic Plain, *J. Geophys. Res. Atmos.* **124**, pp. 4141-4157. https://doi.org/10.1029/2018JD029758

Bilal, M., Nichol, J.E., 2015. Evaluation of MODIS aerosol retrieval algorithms over the Beijing-Tianjin-Hebei region during low to very high pollution events, *J. Geophys. Res. Atmos.* **120**, pp. 7941-7957. https://doi.org/10.1002/2015JD023082

Bollasina, M.A., Ming, Y., Ramaswamy, V., 2011. Anthropogenic Aerosols and the Weakening of the South Asian Summer Monsoon, *Science* **334**, pp. 502-505. https://doi.org/10.1126/science.1204994

Bond, T.C. et al., 2007. Historical emissions of black and organic carbon aerosol from energy-related combustion, 1850–2000, *Global Biogeochem. Cycles* **21**. https://doi.org/10.1029/2006GB002840

Bony, S., Collins, W.D., Fillmore, D.W., 2000. Indian Ocean Low Clouds during the Winter Monsoon, *J. Clim.* **13**, pp. 2028-2043. https://doi.org/10.1175/1520-0442(2000)013<2028:Iolcdt>2.0.Co;2

Boucher, O. et al., 2003. DMS atmospheric concentrations and sulphate aerosol indirect radiative forcing: a sensitivity study to the DMS source representation and oxidation, *Atmos. Chem. Phys*. **3**, pp. 49-65. https://doi.org/10.5194/acp-3-49-2003

Boucher, O. et al., 2013. Clouds and Aerosols. in: Stocker, T.F. et al. (Eds.), Climate Change 2013: The Physical Science Basis. Contribution of Working Group I to the Fifth Assessment Report of the Intergovernmental Panel on Climate Change, Cambridge University Press, Cambridge, United Kingdom and New York, NY, USA, pp. 571–658.

Bringi, V.N. et al., 2003. Raindrop Size Distribution in Different Climatic Regimes from Disdrometer and Dual-Polarized Radar Analysis, *J. Atmos. Sci.* **60**, pp. 354-365. https://doi.org/10.1175/1520-0469(2003)060<0354:Rsdidc>2.0.Co;2

Bringi, V.N., Seliga, T.A., Cooper, W.A., 1984. Analysis of aircraft hydrometeor spectra and differential reflectivity (ZDR) radar measurements during the Cooperative Convective Precipitation Experiment, *Radio Sci.* **19**, pp. 157-167. https://doi.org/10.1029/RS019i001p00157

Brock, J.R., Suck, S.H., 1982. Aerosol Dynamics, *Aerosol Sci. Technol.* **2**, pp. 200-213. https://doi.org/10.1080/02786828308958624

Brooks, J. et al., 2019. Vertical and horizontal distribution of submicron aerosol chemical composition and physical characteristics across northern India during pre-monsoon and monsoon seasons, *Atmos. Chem. Phys.* **19**, pp. 5615-5634. https://doi.org/10.5194/acp-19-5615-2019

Buchard, V. et al., 2016. Evaluation of the surface PM2.5 in Version 1 of the NASA MERRA Aerosol Reanalysis over the United States, *Atmos. Environ.* **125**, pp. 100-111. https://doi.org/10.1016/j.atmosenv.2015.11.004

Bucsela, E.J. et al., 2013. A new stratospheric and tropospheric NO₂ retrieval algorithm for nadir-viewing satellite instruments: applications to OMI, *Atmos. Meas. Tech.* **6**, pp. 2607-2626.10.5194/amt-6-2607-2013

Burney, J., Ramanathan, V., 2014. Recent climate and air pollution impacts on Indian agriculture, *Proc. Natl. Acad. Sci.* **111**, pp. 16319-16324. https://doi.org/10.1073/pnas.1317275111

Cantrell, W., Shaw, G., Leck, C., Granat, L., Cachier, H., 2000. Relationships between cloud condensation nuclei spectra and aerosol particles on a south-north transect of the Indian Ocean, *J. Geophys. Res. Atmos.* **105**, pp. 15313-15320. https://doi.org/10.1029/2000JD900219

Carslaw, K.S., Lee, L.A., Reddington, C.L., Mann, G.W., Pringle, K.J., 2013. The magnitude and sources of uncertainty in global aerosol, *Faraday Discuss.* **165**, pp. 495-512. https://doi.org/10.1039/C3FD00043E

Chakravarty, K., Raj, E.P., 2013. Raindrop size distributions and their association with characteristics of clouds and precipitation during monsoon and post-monsoon periods over a tropical Indian station, *Atmos. Res.***124**, pp. 181-189. https://doi.org/10.1016/j.atmosres.2013.01.005

Chakravarty, K., Raj, E.P., Bhattacharya, A., Maitra, A., 2013. Microphysical characteristics of clouds and precipitation during pre-monsoon and monsoon period over a tropical Indian station, *J. Atmos. Sol.-Terr. Phys.* **94**, pp. 28-33. https://doi.org/10.1016/j.jastp.2012.12.016

Chamberlain, A.C., 1953. CXXI. Experiments on the deposition of iodine 131 vapour onto surfaces from an airstream, *London Edinburgh Philos. Mag. J. Sci.* **44**, pp. 1145-1153. https://doi.org/10.1080/14786441008520374

Chang, D.Y. et al., 2017. Aerosol physicochemical effects on CCN activation simulated with the chemistry-climate model EMAC, *Atmos. Environ.* **162**, pp. 127-140. https://doi.org/10.1016/j.atmosenv.2017.03.036

Charlson, R.J., Langner, J., Rodhe, H., Leovy, C.B., Warren, S.G., 1991. Perturbation of the northern hemisphere radiative balance by backscattering from anthropogenic sulfate aerosols, *Tellus A: Dyn. Meteorol. Oceanogr.* **43**, pp. 152-163. https://doi.org/10.3402/tellusa.v43i4.11944

Charlson, R.J. et al., 1992. Climate Forcing by Anthropogenic Aerosols, *Science* **255**, pp. 423-430. https://doi.org/10.1126/science.255.5043.423

Chauhan, A., Singh, R.P., 2020. Decline in PM2.5 concentrations over major cities around the world associated with COVID-19, *Environ. Res.* **187**, p. 109634. https://doi.org/10.1016/j.envres.2020.109634

Chen, B., Yang, J., Pu, J., 2013. Statistical Characteristics of Raindrop Size Distribution in the Meiyu Season Observed in Eastern China, *J. Meteorol. Soc. Japan. II* **91**, pp. 215-227. https://doi.org/10.2151/jmsj.2013-208

Chen, Q. et al., 2019. The Roles of Mineral Dust as Cloud Condensation Nuclei and Ice Nuclei During the Evolution of a Hail Storm, *J. Geophys. Res. Atmos.* **124**, pp. 14262-14284. https://doi.org/10.1029/2019JD031403

Chen, Y.-C., Christensen, M.W., Stephens, G.L., Seinfeld, J.H., 2014. Satellite-based estimate of global aerosol–cloud radiative forcing by marine warm clouds, *Nat. Geosci.* **7**, pp. 643-646. https://doi.org/10.1038/ngeo2214

Christensen, M.W. et al., 2017. Unveiling aerosol–cloud interactions – Part 1: Cloud contamination in satellite products enhances the aerosol indirect forcing estimate, *Atmos. Chem. Phys.* **17**, pp. 13151-13164. https://doi.org/10.5194/acp-17-13151-2017

Chylek, P., Wong, J., 1995. Effect of absorbing aerosols on global radiation budget, *Geophys. Res. Lett.* **22**, pp. 929-931. https://doi.org/10.1029/95GL00800

Coakley, J.A., Cess, R.D., Yurevich, F.B., 1983. The Effect of Tropospheric Aerosols on the Earth's Radiation Budget: A Parameterization for Climate Models, *J. Atmos. Sci.* **40**, pp. 116-138. https://doi.org/10.1175/1520-0469(1983)040<0116:Teotao>2.0.Co;2

Curier, R.L. et al., 2008. Retrieval of aerosol optical properties from OMI radiances using a multiwavelength algorithm: Application to western Europe, *J. Geophys. Res. Atmos.* **113**. https://doi.org/10.1029/2007jd008738

Cusworth, D.H. et al., 2018. Quantifying the influence of agricultural fires in northwest India on urban air pollution in Delhi, India, *Environ. Res. Lett.* **13**, p. 044018. https://doi.org/10.1088/1748-9326/aab303

D'Almeida, G.A., Koepke, P., Shettle, E.P., 1991. Atmospheric aerosols: global climatology and radiative characteristics. A. Deepak Pub, Hampton, Va., USA.

Das, S.K., Konwar, M., Chakravarty, K., Deshpande, S.M., 2017. Raindrop size distribution of different cloud types over the Western Ghats using simultaneous measurements from Micro-Rain Radar and disdrometer, *Atmos. Res.***186**, pp. 72-82. https://doi.org/10.1016/j.atmosres.2016.11.003

Dave, P., Bhushan, M., Venkataraman, C., 2017. Aerosols cause intraseasonal short-term suppression of Indian monsoon rainfall*, Sci. Rep.* **7**, p. 17347. https://doi.org/10.1038/s41598-017-17599-1

Dee, D.P. et al., 2011. The ERA-Interim reanalysis: configuration and performance of the data assimilation system, *Q.J.R. Meteorol. Soc.* **137**, pp. 553-597. https://doi.org/10.1002/qj.828

Dey, S., Di Girolamo, L., 2010. A climatology of aerosol optical and microphysical properties over the Indian subcontinent from 9 years (2000–2008) of Multiangle Imaging Spectroradiometer (MISR) data, *J. Geophys. Res. Atmos.* **115**. https://doi.org/10.1029/2009JD013395

Dey, S., Di Girolamo, L., 2011. A decade of change in aerosol properties over the Indian subcontinent, *Geophys. Res. Lett.* **38**. https://doi.org/10.1029/2011GL048153

Dey, S. et al., 2012. Variability of outdoor fine particulate (PM2.5) concentration in the Indian Subcontinent: A remote sensing approach, *Remote Sens. Environ.* **127**, pp. 153-161. https://doi.org/10.1016/j.rse.2012.08.021

Dey, S., Tripathi, S.N., Singh, R.P., Holben, B.N., 2004. Influence of dust storms on the aerosol optical properties over the Indo-Gangetic basin, *J. Geophys. Res. Atmos.* **109**. https://doi.org/10.1029/2004JD004924

Diner, D.J. et al., 1998. Multi-angle Imaging SpectroRadiometer (MISR) instrument description and experiment overview, *IEEE Trans. Geosci. Remote. Sens.* **36**, pp. 1072-1087. https://doi.org/10.1109/36.700992

Dirksen, R. et al.,2017. In-flight calibration of the ozone monitoring instrument. *Proc. SPIE 10567, International Conference on Space Optics.* https://doi.org/10.1117/12.2308149

Doelling, D.R. et al., 2016. Advances in Geostationary-Derived Longwave Fluxes for the CERES Synoptic (SYN1deg) Product, *J. Atmos. Ocean. Technol.* **33**, pp. 503-521. https://doi.org/10.1175/jtech-d-15-0147.1

Erlick, C., Frederick, J.E., 1998. *J. Geophys. Res. Atmos.* **103**, pp. 23275-23285. https://doi.org/10.1029/98JD02119

Fan, J. et al., 2013. Microphysical effects determine macrophysical response for aerosol impacts on deep convective clouds, *Proc. Natl. Acad. Sci.* **110**, pp. E4581-E4590. https://doi.org/10.1073/pnas.1316830110

Fan, J., Wang, Y., Rosenfeld, D., Liu, X., 2016. Review of Aerosol?Cloud Interactions: Mechanisms, Significance, and Challenges, *J. Atmos. Sci.*, **73**, pp. 4221-4252. https://doi.org/10.1175/jas-d-16-0037.1

Fan, J. et al., 2009. Dominant role by vertical wind shear in regulating aerosol effects on deep convective clouds, . *J. Geophys. Res. Atmos.***114**. https://doi.org/10.1029/2009JD012352

Forster, P. et al., 2007. Changes in Atmospheric Constituents and in Radiative Forcing Chapter 2. Cambridge University Press, United Kingdom.

Fosu, B.O., Wang, S.-Y.S., 2015. Bay of Bengal: coupling of pre-monsoon tropical cyclones with the monsoon onset in Myanmar, *Clim. Dyn.* **45**, pp. 697-709. https://doi.org/10.1007/s00382-014-2289-z

Freud, E., Rosenfeld, D., Kulkarni, J.R., 2011. Resolving both entrainment-mixing and number of activated CCN in deep convective clouds, *Atmos. Chem. Phys.* **11**, pp. 12887-12900. https://doi.org/10.5194/acp-11-12887-2011

Gautam, R. et al., 2011. Accumulation of aerosols over the Indo-Gangetic plains and southern slopes of the Himalayas: distribution, properties and radiative effects during the 2009 pre-monsoon season, *Atmos. Chem. Phys*. **11**, pp. 12841-12863. https://doi.org/10.5194/acp-11-12841-2011

Gayatri, K., Patade, S., Prabha, T.V., 2017. Aerosol–Cloud Interaction in Deep Convective Clouds over the Indian Peninsula Using Spectral (Bin) Microphysics, *J. Atmos. Sci.*, **74**, pp. 3145-3166. https://doi.org/10.1175/jas-d-17-0034.1

Gelaro, R. et al., 2017. The Modern-Era Retrospective Analysis for Research and Applications, Version 2 (MERRA-2), *J. Clim.* **30**, pp. 5419-5454. https://doi.org/10.1175/jcli-d-16-0758.1

Ghude, S. et al., 2017. Winter Fog Experiment Over the Indo-Gangetic Plains of India, *Curr. Sci.* **112**, p. 767. https://doi.org/10.18520/cs/v112/i04/767-784

Giglio, L., Descloitres, J., Justice, C.O., Kaufman, Y.J., 2003. An Enhanced Contextual Fire Detection Algorithm for MODIS, *Remote Sens. Environ.* **87**, pp. 273-282. https://doi.org/10.1016/S0034-4257(03)00184-6

Gilardoni, S., Fuzzi, S., 2017. Chemical Composition of Aerosols of Different Origin. Atmospheric Aerosols, pp. 183-221. https://doi.org/10.1002/9783527336449.ch4

Giles, D.M. et al., 2019. Advancements in the Aerosol Robotic Network (AERONET) Version 3 database – automated near-real-time quality control algorithm with improved cloud screening for Sun photometer aerosol optical depth (AOD) measurements, *Atmos. Meas. Tech.* **12**, pp. 169-209. https://doi.org/10.5194/amt-12-169-2019

Gliß, J. et al., 2021. AeroCom phase III multi-model evaluation of the aerosol life cycle and optical properties using ground- and space-based remote sensing as well as surface in situ observations, *Atmos. Chem. Phys.* **21**, pp. 87-128. https://doi.org/10.5194/acp-21-87-2021

Gogoi, M.M. et al., 2020. Airborne in situ measurements of aerosol size distributions and black carbon across the Indo-Gangetic Plain during SWAAMI–RAWEX, *Atmos. Chem. Phys.* **20**, pp. 8593-8610. https://doi.org/10.5194/acp-20-8593-2020

Grabowski, W.W., 2015. Untangling Microphysical Impacts on Deep Convection Applying a Novel Modeling Methodology, *J. Atmos. Sci.* **72**, pp. 2446-2464. https://doi.org/10.1175/jas-d-14-0307.1

Gryspeerdt, E., Goren, T., Smith, T.W.P., 2021. Observing the timescales of aerosol–cloud interactions in snapshot satellite images, *Atmos. Chem. Phys.* **21**, pp. 6093-6109. https://doi.org/10.5194/acp-21-6093-2021

Gryspeerdt, E. et al., 2019. Constraining the aerosol influence on cloud liquid water path, *Atmos. Chem. Phys.* **19**, pp. 5331-5347. https://doi.org/10.5194/acp-19-5331-2019

Gryspeerdt, E. et al., 2020. Surprising similarities in model and observational aerosol radiative forcing estimates, *Atmos. Chem. Phys.* **20**, pp. 613-623. https://doi.org/10.5194/acp-20-613-2020

Gryspeerdt, E., Quaas, J., Bellouin, N., 2016. Constraining the aerosol influence on cloud fraction, *J. Geophys. Res. Atmos.* **121**, pp. 3566-3583. https://doi.org/10.1002/2015JD023744

Han, L., Zhou, W., Li, W., 2018. Growing Urbanization and the Impact on Fine Particulate Matter (PM2.5) Dynamics, *Sustainability* **10**, p. 1696. https://doi.org/10.3390/su10061696

Hansen, J., Sato, M., Ruedy, R., 1997. Radiative forcing and climate response, *J. Geophys. Res. Atmos.* **102**, pp. 6831-6864. https://doi.org/10.1029/96JD03436

Haque, I., Patel, P.P., 2018. Growth of metro cities in India: trends, patterns and determinants, *Urban Res. Pract.* **11**, pp. 338-377. https://doi.org/10.1080/17535069.2017.1344727

Haywood, J., Boucher, O., 2000. Estimates of the direct and indirect radiative forcing due to tropospheric aerosols: A review, *Rev. Geophys.* **38**, pp. 513-543. https://doi.org/10.1029/1999RG000078

Hazra, A., Goswami, B.N., Chen, J.-P.,2013. Role of Interactions between Aerosol Radiative Effect, Dynamics, and Cloud Microphysics on Transitions of Monsoon Intraseasonal Oscillations, *J. Atmos. Sci.* **70**, pp. 2073-2087. https://doi.org/10.1175/jas-d-12-0179.1

He, Q., Zhang, M., Huang, B., Tong, X., 2017. MODIS 3 km and 10 km aerosol optical depth for China: Evaluation and comparison, *Atmos. Environ.* **153**, pp. 150-162. https://doi.org/10.1016/j.atmosenv.2017.01.023

Hersbach, H. et al., 2020. The ERA5 global reanalysis, *Q.J.R. Meteorol. Soc.* **146**, pp. 1999-2049. https://doi.org/10.1002/qj.3803

Hersbach, H., Dee, D., 2016. ERA5 reanalysis is in production, *ECMWF Newsletter* **147**

Hess, M., Koepke, P., Schult, I., 1998. Optical Properties of Aerosols and Clouds: The Software Package OPAC, *Bull. Amer. Meteor.* **79**, pp. 831-844. https://doi.org/10.1175/1520-0477(1998)079<0831:Opoaac>2.0.Co;2

Hinds, W.C., 1982. Aerosol Technology. John Wiley & Sons, New York.

Hingmire, D. et al.,2019. Widespread fog over the Indo-Gangetic Plains and possible links to boreal winter teleconnections, *Clim. Dyn.* **52**, pp. 5477-5506. https://doi.org/10.1007/s00382-018-4458-y

Hinkelman, L.M., 2019. The Global Radiative Energy Budget in MERRA and MERRA-2: Evaluation with Respect to CERES EBAF Data, *J. Clim.* **32**, pp. 1973-1994. https://doi.org/10.1175/jcli-d-18-0445.1

Hoffmann, L. et al., 2019. From ERA-Interim to ERA5: the considerable impact of ECMWF's next-generation reanalysis on Lagrangian transport simulations, *Atmos. Chem. Phys.* **19**, pp. 3097-3124. https://doi.org/10.5194/acp-19-3097-2019

Holben, B., Vermote, E., Kaufman, Y.J., Tanre, D., Kalb, V., 1992. Aerosol retrieval over land from AVHRR data-application for atmospheric correction, *IEEE Trans. Geosci. Remote Sens.* **30**, pp. 212-222. https://doi.org/10.1109/36.134072

Holben, B.N. et al.,1998. AERONET—A Federated Instrument Network and Data Archive for Aerosol Characterization, *Remote Sens. Environ.* **66**, pp. 1-16. https://doi.org/10.1016/S0034-4257(98)00031-5

Houze, R.A., 2014. Chapter 6 - Nimbostratus and the Separation of Convective and Stratiform Precipitation. in: Houze, R.A. (Ed.), International Geophysics, Academic Press, pp. 141-163.

Hsu, N.C. et al., 2012. Global and regional trends of aerosol optical depth over land and ocean using SeaWiFS measurements from 1997 to 2010, *Atmos. Chem. Phys.* **12**, pp. 8037-8053. https://doi.org/10.5194/acp-12-8037-2012

Hsu, N.C. et al.,2013. Enhanced Deep Blue aerosol retrieval algorithm: The second generation, *J. Geophys. Res. Atmos.* **118**, pp. 9296-9315. https://doi.org/10.1002/jgrd.50712

IPCC, 2013. Climate Change 2013: The Physical Science Basis. Contribution of Working Group I to the Fifth Assessment Report of the Intergovernmental Panel on Climate Change. Cambridge University Press, Cambridge, United Kingdom and New York, NY, USA 1535 pp.

IPCC ,2021. Climate Change 2021: The Physical Science Basis. Contribution of Working Group I to the Sixth Assessment Report of the Intergovernmental Panel on Climate Change Cambridge University Press.

Jaenicke, R., 1980a. Atmospheric aerosols and global climate, *J. Aerosol Sci.* **11**, pp. 577-588. https://doi.org/10.1016/0021-8502(80)90131-7

Jaenicke, R., 1980b. NATURAL AEROSOLS*, *Ann. N. Y. Acad. Sci.* **338**, pp. 317-329. https://doi.org/10.1111/j.1749-6632.1980.tb17129.x

Jethva, H., Torres, O., 2011. Satellite-based evidence of wavelength-dependent aerosol absorption in biomass burning smoke inferred from Ozone Monitoring Instrument, *Atmos. Chem. Phys.* **11**, pp. 10541-10551. https://doi.org/10.5194/acp-11-10541-2011

Jia, H., Ma, X., Quaas, J., Yin, Y., Qiu, T., 2019. Is positive correlation between cloud droplet effective radius and aerosol optical depth over land due to retrieval artifacts or real physical processes?, *Atmos. Chem. Phys.* **19**, pp. 8879-8896. https://doi.org/10.5194/acp-19-8879-2019

Jia, H., Ma, X., Yu, F., Quaas, J., 2021. Significant underestimation of radiative forcing by aerosol–cloud interactions derived from satellite-based methods, *Nat. Comm.* **12**, p. 3649. https://doi.org/10.1038/s41467-021-23888-1

Jose, S., Mishra, A.K., Singh, S., 2021. A correlational study on size differentiated aerosols on monsoonal and pre-monsoonal cloud properties over the Indo Gangetic Basin, *Atmos. Res.* **262**, p. 105796. https://doi.org/10.1016/j.atmosres.2021.105796

Jose, S., Nair, V.S., Babu, S.S., 2020. Anthropogenic emissions from South Asia reverses the aerosol indirect effect over the northern Indian Ocean, *Sci. Rep.* **10**, p. 18360. https://doi.org/10.1038/s41598-020-74897-x

Joseph, P.V., Sijikumar, S.,2004. Intraseasonal Variability of the Low-Level Jet Stream of the Asian Summer Monsoon, *J. Clim.* **17**, pp. 1449-1458. https://doi.org/10.1175/1520-0442(2004)017<1449:Ivotlj>2.0.Co;2

Joshi, R., Singh, N., Deshpande, S., Damle, S., Pant, G., 2006. UHF wind profiler observations of monsoon low level jet over Pune, *Indian J. Radio Space Phys.* **35**, pp. 349-359

Joss, J., Waldvogel, A., 1967. Ein Spektrograph für Niederschlagstropfen mit automatischer Auswertung, *Pure Appl. Geophys.* **68**, pp. 240-246. https://doi.org/10.1007/BF00874898

Junge, C.E., 1958. Atmospheric Chemistry. in: Landsberg, H.E., Van Mieghem, J. (Eds.), Advances in Geophysics, Elsevier, pp. 1-108.

Junge, C.E., 1964. Air Chemistry and Radioactivity. Academic Press, New York 220-221 pp.

Junge, C.E., Chagnon, C.W., Manson, J.E., 1961. A World-wide Stratospheric Aerosol Layer, *Science* **133**, pp. 1478-1479. https://doi.org/10.1126/science.133.3463.1478-a

Kanamitsu, M., 1989. Description of the NMC Global Data Assimilation and Forecast System, *Weather Forecast.* **4**, pp. 335-342. https://doi.org/10.1175/1520-0434(1989)004<0335:Dotngd>2.0.Co;2

Kanawade, V.P. et al., 2020. What caused severe air pollution episode of November 2016 in New Delhi?, *Atmos. Environ.* **222**, p. 117125 .https://doi.org/10.1016/j.atmosenv.2019.117125

Kant, S., Panda, J., Gautam, R., 2019. A seasonal analysis of aerosol-cloud-radiation interaction over Indian region during 2000–2017, *Atmos. Environ.* **20**1, pp. 212-222. https://doi.org/10.1016/j.atmosenv.2018.12.044

Kaskaoutis, D.G. et al., 2011. Extremely large anthropogenic-aerosol contribution to total aerosol load over the Bay of Bengal during winter season, *Atmos. Chem. Phys.* **11**, pp. 7097-7117. https://doi.org/10.5194/acp-11-7097-2011

Kaskaoutis, D.G. et al., 2012. Variability and trends of aerosol properties over Kanpur, northern India using AERONET data (2001–10), *Environ. Res. Lett.* **7**, pp. 24003-24009. . https://doi.org/10.1088/1748-9326/7/2/024003

Kaufman, Y.J., Tanré, D., 1996. Strategy for direct and indirect methods for correcting the aerosol effect on remote sensing: From AVHRR to EOS-MODIS, *Remote Sens. Environ.* **55**, pp. 65-79. https://doi.org/10.1016/0034-4257(95)00193-X

Kedia, S., Ramachandran, S., Kumar, A., Sarin, M.M., 2010. Spatiotemporal gradients in aerosol radiative forcing and heating rate over Bay of Bengal and Arabian Sea derived on the basis of optical, physical, and chemical properties, *J. Geophys. Res. Atmos.* **115.** https://doi.org/10.1029/2009JD013136

Khain, A.P. et al., 2015. Representation of microphysical processes in cloud-resolving models: Spectral (bin) microphysics versus bulk parameterization, *Rev. Geophys.* **53**, pp. 247-322. https://doi.org/10.1002/2014RG000468

Kiehl, J.T., 1994. On the Observed Near Cancellation between Longwave and Shortwave Cloud Forcing in Tropical Regions, *J. Clim.* **7**, pp. 559-565. https://doi.org/10.1175/1520-0442(1994)007<0559:Otoncb>2.0.Co;2

Kiehl, J.T., Ramanathan, V., 1990. Comparison of cloud forcing derived from the Earth Radiation Budget Experiment with that simulated by the NCAR community climate model, *J. Geophys. Res. Atmos.* **95**, pp. 11679-11698. https://doi.org/10.1029/JD095iD08p11679

King, M.D., Platnick, S., Menzel, W.P., Ackerman, S.A., Hubanks, P.A., 2013. Spatial and Temporal Distribution of Clouds Observed by MODIS Onboard the Terra and Aqua Satellites, *IEEE Trans. Geosci. Remote Sens.* **51**, pp. 3826-3852. https://doi.org/10.1109/TGRS.2012.2227333

Kirankumar, N.V.P., Rao, T.N., Radhakrishna, B., Rao, D.N.,2008. Statistical Characteristics of Raindrop Size Distribution in Southwest Monsoon Season, *J. Appl. Meteorol. Climatol.* **47**, pp. 576-590. https://doi.org/10.1175/2007jamc1610.1

Kollias, P., Albrecht, B.A., Marks Jr., F.D., 2001. Raindrop sorting induced by vertical drafts in convective clouds, *Geophys. Res. Lett.* **28,** pp. 2787-2790. https://doi.org/10.1029/2001gl013131

Kompalli, S.K. et al., 2020. Seasonal contrast in size distributions and mixing state of black carbon and its association with PM1.0 chemical composition from the eastern coast of India, *Atmos. Chem. Phys.* **20**, pp. 3965-3985. https://doi.org/10.5194/acp-20-3965-2020

Konwar, M., Das, S.K., Deshpande, S.M., Chakravarty, K., Goswami, B.N.,2014. Microphysics of clouds and rain over the Western Ghat, *J. Geophys. Res. Atmos.* **119**, pp. 6140-6159. https://doi.org/10.1002/2014jd021606

Koren, I., Dagan, G., Altaratz, O., 2014. From aerosol-limited to invigoration of warm convective clouds, *Science* **344**, pp. 1143-1146. https://doi.org/10.1126/science.1252595

Koren, I., Feingold, G.,2011. Aerosol–cloud–precipitation system as a predator-prey problem, *Proc. Natl. Acad. Sci.***108**, pp. 12227-12232. https://doi.org/10.1073/pnas.1101777108

Koren, I., Feingold, G., Remer, L.A.,2010. The invigoration of deep convective clouds over the Atlantic: aerosol effect, meteorology or retrieval artifact?, *Atmos. Chem. Phys.* **10**, pp. 8855-8872. https://doi.org/10.5194/acp-10-8855-2010

Koren, I., Kaufman, Y., Rosenfeld, D., Remer, L., Rudich, Y., 2005. Aerosol invigoration and restructuring of Atlantic convective clouds, *Geophys. Res. Lett.* **32**. https://doi.org/10.1029/2005GL023187

Kulkarni, J. et al., 2012. The Cloud Aerosol Interaction and Precipitation Enhancement Experiment (CAIPEEX): overview and preliminary results, *Curr. Sci.* **102**.

Kumar, M. et al.,2018. Long-term aerosol climatology over Indo-Gangetic Plain: Trend, prediction and potential source fields, *Atmos. Environ.* **180**, pp. 37-50. https://doi.org/10.1016/j.atmosenv.2018.02.027

Lakshmi, N.B., Nair, V.S., Suresh Babu, S., 2017. Vertical Structure of Aerosols and Mineral Dust Over the Bay of Bengal From Multisatellite Observations, *J. Geophys. Res. Atmos.* **122**, pp. 12,845-812,861. https://doi.org/10.1002/2017JD027643

Latha, R., Murthy, B.S., Lipi, K., Srivastava, M.K., Kumar, M., 2017. Absorbing Aerosols, Possible Implication to Crop Yield - A Comparison between IGB Stations, *Aerosol Air Qual. Res.* **17**, pp. 693-705. https://doi.org/10.4209/aaqr.2016.02.0054

Lau, K.M., Kim, K.M., 2006. Observational relationships between aerosol and Asian monsoon rainfall, and circulation, *Geophys. Res. Lett.* **33**. https://doi.org/10.1029/2006gl027546

Lau, W.K.M., Kim, K.-M., 2010. Fingerprinting the impacts of aerosols on long-term trends of the Indian summer monsoon regional rainfall, Geophys. *Res. Lett.* .**37**. https://doi.org/10.1029/2010GL043255

Lavanya, S., Kirankumar, N.V.P., Aneesh, S., Subrahmanyam, K.V., Sijikumar, S., 2019. Seasonal variation of raindrop size distribution over a coastal station Thumba: A quantitative analysis, *Atmos. Res*. **229**, pp. 86-99. https://doi.org/10.1016/j.atmosres.2019.06.004

Lawrence, M.G., Lelieveld, J., 2010. Atmospheric pollutant outflow from southern Asia: a review, *Atmos. Chem. Phys.* **10**, pp. 11017-11096. https://doi.org/10.5194/acp-10-11017-2010

Levy, R.C. et al., 2013. The Collection 6 MODIS aerosol products over land and ocean, *Atmos. Meas. Tech.* **6**, pp. 2989-3034. https://doi.org/10.5194/amt-6-2989-2013

Levy, R.C. et al., 2010. Global evaluation of the Collection 5 MODIS dark-target aerosol products over land, *Atmos. Chem. Phys.* **10**, pp. 10399-10420. https://doi.org/10.5194/acp-10-10399-2010

Li, Z. et al., 2017. Aerosol and boundary-layer interactions and impact on air quality, *Natl. Sci. Rev.* **4**, pp. 810-833. https://doi.org/10.1093/nsr/nwx117 %J National Science Review

Li, Z., Yu, W., Li, T., Murty, V.S.N., Tangang, F., 2013. Bimodal Character of Cyclone Climatology in the Bay of Bengal Modulated by Monsoon Seasonal Cycle*, *J. Clim.* **26**, pp. 1033-1046. https://doi.org/10.1175/JCLI-D-11-00627

Liu, T. et al., 2018. Seasonal impact of regional outdoor biomass burning on air pollution in three Indian cities: Delhi, Bengaluru, and Pune, *Atmos. Environ.* **172**, pp. 83-92. https://doi.org/10.1016/j.atmosenv.2017.10.024

Liu, Y., Wu, W., Jensen, M.P., Toto, T., 2011. Relationship between cloud radiative forcing, cloud fraction and cloud albedo, and new surface-based approach for determining cloud albedo, *Atmos. Chem. Phys.* **11**, pp. 7155-7170. https://doi.org/10.5194/acp-11-7155-2011

Loeb, N.G., Kato, S., Loukachine, K., Manalo-Smith, N., Doelling, D.R.,2007. Angular Distribution Models for Top-of-Atmosphere Radiative Flux Estimation from the Clouds and the Earth’s Radiant Energy System Instrument on the Terra Satellite. Part II: Validation, *J. Atmos. Ocean. Technol.* **24**, pp. 564-584. https://doi.org/10.1175/jtech1983.1

Loeb, N.G., Manalo-Smith, N., Su, W., Shankar, M., Thomas, S., 2016. CERES Top-of-Atmosphere Earth Radiation Budget Climate Data Record: Accounting for in-Orbit Changes in Instrument Calibration, *Remote Sens.* **8**, p. 182. https://doi.org/10.3390/rs8030182

Lohmann, U., 2017. Anthropogenic Aerosol Influences on Mixed-Phase Clouds, *Curr. Clim. Change Rep.* **3**, pp. 32-44. https://doi.org/10.1007/s40641-017-0059-9

Lohmann, U., Feichter, J. ,2005. Global indirect aerosol effects: a review, *Atmos. Chem. Phys.* **5**, pp. 715-737. https://doi.org/10.5194/acp-5-715-2005

Maguire II, W.B., Avery, S.K., 1994. Retrieval of Raindrop Size Distributions Using Two Doppler Wind Profilers: Model Sensitivity Testing, *J. Appl. Meteorol.* **33**, pp. 1623-1635. https://doi.org/10.1175/1520-0450(1994)033<1623:rorsdu>2.0.co;2

Mani, A., Chacko, O., Hariharan, S.,1969. A Study of Ångström's turbidity parameters from solar radiation measurements in India, *Tellus* **21**, pp. 829-843. https://doi.org/10.3402/tellusa.v21i6.10149

Mani, A., Chacko, O., Iyer, N.V., 1973. Atmospheric turbidity over India from solar radiation measurements, *Sol. Energy* **14**, pp. 185-195. https://doi.org/10.1016/0038-092X(73)90033-9

Manoj, M.G., Devara, P.C.S., Safai, P.D., Goswami, B.N., 2011. Absorbing aerosols facilitate transition of Indian monsoon breaks to active spells, *Clim. Dyn.* **37**, pp. 2181-2198. https://doi.org/10.1007/s00382-010-0971-3

Manoj, M.R., Satheesh, S.K., Moorthy, K.K., Gogoi, M.M., Babu, S.S., 2019. Decreasing Trend in Black Carbon Aerosols Over the Indian Region, *Geophys. Res. Lett.* **46**, pp. 2903-2910. https://doi.org/10.1029/2018GL081666

Mao, K.B. et al.,2014. Global aerosol change in the last decade: An analysis based on MODIS data, *Atmos. Environ.* **94**, pp. 680-686. https://doi.org/10.1016/j.atmosenv.2014.04.053

Marshall, S.F., Covert, D.S., Charlson, R.J., 1995. Relationship between asymmetry parameter and hemispheric backscatter ratio: implications for climate forcing by aerosols, *Appl. Opt.* **34**, pp. 6306-6311. https://doi.org/10.1364/AO.34.006306

McClatchey, R., Fenn, R., Selby, J., Volz, F., Garing, J.,1972. Optical Properties of the Atmosphere (Third Edition), *Environ. Res. Pap.* **32**, p. 113

Mehta, M., Singh, R., Singh, A., Singh, N., Anshumali,2016. Recent global aerosol optical depth variations and trends — A comparative study using MODIS and MISR level 3 datasets, *Remote Sens. Environ.* **181**, pp. 137-150. https://doi.org/10.1016/j.rse.2016.04.004

Menon, S., Hansen, J., Nazarenko, L., Luo, Y.,2002. Climate Effects of Black Carbon Aerosols in China and India, *Science* **297**, pp. 2250-2253. https://doi.org/10.1126/science.1075159

Mhawish, A., Banerjee, T., Broday, D.M., Misra, A., Tripathi, S.N., 2017. Evaluation of MODIS Collection 6 aerosol retrieval algorithms over Indo-Gangetic Plain: Implications of aerosols types and mass loading, *Remote Sens. Environ.* **201**, pp. 297-313. https://doi.org/10.1016/j.rse.2017.09.016

Mishchenko, M.I. et al., 2007. Long-Term Satellite Record Reveals Likely Recent Aerosol Trend, *Science* **315**, pp. 1543-1543. https://doi.org/10.1126/science.1136709

Molod, A., Takacs, L., Suarez, M., Bacmeister, J., 2015. Development of the GEOS-5 atmospheric general circulation model: evolution from MERRA to MERRA2, *Geosci. Model Dev.* **8**, pp. 1339-1356. https://doi.org/10.5194/gmd-8-1339-2015

Moorthy, K.K., Babu, S.S., Manoj, M.R., Satheesh, S.K.,2013. Buildup of aerosols over the Indian Region, *Geophys. Res. Lett.* **40**, pp. 1011-1014. https://doi.org/10.1002/grl.50165

Moorthy, K.K., Babu, S.S., Satheesh, S.K.,2005a. Aerosol Characteristics and Radiative Impacts over the Arabian Sea during the Intermonsoon Season: Results from ARMEX Field Campaign, *J. Atmos. Sci.* **62**, pp. 192-206. https://doi.org/10.1175/jas-3378.1

Moorthy, K.K., Nair, V.S., Babu, S.S., Satheesh, S.K.,2009. Spatial and vertical heterogeneities in aerosol properties over oceanic regions around India: Implications for radiative forcing, *Q.J.R. Meteorol. Soc.***135**, pp. 2131-2145. https://doi.org/10.1002/qj.525

Moorthy, K.K. et al.,2001. Aerosol optical depths over peninsular India and adjoining oceans during the INDOEX campaigns: Spatial, temporal, and spectral characteristics, *J. Geophys. Res. Atmos.***106**, pp. 28539-28554. https://doi.org/10.1029/2001JD900169

Moorthy, K.K., Satheesh, S., Kotamarthi, V.J.C.S., 2016. Evolution of aerosol research in India and the RAWEX-GVAX: an overview, *Curr. Sci.* **111**, pp. 53-75

Moorthy, K.K., Satheesh, S.K., Babu, S.S., Dutt, C.B.S., 2008. Integrated Campaign for Aerosols, gases and Radiation Budget (ICARB): An overview, *J. Earth Syst. Sci.***117**, pp. 243-262. https://doi.org/10.1007/s12040-008-0029-7

Moorthy, K.K. et al., 2005b. Wintertime spatial characteristics of boundary layer aerosols over peninsular India, *J. Geophys. Res. Atmos.***110**. https://doi.org/10.1029/2004JD005520

Muhammad, S., Long, X., Salman, M., 2020. COVID-19 pandemic and environmental pollution: A blessing in disguise?, *Sci. Total Environ.***728**, p. 138820. https://doi.org/10.1016/j.scitotenv.2020.138820

Myhre, G. et al., 2017. Multi-model simulations of aerosol and ozone radiative forcing due to anthropogenic emission changes during the period 1990–2015, *Atmos. Chem. Phys.* **17**, pp. 2709-2720. https://doi.org/10.5194/acp-17-2709-2017

Nair, V.S., Babu, S.S., Manoj, M.R., Moorthy, K.K., Chin, M., 2017. Direct radiative effects of aerosols over South Asia from observations and modeling, *Clim. Dyn.* **49**, pp. 1411-1428. https://doi.org/10.1007/s00382-016-3384-0

Nair, V.S., Babu, S.S., Moorthy, K.K., Prijith, S.S., 2013a. Spatial Gradients in Aerosol-Induced Atmospheric Heating and Surface Dimming over the Oceanic Regions around India: Anthropogenic or Natural?, *J. Clim.* **26**, pp. 7611-7621. https://doi.org/10.1175/JCLI-D-12-00616.1

Nair, V.S., Jayachandran, V.N., Kompalli, S.K., Gogoi, M.M., Babu, S.S., 2020. Cloud condensation nuclei properties of South Asian outflow over the northern Indian Ocean during winter, *Atmos. Chem. Phys*. **20**, pp. 3135-3149. https://doi.org/10.5194/acp-20-3135-2020

Nair, V.S. et al., 2007. Wintertime aerosol characteristics over the Indo-Gangetic Plain (IGP): Impacts of local boundary layer processes and long-range transport, *J. Geophys. Res. Atmos.***112**. https://doi.org/10.1029/2006jd008099

Nair, V.S., Moorthy, K.K., Babu, S.S.,2013b. Influence of continental outflow and ocean biogeochemistry on the distribution of fine and ultrafine particles in the marine atmospheric boundary layer over Arabian Sea and Bay of Bengal, *J. Geophys. Res. Atmos.***118**, pp. 7321-7331. https://doi.org/10.1002/jgrd.50541

Nakajima, T., King, M.D.,1990. Determination of the Optical Thickness and Effective Particle Radius of Clouds from Reflected Solar Radiation Measurements. Part I: Theory, *J. Atmos. Sci.* **47**, pp. 1878-1893. https://doi.org/10.1175/1520-0469(1990)047<1878:Dotota>2.0.Co;2

Narayanan, M.S., Rao, B.M., Shah, S., Prasad, V.S., Bhat, G.S., 2004. Role of atmospheric stability over the Arabian Sea and the unprecedented failure of monsoon 2002, *Curr. Sci.* **86**, pp. 938-947

Nigam, S., Bollasina, M., 2010. “Elevated heat pump” hypothesis for the aerosol-monsoon hydroclimate link: “Grounded” in observations?, *J. Geophys. Res. Atmos.***115**. https://doi.org/10.1029/2009jd013800

Niranjan, K., Madhavan, B.L., Sreekanth, V., 2007. Micro pulse lidar observation of high altitude aerosol layers at Visakhapatnam located on the east coast of India, *Geophys. Res. Lett.* **34** https://doi.org/10.1029/2006gl028199

Novakov, T. et al., 2003. Large historical changes of fossil-fuel black carbon aerosols, *Geophys. Res. Lett.* **30**. https://doi.org/10.1029/2002GL016345

O'Dowd, C.D., de Leeuw, G., 2007. Marine aerosol production: a review of the current knowledge, *Phil. Trans. R. Soc. A.* **365**, pp. 1753-1774. https://doi.org/10.1098/rsta.2007.2043

Pan, L.L. et al., 2016. Transport of chemical tracers from the boundary layer to stratosphere associated with the dynamics of the Asian summer monsoon, *J. Geophys. Res. Atmos.***121**, pp. 14,159-114,174. https://doi.org/10.1002/2016JD025616

Pan, X. et al., 2015. A multi-model evaluation of aerosols over South Asia: common problems and possible causes, *Atmos. Chem. Phys.* **15**, pp. 5903-5928. https://doi.org/10.5194/acp-15-5903-2015

Pandey, S.K., Vinoj, V., Landu, K., Babu, S.S., 2017. Declining pre-monsoon dust loading over South Asia: Signature of a changing regional climate, *Sci. Rep.* **7**, p. 16062. https://doi.org/10.1038/s41598-017-16338-w

Pandis, S.N., Wexler, A.S., Seinfeld, J.H., 1995. Dynamics of Tropospheric Aerosols, *J. Phys. Chem.* **99**, pp. 9646-9659. https://doi.org/10.1021/j100024a003

Patil, N., Dave, P., Venkataraman, C., 2017. Contrasting influences of aerosols on cloud properties during deficient and abundant monsoon years, *Sci. Rep.* **7**, p. 44996. https://doi.org/10.1038/srep44996

Pilinis, C., Pandis, S.N., Seinfeld, J.H., 1995. Sensitivity of direct climate forcing by atmospheric aerosols to aerosol size and composition, *J. Geophys. Res. Atmos.***100**, pp. 18739-18754. https://doi.org/10.1029/95JD02119

Platnick, S. et al., 2017. The MODIS Cloud Optical and Microphysical Products: Collection 6 Updates and Examples From Terra and Aqua, *IEEE Trans. Geosci. Remote Sens.***55**, pp. 502-525. https://doi.org/10.1109/tgrs.2016.2610522

Prabha, T.V. et al.,2011. Microphysics of Premonsoon and Monsoon Clouds as Seen from In Situ Measurements during the Cloud Aerosol Interaction and Precipitation Enhancement Experiment (CAIPEEX), *J. Atmos. Sci.***68**, pp. 1882-1901. https://doi.org/10.1175/2011jas3707.1

Prasad, V.K., Badarinath, K.V.S., Eaturu, A., 2008. Biophysical and anthropogenic controls of forest fires in the Deccan Plateau, India, *J. Environ. Manage.* **86**, pp. 1-13. https://doi.org/10.1016/j.jenvman.2006.11.017

Prospero, J.M., Ginoux, P., Torres, O., Nicholson, S.E., Gill, T.E., 2002. Environmental characterization of global sources of atmospheric soil dust identified with the NIMBUS 7 Total Ozone Mapping Sectrometer (TOMS) absorbing aerosol product, *Rev. Geophy.* **40**, pp. 2-1-2-31. https://doi.org/10.1029/2000RG000095

Quaas, J., Stevens, B., Stier, P., Lohmann, U., 2010. Interpreting the cloud cover – aerosol optical depth relationship found in satellite data using a general circulation model, *Atmos. Chem. Phys.* **10**, pp. 6129-6135. https://doi.org/10.5194/acp-10-6129-2010

Quinn, P.K., Bates, T.S., 2005. Regional aerosol properties: Comparisons of boundary layer measurements from ACE 1, ACE 2, Aerosols99, INDOEX, ACE Asia, TARFOX, and NEAQS, *J. Geophys. Res. Atmos.* **110**. https://doi.org/10.1029/2004JD004755

Rajeevan, M., Srinivasan, J., 2000. Net Cloud Radiative Forcing at the Top of the Atmosphere in the Asian Monsoon Region, *J. Clim.* **13**, pp. 650-657. https://doi.org/10.1175/1520-0442(2000)013<0650:Ncrfat>2.0.Co;2

Ramachandran, S., 2018. Atmospheric Aerosols: Characteristics and Radiative Effects, 1st ed. CRC Press.

Ramachandran, S., Jayaraman, A., 2003. Spectral aerosol optical depths over Bay of Bengal and Chennai: II—sources, anthropogenic influence and model estimates, *Atmos. Environ.* **37**, pp. 1951-1962. https://doi.org/10.1016/S1352-2310(03)00084-0

Ramachandran, S., Kedia, S., Srivastava, R., 2012. Aerosol optical depth trends over different regions of India, *Atmos. Environ.* **49**, pp. 338-347. https://doi.org/10.1016/j.atmosenv.2011.11.017

Ramanathan, V., 1987. The role of earth radiation budget studies in climate and general circulation research, *J. Geophys. Res. Atmos.* **92**, pp. 4075-4095. https://doi.org/10.1029/JD092iD04p04075

Ramanathan, V., Carmichael, G., 2008. Global and regional climate changes due to black carbon, *Nat. Geosci.* **1**, pp. 221-227. https://doi.org/10.1038/ngeo156

Ramanathan, V. et al., 1989. Cloud-Radiative Forcing and Climate: Results from the Earth Radiation Budget Experiment, *Science* **243**, pp. 57-63. https://doi.org/10.1126/science.243.4887.57

Ramanathan, V. et al., 2005. Atmospheric brown clouds: Impacts on South Asian climate and hydrological cycle, *Proc. Natl. Acad. Sci.* **102**, pp. 5326-5333. https://doi.org/10.1073/pnas.0500656102

Ramanathan, V., Crutzen, P.J., Kiehl, J.T., Rosenfeld, D., 2001a. Aerosols, Climate, and the Hydrological Cycle, *Science* **294**, pp. 2119-2124. https://doi.org/10.1126/science.1064034

Ramanathan, V. et al., 2001b. Indian Ocean Experiment: An integrated analysis of the climate forcing and effects of the great Indo-Asian haze, *J. Geophys. Res. Atmos.* **106**, pp. 28371-28398. https://doi.org/10.1029/2001jd900133

Ramanathan, V., Ramana, M.V., 2005. Persistent, Widespread, and Strongly Absorbing Haze Over the Himalayan Foothills and the Indo-Gangetic Plains, *Pure Appl. Geophys.***162**, pp. 1609-1626. https://doi.org/10.1007/s00024-005-2685-8

Ramaswamy, V. et al., 2001. Radiative Forcing of Climate Change. pp. 349-416.

Randles, C.A. et al., 2017. The MERRA-2 Aerosol Reanalysis, 1980 Onward. Part I: System Description and Data Assimilation Evaluation, *J. Clim.* **30**, pp. 6823-6850. https://doi.org/10.1175/jcli-d-16-0609.1

Rao, P., 2005. Arabian Sea Monsoon Experiment: An Overview, *Mausam* **56**, pp. 1-6

Rao, S., Dey, S., 2020. Consistent signal of aerosol indirect and semi-direct effect on water clouds in the oceanic regions adjacent to the Indian subcontinent, *Atmos. Res.* **232**, p. 104677. https://doi.org/10.1016/j.atmosres.2019.104677

Rao, T.N., Radhakrishna, B., Nakamura, K., Rao, P.N., 2009. Differences in raindrop size distribution from southwest monsoon to northeast monsoon at Gadanki, *Q.J.R. Meteorol. Soc.* **135**, pp. 1630-1637. https://doi.org/10.1002/qj.432

Rathee, G., 2014. Trends of Land-Use Change in India. pp. 215-238.

Ravi Kiran, V., Rajeevan, M., Gadhavi, H., Rao, S.V.B., Jayaraman, A., 2015. Role of vertical structure of cloud microphysical properties on cloud radiative forcing over the Asian monsoon region, *Clim. Dyn.* **45**, pp. 3331-3345. https://doi.org/10.1007/s00382-015-2542-0

Ravishankara, A.R., David, L.M., Pierce, J.R., Venkataraman, C., 2020. Outdoor air pollution in India is not only an urban problem, *Proc. Natl. Acad. Sci.* **117**, pp. 28640-28644. https://doi.org/10.1073/pnas.2007236117

Remer, L.A. et al., 2005. The MODIS Aerosol Algorithm, Products, and Validation, *J. Atmos. Sci.* **62**, pp. 947-973. https://doi.org/10.1175/JAS3385.1

Remer, L.A. et al., 2008. Global aerosol climatology from the MODIS satellite sensors, *J. Geophys. Res. Atmos.* **113**. https://doi.org/10.1029/2007JD009661

Roca, R., Ramanathan, V., 2000. Scale Dependence of Monsoonal Convective Systems over the Indian Ocean, *J. Clim.* **13**, pp. 1286-1298. https://doi.org/10.1175/1520-0442(2000)013<1286:Sdomcs>2.0.Co;2

Rolph, G., Stein, A., Stunder, B.,2017. Real-time Environmental Applications and Display sYstem: READY, *Environ. Model. Softw.* **95**, pp. 210-228. https://doi.org/10.1016/j.envsoft.2017.06.025

Rosenfeld, D., 1999. TRMM observed first direct evidence of smoke from forest fires inhibiting rainfall, *Geophys. Res. Lett.* **26**, pp. 3105-3108. https://doi.org/10.1029/1999GL006066

Rosenfeld, D., 2000. Suppression of Rain and Snow by Urban and Industrial Air Pollution, *Science* **287**, pp. 1793-1796. https://doi.org/10.1126/science.287.5459.1793

Rosenfeld, D. et al., 2014. Global observations of aerosol-cloud-precipitation-climate interactions, *Rev. Geophys.* **52**, pp. 750-808. https://doi.org/10.1002/2013RG000441

Rosenfeld, D. et al., 2008. Flood or drought: How do aerosols affect precipitation?, *Science* **321**, pp. 1309-1313. https://doi.org/10.1126/science.1160606

Rosenfeld, D., Ulbrich, C.W., 2003. Cloud Microphysical Properties, Processes, and Rainfall Estimation Opportunities. in: Wakimoto, R.M., Srivastava, R. (Eds.), Radar and Atmospheric Science: A Collection of Essays in Honor of David Atlas, American Meteorological Society, Boston, MA, pp. 237-258.

Rosenfeld, D. et al., 2019. Aerosol-driven droplet concentrations dominate coverage and water of oceanic low-level clouds, *Science* **363**, p. eaav0566. https://doi.org/10.1126/science.aav0566

Rosewell, C.J., 1986. Rainfall Kinetic Energy in Eastern Australia, *J. Appl. Meteorol. Climatol.* **25**, pp. 1695-1701. https://doi.org/10.1175/1520-0450(1986)025<1695:Rkeiea>2.0.Co;2

Ruchith, R.D., Deshpande, S.M., Ernet Raj, P., 2016. UHF wind profiler observations of monsoon low-level jet (MLLJ) and its association with rainfall over a tropical Indian station *Atmósfera* **29**, pp. 01-09. https://doi.org/10.20937/ATM.2016.29.01.01

Safai, P.D. et al., 2008. Aerosol characteristics during winter fog at Agra, North India, *J. Atmos. Chem.* **61**, pp. 101-118. https://doi.org/10.1007/s10874-009-9127-4

Sahu, L.K. et al., 2015. Regional biomass burning trends in India: Analysis of satellite fire data, *J. Earth Syst. Sci.* **124**, pp. 1377-1387. https://doi.org/10.1007/s12040-015-0616-3

Saikranthi, K., Radhakrishna, B., Narayana Rao, T., Satheesh, S.K., 2019. Variability in vertical structure of precipitation with sea surface temperature over the Arabian Sea and the Bay of Bengal as inferred by Tropical Rainfall Measuring Mission precipitation radar measurements, *Atmos. Chem. Phys*. **19**, pp. 10423-10432. https://doi.org/10.5194/acp-19-10423-2019

Saltzman, E.S., Brass, G.W., Price, D.A., 1983. The mechanism of sulfate aerosol formation: Chemical and sulfur isotopic evidence, *Geophys. Res. Lett.* **10**, pp. 513-516. https://doi.org/10.1029/GL010i007p00513

Sanwlani, N., Chauhan, P., Navalgund, R.R., 2011. Characterization and transport of aerosols over the Bay of Bengal during the winter monsoon: a comparative study using in-situ and satellite measurements, *Int. J. Remote Sens.* **32**, pp. 1253-1267. https://doi.org/10.1080/01431160903527454

Sarangi, C., Kanawade, V.P., Tripathi, S.N., Thomas, A., Ganguly, D., 2018. Aerosol-induced intensification of cooling effect of clouds during Indian summer monsoon, *Nat. Comm.* **9**, p. 3754. https://doi.org/10.1038/s41467-018-06015-5

Sarangi, C., Tripathi, S.N., Kanawade, V.P., Koren, I., Pai, D.S., 2017. Investigation of the aerosol–cloud–rainfall association over the Indian summer monsoon region, *Atmos. Chem. Phys.* **17**, pp. 5185-5204. https://doi.org/10.5194/acp-17-5185-2017

Sarangi, C., Tripathi, S.N., Mishra, A.K., Goel, A., Welton, E.J., 2016. Elevated aerosol layers and their radiative impact over Kanpur during monsoon onset period, *J. Geophys. Res. Atmos.* 121, pp. 7936-7957. https://doi.org/10.1002/2015JD024711

Sarkar, S., Chauhan, A., Kumar, R., Singh, R.P., 2019. Impact of Deadly Dust Storms (May 2018) on Air Quality, Meteorological, and Atmospheric Parameters Over the Northern Parts of India, *GeoHealth* **3**, pp. 67-80. https://doi.org/10.1029/2018GH000170

Sarkar, S., Singh, R.P., Chauhan, A., 2018. Crop Residue Burning in Northern India: Increasing Threat to Greater India, *J. Geophys. Res. Atmos.* **123**, pp. 6920-6934. https://doi.org/10.1029/2018jd028428

Satheesh, S.K., 2002. Radiative forcing by aerosols over Bay of Bengal region, *Geophys. Res. Lett.* **29**, pp. 40-41-40-44. https://doi.org/10.1029/2002gl015334

Satheesh, S.K., Krishna Moorthy, K., 2005. Radiative effects of natural aerosols: A review, *Atmos. Environ.* **39**, pp. 2089-2110. https://doi.org/10.1016/j.atmosenv.2004.12.029

Satheesh, S.K., Moorthy, K.K., Babu, S.S., Vinoj, V., Dutt, C.B.S., 2008. Climate implications of large warming by elevated aerosol over India, *Geophys. Res. Lett.* **35**. https://doi.org/10.1029/2008GL034944

Satheesh, S.K., Srinivasan, J., Moorthy, K.K., 2006. Spatial and temporal heterogeneity in aerosol properties and radiative forcing over Bay of Bengal: Sources and role of aerosol transport, *J. Geophys. Res. Atmos.* **111**. https://doi.org/10.1029/2005jd006374

Satheesh, S.K., Vinoj, V., Krishnamoorthy, K., 2010. Assessment of Aerosol Radiative Impact over Oceanic Regions Adjacent to Indian Subcontinent Using Multisatellite Analysis, *Adv. Meteorol.* **2010**, p. 139186. https://doi.org/10.1155/2010/139186

Sathiyamoorthy, V. et al., 2013. Characteristics of low clouds over the Arabian Sea, *J. Geophys. Res. Atmos.***118**, pp. 13,489-13,503. https://doi.org/10.1002/2013JD020553

Sato, T. et al., 1990. Computer processing for deriving drop-size distributions and vertical air velocities from VHF Doppler radar spectra, *Radio Sci.* **25**, pp. 961-973. https://doi.org/10.1029/RS025i005p00961

Saud, T., Dey, S., Das, S., Dutta, S., 2016. A satellite-based 13-year climatology of net cloud radiative forcing over the Indian monsoon region, *Atmos. Res.***182**, pp. 76-86. https://doi.org/10.1016/j.atmosres.2016.07.017

Sauvageot, H., Lacaux, J.-P., 1995. The shape of averaged drop size distributions, *J. Atmos. Sci.* **52**, pp. 1070-1083. https://doi.org/10.1175/1520-0469(1995)052<1070:Tsoads>2.0.Co;2

Sayer, A.M. et al., 2014. MODIS Collection 6 aerosol products: Comparison between Aqua's e-Deep Blue, Dark Target, and “merged” data sets, and usage recommendations, *J. Geophys. Res. Atmos.* **119**, pp. 13,965-13,989. https://doi.org/10.1002/2014JD022453

Seela, B.K., Janapati, J., Lin, P., Wang, P.K., Lee, M., 2018. Raindrop Size Distribution Characteristics of Summer and Winter Season Rainfall Over North Taiwan, *J. Geophys. Res. Atmos.*123, pp. 11,602-11,624. https://doi.org/10.1029/2018jd028307

Seethala, C., Horváth, Á., 2010. Global assessment of AMSR-E and MODIS cloud liquid water path retrievals in warm oceanic clouds, *J. Geophys. Res. Atmos.* **115**. https://doi.org/10.1029/2009JD012662

Seinfeld, J.H., Pandis, S.N., 2016. Atmospheric chemistry and physics: from air pollution to climate change, 3rd ed. John Wiley & Sons 1152 pp.

Shankar, M., Thomas, S., Priestley, K., 2010. Pre-launch characterization of spectral response functions for the Clouds and Earth's Radiant Energy System (CERES) instrument sensors. Proc. SPIE. https://doi.org/10.1117/12.859927

Sharma, S. et al., 2020. Effect of restricted emissions during COVID-19 on air quality in India, *Sci. Total Environ.***728**, p. 138878. https://doi.org/10.1016/j.scitotenv.2020.138878

Sikka, D.R.,1997. Desert climate and its dynamics, *Curr. Sci.***72**, pp. 35-46

Singh, R.P., Chauhan, A., 2020. Impact of lockdown on air quality in India during COVID-19 pandemic, *Air Qual. Atmos. Health* **13**, pp. 921-928. https://doi.org/10.1007/s11869-020-00863-1

Small, J.D., Chuang, P.Y., Feingold, G., Jiang, H., 2009. Can aerosol decrease cloud lifetime?, *Geophys. Res. Lett.* **36**. https://doi.org/10.1029/2009GL038888

Smirnov, A. et al., 2002. Diurnal variability of aerosol optical depth observed at AERONET (Aerosol Robotic Network) sites, *Geophys. Res. Lett.* **29**, pp. 30-31-30-34. https://doi.org/10.1029/2002GL016305

Smith, S.J. et al., 2011. Anthropogenic sulfur dioxide emissions: 1850–2005, *Atmos. Chem. Phys.***11**, pp. 1101-1116. https://doi.org/10.5194/acp-11-1101-2011

Sreekanth, T.S., Varikoden, H., Mohan Kumar, G., Resmi, E.A., 2019. Microphysical Features of Rain and Rain events during different Seasons over a Tropical Mountain location using an Optical Disdrometer, *Sci. Rep.* **9**, p. 19083. https://doi.org/10.1038/s41598-019-55583-z

Srinivas, B., Sarin, M.M., 2014. PM2.5, EC and OC in atmospheric outflow from the Indo-Gangetic Plain: Temporal variability and aerosol organic carbon-to-organic mass conversion factor, *Sci. Total Environ.* **487**, pp. 196-205. https://doi.org/10.1016/j.scitotenv.2014.04.002

Srinivas, B., Sarin, M.M., Sarma, V.V.S.S., 2015. Atmospheric outflow of nutrients to the Bay of Bengal: Impact of anthropogenic sources, *J. Mar. Sys.***141**, pp. 34-44. https://doi.org/10.1016/j.jmarsys.2014.07.008

Srivastava, A.K. et al., 2021a. Improved air quality during COVID-19 at an urban megacity over the Indo-Gangetic Basin: From stringent to relaxed lockdown phases, *Urban Clim.* **36**, p. 100791. https://doi.org/10.1016/j.uclim.2021.100791

Srivastava, A.K. et al., 2020. Implications of different aerosol species to direct radiative forcing and atmospheric heating rate, *Atmos. Environ.* **241**, p. 117820. https://doi.org/10.1016/j.atmosenv.2020.117820

Srivastava, A.K., Singh, S., Tiwari, S., Bisht, D.S., 2012a. Contribution of anthropogenic aerosols in direct radiative forcing and atmospheric heating rate over Delhi in the Indo-Gangetic Basin, *Environ. Sci. Pollut. Res.***19**, pp. 1144-1158. https://doi.org/10.1007/s11356-011-0633-y

Srivastava, A.K., Singh, S., Tiwari, S., Kanawade, V.P., Bisht, D.S., 2012b. Variation between near-surface and columnar aerosol characteristics during the winter and summer at Delhi in the Indo-Gangetic Basin, *J. Atmos. Sol.-Terr. Phys.* **77**, pp. 57-66. https://doi.org/10.1016/j.jastp.2011.11.009

Srivastava, A.K. et al., 2014. An early South Asian dust storm during March 2012 and its impacts on Indian Himalayan foothills: A case study, *Sci. Total Environ.* **493**, pp. 526-534. https://doi.org/10.1016/j.scitotenv.2014.06.024

Srivastava, A.K. et al., 2021b. How secondary inorganic aerosols from Delhi influence aerosol optical and radiative properties at a downwind sub-urban site over Indo-Gangetic Basin?, *Atmos. Environ.* **248**, p. 118246. https://doi.org/10.1016/j.atmosenv.2021.118246

Srivastava, R., 2017. Trends in aerosol optical properties over South Asia, *Int. J. Climatol.* **37**, pp. 371-380. https://doi.org/10.1002/joc.4710

Stein, A.F. et al., 2016. NOAA’s HYSPLIT Atmospheric Transport and Dispersion Modeling System, *Bull. Amer. Meteor.* **96**, pp. 2059-2077. https://doi.org/10.1175/BAMS-D-14-00110.1

Stevens, B., Feingold, G., 2009. Untangling aerosol effects on clouds and precipitation in a buffered system, *Nature* **461**, pp. 607-613. https://doi.org/10.1038/nature08281

Stier, P., 2016. Limitations of passive remote sensing to constrain global cloud condensation nuclei, *Atmos. Chem. Phys.* **16**, pp. 6595-6607. https://doi.org/10.5194/acp-16-6595-2016

Storelvmo, T., Leirvik, T., Lohmann, U., Phillips, P.C.B., Wild, M., 2016. Disentangling greenhouse warming and aerosol cooling to reveal Earth’s climate sensitivity, *Nat. Geosci.* **9**, pp. 286-289. https://doi.org/10.1038/ngeo2670

Su, W., Corbett, J., Eitzen, Z., Liang, L., 2015. Next-generation angular distribution models for top-of-atmosphere radiative flux calculation from CERES instruments: methodology, *Atmos. Meas. Tech.* **8**, pp. 611-632. https://doi.org/10.5194/amt-8-611-2015

Subba, T., Gogoi, M.M., Pathak, B., Bhuyan, P.K., Babu, S.S., 2020. Recent trend in the global distribution of aerosol direct radiative forcing from satellite measurements, *Atmos Sci Lett.* **21**, p. e975. https://doi.org/10.1002/asl.975

Szczodrak, M., Austin, P.H., Krummel, P.B., 2001. Variability of Optical Depth and Effective Radius in Marine Stratocumulus Clouds, *J. Atmos. Sci.* **58**, pp. 2912-2926. https://doi.org/10.1175/1520-0469(2001)058<2912:Voodae>2.0.Co;2

Takamura, T., Nakajima, T., 2004. Overview of SKYNET and its Activities, *Óptica Pura Y Aplicada* **37**, pp. 3303-3308

Tapiador, F.J., Haddad, Z.S., Turk, J., 2014. A Probabilistic View on Raindrop Size Distribution Modeling: A Physical Interpretation of Rain Microphysics, *J. Hydrometeorol.* **15**, pp. 427-443. https://doi.org/10.1175/jhm-d-13-033.1

Tegen, I., Fung, I.,1995. Contribution to the atmospheric mineral aerosol load from land surface modification, *J. Geophys. Res. Atmos.* **100**, pp. 18707-18726. https://doi.org/10.1029/95JD02051

Thamban, N.M., Tripathi, S.N., Moosakutty, S.P., Kuntamukkala, P., Kanawade, V.P., 2017. Internally mixed black carbon in the Indo-Gangetic Plain and its effect on absorption enhancement, *Atmos. Res.***197**, pp. 211-223. https://doi.org/10.1016/j.atmosres.2017.07.007

Thampi, B.V., Roca, R., 2014. Investigation of negative cloud radiative forcing over the Indian subcontinent and adjacent oceans during the summer monsoon season, *Atmos. Chem. Phys.* **14**, pp. 6739-6758. https://doi.org/10.5194/acp-14-6739-2014

Thomas, A., Kanawade, V.P., Chakravarty, K., Srivastava, A.K., 2021a. Characterization of raindrop size distributions and its response to cloud microphysical properties, *Atmos. Res.* **249**, p. 105292. https://doi.org/10.1016/j.atmosres.2020.105292

Thomas, A., Kanawade, V.P., Sarangi, C., Srivastava, A.K., 2021b. Effect of COVID-19 shutdown on aerosol direct radiative forcing over the Indo-Gangetic Plain outflow region of the Bay of Bengal, *Sci. Total Environ.* **782**, p. 146918. https://doi.org/10.1016/j.scitotenv.2021.146918

Thomas, A., Sarangi, C., Kanawade, V.P., 2019. Recent Increase in Winter Hazy Days over Central India and the Arabian Sea, *Sci. Rep.* **9**, p. 17406. https://doi.org/10.1038/s41598-019-53630-3

Thomas, S. et al., 2010. Characterization of the clouds and the Earth's radiant energy system (CERES) sensors on Terra and Aqua spacecraft. SPIE.

Tiwari, S. et al., 2018. Pollution concentrations in Delhi India during winter 2015–16: A case study of an odd-even vehicle strategy, *Atmos. Pollut. Res.* **9**, pp. 1137-1145. https://doi.org/10.1016/j.apr.2018.04.008

Tokay, A., Short, D.A., 1996. Evidence from Tropical Raindrop Spectra of the Origin of Rain from Stratiform versus Convective Clouds, *J. Appl. Meteorol. Climatol.* **35**, pp. 355-371. https://doi.org/10.1175/1520-0450(1996)035<0355:Eftrso>2.0.Co;2

Tomasi, C., Lupi, A., 2017. Primary and Secondary Sources of Atmospheric Aerosol. Atmospheric Aerosols, pp. 1-86.

Torres, O., Ahn, C., Chen, Z., 2013. Improvements to the OMI near-UV aerosol algorithm using A-train CALIOP and AIRS observations, *Atmos. Meas. Tech.* **6**, pp. 3257-3270. https://doi.org/10.5194/amt-6-3257-2013

Torres, O. et al., 2007. Aerosols and surface UV products from Ozone Monitoring Instrument observations: An overview, *J. Geophys. Res. Atmos.* **112**. https://doi.org/10.1029/2007JD008809

Tripathi, S.N. et al., 2006. Measurements of atmospheric parameters during Indian Space Research Organization Geosphere Biosphere Programme Land Campaign II at a typical location in the Ganga basin: 1. Physical and optical properties, *J. Geophys. Res. Atmos.***111**. https://doi.org/10.1029/2006JD007278

Turner, J., Colbeck, I., 2008. Physical and Chemical Properties of Atmospheric Aerosols. Environmental Chemistry of Aerosols, pp. 1-29.

Twomey, S.,1977. The Influence of Pollution on the Shortwave Albedo of Clouds *J. Atmos. Sci.* **34**, pp. 1149-1152. https://doi.org/10.1175/1520-0469(1977)034<1149:Tiopot>2.0.Co;2

Ulbrich, C.W., 1983. Natural Variations in the Analytical Form of the Raindrop Size Distribution, *J. Appl. Meteorol. Climatol.* **22**, pp. 1764-1775. https://doi.org/10.1175/1520-0450(1983)022<1764:NVITAF>2.0.CO;2

Ulbrich, C.W., Atlas, D., 2007. Microphysics of Raindrop Size Spectra: Tropical Continental and Maritime Storms, *J. Appl. Meteorol. Climatol.* **46**, pp. 1777-1791. https://doi.org/10.1175/2007jamc1649.1

Vadrevu, K.P., Lasko, K., Giglio, L., Justice, C., 2015. Vegetation fires, absorbing aerosols and smoke plume characteristics in diverse biomass burning regions of Asia, *Environ. Res. Let.***10**, p. 105003. https://doi.org/10.1088/1748-9326/10/10/105003

van den Heever, S.C., Stephens, G.L., Wood, N.B., 2011. Aerosol Indirect Effects on Tropical Convection Characteristics under Conditions of Radiative–Convective Equilibrium, *J.Atmos. Sci*. **68**, pp. 699-718. https://doi.org/10.1175/2010jas3603.1

van der Werf, G.R. et al., 2010. Global fire emissions and the contribution of deforestation, savanna, forest, agricultural, and peat fires (1997–2009), *Atmos. Chem. Phys.***10**, pp. 11707-11735. https://doi.org/10.5194/acp-10-11707-2010

Venkataraman, C., Habib, G., Eiguren-Fernandez, A., Miguel, A.H., Friedlander, S.K., 2005. Residential Biofuels in South Asia: Carbonaceous Aerosol Emissions and Climate Impacts, *Science* 307, pp. 1454-1456. https://doi.org/10.1126/science.1104359

Venter, Z.S., Aunan, K., Chowdhury, S., Lelieveld, J., 2020. COVID-19 lockdowns cause global air pollution declines, *Proc. Natl. Acad. Sci.* **117**, pp. 18984-18990. https://doi.org/10.1073/pnas.2006853117

Verma, S. et al., 2013. Dust events and their influence on aerosol optical properties over Jaipur in Northwestern India, *Environ. Monit. Assess.* **185**, pp. 7327-7342. https://doi.org/10.1007/s10661-013-3103-9

Vinoj, V. et al., 2014. Short-term modulation of Indian summer monsoon rainfall by West Asian dust, *Nat. Geosci.* **7**, pp. 308-313. https://doi.org/10.1038/ngeo2107

Voors, R., Dirksen, R., Dobber, M., Levelt, P., 2006. OMI In-Flight Wavelength Calibration and the Solar Reference Spectrum, Wang, S.-Y., Buckley, B.M., Yoon, J.-H., Fosu, B., 2013. Intensification of premonsoon tropical cyclones in the Bay of Bengal and its impacts on Myanmar, *J. Geophys. Res. Atmos.* **118**, pp. 4373-4384. https://doi.org/10.1002/jgrd.50396

Warneck, P.,2000. Chapter 7 The atmospheric aerosol. in: Warneck, P. (Ed.), International Geophysics, Academic Press, pp. 346-450.

Wen, L. et al., 2016. Statistical characteristics of raindrop size distributions observed in East China during the Asian summer monsoon season using 2-D video disdrometer and Micro Rain Radar data, *J. Geophys. Res. Atmos.* **121**, pp. 2265-2282. https://doi.org/10.1002/2015jd024160

Wexler, A.S., Lurmann, F.W., Seinfeld, J.H., 1994. Modelling urban and regional aerosols—I. model development, *Atmos. Environ.* **28**, pp. 531-546. https://doi.org/10.1016/1352-2310(94)90129-5

Wielicki, B.A. et al., 1996. Clouds and the Earth's Radiant Energy System (CERES): An Earth Observing System Experiment, *Bull. Amer. Meteor.* **77**, pp. 853-868. https://doi.org/10.1175/1520-0477(1996)077<0853:catere>2.0.co;2

Wild, M. et al., 2005. From Dimming to Brightening: Decadal Changes in Solar Radiation at Earth's Surface, *Science* **308**, pp. 847-850. https://doi.org/10.1126/science.1103215

Wood, R., 2012. Stratocumulus Clouds, *Mon. Weather Rev.*140, pp. 2373-2423. https://doi.org/10.1175/mwr-d-11-00121.1

Xian, P. et al., 2019. Current state of the global operational aerosol multi-model ensemble: An update from the International Cooperative for Aerosol Prediction (ICAP), *Q.J.R. Meteorol. Soc.***145**, pp. 176-209. https://doi.org/10.1002/qj.3497

Yang, Y., Lou, S., Wang, H., Wang, P., Liao, H., 2020. Trends and source apportionment of aerosols in Europe during 1980–2018, *Atmos. Chem. Phys.* **20**, pp. 2579-2590. https://doi.org/10.5194/acp-20-2579-2020

Yoon, J., von Hoyningen-Huene, W., Kokhanovsky, A.A., Vountas, M., Burrows, J.P., 2012. Trend analysis of aerosol optical thickness and Ångström exponent derived from the global AERONET spectral observations, *Atmos. Meas. Tech.* **5**, pp. 1271-1299. https://doi.org/10.5194/amt-5-1271-2012

Yu, P. et al., 2017. Efficient transport of tropospheric aerosol into the stratosphere via the Asian summer monsoon anticyclone, *Proc. Natl. Acad. Sci.* **114**, pp. 6972-6977. https://doi.org/10.1073/pnas.1701170114

Zege, E.P., Kokhanovsky, A.A., 1994. Analytical solution to the optical transfer function of a scattering medium with large particles, *Appl. Opt.* **33**, pp. 6547-6554. https://doi.org/10.1364/AO.33.006547

Zhang, G., Sun, J., Brandes, E.A., 2006. Improving Parameterization of Rain Microphysics with Disdrometer and Radar Observations, *J. Atmos. Sci.* **63**, pp. 1273-1290. https://doi.org/10.1175/jas3680.1

Zhang, Y., Yu, F., Luo, G., Chen, J.-P., Chou, C.C.-K., 2020. Impact of Mineral Dust on Summertime Precipitation Over the Taiwan Region, *J. Geophys. Res. Atmos.***125**, p. e2020JD033120. https://doi.org/10.1029/2020JD033120

Zhu, Y., Rosenfeld, D., Li, Z.,2018. Under What Conditions Can We Trust Retrieved Cloud Drop Concentrations in Broken Marine Stratocumulus?, *J. Geophys. Res. Atmos.***123**, pp. 8754-8767. https://doi.org/10.1029/2017jd028083

Aerosol and cloud radiative properties over India and adjoining Seas

by Abin Thomas

Submission date: 20-Oct-2021 02:12PM (UTC+0530)
Submission ID: 1678950407
File name: draft_plagiarism_v4.pdf (5.46M)
Word count: 26135
Character count: 135981

Dr. Vijay P. Kanawade
UGC-Assistant Professor
Centre for Earth, Ocean & Atmospheric Sciences
University of Hyderabad
Hyderabad-500 046, Telangana, INDIA.

Aerosol and cloud radiative properties over India and adjoining Seas

ORIGINALITY REPORT

30%	11%	29%	2%
SIMILARITY INDEX	INTERNET SOURCES	PUBLICATIONS	STUDENT PAPERS

PRIMARY SOURCES

1 Abin Thomas, Vijay P. Kanawade, Kaustav Chakravarty, Atul K. Srivastava. "Characterization of raindrop size distributions and its response to cloud microphysical properties", Atmospheric Research, 2021
Publication — **10%**

Paper from student Thesis

Dr. Vijay P. Kanawade
UGC-Assistant Professor
Centre for Earth, Ocean & Atmospheric Sciences
University of Hyderabad
Hyderabad-500 046, Telangana, INDIA.

2 Abin Thomas, Vijay P. Kanawade, Chandan Sarangi, Atul K. Srivastava. "Effect of COVID-19 shutdown on aerosol direct radiative forcing over the Indo-Gangetic Plain outflow region of the Bay of Bengal", Science of The Total Environment, 2021
Publication — **7%**

Paper from student The

Dr. Vijay P. Kanawade
UGC-Assistant Professor
Centre for Earth, Ocean & Atmospheric Sciences
University of Hyderabad
Hyderabad-500 046, Telangana, INDIA.

3 Abin Thomas, Chandan Sarangi, Vijay P. Kanawade. "Recent Increase in Winter Hazy Days over Central India and the Arabian Sea", Scientific Reports, 2019
Publication — **3%**

Paper from student The

Dr. Vijay P. Kanawade
UGC-Assistant Professor
Centre for Earth, Ocean & Atmospheric Sciences
University of Hyderabad
Hyderabad-500 046, Telangana, INDIA.

4 www.nature.com
Internet Source — **2%**

Paper from Student Thesis

Dr. Vijay P. Kanawade
UGC-Assistant Professor
Sciences

5	ceres.larc.nasa.gov Internet Source	1 %
6	Zhanqing Li, W. K.-M. Lau, V. Ramanathan, G. Wu et al. "Aerosol and monsoon climate interactions over Asia", Reviews of Geophysics, 2016 Publication	<1 %
7	Chandan Sarangi, Sachchida Nand Tripathi, Vijay P. Kanawade, Ilan Koren, D. Sivanand Pai. "Investigation of the aerosol–cloud–rainfall association over the Indian summer monsoon region", Atmospheric Chemistry and Physics, 2017 Publication	<1 %
8	Ankan Sarkar, K.K. Amal, Thumree Sarkar, Jagabandhu Panda, Debashis Paul. "Variability in air-pollutants, aerosols, and associated meteorology over peninsular India and neighboring ocean regions during COVID-19 lockdown to unlock phases", Atmospheric Pollution Research, 2021 Publication	<1 %
9	"Observed Climate Variability and Change over the Indian Region", Springer Science and Business Media LLC, 2017 Publication	<1 %

10 Subin Jose, Vijayakumar S. Nair, S. Suresh Babu. "Anthropogenic emissions from South Asia reverses the aerosol indirect effect over the northern Indian Ocean", Scientific Reports, 2020 <1%
Publication

Papr from student Thesis

11 Submitted to University of Hyderabad, Hyderabad <1%
Student Paper

Dr. Vijay P. Kanawade
UGC-Assistant Professor
Centre for Earth, Ocean & Atmospheric Sciences
University of Hyderabad
Hyderabad-500 046, Telangana, INDIA.

---

12 V.P. Kanawade, A.K. Srivastava, K. Ram, E. Asmi, V. Vakkari, V.K. Soni, V. Varaprasad, C. Sarangi. "What caused severe air pollution episode of November 2016 in New Delhi?", Atmospheric Environment, 2020 <1%
Publication

---

13 dspace.aries.res.in <1%
Internet Source

---

14 Sagnik Dey. "A climatology of aerosol optical and microphysical properties over the Indian subcontinent from 9 years (2000–2008) of Multiangle Imaging Spectroradiometer (MISR) data", Journal of Geophysical Research, 08/05/2010 <1%
Publication

---

15 Trailokya Saud, Sagnik Dey, Sushant Das, Soumi Dutta. "A satellite-based 13-year climatology of net cloud radiative forcing over <1%

the Indian monsoon region", Atmospheric Research, 2016
Publication

---

16 "Atmospheric Aerosols", Wiley, 2017 <1%
Publication

---

17 www.ncbi.nlm.nih.gov <1%
Internet Source

---

18 hdl.handle.net <1%
Internet Source

---

19 Sumita Kedia, Subrata Kumar Das, Sahidul Islam, Anupam Hazra, Naveen Kumar. "It is found that aerosol impact and feedback on monsoon rainfall can be positive, negative, or neutral Aerosols impact on the convective and non-convective rain distribution over the Indian region: Results from WRF-Chem simulation", Atmospheric Environment, 2019 <1%
Publication

---

20 O. Alizadeh Choobari, P. Zawar-Reza, A. Sturman. "The global distribution of mineral dust and its impacts on the climate system: A review", Atmospheric Research, 2014 <1%
Publication

---

21 Vijayakumar S. Nair, S. Suresh Babu, K. Krishna Moorthy, S. S. Prijith. "Spatial Gradients in Aerosol-Induced Atmospheric Heating and Surface Dimming over the <1%

Oceanic Regions around India: Anthropogenic or Natural?", Journal of Climate, 2013
Publication

---

22 www.atmos-chem-phys.net
Internet Source
<1%

---

23 Qinjian Jin, Jiangfeng Wei, William K.M. Lau, Bing Pu, Chien Wang. "Interactions of Asian mineral dust with Indian summer monsoon: Recent advances and challenges", Earth-Science Reviews, 2021
Publication
<1%

---

24 B. V. Thampi, R. Roca. "Investigation of negative cloud radiative forcing over the Indian subcontinent and adjacent oceans during the summer monsoon season", Atmospheric Chemistry and Physics Discussions, 2013
Publication
<1%

---

25 R. Cherian. "Examination of aerosol distributions and radiative effects over the Bay of Bengal and the Arabian Sea region during ICARB using satellite data and a general circulation model", Atmospheric Chemistry and Physics, 02/01/2012
Publication
<1%

---

26 www.atmos-meas-tech.net
Internet Source
<1%

27	Bali, Kunal, Amit Kumar Mishra, and Sachchidanand Singh. "Impact of anomalous forest fire on aerosol radiative forcing and snow cover over Himalayan region", Atmospheric Environment, 2016. Publication	<1 %
28	www.intechopen.com Internet Source	<1 %
29	Govardhan, Gaurav R., Ravi S. Nanjundiah, S.K. Satheesh, K. Krishna Moorthy, and Toshihiko Takemura. "Inter-comparison and performance evaluation of chemistry transport models over Indian region", Atmospheric Environment, 2016. Publication	<1 %
30	Submitted to Indian School of Mines Student Paper	<1 %
31	Manu Mehta, Narendra Singh, Anshumali. "Global trends of columnar and vertically distributed properties of aerosols with emphasis on dust, polluted dust and smoke - inferences from 10-year long CALIOP observations", Remote Sensing of Environment, 2018 Publication	<1 %
32	Sagnik Dey, Nidhi Nishant, Kamalika Sengupta, Sudipta Ghosh. "Cloud climatology	<1 %

over the oceanic regions adjacent to the Indian Subcontinent: inter-comparison between passive and active sensors", International Journal of Remote Sensing, 2015
Publication

33	Brunna Penna, Dirceu Herdies, Simone Costa. "Estimates of direct radiative forcing due to aerosols from the MERRA-2 reanalysis over the Amazon region", Atmospheric Chemistry and Physics Discussions, 2018 Publication	<1%
34	Chandan Sarangi, Vijay P. Kanawade, Sachchida N. Tripathi, Abin Thomas, Dilip Ganguly. "Aerosol-induced intensification of cooling effect of clouds during Indian summer monsoon", Nature Communications, 2018 Publication	<1%
35	acp.copernicus.org Internet Source	<1%
36	eprints.whiterose.ac.uk Internet Source	<1%
37	Alaa Mhawish, Tirthankar Banerjee, David M. Broday, Amit Misra, Sachchida N. Tripathi. "Evaluation of MODIS Collection 6 aerosol retrieval algorithms over Indo-Gangetic Plain: Implications of aerosols types and mass loading", Remote Sensing of Environment, 2017	<1%

Co-author paper by student

Dr. Vijay P. Kanawade
UGC-Assistant Professor
Centre for Earth, Ocean & Atmospheric Sciences
University of Hyderabad
Hyderabad-500 046, Telangana, INDIA.

Publication

38 Vijayakumar S. Nair, S. Suresh Babu, M. R. Manoj, K. Krishna Moorthy, Mian Chin. "Direct radiative effects of aerosols over South Asia from observations and modeling", Climate Dynamics, 2016 <1%

Publication

39 Rohit Mangla, Indu J, Chakra S.S.. "Inter-comparison of multi-satellites and Aeronet AOD over Indian Region", Atmospheric Research, 2020 <1%

Publication

40 Submitted to University of Exeter <1%

Student Paper

41 Balaji Kumar Seela, Jayalakshmi Janapati, Pay-Liam Lin, K. Krishna Reddy, Ryuichi Shirooka, Pao K. Wang. "A Comparison Study of Summer Season Raindrop Size Distribution Between Palau and Taiwan, Two Islands in Western Pacific", Journal of Geophysical Research: Atmospheres, 2017 <1%

Publication

42 Goutam Choudhury, Bhishma Tyagi, Naresh Krishna Vissa, Jyotsna Singh, Chandan Sarangi, Sachchida Nand Tripathi, Matthias Tesche. "Aerosol-enhanced high precipitation events near the Himalayan foothills", Atmospheric Chemistry and Physics, 2020 <1%

Publication

43 Satyendra K. Pandey, V. Vinoj, K. Landu, S. Suresh Babu. "Declining pre-monsoon dust loading over South Asia: Signature of a changing regional climate", Scientific Reports, 2017 <1%
Publication

44 Submitted to National Institute of Technology, Rourkela <1%
Student Paper

45 epdf.tips <1%
Internet Source

46 N.B. Lakshmi, Vijayakumar S. Nair, S. Suresh Babu. "Assessment of the vertical distribution of speciated aerosol absorption over South Asia using spaceborne LIDAR and ground-based observations", Remote Sensing of Environment, 2020 <1%
Publication

47 Vijayakumar S. Nair. "Surprising observation of large anthropogenic aerosol fraction over the “near-pristine” southern Bay of Bengal: Climate implications", Journal of Geophysical Research, 11/02/2010 <1%
Publication

48 www.mdpi.com <1%
Internet Source

49	deq.wyoming.gov Internet Source	<1%
50	Ali Tokay, Walter A. Petersen, Patrick Gatlin, Matthew Wingo. "Comparison of Raindrop Size Distribution Measurements by Collocated Disdrometers", Journal of Atmospheric and Oceanic Technology, 2013 Publication	<1%
51	Papori Dahutia, Binita Pathak, Pradip Kumar Bhuyan. "Aerosols characteristics, trends and their climatic implications over Northeast India and adjoining South Asia", International Journal of Climatology, 2018 Publication	<1%
52	Pathak, B., T. Subba, P. Dahutia, P.K. Bhuyan, K. Krishna Moorthy, M.M. Gogoi, S. Suresh Babu, L. Chutia, P. Ajay, J. Biswas, C. Bharali, A. Borgohain, P. Dhar, A. Guha, B.K. De, T. Banik, M. Chakraborty, S.S. Kundu, S. Sudhakar, and S.B. Singh. "Aerosol characteristics in north-east India using ARFINET spectral optical depth measurements", Atmospheric Environment, 2016. Publication	<1%
53	Sumita Kedia, S. Ramachandran, B.N. Holben, S.N. Tripathi. "Quantification of aerosol type, and sources of aerosols over the Indo-	<1%

Gangetic Plain", Atmospheric Environment, 2014
Publication

---

54 T. Narayana Rao. "Differences in raindrop size distribution from southwest monsoon to northeast monsoon at Gadanki", Quarterly Journal of the Royal Meteorological Society, 07/2009 <1%
Publication

---

55 www.preprints.org <1%
Internet Source

---

56 David Neubauer, Matthew W. Christensen, Caroline Poulsen, Ulrike Lohmann. "Unveiling aerosol-cloud interactions Part 2: Minimizing the effects of aerosol swelling and wet scavenging in ECHAM6-HAM2 for comparison to satellite data", Copernicus GmbH, 2017 <1%
Publication

---

57 Submitted to Higher Education Commission Pakistan <1%
Student Paper

---

58 M. Kumar, K.S. Parmar, D.B. Kumar, A. Mhawish, D.M. Broday, R.K. Mall, T. Banerjee. "Long-term aerosol climatology over Indo-Gangetic Plain: Trend, prediction and potential source fields", Atmospheric Environment, 2018 <1%
Publication

59	T. M. Midhuna, Biswadip Gharai, Subin Jose, P. V. N Rao. "Study on Regional Variations of Aerosol Loading Using Long Term Satellite Data Over Indian Region", Journal of the Indian Society of Remote Sensing, 2016 Publication	<1 %
60	V. Ravi Kiran, M. Rajeevan, H. Gadhavi, S. Vijaya Bhaskara Rao, A. Jayaraman. "Role of vertical structure of cloud microphysical properties on cloud radiative forcing over the Asian monsoon region", Climate Dynamics, 2015 Publication	<1 %
61	William K. M. Lau. "The aerosol-monsoon climate system of Asia: A new paradigm", Journal of Meteorological Research, 2016 Publication	<1 %
62	link.springer.com Internet Source	<1 %
63	ntrs.nasa.gov Internet Source	<1 %
64	Archita Rana, Shiguo Jia, Sayantan Sarkar. "Black carbon aerosol in India: A comprehensive review of current status and future prospects", Atmospheric Research, 2019 Publication	<1 %

65 D.G. Kaskaoutis, P.R. Sinha, V. Vinoj, P.G. Kosmopoulos, S.N. Tripathi, Amit Misra, M. Sharma, R.P. Singh. "Aerosol properties and radiative forcing over Kanpur during severe aerosol loading conditions", Atmospheric Environment, 2013
Publication
<1%

---

66 Dominique Bouniol, Rémy Roca, Thomas Fiolleau, D. Emmanuel Poan. "Macrophysical, Microphysical, and Radiative Properties of Tropical Mesoscale Convective Systems over Their Life Cycle", Journal of Climate, 2016
Publication
<1%

---

67 Submitted to King's College
Student Paper
<1%

---

68 Kirti Soni, Sangeeta Kapoor, Kulwinder Singh Parmar, Dimitris G. Kaskaoutis. "Statistical analysis of aerosols over the Gangetic–Himalayan region using ARIMA model based on long-term MODIS observations", Atmospheric Research, 2014
Publication
<1%

---

69 Ningombam, Shantikumar S., S.P. Bagare, A.K. Srivastava, B.J. Sohn, H.-J. Song, and E. Larson. "Aerosol radiative forcing over a high-altitude station Merak, in the trans-Himalayan region during advection of anthropogenic
<1%

events from the Indo-Gangetic Plain",
Atmospheric Environment, 2014.
Publication

---

70 lup.lub.lu.se <1%
Internet Source

---

71 Balaji Kumar Seela, Jayalakshmi Janapati, Pay-Liam Lin, Pao K. Wang, Meng-Tze Lee. "Raindrop Size Distribution Characteristics of Summer and Winter Season Rainfall Over North Taiwan", Journal of Geophysical Research: Atmospheres, 2018 <1%
Publication

---

72 Global Environmental Changes in South Asia, 2010. <1%
Publication

---

73 Submitted to IIT Delhi <1%
Student Paper

---

74 Imran A. Girach, Narendra Ojha, Prabha R. Nair, Andrea Pozzer, Yogesh K. Tiwari, K. Ravi Kumar, Jos Lelieveld. "Variations in O₃, CO, and CH₄ over the Bay of Bengal during the summer monsoon season: Ship-borne measurements and model simulations", Copernicus GmbH, 2016 <1%
Publication

75	K. Krishna Moorthy. "Spatial and vertical heterogeneities in aerosol properties over oceanic regions around India: Implications for radiative forcing", Quarterly Journal of the Royal Meteorological Society, 2009 Publication	<1%
76	Submitted to Queen Mary and Westfield College Student Paper	<1%
77	R. Bennartz. "Global assessment of marine boundary layer cloud droplet number concentration from satellite", Journal of Geophysical Research, 01/18/2007 Publication	<1%
78	R. Roca. "A study of convective systems, water vapor and top of the atmosphere cloud radiative forcing over the Indian Ocean using INSAT-1B and ERBE data", Meteorology and Atmospheric Physics, 09/2005 Publication	<1%

Exclude quotes	On	Exclude matches	< 14 words
Exclude bibliography	On		

SCIENTIFIC REPORTS
natureresearch

OPEN

Recent Increase in Winter Hazy Days over Central India and the Arabian Sea

Abin Thomas[1], Chandan Sarangi[2*] & Vijay P. Kanawade[1*]

Indian subcontinent is greatly vulnerable to air pollution, especially during the winter season. Here, we use 15 years (2003–2017) of satellite and model reanalysis datasets over India and adjoining Seas to estimate the trend in hazy days (i.e. days with high aerosol loading) during the dry winter season (November to February). The number of hazy days is increasing at the rate of ~2.6 days per year over Central India. Interestingly, this is higher than over the Indo-Gangetic Plain (~1.7 days/year), a well known global hotspot of particulate pollution. Consistent increasing trends in absorbing aerosols are also visible in the recent years. As a result, the estimated atmospheric warming trends over Central India are two-fold higher than that over Indo-Gangetic Plain. This anomalous increment in hazy days over Central India is associated with the relatively higher increase in biomass burning over the region. Moreover, the trend in aerosol loading over the Arabian Sea, which is located downwind to Central India, is also higher than that over the Bay of Bengal during the dry winter season. Our findings not only draw attention to the rapid deteriorating air quality over Central India, but also underline the significance of increasing biomass burning under the recent climate change.

Aerosols are ubiquitous in the atmosphere. While natural aerosols constitute the largest fraction of global aerosol burden, regional hotspots of high aerosol loading coincide with regions of high population density, urbanization and industrialization, or biomass burning. The long-term measurements of aerosols[1–3], observational campaigns[4–6], and remote sensing from ground and space[7,8] have provided requisite datasets to improve our understanding of the physical, optical and chemical properties of aerosols. The extensive observational and modelling efforts over the last two decades have aided remarkably to advance our knowledge of aerosols influence of the climate[9]. For instance, the cooling effect from increasing aerosols has masked about one-third of the increasing greenhouse warming over the past half-century[10]. However, the lack of understanding of the variability of aerosols and their effects at regional scale contribute to the existing large uncertainty in aerosol feedbacks in future climate predictions.

The Indian subcontinent and adjoining Seas experience a tropical and sub-tropical climate and have been a focus of the study for aerosols over the last two decades. Observational campaigns (e.g. Indian Space Research Organization-Geosphere Biosphere Programme, ISRO-GBP; Indian Ocean Experiment, INDOEX; Arabian Sea Monsoon Experiment, ARMEX) have shown large aerosol negative radiative forcing at the surface and relatively large atmospheric warming than top of the atmosphere (TOA)[11–13]. The wintertime hazardous air pollution scenarios over the densely populated regions of India have recently received the utmost scientific attention. The winter season is characterized by a shallower boundary layer, lower wind speed and low precipitation, leading to the accumulation of aerosols near the surface[2,14,15]. Along with the obvious health impacts, studies have shown that the high aerosol loading in winter can reduce radiation reaching to the surface by about 25%, thereby decreasing crop yield[16–18]. Nonetheless, aerosols act as cloud condensation nuclei and affect cloud formation and rainfall[19]. Therefore, accurate knowledge of trend in aerosols over India during the winter season is extremely essential for reducing uncertainty in future climate, health, and economic predictions.

In India, several recent studies have used satellite and ground based measurements spanning over decade to find the trend in aerosol loading over Indian region[2,20–28]. *Dey and Girolamo*[20] and *Dey et al.*[26], found a significant rise in anthropogenic aerosols over the Indian subcontinent during 2000–2010 using MISR aerosol optical depth (AOD) data. These studies highlighted that the rural areas of IGP are more polluted than that of urban cities in the

[1]Centre for Earth, Ocean and Atmospheric Sciences, University of Hyderabad, Hyderabad, Telangana, 500046, India. [2]Pacific Northwest National Laboratory, Richland, Washington, 99352, USA. *email: chandansarangi591@gmail.com; vijaykanawade03@yahoo.co.in

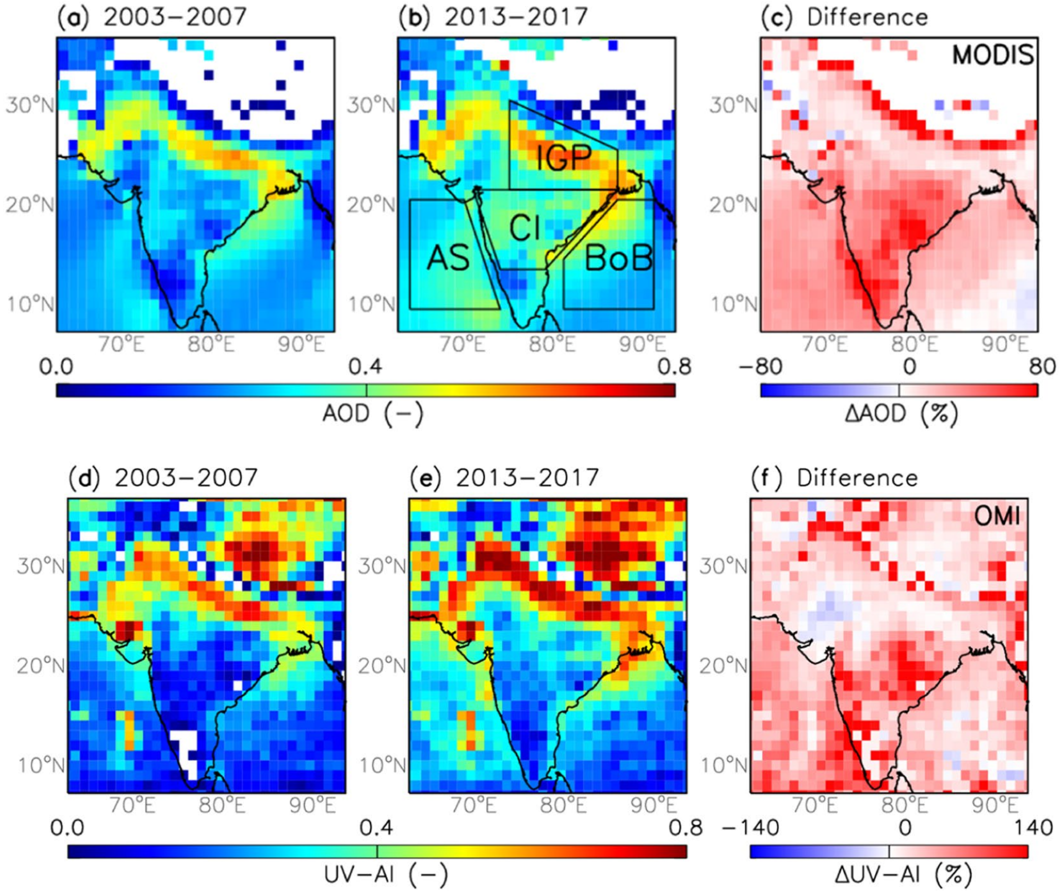

Figure 1. Averaged spatial distribution of MODIS AOD for November through February over the time periods (**a**) 2003–2007 (past years), (**b**) 2013–2017 (recent years) and (**c**) the percentage difference between the recent and the past years. The study regions are bounded by solid black line shown in (**b**); IGP: Indo-Gangetic Plain, AS: Arabian Sea, CI: Central India and BoB: Bay of Bengal. Averaged spatial distribution of OMI UV-AI for November through February over the time periods (**d**) 2003–2007, (**e**) 2013–2017, and (**f**) the percentage difference between the recent and the past years.

peninsular India. *Kaskaoutis et al.*[22], found an increasing trend in AOD over Kanpur (located in IGP), especially during the post-monsoon and winter seasons based on Aerosol Robotic Network (AERONET) AOD data from 2001 to 2010. *Hsu et al.*[25], also found an increasing trend in fine mode anthropogenic aerosols over North India and Bay of Bengal (BoB), particularly during the dry winter and post-monsoon seasons using SeaWiFS measurement from 1997 to 2010. *Ramachandran et al.*[23], attributed the incremental trend in aerosols over New Delhi to anthropogenic aerosols and over Northeast India to increase in forest fire and biomass burning emissions. *Babu et al.*[2], showed an increasing trend in anthropogenic contribution to total aerosol loading during the dry winter season. *Moorthy et al.*[21], *also* found an increasing trend in aerosol loading in the current decade than its value in 1985. *Srivasthava*[24] highlighted that the more than 70% of the Indian subcontinent shows a positive trend in AOD from 2 to 6% during the winter and pre-monsoon seasons, with a trend of >6% over BoB. *Kumar et al.*[27], recently found a relatively high aerosol loading over IGP as compared to other parts of India, but a statistically insignificant increasing trend of 0.002 AOD/year using MODIS-TERRA and nine ground-based stations data. They also observed a strong seasonality in aerosol loading with the dominance of fine mode aerosols over IGP, especially during the dry winter season. Most of these previous studies highlight the increasing trend of aerosol loading over highly polluted IGP and northern BoB in last two decades due to anthropogenic emissions.

Using 15 years of satellite (MODIS and OMI) observations and reanalysis (MERRA-2) data products, we illustrate that aerosol loading over Central India and the Arabian Sea during the dry winter season is increasing at a greater rate than that over IGP and the BoB in the recent years. We focused our analyses for the dry winter season (November to February) since the number of hazy days is highest during the season. A hazy day is referred to as the day with high aerosol loading (i.e. AOD greater than 66th percentile value over a location).

Results and Discussion

Trend in the number of hazy days.

The entire time period (2003–2017) is split into two sub-periods; past years (2003–2007) and recent years (2013–2017) to highlight changes in aerosol loading in the current decade compared to that of the previous decade. Figure 1 shows averaged spatial distribution of MODIS columnar AOD and OMI UV aerosol index (UV-AI) over India and adjoining Seas for the past and the recent years. The increased

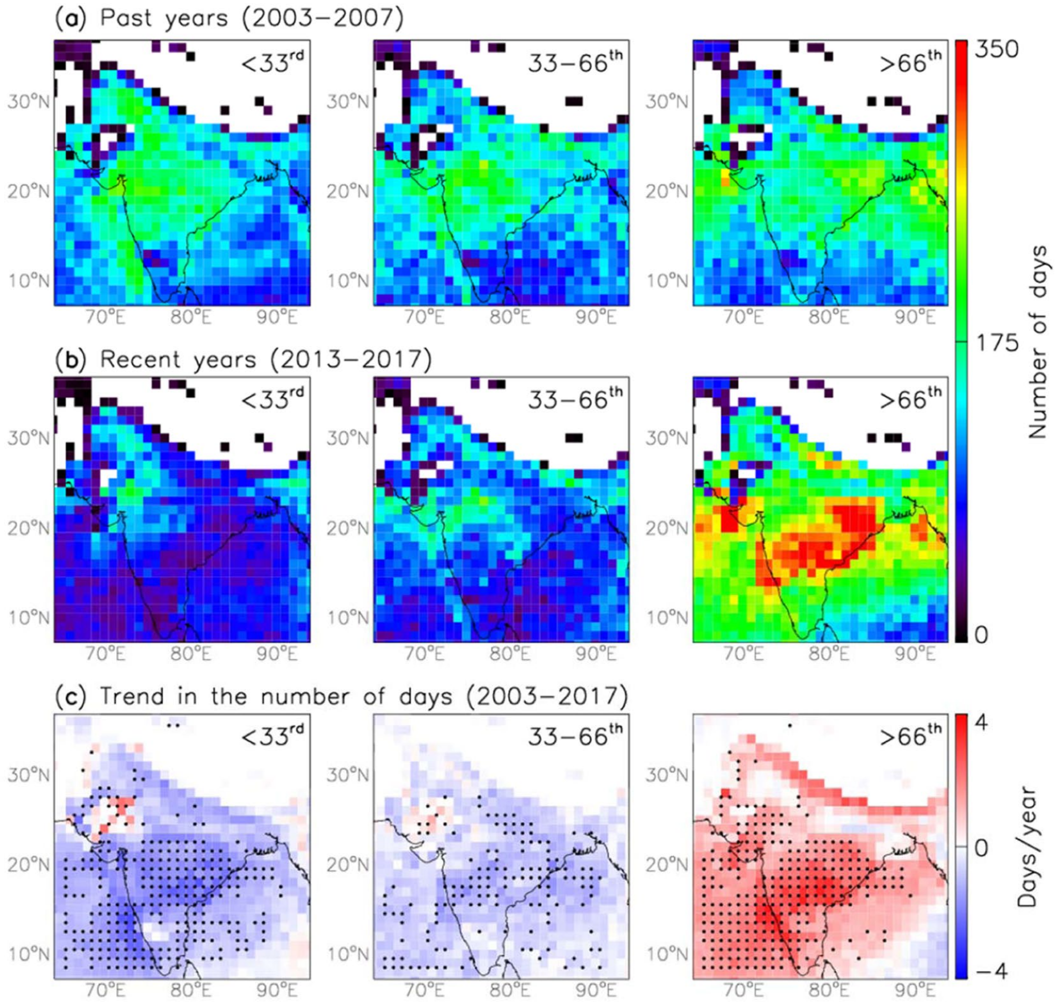

Figure 2. Trend in the number of days with aerosol loading from low to high regimes. (**a**) The number of days with low (<33rd percentile value of AOD), medium (33–66th) and high (>66th) aerosol loading for November-February of 2003–2007 (**b**) same as (**a**) except that for 2013–2017. (**c**) Trend in the number of days with <33rd, 33–66th and >66th percentile values of AOD for November–February of 2003–2017. Black dots indicate statistical significance using Student's t-test at a confidence interval of 95%.

aerosol loading in the recent years (2013–2017) is clearly evident, analogous to several previous studies[2,20–25,27]. The rate of change in the aerosol loading between the past and the recent years is distinctive regionally due to the variability in aerosol emission rates and latitudinal diverse climatic conditions. OMI retrieved UV-AI, which is a measure of UV-absorbing aerosol particles such as soot/smoke and mineral dust, show similar distinctive enhancement as that of AOD over Central India. This suggests the incremental dominance of absorbing aerosols over Central India in the recent years.

We first compare the number of days from low to high aerosol loading between the past and the recent years. In order to do this, the daily AOD observations are segregated into three percentile bins: AOD less than 33rd percentile, between the value 33rd and 66th percentile, and greater than 66th percentile values over each 1° × 1° grid based on the AOD values for November through February of the year 2003. The bins are identified as three distinct aerosol loading regimes; low (<33rd percentile), medium (33–66th percentiles), and high (>66th percentile). Then, the number of days for each of these regimes is counted during the past (Fig. 2(a)) and the recent (Fig. 2(b)) time periods. The number of days with low and medium aerosol loading has reduced in the recent years as compared to the past years (Fig. 2(a,b)). But, the days with high aerosol loading (>66th percentile) have increased in the recent years over India and adjoining Seas (Fig. 2(a,b)). Interestingly, the rate of increase in the number of high aerosol loading (i.e. hazy) days over CI is higher (~2.6 days/season) than over IGP (~1.8 days/season) (Fig. S1). This rate is also higher over the AS (~1.9 days/season) than over the BoB (~1.1 days/season). Noticeably, all the four regions have about two-fold high aerosol loading days in the year 2017 as compared to the year 2003 (Fig. S1).This indicates that the aerosol burden over India is typically shifted to higher values in the recent decade relative to the previous decade. It should be noted that MODIS retrieved AOD over IGP in the dry winter season is often plagued under foggy conditions, but we have removed AOD > 1.0 to avoid fog/cloud contaminated AOD retrievals in our analysis[29,30]. Wintertime fog thickens overnight and on till about an hour after sunrise. Then,

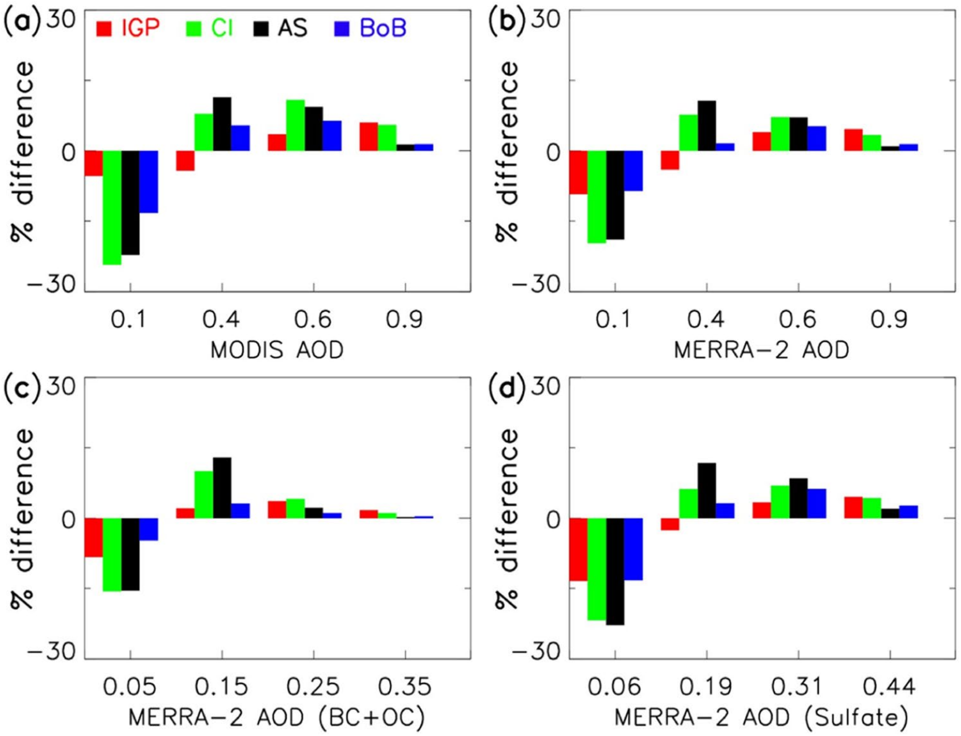

Figure 3. The percentage difference in the frequency distribution of (**a**) MODIS AOD, (**b**) MERRA-2 AOD, (**c**) MERRA-2 (BC + OC) AOD and (**d**) MERRA-2 sulfate AOD between the past and the recent years over different study regions.

it gradually disperse or thin out by noontime via effective ventilation[31] and since AQUA instrument onboard MODIS has overpass over India at about 1:30 pm local time, chances of fog to influence the results are negligible.

Further, the trend in the number of days for each of the percentile regime is calculated from 2003 to 2017 (Fig. 2(c)). The trend in the number of days with low to medium aerosol loading days is found to be negative over India and adjoining Seas. But, the trend in the number of days with high aerosol loading days is found to be positive, with significantly positive values over CI and the AS as compared to IGP, analogous to our finding from Fig. 2(b). Previous studies have reported increasing aerosol loading trend over India using both the ground-based[2,21,22,28] and satellite observations[1,20,23,24,32]. But, we find that the increasing aerosol loading trend is more pronounced over CI and the AS, with >2 days per season over the time period from 2003 to 2017. *Moorthy et al.*[33], also revealed that the rate of increase in columnar AOD was more rapid (~4%) during the time period from 2000 to 2011 compared to the previous decade and that Central Peninsular India showed the highest increasing trend (3.63%/year) than the Southern Peninsular and Northern India, with higher rates during the winter season as compared to other seasons. A recent study also showed less significant increasing trends in AOD over IGP over last decade[27].

The difference in the percentage frequency distribution for MODIS AOD between the past and the recent years shows a decreasing frequency of low aerosol loading (AOD bin of 0.1), whereas it shows an increasing frequency of medium to high aerosol loading (AOD bin >0.4) (Fig. 3(a)) over all study regions. We also find that MERRA-2 reanalysis data is able to reproduce similar intensity-frequency variation in the AOD (Fig. 3(b)). In order to examine the changes in various aerosol species associated with the observed increasing trend in total aerosol loading, we calculate the percentage frequency distribution for species-wise AOD separately for the past and the recent years for different regions of India (Fig. S2). The differences in the percentage frequency distribution for these variables between the past and the recent years are then plotted in Fig. 3(c,d). The BC and OC AOD is clubbed together as they are co-emitted from various local sources, both anthropogenic aerosols and biomass burning. The natural emissions like sea salt (SS) and dust AOD, which are mostly transported into CI and IGP domain, are also shown in Fig. S3. Intensity-frequency variability similar to that seen for composite AOD (Fig. 3(a,b) is present for BC + OC and sulfate (Fig. 3(c,d)) species over both IGP and CI regions. Interestingly, similar changes are not seen for the case of transported species i.e. SS and dust AOD which indicates that the change in total aerosol loading may be attributed to increase in the local emissions. Moreover, the intensity-frequency variation is more prominent over CI and the AS compared to that over IGP. Further, the differences in the vertical aerosol mixing ratio profiles illustrate significant enhancement in BC and OC from the surface to 700hPa (~3.1 km) which imply near-surface sources (Fig. S5). But, the anomalous enhancements in BC and OC mixing ratios are higher over CI in the recent years than over the IGP.

Interestingly, the intensity-frequency changes in AOD observed over the AS region is more prominent compared to the BoB region. In addition, the anthropogenic species over the AS, particularly BC, OC, and sulfate, are found to be three times higher than SS aerosols during the winter season (Figs. 3 and S3). The mean wind

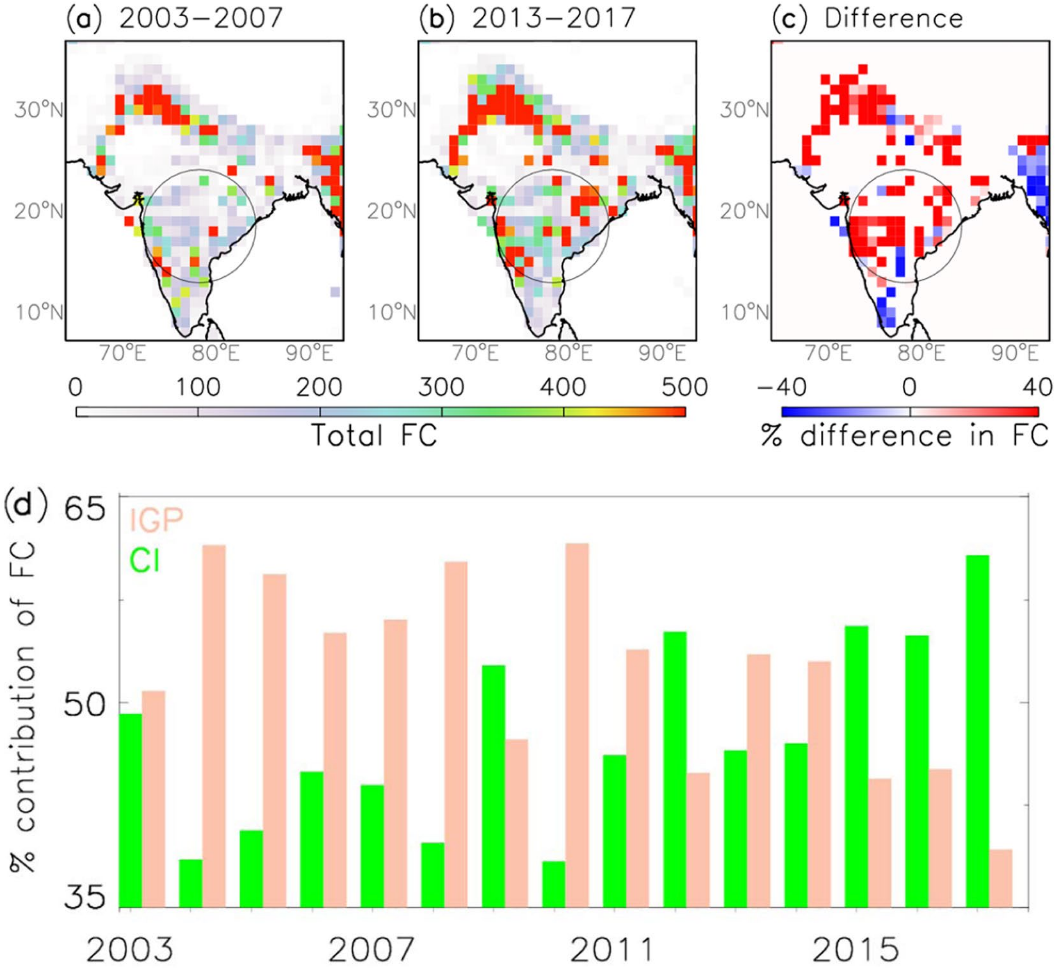

Figure 4. (**a**) Spatial map of 1° × 1° gridded total fire counts (FC) for November-February of 2003–2007 (past years). (**b**) Same as (**a**) except that for 2013–2017 (recent years). (**c**) The difference between the past and the recent years. (**d**) The change in percentage contribution of fire counts over CI and IGP for November-February of 2003 to 2017.

circulation clearly illustrates predominant northeasterly flow over the continental region mostly flowing into the AS i.e. the AS is located in the downwind regions of CI (Fig. S4). Thus, the BC, OC, and sulfate aerosols over the AS are probably transported from local anthropogenic emissions over the CI. This also explains the high percentage change in aerosol loading over the AS than the BoB in the recent years (Fig. 3). This suggests that the increase in continental aerosol emissions has profound impact on the aerosol loading over the adjacent marine regions. This finding is different from previous investigators as those studies indicated that the aerosol loading over the BoB is higher than over the AS, and that the relative contribution of anthropogenic aerosol mass tend to be higher over the BoB[34–37]. It could be noted that most of these studies used data prior to the year 2012, except the recent study by Srivastava[24], further highlighting the significance of our finding on aerosol perturbations in the recent years (2013–2017).

Rapid urbanization in developing nations like India is generally the primary source of the overall aerosol burden[38,39]. For example, out of the ten most populous metropolitan areas in India, five of them lie within CI region (Bangalore, Hyderabad, Mumbai, Nagpur and Pune) and these cities are known for rapid change in the land use and land cover over the last decade[40]. It should be noted that forests, shrubs, and cropland contributes to a large fraction of the land cover over Central India. As a result, the biomass burning activities peak within the two central states (Madhya Pradesh and Maharashtra), accounting for about 36% of the total fire counts in India[41]. Besides, the Eastern Ghats in Central Eastern India is a dense active fire hotspot, owing to shifting cultivation practices and clearing of mixed deciduous forest in the late winter season[42,43]. Therefore, biomass burning (e.g. forest fires, crop residue burning, trash/wood burning), which is a major sources of aerosol loading over India[44], can contribute significantly to this anomalous enhancement in AOD in the recent decade. Figure 4(a–c) presents spatial map of 1° × 1° gridded total fire counts over India during the past and the recent years and difference between them. The spatio-temporal variability in fire counts over CI (Fig. 4(a,b)) is consistent with the spatial variability in aerosol loading and AI (Fig. 1). Further, the monthly fire count difference (Fig. S6) correlates spatially with the monthly trend in the number of days with high aerosol loading (Fig. S7), particularly over CI. We have then counted the number of fire hotspots for each year over IGP and CI, and calculated the percentage contribution of fire counts from both the regions. Note that the number of 1° × 1° gridded pixels in IGP and CI are equal (n = 75). The relative percentage of fire counts over CI and IGP are plotted in Fig. 4(d). The percentage contribution of fire counts over CI has increased at a rate of 20% from 2003 to 2017 indicating that the fire counts over CI is higher than that over IGP in the recent years. Thus, the greater rate of enhancement in high aerosol loading days over CI in the recent years (Fig. 2(b)) can be associated with relatively large enhancement in fire emissions over CI (Fig. 4(c)) compared to IGP. Moreover, a recent study show that a large fraction of aerosols from biomass burning activities over northern western states can also extend over parts of Central India[45] as well as northwestern parts of Bay of Bengal[34]. Therefore, the observed enhancement in the recent aerosol loading over CI can be a combined result of rapid urbanization, enhanced localized fire emissions, and long-range transport of aerosols from the IGP region.

Change in aerosol direct radiative forcing. Aerosol direct radiative forcing counteracts, in part, the warming due to greenhouse gases[10,46], but the effects may vary temporally and spatially. High aerosol direct radiative forcing is usually found over India due to the combined effect of dust, smoke and other aerosols[32]. In this section, we present the change in the ADRF at the top of the atmosphere, on the atmosphere and at the surface using MERRA-2 data. Figures S8–S10 presents the averaged spatial distribution of the ADRF at the TOA, on the atmosphere and at the surface, respectively, during the past and the recent years and the difference between these two time periods. *Nair et al.*[47], have shown that aerosol forcing at the TOA is modulated mostly by anthropogenic aerosols. It is clear that the increasing trends in aerosol loading over India and adjoining Seas, especially off the eastern and western coasts, led to increased cooling at the TOA in recent years (Fig. S8). *Kaskaoutis et al.*[34], have observed significant fraction of soot aerosols over northwestern BoB during the winter. In fact, the aerosol-induced atmospheric forcing efficiency was found higher for the BoB (31 W/m^2) as compared to the AS (18 W/m^2)[48], but we find that ADRF on the atmosphere is higher over the AS in the recent years. It is apparent that there is increased atmospheric warming (Fig. S8), increased surface cooling (Fig. S9), and increased TOA cooling (Fig. S10) over India and adjoining Seas owing to increased aerosol loading (Figs. 1 and 2) in the recent years.

To illustrate how the forcing has changed over the study period, we calculate ADRF for each region separately (Fig. S11). The overall atmospheric (positive) and surface (negative) forcing is highest over IGP compared to CI and adjoining Seas (Fig. S11). But, what is interesting is that the difference between the recent and the past years in atmospheric warming over CI (4.50 W/m^2) overtakes IGP (2.01 W/m^2) (Table S2). Concurrently, the mean difference in ADRF on the atmosphere between the recent and the past years is higher over the AS (3.67 W/m^2) than that of the BoB (0.48 W/m^2), as opposed to previous studies[48,49]. This suggests that aerosols exerted as much as seven times more atmospheric warming over the AS than the BoB in recent years. The regionally averaged ADRF on the surface and at the TOA are also higher over the AS than the BoB (Table S2), contradicting to the previous study which showed larger values over the BoB for February 2003[50]. These findings imply that the increasing fire activity over CI has altered the forcing at much expected level over CI and downwind AS than the polluted IGP. The enhanced atmospheric heating and surface cooling over CI and the AS can lead to increase in lower tropospheric stability. The stable atmospheric condition would then favor more accumulation of aerosols close to the surface and can further accelerate occurrence of hazy days (Fig. S12), and thus, creating a positive feedback mechanism. Nonetheless, the increase in LTS can itself be influenced by the increase in aerosol-induced atmospheric warming[51]. Therefore, this aerosol-LTS coupling can induce a positive feedback cycle on aerosol accumulation in the boundary layer and enhance aerosol loading over CI and the AS. Moreover, enhanced atmospheric stability may also enhance low-level cloud amount over the AS and the BoB, leading to a negative feedback on the climate system in a warming anthropogenic future.

Conclusions

Indian subcontinent, one of the world's fastest growing regions in terms of urbanization and population, is greatly vulnerable to particulate pollution. The winter time hazy scenarios and their radiation feedbacks exert a profound impact on the weather and climate. Using 15 years (2003–2017) of satellite and reanalysis datasets, this study investigates the trend in the number of hazy days (i.e. days with high aerosol loading) and the aerosol-induced direct radiation feedbacks on the surface-atmosphere system over India and adjoining Seas for the dry winter season (November–February).

The major findings of this study are as follows;

1. Overall, aerosol loading over India and adjoining Seas is rapidly increasing in the recent years.
2. The number of hazy days are increasing at the rate of about 2 days per year over India, with a higher rate over CI (~2.6 days/year) than that of over IGP (~1.7 days/year).
3. Since the AS is located downwind to the CI, the number of hazy days over the AS is also higher than that over the BoB during the dry winter season.
4. Collocated similar enhancements in UV aerosol index as that of AOD suggests the dominance of absorbing aerosols over Central India in the recent years.
5. Consequently, aerosol-induced atmospheric warming (4.50 W/m^2) and surface cooling (−9.44 W/m^2) due to aerosol direct radiative forcing is highest over CI as compared to other study regions in the recent years. The enhanced atmospheric warming over CI is about two-fold to that of over IGP (2.01 W/m^2).
6. The higher aerosol loading over CI is attributed to the recent increase in biomass burning activities over the region.
7. Surprisingly, aerosols exerted as much as seven times more atmospheric warming over the AS in the recent years than over the BoB. This contradicts to majority of previous studies which showed higher atmospheric warming over the BoB than the AS during the winter season. This finding is substantiated by the mean changes in wind speed and lower tropospheric stability over CI and the AS.

Although the high aerosol loading is observed over IGP than other regions, our study reveals that aerosol loading over CI has escalated greatly in the recent years. Thus, our findings provide new insights to better constrain aerosols role in the climate over Indian subcontinent.

Methods

In this study, we have used the geographical region bounded by latitude, 7–38°N, and longitude, 66–94°E. This region further divided into four sub-regions viz., Indo-Gangetic Plain (IGP), Central India (CI), Arabian Sea (AS) and Bay of Bengal (BoB) (Fig. 1b). The columnar composite AOD from Moderate-resolution Imaging Spectroradiometer (MODIS) onboard AQUA is used. The modeled aerosol species concentration (sulfate, BC, OC, sea salt, and dust) in terms of their optical depth and radiation fluxes are used from the Modern-Era Retrospective Analysis for Research and Application - version 2 (MERRA-2). These observations and modelled values at daily resolution over the time period from 2003 to 2017 for the time period from October through February are used. Also the composition of aerosols and the meteorological conditions have insignificant monthly variability during the dry winter season[18]. Table S1 summarizes data products and their temporal and spatial resolution.

MODIS. The Moderate-resolution Imaging Spectroradiometer sensor onboard polar orbiting Earth Observing System (EOS) satellite AQUA flies at an altitude of 705 km, with a swath width of 2330 km and equator crossing at 13:30 local time. It measures the reflected solar radiance and terrestrial emission in a wavelength band ranging from 0.41–14.4 μm divided into 36 channels, categorized with horizontal resolutions varying between 0.25 and 1 square kilometer[52]. Here, we have used the level3 Dark Target and Deep Blue combined AOD of collection 6.1 at 0.55 μm at a grid resolution of $1° \times 1°$ [53–55]. The estimated maximum uncertainty is approximately $\pm 0.05 \times$ AOD over Oceans and $\pm 0.15 \times$ AOD over continents. The technical details, algorithm and validation details can be found in *Remer et al.*[52]. The collection 6 MODIS active fire location product at 1 km resolution was also used as proxy for biomass burning hot spots. The product utilizes thermal anomalies in infrared wavelengths (4 and 11 μm)[56].

OMI. In addition to MODIS, AURA Ozone Monitoring Instrument (OMI) daily UV aerosol index (UV-AI) is used (OMAERUVd.003) in this analysis. AURA OMI is a nadir-viewing spectrometer onboard NASA's Aura satellite. It measures direct and backscattered solar radiation in the UV-visible range from 264 to 504 nm. The retrieval technique and validation is given in *Bucsela et al.*[57]. UV-AI is based on a spectral contrast method in a UV region where the ozone absorption is negligible. Positive values of UV-AI indicate absorbing aerosols (smoke and dust) whereas near-zero or negative values indicate non-absorbing aerosols (sulfate and sea salt) and clouds[58]. While, UV-AI is good indicator of absorbing aerosols, its value is dependent on the smoke plume altitude[59]. The OMI retrieval algorithm for aerosol detection has been validated with ground-based measurements[60]. OMI UV-AI is available from the NASA Goddard Earth Sciences, Data and Information Services Center (GES DISC; http://disc.sci.gsfc.nasa.gov).

MERRA-2. The Modern-Era Retrospective Analysis for Research and Application - version 2[61] uses the Goddard Earth Observing System-5 (GEOS-5) atmospheric general circulation model[62] that is coupled with the Goddard Global Ozone Chemistry Aerosol Radiation and Transport model (GOCART)[63]. The GOCART model simulates AOD for five major aerosol species like OC, BC, sea salt, dust and sulfate using multi-satellite based (MODIS,AVHRR and MISR) and ground-based (AERONET) AOD data. GEOS-5 model provides the data from 1980 to present in hourly and monthly gridded data with the resolution of $0.5° \times 0.625°$ in latitude and longitude from the surface to the top layer of 0.01 hPa with 72 vertical levels[64]. The MERRA-2 simulated AOD compares well with ground-based and satellite measurements globally[64,65]. It is freely available from NASA Goddard Earth Sciences (GES) Data and Information Services Center (DISC) https://disc.gsfc.nasa.gov/. In order to calculate clear-sky aerosol direct radiative forcing (ADRF) from the radiative fluxes from MERRA-2 data[65], the difference between the radiation flux under clear sky condition in the presence of aerosol and without aerosol is calculated. The hourly variables; SWGNTCLR (surface net downward shortwave flux assuming clear-sky), SWGNTCLRCLN (surface net downward shortwave flux assuming clear-sky and no aerosol), LWGNTCLR (surface net downward longwave flux assuming clear sky) and LWGNTCLRCLN (surface net downward longwave flux assuming clear-sky and no aerosol) are used to calculate ADRF at surface ($\mathrm{ADRF}_{\mathrm{SURF}}$). Concurrently, ADRF at the top of the atmosphere ($\mathrm{ADRF}_{\mathrm{TOA}}$) is calculated from hourly variables, SWTNTCLR (TOA net downward shortwave flux assuming clear sky), SWTNTCLRCLN (TOA net downward shortwave flux assuming clear-sky and no aerosol), LWTUPCLR (upwelling longwave flux at TOA assuming clear-sky) and LWTUPCLRCLN (upwelling longwave flux at TOA assuming clear-sky and no aerosol). These radiation variables can be found in the MERRA-2 product, tavg1_2d_rad_Nx. Overall, MERRA-2 simulated radiative fluxes agrees well with CERES EBAF Edition 2.8 satellite product over 2001–2015[66]. MERRA-2 simulated both shortwave and longwave radiative fluxes are used to derive the total aerosol direct radiative forcing (ARDF). ADRF at the surface ($ADRF_{\mathrm{SUR}}$) and at top of the atmosphere ($ADRF_{\mathrm{TOA}}$) are calculated by the following formula.

$$\mathrm{ADRF}_{\mathrm{SUR}} = (\mathrm{SWGNTCLR} + \mathrm{LWGNTCLR}) - (\mathrm{SWGNTCLRCLN} + \mathrm{LWGNTCLRCLN})$$
$$\mathrm{ADRF}_{\mathrm{TOA}} = (\mathrm{SWTNTCLR} + \mathrm{LWTUPCLR}) - (\mathrm{SWTNTCLRCLN} + \mathrm{LWTUPCLRCLN})$$

The ADRF on the atmosphere, which indicates the energy trapped by all aerosols in the atmosphere, is calculated by taking the difference between ADRF at the TOA and ADRF at the surface.

GDAS. We used potential temperature at the free troposphere pressure level (i.e. 700 hPa) and the surface to calculate lower tropospheric stability (LTS) using the NOAA-NCEP (National Oceanic and Atmospheric Administration National Centers for Environmental Prediction) Global Data Assimilation System (GDAS) assimilated meteorological datasets[67]. The variables are available at 1° × 1° spatial resolution with 21 vertical levels (1000 hPa −100 hPa) at synoptic hours. LTS is calculated as; $LTS = \theta_{700} - \theta_{surface}$.

Data availability

Satellite (MODIS-AQUA and AURA-OMI) and model reanalysis (MERRA-2) datasets are freely accessible to the public from irrespective websites (Refer to Table S1 in the Supplementary Material).

Received: 21 June 2019; Accepted: 29 October 2019;

References

1. Andrews, E. *et al*. Climatology of aerosol radiative properties in the free troposphere. *Atmos. Res.* **102**, 365–393, https://doi.org/10.1016/j.atmosres.2011.08.017 (2011).
2. Babu, S. S. *et al*. Trends in aerosol optical depth over Indian region: Potential causes and impact indicators. *J. Geophys. Res. Atmos.* **118**(11), 794–711,806, https://doi.org/10.1002/2013JD020507 (2013).
3. Putaud, J. P. *et al*. A European aerosol phenomenology – 3: Physical and chemical characteristics of particulate matter from 60 rural, urban, and kerbside sites across Europe. *Atmos. Environ.* **44**, 1308–1320, https://doi.org/10.1016/j.atmosenv.2009.12.011 (2010).
4. Moorthy, K. K., Satheesh, S. K., Babu, S. S. & Dutt, C. B. S. Integrated Campaign for Aerosols, gases and Radiation Budget (ICARB): An overview. *J. Earth Syst. Sci.* **117**, 243–262, https://doi.org/10.1007/s12040-008-0029-7 (2008).
5. Tripathi, S. N. *et al*. Measurements of atmospheric parameters during Indian Space Research Organization Geosphere Biosphere Programme Land Campaign II at a typical location in the Ganga basin: 1. Physical and optical properties. *J. Geophys. Res. Atmos.* **111**, https://doi.org/10.1029/2006JD007278 (2006).
6. Quinn, P. K. & Bates, T. S. Regional aerosol properties: Comparisons of boundary layer measurements from ACE 1, ACE 2, Aerosols99, INDOEX, ACE Asia, TARFOX, and NEAQS. *J. Geophys. Res. Atmos.* **110**, https://doi.org/10.1029/2004jd004755 (2005).
7. Remer, L. A. *et al*. Global aerosol climatology from the MODIS satellite sensors. *J. Geophys. Res. Atmos.* **113**, https://doi.org/10.1029/2007JD009661 (2008).
8. Holben, B. N. *et al*. AERONET—A Federated Instrument Network and Data Archive for Aerosol Characterization. *Remote Sens. Environ.* **66**, 1–16, https://doi.org/10.1016/S0034-4257(98)00031-5 (1998).
9. IPCC. Climate Change 2013: The Physical Science Basis. Contribution of Working Group I to the Fifth Assessment Report of the Intergovernmental Panel on Climate Change, [Stocker, T. F. *et al*. (ed.)]. Cambridge University Press, Cambridge, United Kingdom and New York, NY, USA, 1535 pp (2013).
10. Storelvmo, T., Leirvik, T., Lohmann, U., Phillips, P. C. B. & Wild, M. Disentangling greenhouse warming and aerosol cooling to reveal Earth's climate sensitivity. *Nat. Geosci.* **9**, 286, https://doi.org/10.1038/ngeo2670
11. David, L. M. *et al*. Aerosol Optical Depth Over India. *J. Geophys. Res. Atmos.* **123**, 3688–3703, https://doi.org/10.1002/2017JD027719 (2018).
12. Kaskaoutis, D. G., Badarinath, K. V. S., Kharol, K. S., Sharma, R. A. & Kambezidis, H. D. Variations in the aerosol optical properties and types over the tropical urban site of Hyderabad, India. *J. Geophys. Res. Atmos.* **114**, https://doi.org/10.1029/2009JD012423 (2009).
13. Satheesh, S. K., Moorthy, K. K., Kaufman, Y. J. & Takemura, T. Aerosol optical depth, physical properties and radiative forcing over the Arabian Sea. *Meteorol. Atmos. Phys.* **91**, 45–62, https://doi.org/10.1007/s00703-004-0097-4 (2006).
14. Pan, X. *et al*. A multi-model evaluation of aerosols over South Asia: common problems and possible causes. *Atmos. Chem. Phys.* **15**, 5903–5928, https://doi.org/10.5194/acp-15-5903-2015 (2015).
15. Prijith, S. S., Rajeev, K., Thampi, B. V., Nair, S. K. & Mohan, M. Multi-year observations of the spatial and vertical distribution of aerosols and the genesis of abnormal variations in aerosol loading over the Arabian Sea during Asian summer monsoon season. *J. Atmospheric Sol.-Terr. Phys.* **105–106**, 142–151, https://doi.org/10.1016/j.jastp.2013.09.009 (2013).
16. Burney, J. & Ramanathan, V. Recent climate and air pollution impacts on Indian agriculture. *Proc. Natl. Acad. Sci. USA* **111**, 16319–16324, https://doi.org/10.1073/pnas.1317275111 (2014).
17. Chameides, W. L. *et al*. Case study of the effects of atmospheric aerosols and regional haze on agriculture: An opportunity to enhance crop yields in China through emission controls? *Proc. Natl. Acad. Sci. USA* **96**, 13626–13633, https://doi.org/10.1073/pnas.96.24.13626 (1999).
18. Latha, R., Murthy, B. S., Lipi, K., Srivastava, M. K. & Kumar, M. Absorbing Aerosols, Possible Implication to Crop Yield - A Comparison between IGB Stations. *Aerosol Air Qual. Res.* **17**, 693–705, https://doi.org/10.4209/aaqr.2016.02.0054 (2017).
19. Sarangi, C., Kanawade, V. P., Tripathi, S. N., Thomas, A. & Ganguly, D. Aerosol-induced intensification of cooling effect of clouds during Indian summer monsoon. *Nat. Commun.* **9**, 3754, https://doi.org/10.1038/s41467-018-06015-5 (2018).
20. Dey, S. & Di Girolamo, L. A decade of change in aerosol properties over the Indian subcontinent. *Geophys. Res. Lett.* **38**, https://doi.org/10.1029/2011GL048153 (2011).
21. Moorthy, K. K., Babu, S. S., Manoj, M. R. & Satheesh, S. K. Buildup of aerosols over the Indian Region. *Geophys. Res. Lett.* **40**, 1011–1014, https://doi.org/10.1002/grl.50165 (2013).
22. Kaskaoutis, D. G. *et al*. Variability and trends of aerosol properties over Kanpur, northern India using AERONET data (2001–10). *Environ. Res. Lett.* **7**, 024003 (2012).
23. Ramachandran, S., Kedia, S. & Srivastava, R. Aerosol optical depth trends over different regions of India. *Atmos. Environ.* **49**, 338–347, https://doi.org/10.1016/j.atmosenv.2011.11.017 (2012).
24. Srivastava, R. Trends in aerosol optical properties over South Asia. *Int. J. Climatol.* **37**, 371–380, https://doi.org/10.1002/joc.4710 (2017).
25. Hsu, N. C. *et al*. Global and regional trends of aerosol optical depth over land and ocean using SeaWiFS measurements from 1997 to 2010. *Atmos. Chem. Phys.* **12**, 8037–8053, https://doi.org/10.5194/acp-12-8037-2012 (2012).
26. Dey, S. *et al*. Variability of outdoor fine particulate (PM2.5) concentration in the Indian Subcontinent: A remote sensing approach. *Remote Sens. Environ.* **127**, 153–161, https://doi.org/10.1016/j.rse.2012.08.021 (2012).
27. Kumar, M. *et al*. Long-term aerosol climatology over Indo-Gangetic Plain: Trend, prediction and potential source fields. *Atmos. Environ.* **180**, 37–50, https://doi.org/10.1016/j.atmosenv.2018.02.027 (2018).
28. Manoj, M. R., Satheesh, S. K., Moorthy, K. K., Gogoi, M. M. & Babu, S. S. Decreasing Trend in Black Carbon Aerosols Over the Indian Region. *Geophys. Res. Lett.* **46**, 2903–2910, https://doi.org/10.1029/2018GL081666 (2019).
29. Sarangi, C., Tripathi, S. N., Kanawade, V. P., Koren, I. & Pai, D. S. Investigation of the aerosol–cloud–rainfall association over the Indian summer monsoon region. *Atmos. Chem. Phys.* **17**, 5185–5204, https://doi.org/10.5194/acp-17-5185-2017 (2017).
30. Koren, I., Kaufman, Y. J., Rosenfeld, D., Remer, L. A. & Rudich, Y. Aerosol invigoration and restructuring of Atlantic convective clouds. *Geophys. Res. Lett.* **32**, https://doi.org/10.1029/2005gl023187 (2005).

31. Gaur, A., Tripathi, S. N., Kanawade, V. P., Tare, V. & Shukla, S. P. Four-year measurements of trace gases (SO2, NOx, CO, and O3) at an urban location, Kanpur, in Northern India. *J. Atmos. Chem.* **71**, 283–301, https://doi.org/10.1007/s10874-014-9295-8 (2014).
32. Kaufman, Y. J., Tanré, D. & Boucher, O. A satellite view of aerosols in the climate system. *Nature* **419**, 215, https://doi.org/10.1038/nature01091 (2002).
33. Krishna Moorthy, K., Suresh Babu, S., Manoj, M. R. & Satheesh, S. K. Buildup of aerosols over the Indian Region. *Geophys. Res. Lett.* **40**, 1011–1014, https://doi.org/10.1002/grl.50165 (2013).
34. Kaskaoutis, D. G. *et al.* Extremely large anthropogenic-aerosol contribution to total aerosol load over the Bay of Bengal during winter season. *Atmos. Chem. Phys.* **11**, 7097–7117, https://doi.org/10.5194/acp-11-7097-2011 (2011).
35. Lawrence, M. G. & Lelieveld, J. Atmospheric pollutant outflow from southern Asia: a review. *Atmos. Chem. Phys.* **10**, 11017–11096, https://doi.org/10.5194/acp-10-11017-2010 (2010).
36. Ramachandran, S. & Jayaraman, A. Spectral aerosol optical depths over Bay of Bengal and Chennai: II-sources, anthropogenic influence and model estimates. *Atmos. Environ.* **37**, 1951–1962, https://doi.org/10.1016/S1352-2310(03)00084-0 (2003).
37. Sanwlani, N., Chauhan, P. & Navalgund, R. R. Characterization and transport of aerosols over the Bay of Bengal during the winter monsoon: a comparative study using *in-situ* and satellite measurements. *Int. J. Remote Sens.* **32**, 1253–1267, https://doi.org/10.1080/01431160903527454 (2011).
38. Han, L., Zhou, W. & Li, W. Growing Urbanization and the Impact on Fine Particulate Matter (PM2.5) Dynamics. *Sustainability* **10**, 1696, https://doi.org/10.3390/su10051696 (2018).
39. Haque, I. & Patel, P. P. Growth of metro cities in India: trends, patterns and determinants. *Urban Res. Pract.* **11**, 338–377, https://doi.org/10.1080/17535069.2017.1344727 (2018).
40. Rathee, G. In *Urbanization in Asia: Governance, Infrastructure and the Environment* (eds Kala Seetharam Sridhar & Guanghua Wan) 215-238 (Springer India, 2014).
41. Sahu, L. K. *et al.* Regional biomass burning trends in India: Analysis of satellite fire data. *J. Earth Syst. Sci.* **124**, 1377–1387, https://doi.org/10.1007/s12040-015-0616-3 (2015).
42. Prasad, V. K., Badarinath, K. V. S. & Eaturu, A. Biophysical and anthropogenic controls of forest fires in the Deccan Plateau, India. *J. Environ. Manage.* **86**, 1–13, https://doi.org/10.1016/j.jenvman.2006.11.017 (2008).
43. Vadrevu, K. P., Lasko, K., Giglio, L. & Justice, C. Vegetation fires, absorbing aerosols and smoke plume characteristics in diverse biomass burning regions of Asia. *Environ. Res. Lett.* **10**, 105003, https://doi.org/10.1088/1748-9326/10/10/105003 (2015).
44. Venkataraman, C. *et al.* Emissions from open biomass burning in India: Integrating the inventory approach with high-resolution Moderate Resolution Imaging Spectroradiometer (MODIS) active-fire and land cover data. *Glob. Biogeochem*. Cycles **20**, https://doi.org/10.1029/2005gb002547 (2006).
45. Sarkar, S., Singh, R. P. & Chauhan, A. Crop Residue Burning in Northern India: Increasing Threat to Greater India. *J. Geophys. Res. Atmos.* **123**, 6920–6934, https://doi.org/10.1029/2018jd028428 (2018).
46. Wild, M. *et al.* From Dimming to Brightening: Decadal Changes in Solar Radiation at Earth's Surface. *Science* **308**, 847–850, https://doi.org/10.1126/science.1103215 (2005).
47. Nair, V. S., Babu, S. S., Manoj, M. R., Moorthy, K. K. & Chin, M. Direct radiative effects of aerosols over South Asia from observations and modeling. *Clim. Dyn.* **49**, 1411–1428, https://doi.org/10.1007/s00382-016-3384-0 (2017).
48. Moorthy, K. K., Nair, V. S., Babu, S. S. & Satheesh, S. K. Spatial and vertical heterogeneities in aerosol properties over oceanic regions around India: Implications for radiative forcing. *Q. J. Royal Meteorol. Soc.* **135**, 2131–2145, https://doi.org/10.1002/qj.525 (2009).
49. Dey, S., Sarkar, S. & Singh, R. P. Comparison of aerosol radiative forcing over the Arabian Sea and the Bay of Bengal. *Adv. Space Res.* **33**, 1104–1108, https://doi.org/10.1016/S0273-1177(03)00737-3 (2004).
50. Vinoj, V., Babu, S. S., Satheesh, S. K., Moorthy, K. K. & Kaufman, Y. J. Radiative forcing by aerosols over the Bay of Bengal region derived from shipborne, island-based, and satellite (Moderate-Resolution Imaging Spectroradiometer) observations. *J. Geophys. Res. Atmos.* 1**09**, https://doi.org/10.1029/2003JD004329 (2004).
51. Sarangi, C., Tripathi, S. N., Mishra, A. K., Goel, A. & Welton, E. J. Elevated aerosol layers and their radiative impact over Kanpur during monsoon onset period. *J. Geophys. Res. Atmos.* **121**, 7936–7957, https://doi.org/10.1002/2015jd024711 (2016).
52. Remer, L. A. *et al.* The MODIS Aerosol Algorithm, Products, and Validation. *J. Atmos. Sci.* **62**, 947–973, https://doi.org/10.1175/jas3385.1 (2005).
53. Levy, R. C. *et al.* The Collection 6 MODIS aerosol products over land and ocean. *Atmos. Meas. Tech.* **6**, 2989–3034, https://doi.org/10.5194/amt-6-2989-2013 (2013).
54. Hsu, N. C. *et al.* Enhanced Deep Blue aerosol retrieval algorithm: The second generation. *J. Geophys. Res. Atmos.* **118**, 9296–9315, https://doi.org/10.1002/jgrd.50712 (2013).
55. Sayer, A. M. *et al.* MODIS Collection 6 aerosol products: Comparison between Aqua's e-Deep Blue, Dark Target, and "merged" data sets, and usage recommendations. *J. Geophys. Res. Atmos.* **119**(13), 965–913,989, https://doi.org/10.1002/2014jd022453 (2014).
56. Giglio, L., Descloitres, J., Justice, C. O. & Kaufman, Y. J. An Enhanced Contextual Fire Detection Algorithm for MODIS. *Remote Sens. Environ.* **87**, 273–282, https://doi.org/10.1016/S0034-4257(03)00184-6 (2003).
57. Bucsela, E. J. *et al.* A new stratospheric and tropospheric NO2 retrieval algorithm for nadir-viewing satellite instruments: applications to OMI. *Atmos. Meas. Tech.* **6**, 2607–2626, https://doi.org/10.5194/amt-6-2607-2013 (2013).
58. Torres, O. *et al.* Aerosols and surface UV products from Ozone Monitoring Instrument observations: An overview. Journal of Geophysical Research: Atmospheres **112**, https://doi.org/10.1029/2007jd008809 (2007).
59. Eck, T. F. *et al.* Characterization of the optical properties of biomass burning aerosols in Zambia during the 1997 ZIBBEE field campaign. *J. Geophys. Res. Atmos.* **106**, 3425–3448, https://doi.org/10.1029/2000jd900555 (2001).
60. Curier, R. L. *et al.* Retrieval of aerosol optical properties from OMI radiances using a multiwavelength algorithm: Application to western Europe *J. Geophys. Res. Atmos*. **113**, https://doi.org/10.1029/2007jd008738 (2008).
61. Gelaro, R. *et al.* The Modern-Era Retrospective Analysis for Research and Applications, Version 2 (MERRA-2). *J. Climatol.* **30**, 5419–5454, https://doi.org/10.1175/jcli-d-16-0758.1 (2017).
62. Molod, A., Takacs, L., Suarez, M. & Bacmeister, J. Development of the GEOS-5 atmospheric general circulation model: evolution from MERRA to MERRA2. *Geosci. Model Dev.* **8**, 1339–1356, https://doi.org/10.5194/gmd-8-1339-2015 (2015).
63. Chin, M. *et al.* Tropospheric aerosol optical thickness from the GOCART model and comparisons with satellite and Sun photometer measurements. *J. Atmos. Sci.* **59**, 461–483, 10.1175/1520-0469(2002)059<0461:Taotft>2.0.Co;2 (2002).
64. Buchard, V. *et al.* The MERRA-2 Aerosol Reanalysis, 1980 Onward. Part II: Evaluation and Case Studies. *J. Clim.* **30**, 6851–6872, https://doi.org/10.1175/jcli-d-16-0613.1 (2017).
65. Randles, C. A. *et al.* The MERRA-2 Aerosol Reanalysis, 1980 Onward. Part I: System Description and Data Assimilation Evaluation. *J. Clim.* **30**, 6823–6850, https://doi.org/10.1175/jcli-d-16-0609.1 (2017).
66. Hinkelman, L. M. The Global Radiative Energy Budget in MERRA and MERRA-2: Evaluation with Respect to CERES EBAF Data. *J. Clim.* **32**, 1973–1994, https://doi.org/10.1175/jcli-d-18-0445.1 (2019).
67. David, F. P. & John, C. D. The National Meteorological Center's Spectral Statistical-Interpolation Analysis System. *Mon. Weather Rev.* **120**, 1747–1763, https://doi.org/10.1175/1520-0493(1992)120 (1992).

Acknowledgements

V.P.K. would like to thank the University Grants Commission, Government of India for Start-Up Grant (Ref. No. F.4-5/230-FRP/2015/BSR) and Department of Science & Technology (DST)-SERB Grant (ECR/2016/001333). Satellite (MODIS-AQUA and AURA-OMI) and reanalysis (MERRA-2) datasets used in this study are acknowledged. Authors are thankful to anonymous reviewers for their critical comments and suggestions that helped to improve the impact of the paper.

Author contributions

C.S. and V.P.K. conceived the study. A.T. and C.S. did the data analysis. A.T. and V.P.K. wrote the initial manuscript. All authors reviewed the manuscript.

Competing interests

The authors declare no competing interests.

Additional information

Supplementary information is available for this paper at https://doi.org/10.1038/s41598-019-53630-3.

Correspondence and requests for materials should be addressed to C.S. or V.P.K.

Science of the Total Environment 782 (2021) 146918

Contents lists available at ScienceDirect

Science of the Total Environment

journal homepage: www.elsevier.com/locate/scitotenv

Effect of COVID-19 shutdown on aerosol direct radiative forcing over the Indo-Gangetic Plain outflow region of the Bay of Bengal

Abin Thomas [a], Vijay P. Kanawade [a,*], Chandan Sarangi [b,c], Atul K. Srivastava [d]

[a] Centre for Earth, Ocean and Atmospheric Sciences, University of Hyderabad, India
[b] Department of Civil Engineering, Indian Institute of Technology Madras, Chennai, India
[c] Laboratory for Atmospheric and Climate Sciences, Indian Institute of Technology Madras, Chennai, India
[d] Indian Institute of Tropical Meteorology, Ministry of Earth Sciences, New Delhi, India

HIGHLIGHTS

- Direct indication of anthropogenic impact on ADRF over the IGP outflow region of the BoB
- ADRF over the BoB is higher when the winds originated from the IGP.
- COVID-19 shutdown reflected ~20–25% reduction in ADRF over the IGP outflow region.

GRAPHICAL ABSTRACT

The aerosol direct radiative forcing over the Bay of Bengal (BoB) is much higher in magnitude when the winds originate from Indo-Gangetic Plains during the pre-monsoon season (March–May) compared to the seasonal average.

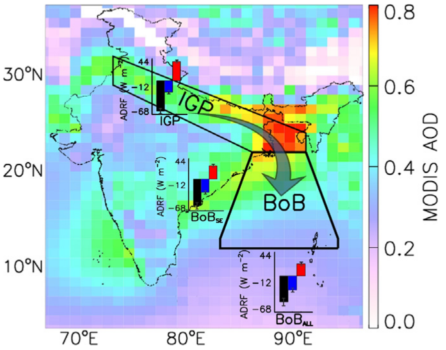

ARTICLE INFO

Article history:
Received 9 December 2020
Received in revised form 13 March 2021
Accepted 30 March 2021
Available online 6 April 2021

Editor: Philip K. Hopke

Keywords:
Continental transport, outflow
Aerosol direct radiative forcing
COVID-19
Indo-Gangetic Plains

ABSTRACT

The Indo Gangetic Plain (IGP), one of the most densely populated regions of the world, is a global hotspot of anthropogenic aerosol emissions. In the pre-monsoon season (March–May), the strong westerlies carry transported dust aerosols along with anthropogenic aerosols onto the Bay of Bengal (BoB). The outflow from IGP modulates the aerosol loading and the aerosol direct radiative forcing (ADRF) over the BoB. The quantification of the anthropogenic aerosol impact on the radiative forcing over the outflow region remains inadequate. The enforced shutdown amid the COVID-19 pandemic eased the anthropogenic activities across the country, which helped to examine the magnitude and variability of aerosol loading and subsequent changes in ADRF over IGP and the outflow region of the BoB. Wind trajectory analysis illustrates that the ADRF over the BoB is greater during the days when the winds originated from the IGP region (at the surface -54.2 ± 6.4 W m^{-2}, at the top of the atmosphere, -26.9 ± 3.4 W m^{-2} and on the atmosphere, 27.0 ± 3.1 W m^{-2}) compared to the seasonal average (-46.3 ± 7.1 W m^{-2}, -24.9 ± 4.0 W m^{-2} and 20.6 ± 3.2 W m^{-2}, respectively). This indicates that anthropogenic aerosols emission from IGP can contribute an additional 31% of the atmospheric ADRF over the IGP outflow region of the BoB. The reduced aerosol loading during the shutdown period resulted in a reduction of ADRF at the surface, at the top of the atmosphere, and on the atmosphere over the IGP outflow region of the BoB by 22.0 ± 3.1%, 20.9 ± 3.4% and 23.2 ± 3.3%, respectively. This resultant 20–25% reduction in ADRF over the IGP outflow region of BOB matches well with 10–25% reduction in aerosol optical depth (AOD) over the IGP during the shutdown period showing a robust coupling between IGP aerosol emissions and ADRF over the BoB.

---

* Corresponding author.
E-mail address: vijaykanawade03@yahoo.co.in (V.P. Kanawade).

https://doi.org/10.1016/j.scitotenv.2021.146918
0048-9697/

1. Introduction

The global net radiative forcing due to aerosols is negative (IPCC, 2013) and estimated to offset about one-third of the atmospheric warming due to greenhouse gases since the 1950s (Storelvmo et al., 2016). However, the uncertainties in the net aerosol forcing estimates remain due to the complex feedback mechanisms and spatio-temporal variability (Bellouin et al., 2020; Bender, 2020; Li et al., 2009). The South Asian region, especially the Indo-Gangetic plain (IGP) in northern India, is a global pollution hotspot due to a variety of natural and anthropogenic emissions of aerosols (Brooks et al., 2019; Dey et al., 2004; Rana et al., 2019; Singh et al., 2017; Srivastava et al., 2020; Srivastava et al., 2012a). The aerosol loading over the Indian subcontinent and surrounding marine regions has been on the rise due to anthropogenic emissions (Babu et al., 2013; Hsu et al., 2012; Krishna Moorthy et al., 2013; Kumar et al., 2018; Mehta et al., 2021; Srivastava, 2017; Thomas et al., 2019). The IGP region has been the focus in many studies due to high aerosol loading, strong seasonal variability of aerosol composition, complex mixing processes, and its outflow into the Bay of Bengal (BoB) (Nair et al., 2017; Srinivas and Sarin, 2013; Srinivas and Sarin, 2014). The pre-monsoon season (March–May) is marked by an increment in the coarse mode aerosols over north India due to mineral dust advection by the westerly winds (Beegum et al., 2008; Srivastava et al., 2014). The western IGP is more influenced by the dust, and central to eastern IGP has a dominance of anthropogenic aerosols due to coal-based power plants, vehicular emissions, agricultural burning (Gautam et al., 2011; Gogoi et al., 2020; Tobler et al., 2020).

Aerosols in this region come from a complex mixture of sources and include absorbing aerosols like black carbon (BC), brown carbon, dust, and secondary aerosol production (Srivastava et al., 2021b). The mixing of aerosol species and the complexity associated with it makes it difficult to constrain the aerosol properties, and therefore to estimate the direct radiative forcing and climate impacts of aerosols in this region (Kompalli et al., 2020; Srivastava et al., 2020; Srivastava et al., 2018; Thamban et al., 2017). The vertical distribution of aerosols during the pre-monsoon season shows two distinct aerosol layers; a surface layer where the extinction coefficient decreases with altitude and an elevated dust layer mixed with anthropogenic aerosols between 1.5 km to 5.5 km (Brooks et al., 2019; Sarangi et al., 2016; Srivastava et al., 2012b). This elevated layer is known to alter the monsoon circulation via the ‘elevated heat pump’ leading to an early onset of the monsoon (Lau and Kim, 2006; Menon et al., 2002; Nigam and Bollasina, 2010).

The westerly winds in the pre-monsoon season result in an outflow of dust and anthropogenic aerosols from IGP onto the BoB (Banerjee et al., 2019; Lelieveld et al., 2001; Moorthy et al., 2009; Ramanathan et al., 2001). The outflow from IGP influences the aerosol composition and direct radiative forcing by transporting anthropogenic aerosols as far as southern BoB with a strong north-south gradient (Nair et al., 2013a; Nair et al., 2009; Rastogi et al., 2020; Satheesh et al., 2006). Satellite vertical profiles over the BoB during the pre-monsoon has shown that dust from continental region accounts for 22% of the total aerosol extinction, but the long-term (2006–17) trend shows a decrease in dust aerosols over the BoB (Lakshmi et al., 2017). The winter outflow is dominated by BC and OC aerosols due to fossil fuel and biomass burning from IGP (Bikkina et al., 2016). This influx of aerosols is a source of nutrients over the BoB region and is known to influence the primary productivity over the region for this 4-5 month period (Nair et al., 2013b; Srinivas et al., 2015). The north-eastern BoB is found to have an aerosol-induced atmospheric heating rate as high as ~0.5 K/day during pre-monsoon season due to the influence of anthropogenic aerosols, which could affect the regional circulation (Nair et al., 2013a). The outflow is known to influence the warm clouds with low liquid water path (LWP) over the northern Indian Ocean, causing a warming effect in the region (Jose et al., 2020).

COVID-19 global pandemic has led countries around the world to enforce lockdown (shutdown of anthropogenic activities and movement of peoples) to contain the spread of the virus. The decline in traffic and industrial production has led to a decrease in emission of greenhouse gases, aerosol loading and an overall improvement of air quality in major cities around the globe (Chauhan and Singh, 2020; Muhammad et al., 2020; Singh and Chauhan, 2020). In India, the lockdown was announced in 4 different phases; phase-1: 24 March–14 April, phase-2: 15 April–3 May, phase-3: 4 May–17 May and phase-4: 18 May–31 May 2020. Phase 1 and 2 were the strictest, and the country came to an almost standstill in this period, with all services shutdown except essential transportation and services (e.g., Hospitals). The average $PM_{2.5}$ concentration dropped by about 43% in measurement sites all over India during phase1 and 2 as compared to the previous years (Sharma et al., 2020). Another study reported a drop in the average air quality index (AQI) from ~135 to ~110 in the last week of March 2020 when the lockdown initiated, and similar improvements were reported over other cities in India (Singh and Chauhan, 2020). Mahato et al. (2020) reported a reduction of ~50% in particulate matter (PM) during lockdown (24 March – 31 May) over Delhi as compared to the pre-lockdown time period (1–23 March 2020). AOD and absorption AOD showed a reduction of ~30% over the IGP during COVID-19 shutdown, with concentrations of PM_{10}, $PM_{2.5}$, NO, NO_2 and CO lower by about 58%, 47%, 76%, 68% and 58%, respectively, at Delhi (Srivastava et al., 2021a). The obvious reduction in anthropogenic emissions due to the enforced lockdown amid the COVID-19 pandemic has given unique opportunity to observe the change in ADRF at the outflow region from the IGP in the absence/reduction of anthropogenic emissions. Here, we examine the effect of the COVID-19 shutdown on the ADRF over the Indo-Gangetic Plain outflow region of the BoB during pre-monsoon season. It is to be noted that the change in meteorology and atmospheric dynamics can further complicate the behaviour of aerosols (Guttikunda et al., 2019).

2. Data and methods

2.1. MODIS

The Moderate-resolution imaging spectroradiometer sensor (MODIS) measures the reflectance from the earth's surface in 36 channels in the wavelength range of 0.41–14.4 μm (Remer et al., 2005). The sensor is onboard the EOS-AQUA satellite and crosses the equator at 13:30 local time. In this study, we have used the level-3 Dark Target and Deep Blue combined AOD of collection 6.1 at 0.55 μm with a grid resolution of 1° × 1° (Hsu et al., 2013; Levy et al., 2013; Sayer et al., 2014). Mhawish et al. (2017) evaluated the MODIS AOD against AERONET sites over the IGP and found that the combined Dark Target and Deep Blue algorithm has better accuracy than individual algorithms.

2.2. OMI

The Ozone Measuring Instrument onboard the EOS-AURA satellite has a nadir viewing spectrometer, which measures in UV–visible range (264–504 nm). The OMAERUV algorithm uses 354 and 388 nm reflectance to derive aerosol absorption optical depth (AAOD) at 388 nm (Curier et al., 2008; Torres et al., 2013; Torres et al., 2007). The AAOD at 1° × 1° resolution is available from OMAERUVd.003 product. The daily tropospheric column NO_2 at 0.25° × 0.25° resolution was used in the study. Irie et al. (2008a) describe the retrieval algorithm for the tropospheric NO_2 column, and the validation study showed a bias of 20% globally (Irie et al., 2008b). The daily AAOD and tropospheric NO_2 column are downloaded from the NASA Goddard Earth Sciences, Data and Information Services Center website (http://disc.sci.gsfc.nasa.gov).

2.3. MERRA-2

The Modern-Era Retrospective Analysis for Research and Application version 2 (MERRA-2) was released by the Global Modelling and Assimilation Office (Gelaro et al., 2017). It uses Goddard Earth Observing

System-5 (GEOS-5) atmospheric general circulation model for climate analysis (Molod et al., 2015) and is coupled with the Goddard Global Ozone Chemistry Aerosol Radiation and Transport model (GOCART). The aerosol and meteorological parameters are assimilated in conjunction after careful cloud screening and homogenization of multiple satellite AOD (MODIS, AVHRR and MISR) inputs with and ground-based (AERONET) AOD data (Buchard et al., 2017; Randles et al., 2017). The radiative fluxes data from MERRA-2 was evaluated against CERES EBAF Edition 2.8 satellite product over 2001–2015, and the MERRA-2 radiative fluxes were able to capture the global trends and variability during the period of study (Hinkelman, 2019). The AOD from 'M2I3NXGAS' product and radiation fluxes from 'M2T1NXRAD' product was used in the analysis. Both the products were temporally collocated to match with the overpass time of EOS-AQUA satellite. The data at a grid resolution of 1° × 1° was downloaded from NASA Goddard Earth Sciences (GES) Data and Information Services Center (DISC) https://disc.gsfc.nasa.gov/.

The clear-sky aerosol direct radiative forcing (ADRF) is calculated from the radiative fluxes (shortwave and longwave) by taking the difference between the fluxes in clear-sky conditions with aerosols and without aerosol. The hourly variables; SWGNTCLR (surface net downward shortwave flux assuming clear-sky), SWGNTCLRCLN (surface net downward shortwave flux assuming clear-sky and no aerosol), LWGNTCLR (surface net downward longwave flux assuming clear sky) and LWGNTCLRCLN (surface net downward longwave flux assuming clear-sky and no aerosol) are used to calculate ADRF at the surface ($ADRF_{SURF}$). Concurrently, ADRF at the top of the atmosphere ($ADRF_{TOA}$) is calculated from hourly variables, SWTNTCLR (TOA net downward shortwave flux assuming clear sky), SWTNTCLRCLN (TOA net downward shortwave flux assuming clear-sky and no aerosol), LWTUPCLR (upwelling longwave flux at TOA assuming clear-sky) and LWTUPCLRCLN (upwelling longwave flux at TOA assuming clear-sky and no aerosol).

$$ADRF_{SUR} = (SWGNTCLR + LWGNTCLR) - (SWGNTCLRCLN + LWGNTCLRCLN)$$

$$ADRF_{TOA} = (SWTNTCLR + LWTUPCLR) - (SWTNTCLRCLN + LWTUPCLRCLN)$$

The ADRF on the atmosphere ($ADRF_{ATM}$), which indicates the energy trapped by all aerosols in the atmosphere, is calculated by taking the difference between $ADRF_{TOA}$ and $ADRF_{SURF}$.

2.4. HYSPLIT model

The Hybrid Single Particle Lagrangian Integrated Trajectory (HYSPLIT) Model is extensively used to compute air mass forward trajectories (Rolph et al., 2017; Stein et al., 2016). The PC-based version of the model developed by the NOAA air resources laboratory with Global Data assimilation system (GDAS) 1° × 1° meteorology data as the input is used in this study. The forward trajectories simulated by the model from Kolkata (22.57°N, 88.42°E) were used to identify the days in the pre-monsoon season with trajectories towards the Bay of Bengal. The trajectories were calculated at 00 h UTC (05:30 local time) and at two altitude levels 500 m and 1500 m above the ground. The model was also run from Kanpur (26.28°N, 80.21°E) to establish the general flow of the air mass through IGP in this season (Fig. S1).

2.5. Data analysis

The satellite retrievals are used in conjunction with the reanalysis data products to understand the anthropogenic impact on the ADRF over the IGP and also over the BoB associated with the outflow from IGP. The five-year average (2015–19) during the pre-monsoon season (March to May) is compared with the days when trajectories are towards southeast from Kolkata flowing into the BoB and the days when trajectories are flowing in other directions. The region of interest is marked in Fig. 1a as IGP and BoB based on the airmass trajectory flow as shown in Fig. 2.

3. Results and discussions

3.1. Average aerosol conditions during pre-monsoon

Fig. 1 shows the five-year (2015–2019) averaged MODIS AOD, MERRA-2 AOD, OMI AAOD, and OMI retrieved tropospheric NO_2 column for the pre-monsoon (March–May) season. AOD, as observed by MODIS AQUA (Fig. 1a) and the MERRA-2 AOD (Fig. 1b) compared well and were the highest across the IGP, mainly in the eastern part. The OMI AAOD was also showed high values over IGP and northern BoB (Fig. 1c). The tropospheric NO_2 column shows elevated anthropogenic emission sources over IGP (Fig. 1d). The pre-monsoon season has the highest AOD over IGP due to local emissions and dust transport from north-westerly winds. The eastern IGP is influenced more by anthropogenic aerosols (Gogoi et al., 2020), which was substantiated by the high column NO_2 concentration. Even with the rise in population and industrialization, the trend of total aerosol loading during the pre-monsoon season was found to be insignificant over the IGP region due to the dust influx (Babu et al., 2013). The dust influx over the IGP is known to overshadow the diurnal pattern of local anthropogenic aerosol emissions during the pre-monsoon season and increases the aerosol loading by about 50% (Dey et al., 2004). But a recent study shows that the dust influx over the IGP region during the pre-monsoon has reduced by 10–20% in recent years (Pandey et al., 2017).

The pre-monsoon season is the time of reversal of wind direction from winter to summer. The wind is predominantly westerly over the Indian landmass, and the wind speed increases from March to May as the season progresses (Beegum et al., 2008; Satheesh, 2002). Over BoB, this period is marked by an increase in cyclone frequency and moisture in the mid-troposphere (Balaguru et al., 2016; Li et al., 2013), a precursor condition to the onset of monsoon. The wind flow across the Indian Ocean is zonal during this transition period and carries pollution from India's east coast onto the BoB (Niranjan et al., 2007; Satheesh et al., 2010).

In order to analyze the aerosol loading over BoB due to transport from IGP, the HYSPLIT forward trajectories originating from Kolkata at the eastern IGP and Kanpur at the central IGP are calculated (Fig. S1). More than 90% of forward trajectories from both locations are flowing towards the east. The days when the wind flow from Kolkata is directly onto the BoB are identified and are used in further analysis to determine the transport of aerosols into the BoB. The model run at two altitudes from Kolkata is considered in the study as it is located towards the eastern side of IGP (Fig. S1a and S1b). Two different origin heights (500 m and 1500 m) are taken into account to take into account both the surface aerosol layer and the elevated aerosol layer (if any) during the pre-monsoon over IGP (Brooks et al., 2019; Sarangi et al., 2016). Over the IGP, the lower layers of the atmosphere (<1.5 km) have a higher concentration of absorbing aerosol species, and the elevated layer is dominated by dust and other scattering aerosols in the pre-monsoon season (Brooks et al., 2019). The southeastward trajectories that flow directly into the BoB account for ~16% of the trajectories that originate from Kolkata during this period at 500 m, and most of them flow through BoB at an altitude below 2 km (Fig. 2). A similar pattern was also seen for the air mass initiating at 1500 m (Fig. S1). The majority of these southeastward trajectories flow over the eastern side of the BoB, influencing the aerosol loading over the region (Fig. 2).

The days when the trajectories from Kolkata are flowing directly into the BoB are grouped as BoB_{SE} for both 500 m and 1500 m model origin heights. Fig. 2b shows the mean ADRF at the surface, top of the atmosphere, and in the atmosphere over IGP, BoB, and for the days when the trajectories from IGP are onto the BoB region (IGP_{ALL}, BoB_{ALL} and BoB_{SE}). The five-year average of pre-monsoon ADRF derived from the MERRA-2 dataset over IGP is -56.2 ± 5.8 W m^{-2}, -20.1 ± 3.7 W m^{-2}

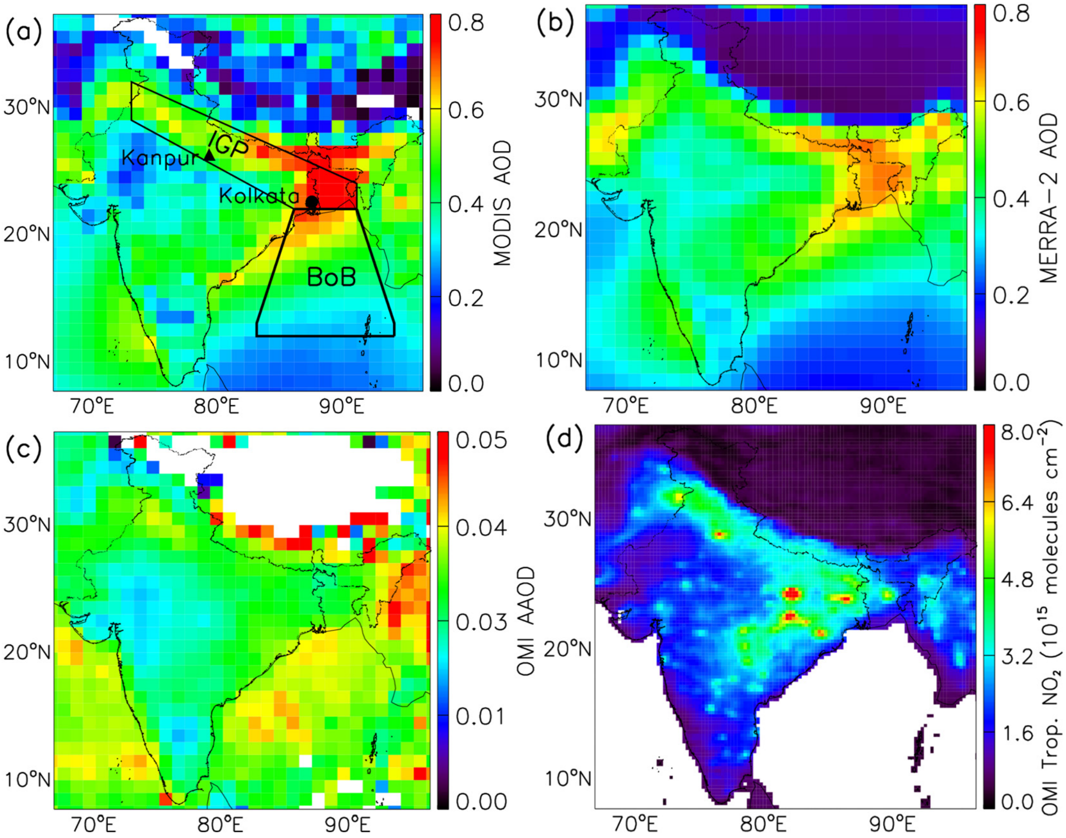

Fig. 1. Averaged (a) MODIS AOD, (b) MERRA-2 AOD, (c) OMI AAOD and (d) OMI tropospheric NO_2 column for the pre-monsoon season (March through May) of 2015–19. The solid triangle and circle symbols indicate the city of Kanpur and Kolkata.

and 35.9 ± 2.9 W m^{-2}, respectively at the surface, top of the atmosphere and in the atmosphere. ADRF corresponding to BoB_{SE} (−54.2 ± 6.4 W m^{-2}, −26.9 ± 3.4 W m^{-2} and 27.0 ± 3.1 W m^{-2}) has the higher magnitude when compared to BoB_{ALL} case (−46.3 ± 7.1 W m^{-2}, −24.9 ± 4.0 Wm^{-2} and 20.6 ± 3.2 W m^{-2}). The difference in the ADRF between BoB_{ALL} and BoB_{SE} (Fig. S2) is more prominent in atmospheric forcing (−27.6 ± 6.8%) than the surface (−14.8 ± 5.2%) or at the top of the atmosphere (−5.7 ± 4.6%). The presence of absorbing aerosols in the lower level transport from IGP is evident from the difference in the atmospheric forcing.

Satheesh (2002) reported a net surface ADRF of −27 W m^{-2} and TOA forcing of −4 W m^{-2} from shipborne observations over the BoB during March 2001. Similarly, the average ADRF over the BoB during the pre-monsoon season of 2006 was observed to be −22.4 W m^{-2}, −12.0 W m^{-2}, and 10.4 W m^{-2}at the surface, top of the atmosphere, and in the atmosphere, respectively (Kedia et al., 2010). Our estimates of the mean ADRF based on the time period of 2015–19 indicates that ADRF over the BoB has doubled in the recent past decade (BoB_{ALL}: −46.3 ± 7.1 W m^{-2}, −24.9 ± 4.0 Wm^{-2}, and 20.6 ± 3.2 W m^{-2}, at the surface, top of the atmosphere, and in the atmosphere, respectively) as compared to the previous study by Kedia et al. (2010).

3.2. COVID-19 shutdown: cleaner atmospheric scenario

The decrease in the aerosol loading and GHGs due to the COVID-19 lockdown has been reported widely around the globe (Chauhan and

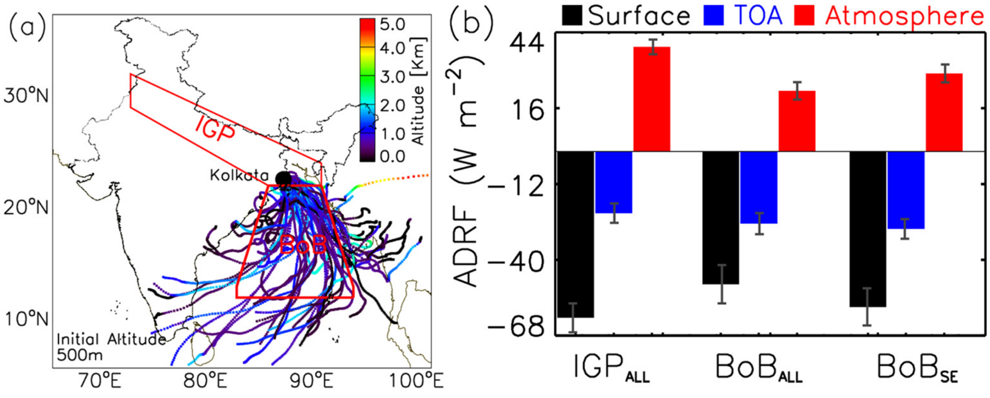

Fig. 2. (a) Five-day forward southeastward trajectories from Kolkata during the pre-monsoon season of 2015–19 with the model start height 500 m above the ground level. The colorbar indicates the altitude of the trajectory. (b) Mean ADRF at the surface, top of the atmosphere and in the atmosphere over IGP and the BoB during pre-monsoon of 2015–2019 and ADRF over the BoB when the southeastward forward trajectories from Kolkata are flowing onto the BoB. (For interpretation of the references to color in this figure legend, the reader is referred to the web version of this article.)

Singh, 2020; Muhammad et al., 2020). The satellite and reanalysis datasets in this study have also shown similar reductions over the Indian region (Fig. 3). The difference is calculated for the pre-monsoon season of 2020 over India against the five-year (2015–19) average of the same time period. In Fig. 3a, MODIS AOD showed a decrease of 17.9 ± 8.5% and 19.1 ± 6.6% over the IGP and BoB, respectively. A slight increment in AOD is observed over central west India can be attributed to the frequent dust storms and transport from the Thar desert (Badarinath et al., 2007; Sikka, 1997) due to the prevailing wind conditions. The reduction in anthropogenic aerosol loading during the lockdown is captured well by the MERRA- 2 reanalysis data products, which are evident from the reduction in total AOD (Fig. 3b). The reduction over IGP is much prominent for OMI - AAOD (35.8 ± 11.3%), showing a significant reduction of absorbing aerosols over the region (Fig. 3c). The OMI tropospheric NO_2 also had a reduction of 8.7 ± 10.2% over the IGP, underlying the reduction in anthropogenic emissions during this period. The cleaner atmospheric condition in the pre-monsoon of 2020 is clearly due to the decrease in emissions that came as a result of the COVID-19 lockdown.

Babu et al. (2008) has shown the existence of BC aerosol layer over northern BoB at an altitude of 2000 m due to transport from the Indian subcontinent. The maximum AOD and BC mass fraction over northern BoB is observed during April–May, and the variation has been matched with that of the East Coast of India (Satheesh et al., 2006). Thus, the reduction in aerosol loading over northern BoB in the present case is also associated with that of the IGP, with reduced emission sources due to COVID-19 shutdown.

The reduction in anthropogenic aerosol loading has led to a decrease in ADRF, as seen in Fig. 4. The reduction in ADRF in the pre-monsoon of 2020 over IGP compared to the average of the previous five years was 17.4 ± 4.9%, 17.2 ± 4.8% and 17.4 ± 5.5% at the surface, TOA and in the atmosphere, respectively. In BoB_{ALL}, this reduction was seen as 19.7 ± 5.3%, 20.9 ± 5.6% and 18.3 ± 5.5% and during BoB_{SE}, it was 22.0 ± 3.1%, 20.9 ± 3.4% and 23.2 ± 3.3%. The reduction in the atmospheric ADRF (~20–25%) during BoB_{SE} is much greater than BoB_{ALL}, highlighting the influence of absorbing aerosol transport from IGP. This 20–25% reduction in the atmospheric forcing due to aerosols in BoB_{SE} matches with the ~10–25% reduction in total AOD and ~24–45% reduction in AAOD over IGP due to the lockdown. This clearly indicates the robust relation of the ADRF over the BoB with the anthropogenic emissions from IGP. The reduction in ADRF over the IGP (~17%) is lower compared to the BoB_{SE} due to the pre-monsoon dust influx over the region, which possibly diluted the overall reduction in aerosol loading (Fig. S3).

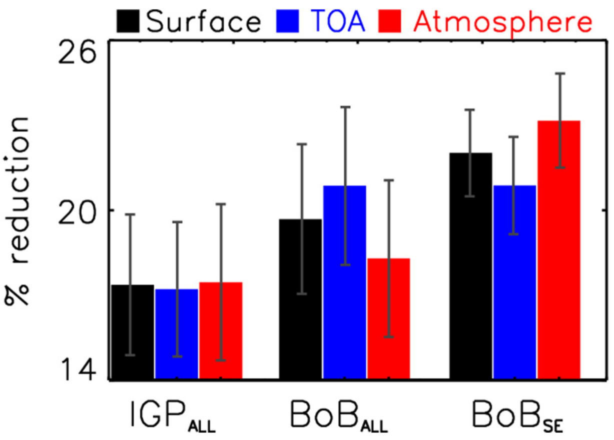

Fig. 4. Percentage difference in the mean ADRF at the surface, top of the atmosphere and in the atmosphere for the pre-monsoon season between 2020 and the five-year average (2015–2019) over Indo-Gangetic Plain and Bay of Bengal. BoB_{SE} indicates the days when Southeast forward trajectories from Kolkata reaching onto BoB.

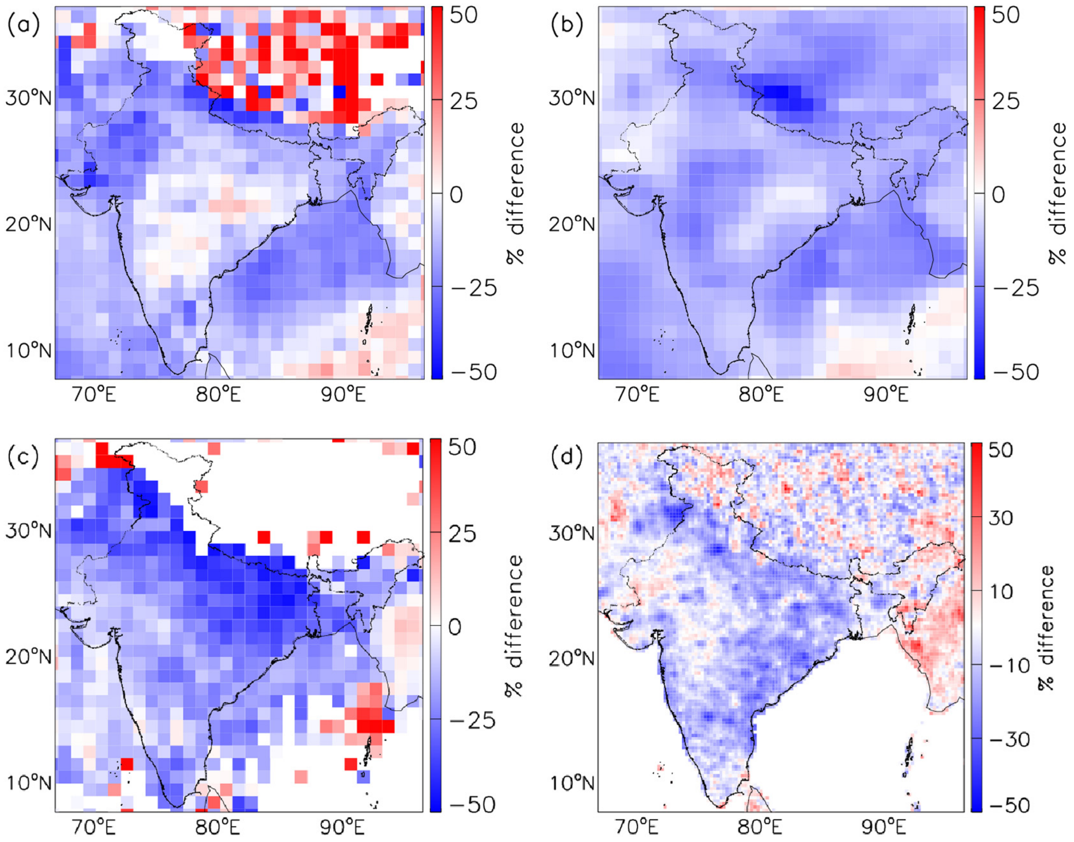

Fig. 3. Percentage difference in (a) MODIS AOD, (b) MERRA-2 AOD, (c) OMI AAOD and (d) OMI tropospheric column NO_2 for the pre-monsoon season between 2020 and five-year average (2015–19).

4. Conclusions

The high aerosol loading over IGP during the pre-monsoon season influences the aerosol composition and thus the ADRF over the BoB due to the prevailing wind pattern. The ADRF calculated from MERRA-2 radiation fluxes over the IGP showed an average value of -56.2 ± 5.8 W m^{-2}, -20.1 ± 3.7 W m^{-2} and 35.9 ± 2.9 W m^{-2}, respectively at the surface, top of the atmosphere and in the atmosphere. The ADRF is high over BoB during the days when the wind trajectories are from the IGP region (-54.2 ± 6.4 W m^{-2}, -26.9 ± 3.4 W m^{-2} and 27.0 ± 3.1 W m^{-2}) compared to the seasonal average (-46.3 ± 7.1 W m^{-2}, -24.9 ± 4.0 Wm^{-2} and 20.6 ± 3.2 W m^{-2}). This shows the influence over aerosol transport from IGP on the ADRF over BoB. The COVID -19 pandemic and the lockdown that followed in order to mitigate the spread of the virus was an unprecedented scenario. The industrial and transportation sectors, which were a significant contributor to the emissions in the polluted IGP, came to an almost halt. This has helped in analyzing the impact of anthropogenic aerosol forcing during the pre-monsoon season, which has a complex aerosol composition due to the mixing of transported natural dust aerosols and local anthropogenic aerosols. Our analysis showed a reduction of ~10–25% in AOD and 24–45% in AAOD over the IGP region. This leads to 20–25% reduction in ADRF over the IGP outflow region of the BOB, and this reduction in ADRF over the BoB is higher when the winds are originating from IGP. The ADRF at the top of the atmosphere, at the surface and on the atmosphere over the BoB reduced by $22.0 \pm 3.1\%$, $20.9 \pm 3.4\%$ and $23.2 \pm 3.3\%$, respectively. This implies the robustness of the relation of ADRF over the BoB to the emissions from IGP during the pre-monsoon season. The ADRF change over the BoB can alter the meridional circulation through thermodynamic feedbacks in the atmosphere. The changes in cloud properties and the storms due to the reduced aerosol loading could have a much stronger alteration in the forcing over this region. Our findings warrant more detailed observational and modelling studies to quantify this association as the variability in ADRF over the BoB could influence the monsoon circulation and cyclone genesis by perturbing the land-sea thermal gradients.

CRediT authorship contribution statement

Abin Thomas: Methodology, Formal analysis, Software, Visualization, Validation, Writing – original draft, Writing – review & editing. **Vijay P. Kanawade:** Conceptualization, Methodology, Formal analysis, Writing – review & editing, Supervision. **Chandan Sarangi:** Methodology, Resources, Investigation, Writing – review & editing. **Atul K. Srivastava:** Resources, Investigation, Writing – review & editing.

Declaration of competing interest

The authors declare that they have no known competing financial interests or personal relationships that could have appeared to influence the work reported in this paper.

Acknowledgments and data availability

VPK would like to thank University Grants Commission, Government of India, for UGC Start-Up Grant [Ref. No. F.4-5(230-FRP/2015/BSR)]. AT was supported by University Grants Commission Junior Research Fellowship. CS is supported by the New Faculty Initiation Grant project number CE/20-21/065/NFIG/008961 from Indian Institute of Technology Madras. The authors acknowledge Director, Indian Institute of Tropical Meteorology, Ministry of Earth Sciences, India. The authors acknowledge the use of publicly available data from the NASA Goddard Earth Sciences (GES) Data and Information Services Center (DISC).

MODIS cloud level 3 collection 6.1 is publicly available from LAADS DAAC at https://ladsweb.modaps.eosdis.nasa.gov/missions-and-measurements/science-domain/cloud.

MERRA-2 and OMI data is available at MDISC https://disc.gsfc.nasa.gov/.

Appendix A. Supplementary data

Supplementary data to this article can be found online at https://doi.org/10.1016/j.scitotenv.2021.146918.

References

Babu, S.S., Satheesh, S.K., Moorthy, K.K., Dutt, C.B.S., Nair, V.S., Alappattu, D.P., et al., 2008. Aircraft measurements of aerosol black carbon from a coastal location in the north-east part of peninsular India during ICARB. J. Earth Syst. Sci. 117, 263–271. https://doi.org/10.1007/s12040-008-0030-1.

Babu, S.S., Manoj, M.R., Moorthy, K.K., Gogoi, M.M., Nair, V.S., Kompalli, S.K., et al., 2013. Trends in aerosol optical depth over Indian region: potential causes and impact indicators. J. Geophys. Res. - Atmos. 118, 11,794–11,806. doi:https://doi.org/10.1002/2013jd020507.

Badarinath, K.V.S., Kharol, S.K., Kaskaoutis, D.G., Kambezidis, H.D., 2007. Case study of a dust storm over Hyderabad area, India: its impact on solar radiation using satellite data and ground measurements. Sci. Total Environ. 384, 316–332. https://doi.org/10.1016/j.scitotenv.2007.05.031.

Balaguru, K., Leung, L.R., Lu, J., Foltz, G.R., 2016. A meridional dipole in premonsoon Bay of Bengal tropical cyclone activity induced by ENSO. J. Geophys. Res. - Atmos. 121, 6954–6968. https://doi.org/10.1002/2016jd024936.

Banerjee, P., Satheesh, S.K., Moorthy, K.K., Nanjundiah, R.S., Nair, V.S., 2019. Long-range transport of mineral dust to the Northeast Indian Ocean: regional versus remote sources and the implications. J. Clim. 32, 1525–1549. https://doi.org/10.1175/JCLI-D-18-0403.1.

Beegum, S.N., Moorthy, K.K., Nair, V.S., Babu, S.S., Satheesh, S.K., Vinoj, V., et al., 2008. Characteristics of spectral aerosol optical depths over India during ICARB. J. Earth Syst. Sci. 117, 303–313. https://doi.org/10.1007/s12040-008-0033-y.

Bellouin, N., Quaas, J., Gryspeerdt, E., Kinne, S., Stier, P., Watson-Parris, D., et al., 2020. Bounding global aerosol radiative forcing of climate change. 58, e2019RG000660. Rev. Geophys. doi:https://doi.org/10.1029/2019RG000660.

Bender, F. A-M., 2020. Aerosol forcing: still uncertain, still relevant. AGU Advances. 1, e2019AV000128. doi:https://doi.org/10.1029/2019av000128.

Bikkina, S., Kawamura, K., Sarin, M., 2016. Stable carbon and nitrogen isotopic composition of fine mode aerosols (PM2.5) over the Bay of Bengal: impact of continental sources. Tellus Ser. B Chem. Phys. Meteorol. 68, 31518. https://doi.org/10.3402/tellusb.v68.31518.

Brooks, J., Allan, J.D., Williams, P.I., Liu, D., Fox, C., Haywood, J., et al., 2019. Vertical and horizontal distribution of submicron aerosol chemical composition and physical characteristics across northern India during pre-monsoon and monsoon seasons. Atmos. Chem. Phys. 19, 5615–5634. https://doi.org/10.5194/acp-19-5615-2019.

Buchard, V., Randles, C.A., da Silva, A.M., Darmenov, A., Colarco, P.R., Govindaraju, R., et al., 2017. The MERRA-2 aerosol reanalysis, 1980 onward. Part II: evaluation and case studies. J. Clim. 30, 6851–6872. https://doi.org/10.1175/JCLI-D-16-0613.1.

Chauhan, A., Singh, R.P., 2020. Decline in PM2.5 concentrations over major cities around the world associated with COVID-19. Environ. Res. 187, 109634. https://doi.org/10.1016/j.envres.2020.109634.

Curier, R.L., Veefkind, J.P., Braak, R., Veihelmann, B., Torres, O., de Leeuw, G., 2008. Retrieval of aerosol optical properties from OMI radiances using a multiwavelength algorithm: application to western Europe. J. Geophys. Res. – Atmos. 113. doi:https://doi.org/10.1029/2007jd008738.

Dey, S., Tripathi, S.N., Singh, R.P., Holben, B.N., 2004. Influence of dust storms on the aerosol optical properties over the Indo-Gangetic basin. J. Geophys. Res. – Atmos. 109. doi:https://doi.org/10.1029/2004jd004924.

Gautam, R., Hsu, N.C., Tsay, S.C., Lau, K.M., Holben, B., Bell, S., et al., 2011. Accumulation of aerosols over the Indo-Gangetic plains and southern slopes of the Himalayas: distribution, properties and radiative effects during the 2009 pre-monsoon season. Atmos. Chem. Phys. 11, 12841–12863. https://doi.org/10.5194/acp-11-12841-2011.

Gelaro, R., McCarty, W., Suárez, M.J., Todling, R., Molod, A., Takacs, L., et al., 2017. The Modern-Era Retrospective Analysis for Research and Applications, Version 2 (MERRA-2). J. Clim. 30, 5419–5454. doi:https://doi.org/10.1175/JCLI-D-16-0758.1.

Gogoi, M.M., Jayachandran, V.N., Vaishya, A., Babu, S.N.S., Satheesh, S.K., Moorthy, K.K., 2020. Airborne in situ measurements of aerosol size distributions and black carbon across the Indo-Gangetic Plain during SWAAMI–RAWEX. Atmos. Chem. Phys. 20, 8593–8610. https://doi.org/10.5194/acp-20-8593-2020.

Guttikunda, S.K., Nishadh, K.A., Jawahar, P., 2019. Air pollution knowledge assessments (APnA) for 20 Indian cities. Urban Clim. 27, 124–141. https://doi.org/10.1016/j.uclim.2018.11.005.

Hinkelman, L.M., 2019. The global radiative energy budget in MERRA and MERRA-2: evaluation with respect to CERES EBAF data. J. Clim. 32, 1973–1994. https://doi.org/10.1175/JCLI-D-18-0445.1.

Hsu, N.C., Gautam, R., Sayer, A.M., Bettenhausen, C., Li, C., Jeong, M.J., et al., 2012. Global and regional trends of aerosol optical depth over land and ocean using SeaWiFS measurements from 1997 to 2010. Atmos. Chem. Phys. 12, 8037–8053. https://doi.org/10.5194/acp-12-8037-2012.

Hsu, N.C., Jeong, M.-J., Bettenhausen, C., Sayer, A.M., Hansell, R., Seftor, C.S., et al., 2013. Enhanced Deep Blue aerosol retrieval algorithm: the second generation. J. Geophys. Res. - Atmos. 118, 9296–9315. https://doi.org/10.1002/jgrd.50712.

IPCC, 2013. Climate Change 2013: The Physical Science Basis. Contribution of Working Group I to the Fifth Assessment Report of the Intergovernmental Panel on Climate Change. Cambridge University Press, Cambridge, United Kingdom and New York, NY, USA.

Irie, H., Kanaya, Y., Akimoto, H., Iwabuchi, H., Shimizu, A., Aoki, K., 2008a. First retrieval of tropospheric aerosol profiles using MAX-DOAS and comparison with lidar and sky radiometer measurements. Atmos. Chem. Phys. 8, 341–350. https://doi.org/10.5194/acp-8-341-2008.

Irie, H., Kanaya, Y., Akimoto, H., Tanimoto, H., Wang, Z., Gleason, J.F., et al., 2008b. Validation of OMI tropospheric NO2 column data using MAX-DOAS measurements deep inside the North China Plain in June 2006: Mount Tai Experiment 2006. Atmos. Chem. Phys. 8, 6577–6586. https://doi.org/10.5194/acp-8-6577-2008.

Jose, S., Nair, V.S., Babu, S.S., 2020. Anthropogenic emissions from South Asia reverses the aerosol indirect effect over the northern Indian Ocean. Sci. Rep. 10, 18360. https://doi.org/10.1038/s41598-020-74897-x.

Kedia, S., Ramachandran, S., Kumar, A., Sarin, M.M., 2010. Spatiotemporal gradients in aerosol radiative forcing and heating rate over Bay of Bengal and Arabian Sea derived on the basis of optical, physical, and chemical properties. J. Geophys. Res. – Atmos. 115. doi:https://doi.org/10.1029/2009JD013136.

Kompalli, S.K., Suresh Babu, S.N., Satheesh, S.K., Krishna Moorthy, K., Das, T., Boopathy, R., et al., 2020. Seasonal contrast in size distributions and mixing state of black carbon and its association with PM1.0 chemical composition from the eastern coast of India. Atmos. Chem. Phys. 20, 3965–3985. https://doi.org/10.5194/acp-20-3965-2020.

Kumar, M., Parmar, K.S., Kumar, D.B., Mhawish, A., Broday, D.M., Mall, R.K., et al., 2018. Long-term aerosol climatology over Indo-Gangetic Plain: trend, prediction and potential source fields. Atmos. Environ. 180, 37–50. https://doi.org/10.1016/j.atmosenv.2018.02.027.

Lakshmi, N.B., Nair, V.S., Suresh Babu, S., 2017. Vertical structure of aerosols and mineral dust over the Bay of Bengal from multisatellite observations. J. Geophys. Res. - Atmos. 122, 12,845–12,861. https://doi.org/10.1002/2017JD027643.

Lau, K.-M., Kim, K.-M., 2006. Observational relationships between aerosol and Asian monsoon rainfall, and circulation. Geophys. Res. Lett. 33. https://doi.org/10.1029/2006gl027546.

Lelieveld, J., Crutzen, P.J., Ramanathan, V., Andreae, M.O., Brenninkmeijer, C.A.M., Campos, T., et al., 2001. The Indian Ocean Experiment: widespread air pollution from south and southeast Asia. Science. 291, 1031–1036. https://doi.org/10.1126/science.1057103.

Levy, R.C., Mattoo, S., Munchak, L.A., Remer, L.A., Sayer, A.M., Patadia, F., et al., 2013. The Collection 6 MODIS aerosol products over land and ocean. Atmos. Meas. Tech. 6, 2989–3034. https://doi.org/10.5194/amt-6-2989-2013.

Li, Z., Zhao, X., Kahn, R., Mishchenko, M., Remer, L., Lee, K.H., et al., 2009. Uncertainties in satellite remote sensing of aerosols and impact on monitoring its long-term trend: a review and perspective. Ann. Geophys. 27, 2755–2770. https://doi.org/10.5194/angeo-27-2755-2009.

Li, Z., Yu, W., Li, T., Murty, V.S.N., Tangang, F., 2013. Bimodal character of cyclone climatology in the Bay of Bengal modulated by monsoon seasonal cycle. J. Clim. 26, 1033–1046. https://doi.org/10.1175/JCLI-D-11-00627.1.

Mahato, S., Pal, S., Ghosh, K.G., 2020. Effect of lockdown amid COVID-19 pandemic on air quality of the megacity Delhi, India. Sci. Total Environ. 730, 139086. https://doi.org/10.1016/j.scitotenv.2020.139086.

Mehta, M., Khushboo, R., Raj, R., Singh, N., 2021. Spaceborne observations of aerosol vertical distribution over Indian mainland (2009–2018). Atmos. Environ. 244, 117902. https://doi.org/10.1016/j.atmosenv.2020.117902.

Menon, S., Hansen, J., Nazarenko, L., Luo, Y., 2002. Climate effects of black carbon aerosols in China and India. Science. 297, 2250–2253. https://doi.org/10.1126/science.1075159.

Mhawish, A., Banerjee, T., Broday, D.M., Misra, A., Tripathi, S.N., 2017. Evaluation of MODIS Collection 6 aerosol retrieval algorithms over Indo-Gangetic Plain: implications of aerosols types and mass loading. Remote Sens. Environ. 201, 297–313. https://doi.org/10.1016/j.rse.2017.09.016.

Molod, A., Takacs, L., Suarez, M., Bacmeister, J., 2015. Development of the GEOS-5 atmospheric general circulation model: evolution from MERRA to MERRA2. Geosci. Model Dev. 8, 1339–1356. https://doi.org/10.5194/gmd-8-1339-2015.

Moorthy, K.K., Nair, V.S., Babu, S.S., Satheesh, S.K., 2009. Spatial and vertical heterogeneities in aerosol properties over oceanic regions around India: implications for radiative forcing. Q. J. R. Meteorol. Soc. 135, 2131–2145. https://doi.org/10.1002/qj.525.

Moorthy, K.K., Babu, S.S., Manoj, M.R., Satheesh, S.K., 2013. Buildup of aerosols over the Indian Region. Geophys. Res. Lett. 40, 1011–1014. https://doi.org/10.1002/grl.50165.

Muhammad, S., Long, X., Salman, M., 2020. COVID-19 pandemic and environmental pollution: a blessing in disguise? Sci. Total Environ. 728, 138820. https://doi.org/10.1016/j.scitotenv.2020.138820.

Nair, V.S., Moorthy, K.K., Babu, S.S., Satheesh, S.K., 2009. Optical and physical properties of atmospheric aerosols over the Bay of Bengal during ICARB. J. Atmos. Sci. 66, 2640–2658. https://doi.org/10.1175/2009JAS3032.1.

Nair, V.S., Babu, S.S., Moorthy, K.K., Prijith, S.S., 2013a. Spatial gradients in aerosol-induced atmospheric heating and surface dimming over the oceanic regions around India: anthropogenic or natural? J. Clim. 26, 7611–7621. https://doi.org/10.1175/JCLI-D-12-00616.1.

Nair, V.S., Moorthy, K.K., Babu, S.S., 2013b. Influence of continental outflow and ocean biogeochemistry on the distribution of fine and ultrafine particles in the marine atmospheric boundary layer over Arabian Sea and Bay of Bengal. J. Geophys. Res. - Atmos. 118, 7321–7331. https://doi.org/10.1002/jgrd.50541.

Nair, V.S., Babu, S.S., Manoj, M.R., Moorthy, K.K., Chin, M., 2017. Direct radiative effects of aerosols over South Asia from observations and modeling. Clim. Dyn. 49, 1411–1428. https://doi.org/10.1007/s00382-016-3384-0.

Nigam, S., Bollasina, M., 2010. “Elevated heat pump” hypothesis for the aerosol-monsoon hydroclimate link: “Grounded” in observations? J. Geophys. Res. Atmos. 115. https://doi.org/10.1029/2009jd013800.

Niranjan, K., Madhavan, B.L., Sreekanth, V., 2007. Micro pulse lidar observation of high altitude aerosol layers at Visakhapatnam located on the east coast of India. Geophys. Res. Lett. 34. https://doi.org/10.1029/2006gl028199.

Pandey, S.K., Vinoj, V., Landu, K., Babu, S.S., 2017. Declining pre-monsoon dust loading over South Asia: signature of a changing regional climate. Sci. Rep. 7, 16062. https://doi.org/10.1038/s41598-017-16338-w.

Ramanathan, V., Crutzen, P.J., Lelieveld, J., Mitra, A.P., Althausen, D., Anderson, J., et al., 2001. Indian Ocean Experiment: an integrated analysis of the climate forcing and effects of the great Indo-Asian haze. J. Geophys. Res. - Atmos. 106, 28371–28398. https://doi.org/10.1029/2001jd900133.

Rana, A., Jia, S., Sarkar, S., 2019. Black carbon aerosol in India: a comprehensive review of current status and future prospects. Atmos. Res. 218, 207–230. https://doi.org/10.1016/j.atmosres.2018.12.002.

Randles, C.A., da Silva, A.M., Buchard, V., Colarco, P.R., Darmenov, A., Govindaraju, R., et al., 2017. The MERRA-2 aerosol reanalysis, 1980 onward. Part I: system description and data assimilation evaluation. J. Clim. 30, 6823–6850. https://doi.org/10.1175/JCLI-D-16-0609.1.

Rastogi, N., Agnihotri, R., Sawlani, R., Patel, A., Babu, S.S., Satish, R., 2020. Chemical and isotopic characteristics of PM10 over the Bay of Bengal: effects of continental outflow on a marine environment. Sci. Total Environ. 726, 138438. https://doi.org/10.1016/j.scitotenv.2020.138438.

Remer, L.A., Kaufman, Y.J., Tanré, D., Mattoo, S., Chu, D.A., Martins, J.V., et al., 2005. The MODIS aerosol algorithm, products, and validation. J. Atmos. Sci. 62, 947–973. https://doi.org/10.1175/JAS3385.1.

Rolph, G., Stein, A., Stunder, B., 2017. Real-time Environmental Applications and Display sYstem: READY. Environ. Model. Softw. 95, 210–228. https://doi.org/10.1016/j.envsoft.2017.06.025.

Sarangi, C., Tripathi, S.N., Mishra, A.K., Goel, A., Welton, E.J., 2016. Elevated aerosol layers and their radiative impact over Kanpur during monsoon onset period. J. Geophys. Res. - Atmos. 121, 7936–7957. https://doi.org/10.1002/2015jd024711.

Satheesh, S.K., 2002. Radiative forcing by aerosols over Bay of Bengal region. Geophys. Res. Lett. 29, 40-1–40-4. https://doi.org/10.1029/2002gl015334.

Satheesh, S.K., Srinivasan, J., Moorthy, K.K., 2006. Spatial and temporal heterogeneity in aerosol properties and radiative forcing over Bay of Bengal: sources and role of aerosol transport. J. Geophys. Res. Atmos. 111. https://doi.org/10.1029/2005jd006374.

Satheesh, S.K., Vinoj, V., Krishnamoorthy, K., 2010. Assessment of aerosol radiative impact over oceanic regions adjacent to Indian subcontinent using multisatellite analysis. Adv. Meteorol. 2010, 139186. doi:https://doi.org/10.1155/2010/139186.

Sayer, A.M., Munchak, L.A., Hsu, N.C., Levy, R.C., Bettenhausen, C., Jeong, M.-J., 2014. MODIS Collection 6 aerosol products: comparison between Aqua's e-Deep Blue, Dark Target, and “merged” data sets, and usage recommendations. J. Geophys. Res. Atmos 119, 13,965–13,989. https://doi.org/10.1002/2014jd022453.

Sharma, S., Zhang, M., Anshika, Gao, J., Zhang, H., Kota, S.H., 2020. Effect of restricted emissions during COVID-19 on air quality in India. Sci. Total Environ. 728, 138878. https://doi.org/10.1016/j.scitotenv.2020.138878.

Sikka, D.R., 1997. Desert climate and its dynamics. Curr. Sci. 72, 35–46.

Singh, R.P., Chauhan, A., 2020. Impact of lockdown on air quality in India during COVID-19 pandemic. Air Qual. Atmos. Health 13, 921–928. https://doi.org/10.1007/s11869-020-00863-1.

Singh, N., Mhawish, A., Deboudt, K., Singh, R.S., Banerjee, T., 2017. Organic aerosols over Indo-Gangetic Plain: sources, distributions and climatic implications. Atmos. Environ. 157, 59–74. https://doi.org/10.1016/j.atmosenv.2017.03.008.

Srinivas, B., Sarin, M.M., 2013. Light absorbing organic aerosols (brown carbon) over the tropical Indian Ocean: impact of biomass burning emissions. Environ. Res. Lett. 8, 044042. https://doi.org/10.1088/1748-9326/8/4/044042.

Srinivas, B., Sarin, M.M., 2014. Brown carbon in atmospheric outflow from the Indo-Gangetic Plain: mass absorption efficiency and temporal variability. Atmos. Environ. 89, 835–843. https://doi.org/10.1016/j.atmosenv.2014.03.030.

Srinivas, B., Sarin, M.M., Sarma, V.V.S.S., 2015. Atmospheric outflow of nutrients to the Bay of Bengal: impact of anthropogenic sources. J. Mar. Syst. 141, 34–44. https://doi.org/10.1016/j.jmarsys.2014.07.008.

Srivastava, R., 2017. Trends in aerosol optical properties over South Asia. Int. J. Climatol. 37, 371–380. https://doi.org/10.1002/joc.4710.

Srivastava, A.K., Singh, S., Tiwari, S., Bisht, D.S., 2012a. Contribution of anthropogenic aerosols in direct radiative forcing and atmospheric heating rate over Delhi in the Indo-Gangetic Basin. Environ. Sci. Pollut. Res. 19, 1144–1158. https://doi.org/10.1007/s11356-011-0633-y.

Srivastava, A.K., Singh, S., Tiwari, S., Kanawade, V.P., Bisht, D.S., 2012b. Variation between near-surface and columnar aerosol characteristics during the winter and summer at Delhi in the Indo-Gangetic Basin. J. Atmos. Sol. Terr. Phys. 77, 57–66. https://doi.org/10.1016/j.jastp.2011.11.009.

Srivastava, A.K., Soni, V.K., Singh, S., Kanawade, V.P., Singh, N., Tiwari, S., et al., 2014. An early South Asian dust storm during March 2012 and its impacts on Indian Himalayan foothills: a case study. Sci. Total Environ. 493, 526–534. https://doi.org/10.1016/j.scitotenv.2014.06.024.

Srivastava, P., Dey, S., Srivastava, A.K., Singh, S., Tiwari, S., 2018. Most probable mixing state of aerosols in Delhi NCR, northern India. Atmos. Res. 200, 88–96. https://doi.org/10.1016/j.atmosres.2017.09.018.

Srivastava, A.K., Mehrotra, B.J., Singh, A., Singh, V., Bisht, D.S., Tiwari, S., et al., 2020. Implications of different aerosol species to direct radiative forcing and atmospheric heating rate. Atmos. Environ. 241, 117820. https://doi.org/10.1016/j.atmosenv.2020.117820.

Srivastava, A.K., Bhoyar, P.D., Kanawade, V.P., Devara, P.C.S., Thomas, A., Soni, V.K., 2021a. Improved air quality during COVID-19 at an urban megacity over the Indo-Gangetic Basin: from stringent to relaxed lockdown phases. Urban Clim. 36, 100791. https://doi.org/10.1016/j.uclim.2021.100791.

Srivastava, A.K., Thomas, A., Hooda, R.K., Kanawade, V.P., Hyvärinen, A.P., Bisht, D.S., et al., 2021b. How secondary inorganic aerosols from Delhi influence aerosol optical and radiative properties at a downwind sub-urban site over Indo-Gangetic Basin? Atmos. Environ. 248, 118246. https://doi.org/10.1016/j.atmosenv.2021.118246.

Stein, A.F., Draxler, R.R., Rolph, G.D., Stunder, B.J.B., Cohen, M.D., Ngan, F., 2016. NOAA's HYSPLIT atmospheric transport and dispersion modeling system. Bull. Am. Meteorol. Soc. 96, 2059–2077. https://doi.org/10.1175/BAMS-D-14-00110.1.

Storelvmo, T., Leirvik, T., Lohmann, U., Phillips, P.C.B., Wild, M., 2016. Disentangling greenhouse warming and aerosol cooling to reveal Earth's climate sensitivity. Nat. Geosci. 9, 286–289. https://doi.org/10.1038/ngeo2670.

Thamban, N.M., Tripathi, S.N., Moosakutty, S.P., Kuntamukkala, P., Kanawade, V.P., 2017. Internally mixed black carbon in the Indo-Gangetic Plain and its effect on absorption enhancement. Atmos. Res. 197, 211–223. https://doi.org/10.1016/j.atmosres.2017.07.007.

Thomas, A., Sarangi, C., Kanawade, V.P., 2019. Recent increase in winter hazy days over Central India and the Arabian Sea. Sci. Rep. 9, 17406. https://doi.org/10.1038/s41598-019-53630-3.

Tobler, A., Bhattu, D., Canonaco, F., Lalchandani, V., Shukla, A., Thamban, N.M., et al., 2020. Chemical characterization of PM2.5 and source apportionment of organic aerosol in New Delhi, India. Sci. Total Environ. 745, 140924. https://doi.org/10.1016/j.scitotenv.2020.140924.

Torres, O., Tanskanen, A., Veihelmann, B., Ahn, C., Braak, R., Bhartia, P.K., et al., 2007. Aerosols and surface UV products from Ozone Monitoring Instrument observations: an overview. J. Geophys. Res. Atmos. 112. https://doi.org/10.1029/2007jd008809.

Torres, O., Ahn, C., Chen, Z., 2013. Improvements to the OMI near-UV aerosol algorithm using A-train CALIOP and AIRS observations. Atmos. Meas. Tech. 6, 3257–3270. https://doi.org/10.5194/amt-6-3257-2013.

Atmospheric Research 249 (2021) 105292

Contents lists available at ScienceDirect

Atmospheric Research

journal homepage: www.elsevier.com/locate/atmosres

Characterization of raindrop size distributions and its response to cloud microphysical properties

Abin Thomas[a], Vijay P. Kanawade[a,*], Kaustav Chakravarty[b], Atul K. Srivastava[b]

[a] *Centre for Earth, Ocean and Atmospheric Sciences, University of Hyderabad, Hyderabad, 500046, Telangana, India*
[b] *Indian Institute of Tropical Meteorology, Ministry of Earth Sciences, India*

ARTICLE INFO

Keywords:
Raindrop size distribution
Rain rate
Cloud microphysics
Stratiform and convective rainfall

ABSTRACT

Cloud feedbacks continue to alter with climate change, which remains the largest source of uncertainty in global climate. Raindrop size distribution (DSD) is a fundamental characteristic of cloud microphysical and dynamical processes. This study characterizes the DSD and its response to cloud microphysical properties during the Indian Summer Monsoon season (June-October 2013–2015). The derived rain rate varied from 0.50 to 395.4 mm/h, which was segregated into stratiform rain (mean and standard deviation of 2.12 ± 1.24 mm/h) and convective rain (13.10 ± 14.45 mm/h). We found that as the convective DSD mode diameter gradually shifts to a larger drop size with increasing rain rate, the number concentration of small-sized rain drops decreased by about three orders of magnitude. While the mass-weighted mean diameter and normalized DSD scaling parameter were significantly higher for convective rain than stratiform rain, the normalized DSD scaling parameter was lowest for both convective and stratiform rain compared to previous studies over this region. The stratiform DSD was more skewed towards large raindrop size at a high cloud effective radius compared to a low cloud effective radius. However, the opposite response of the DSD for convective rain suggests the predominance of small-sized cloud/ice hydrometeors. This finding was further corroborated by the presence of narrower DSD at high cloud droplet number concentration compared to a low cloud droplet number concentration for the convective rain. The low wind shear and high convective available potential energy for convective rain further substantiated the persistent convective cores during monsoon accompanied by the formation of large size raindrops in the convective systems. Such a distinct response of DSD to different rain regimes could help in the short-term prediction of extreme rainfall events.

1. Introduction

Solid or liquid minute particles formed from natural and anthropogenic processes in the atmosphere are referred to as aerosols (Kulmala et al., 2013; Zhang, 2010). A small subset of these aerosols act as cloud condensation nuclei (CCN) or ice nuclei (IN), and thereby affect cloud microphysical and rain processes (Koren and Feingold, 2011; Rosenfeld et al., 2008; Sarangi et al., 2017). The variability of cloud systems and rain in space and time is determined by changes in such a variety of microscale physical processes and mesoscale meteorological conditions (Bruintjes, 1999; Dzotsi et al., 2014; Saud et al., 2016). The raindrop size distribution (hereafter referred to as DSD) is a fundamental characteristic of rain microphysical processes. Thus, the characterization of DSD is crucial in many weather applications, including accurate rain estimation and numerical modelling of microphysical processes of rain formation (Rosenfeld and Ulbrich, 2003; Zhang et al., 2006).

The systematic analyses of DSD observations globally - in a variety of geographical locations, climate regimes, seasons, and rain types - have been the focus of the study over last more than three decades (Bringi et al., 2003; Das et al., 2017; Dolan et al., 2018; Niu et al., 2010; Rao et al., 2009; Sauvageot and Lacaux, 1995; Seela et al., 2018; Tokay and Short, 1996; Ulbrich, 1983; Wen et al., 2016). Using ground-based DSD measurements from four sites from equatorial latitude to mid-latitudes, Sauvageot and Lacaux (1995) reported larger mean geometric raindrop diameter in the equatorial latitude site (convective rain, ~1.48 mm) than in the mid-latitude site (stratiform rain, ~0.72 mm). The later studies have also highlighted the large differences in the characteristics of DSD between the stratiform and convective rain regimes (Bringi et al., 2003; Tokay and Short, 1996; Ulbrich and Atlas, 2007), owing to significant differences in terms of cloud microphysics and dynamics in the rain formation processes (Rosenfeld and Ulbrich,

---

[*] Corresponding author.
E-mail address: vijaykanawade03@yahoo.co.in (V.P. Kanawade).

https://doi.org/10.1016/j.atmosres.2020.105292
Received 27 June 2020; Received in revised form 28 August 2020; Accepted 27 September 2020

2003). The DSD can vary dramatically within a rainfall event when a convective rain is followed by stratiform rain. The stratiform rain occurs more often, but the total accumulated rainfall is higher in convective rain. In order to quantify rapidly varying DSD, the three-parameter gamma distribution is often used to characterize DSD (Ulbrich, 1983) than other functional forms, e.g., Gaussian distribution (Maguire II and Avery, 1994) and exponential distribution (Sato et al., 1990). The exponential distribution, when assumed for DSD overestimates the rain rate or radar attenuation, and the gamma distribution is found to be a more accurate approximation of the DSD (Bringi et al., 1984; Goddard and Cherry, 1984; Ulbrich, 1983) since the derived shape-slope (μ–Λ) relation from gamma distribution reflects the characteristic of actual DSD and helps in the retrieval of rain physical parameters (Zhang et al., 2003).

The inter-seasonal variation in DSD has been studied extensively for the Indian summer monsoon season (Chakravarty and Raj, 2013; Chakravarty et al., 2013; Das and Maitra, 2018; Konwar et al., 2014; Lavanya et al., 2019; Radhakrishna et al., 2016; Rao et al., 2009; Sreekanth et al., 2019; Sreekanth et al., 2017). Chakravarty et al. (2013) showed the predominance of higher-level clouds accompanied by bigger cloud drops and smaller raindrops at the surface over Kolkata (Central-eastern India) in the monsoon season. A study over Pune (Central-western India) reported the more number of large-size raindrops in the post-monsoon (October-November) season as compared to small-medium sized raindrops in the monsoon season (June-September), which was corroborated by satellite-based observations of cloud type and cloud effective radius (CER) (Chakravarty and Raj, 2013). A recent study over the windward side of the Western Ghats (Western Peninsular India), based on 7-years of DSD observations, showed that the monsoon season is accompanied by short and less intense rainfall with small-size raindrops (Sreekanth et al., 2019). The DSD parameters retrieved from dual-frequency (UHF and VHF) wind profiler measurements over Gadanki showed the large variability in vertical information of gamma parameters in the convective regime (Kirankumar et al., 2008), which was attributed to two microphysical processes: evaporation and breakup of droplets. Konwar et al. (2014) later showed the prevalence of collision-coalescence processes in stratiform clouds over the windward and leeward side of the Western Ghats.

Previous studies report variation in DSD and its parameters from a tropical site, Pune (Chakravarty and Raj, 2013; Konwar et al., 2014). But these studies compared the variation in DSD and cloud properties between monsoon and post-monsoon seasons. The cloud properties and meteorological conditions are very different between the seasons and, thus the ensuing processes in DSD. Here, we report the instantaneous response of cloud properties and meteorological conditions on the DSD by harmonizing ground-based DSD, satellite-derived cloud properties, and meteorological reanalysis data during monsoon season to highlight some insights into cloud microphysics and dynamics in the rain formation processes.

2. Methods

2.1. Measurement site

The raindrop size distribution measurements were conducted at a tropical sub-urban site, Indian Institute of Tropical Meteorology (IITM), Pune (18.53°N, 73.85°E, 560 m above mean sea level), located ~80 km away on the leeward side of the Western Ghats. The site is located in a valley surrounded by 500–800 m high mountains on three sides and about 200 km to the west of the western Indian coast (Arabian Sea) (Fig. 1). Pune is dominated by south-westerly winds that bring moisture during the monsoon season. During winter (December-February), the winds are predominantly easterly or north-easterly. The ground-based, satellite, and model reanalysis datasets pertaining to this study cover the time period from 15 June to 15 October (2013–2015), since monsoon trough reaches over this region by 15 June and 15 October during onset and withdrawal phases, respectively (Singh and Ranade, 2010). This station receives a mean annual rainfall of 722 mm (Chakravarty and Raj, 2013), and monsoon season brings in most of the rainfall in the region. The rainfall over Pune is much lesser compared to that of sites on the windward side of the Western Ghats (e.g., Mahabaleshwar ~6000 mm and Mumbai ~2167 mm). The average temperature during the monsoon is season is at 25.4 °C, with an increasing trend observed in the last century (Gadgil and Dhorde, 2005).

2.2. Joss Waldvogel disdrometer

The raindrop size distribution measurements were conducted using a Joss Waldvogel disdrometer (Joss and Waldvogel, 1967) with a sampling interval of 30 s. The impact type disdrometer has a 0.005 m^2 sensor surface that records the number of raindrops falling on it. The raindrop size distribution was recorded in a size range from 0.3 to 5.3 mm divided into 20 size channels. The rain rate (mm/h) was derived using the Eq. (1);

$$R = \frac{\pi \times 3.6}{6 \times 10^3} \times \frac{1}{F \times t} \sum_{i=1}^{n} (n_i \times D_i^3) \tag{1}$$

where i is the raindrop size bin, t is the time interval (30 s), F is the size of the sensor surface (0.005 m^2), n_i is the number of rain droplets measured in the raindrop size bin i and D_i is the size of the raindrop size bin i. The drawbacks of JW impact disdrometer has been discussed in previous studies, especially about the surrounding noises and deadtime of the instrument due to large droplets (Sauvageot and Lacaux, 1995; Tokay and Short, 1996). The samples with total raindrop count less than 10 or derived rain rate less than 0.5 mm/h were also discarded to minimize uncertainties in characterizing DSD. The 20th channel in the DSD measurement has been removed from the data due to an unrealistically high droplet count. Therefore, only 19 channels (0.3 to 4.86 mm) have been used in this analysis. To characterize a raindrop size distribution, the gamma model distribution was used (Ulbrich, 1983), given by Eq. (2);

$$N(D) = N_0 \exp(-\Lambda D) * D^{\mu} \tag{2}$$

where N(D) ($m^{-3}\ mm^{-1}$) is the number of raindrops with diameter D (mm), μ (unitless), and Λ (mm^{-1}) are shape and slope parameters, respectively. N_0 ($m^{-3}\ mm^{-1-\mu}$) is the intercept parameter. The shape parameter represents the breadth of the curve, and the positive value indicates that the curve is concave downwards. The slope parameter denotes the extension of the curve towards the broader diameter spectrum.

The gamma parameters are calculated from moments of central tendency given by the nth moment of the distribution given by Eq. (3);

$$M_n = \sum_{i=1}^{n} N(D_i) D_i^n dD_i \tag{3}$$

Then, the mass-weighted mean diameter (mm) is given as,

$$\mathrm{Dm} = \frac{M_4}{M_3} \tag{4}$$

M_3 and M_4 are third and fourth moments of central tendency calculated from Eq. (3).

$$\mu = \frac{3M_4M_2 - 4M_3^2}{M_3^2 - M_4M_2} \tag{5}$$

$$\Lambda = \frac{\mu + 4}{D_m} \tag{6}$$

The normalized DSD scaling parameter (N_w) helps in comparing the shape of two DSDs with different LWC and D_m and is given by Eq.(7);

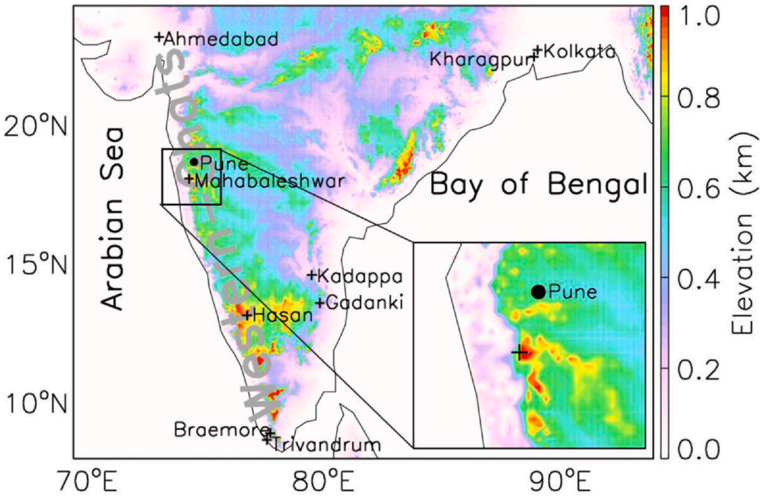

Fig. 1. Indian peninsular map showing the location of the measurement site (Pune, black dot) and other sites (plus sign) from where DSD observations have been reported from the tropical –Peninsular India in the literature. The filled contour shows the surface elevation.

$$N_W = \frac{4^4}{\pi\rho_w}\left[\frac{10^6 LWC}{D_m^4}\right] \tag{7}$$

The liquid water content (LWC in g m^{-3}) was calculated from the rain DSD data using Eq. 8.

$$LWC = \frac{\pi \times \rho_w \times 10^{-6}}{6}\sum_{i=1}^{n} D_i^3 N(D_i) dD_i \tag{8}$$

where, ρ_w is the density of water (10^3 kg m^{-3}).

2.3. MODIS L2 cloud microphysical properties

The Moderate Resolution Imaging Spectrometer (MODIS) onboard NASA's TERRA and AQUA satellites retrieved level 2 collection 6.1 cloud products, MOD06L2 and MYD06L2, respectively, were used in the analysis. The product uses infrared, visible, and near-infrared reflectances to derive the cloud properties at 1 or 5 km resolution (Baum et al., 2012; Platnick et al., 2017). The data was subsetted over a 1° × 1° longitude and latitude box, with the measurement site in the centre.

The aerosol-mediated cloud effects are largely hampered by reliable estimation of CCN production in the terrestrial atmosphere. Aerosol optical depth (AOD) is used as a proxy for aerosol concentration, but AOD is poorly related to CCN production and thereby, cloud droplet number concentrations (CDNC). In order to understand the aerosol feedback to DSD, we have derived CDNC as described by Zhu et al. (2018), based on cloud microphysical properties, using Eq. (9);

$$N_d = c^{\frac{1}{2}}\,\tau^{\frac{1}{2}}\left(\frac{r_e}{k}\right)^{\frac{-5}{2}} \tag{9}$$

where r_e is liquid cloud effective radius (CER_{liq}) and τ is liquid cloud optical depth (COT_{liq}). $c = \frac{5.A}{3.\pi.Q_{ext}}$, $A = \frac{C_w}{\frac{4}{3}.\pi.\rho_w}$ (Szczodrak et al., 2001), and $k = 1.08$ (Freud et al., 2011). Mie scattering efficiency, $Q_{ext} = 2$ and moist condensate coefficient, $C_w = 2.1 \times 10^{-11}$ are assumed as given by (Zhu et al., 2018).

MODIS cloud properties and derived CDNC were collocated with the corresponding DSD by taking an average of the DSD within a 2-h bracket of TERRA and AQUA satellites ascending overpasses during the daytime. TERRA and AQUA have ascending crossing times over India at 11:30 am local time and 1:30 pm local time, respectively. The mean DSD was calculated between 10:30 am and 2:30 pm local time to match with satellite-derived CDNC and microphysical cloud properties.

2.4. ERA5 model reanalysis

ERA5 is the 5th generation of climate reanalysis product from the European Centre for Medium-Range Weather Forecasts (ECMWF) (Dee et al., 2011; Hersbach and Dee, 2016). The meteorological fields are available at a spatial resolution of 0.25° × 0.25° longitude by latitude on 37 vertical pressure levels. The data can be freely downloaded from the climate data website; https://cds.climate.copernicus.eu/cdsapp#!/home. The ERA5 uses the Integrated Forecast System (IFS) Cycle 41r2 4D-Var assimilation system, and data is available from 1950 to present in near real-time. Wind profile and CAPE were used from ERA5 for this analysis. The wind profile was used to calculate wind shear, which is the difference in average wind speed at 700 hPa and 300 hPa. The meteorological fields were taken over a 1° × 1° longitude by latitude box, with the measurement site located in the centre and over the time period from 10:30 am to 2:30 pm local time to collocate with cloud properties retrieved from MODIS and the DSD.

2.5. Rainfall regimes and percentiles analysis

The type of rain is usually classified into convective rain and stratiform rain based on its intensity, horizontal homogeneity and different rain growth mechanisms (Anagnostou and Kummerow, 1997; Yang et al., 2013). Here, we classified the type of rain using the disdrometer derived rain rate based on the method established by Bringi et al. (2003). The method uses the standard deviation of rain rate (1.5 mm/h) as the threshold to classify into convective and stratiform rain. The rain type was identified as convective, if the DSD samples for consecutive 10 min have a mean rain rate greater than 5 mm/h and a standard deviation greater than 1.5 mm/h. The rain type was identified as the stratiform if the mean rain rate greater than 0.5 mm/h and a standard deviation of less than 1.5 mm/h. This method has been adopted in several previous studies (Chen et al., 2013; Marzano et al., 2010; Seela et al., 2018). The variation in DSD with cloud microphysical properties and meteorological conditions was studied by comparing the corresponding DSDs resulting from low and high values of the given cloud microphysical properties / meteorological conditions. Low values are those which are less than 33 percentiles and high values are greater than 66 percentiles. This analysis was performed separately for stratiform and convective rains.

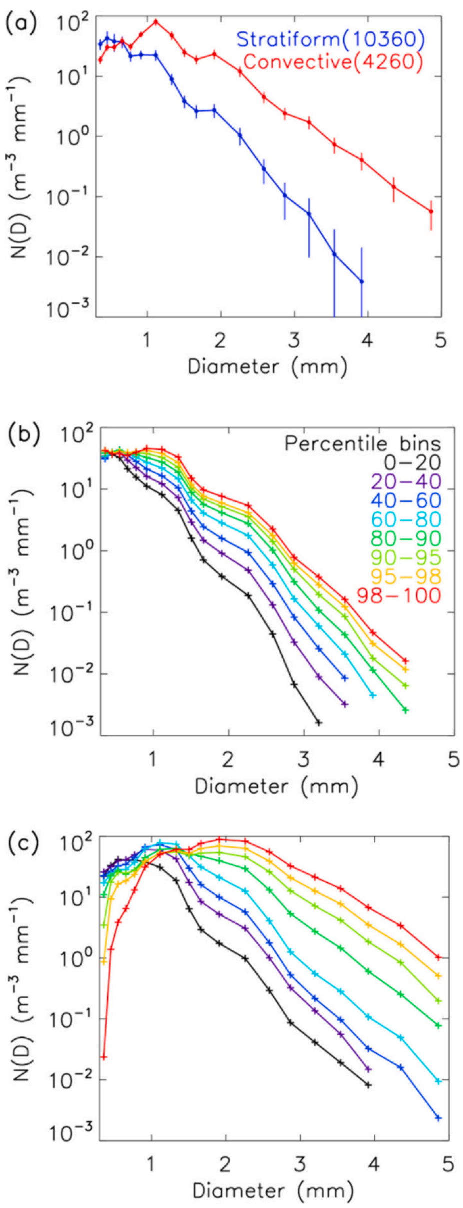

Fig. 2. (a) The averaged raindrop size distribution for stratiform and convective rain over the study period. The error bars indicate the standard deviation across each size bin. The numbers in the legend parenthesis indicate the total number of samples used to calculate mean raindrop size distribution for each rain type, (b) averaged DSD for stratiform rain for chosen rain rate classes (refer to Table 1) and (c) same as (b), but for convective rain.

3. Results

3.1. Stratiform and convective DSD

A total of 30,153 samples were considered in the analysis. The calculated rain rate varied from 0.50 to 395.41 mm/h, with a mean and standard deviation of 3.94 ± 8.62 mm/h. A total of 10,360 and 4260 samples were segregated for stratiform rain and convective rain, respectively. The stratiform rain rate varied from 0.50 to 8.51 mm/h, with a mean and standard deviation of 2.12 ± 1.24 mm/h, whereas the convective rain rate varied from 0.51 to 143.34 mm/h, with a mean and standard deviation of 13.10 ± 14.45 mm/h. Even though the convective rain rate was significantly higher, the stratiform rainfall occurred more frequently than convective (34% and 14%, respectively). The DSD varies significantly with rain rate, and its variability during the Indian summer monsoon season has been studied previously (Chakravarty and Raj, 2013; Chakravarty et al., 2013; Das and Maitra, 2018; Konwar et al., 2014; Lavanya et al., 2019; Sreekanth et al., 2019). We adopt a different approach here to characterize the DSD using percentile analysis.

Table 1
Percentile ranges considered in the analysis for stratiform and convective rain rate.

Rain rate classes	Percentiles	Stratiform rain rate (mm/h)	Convective rain rate (mm/h)
1	0–20	0.5–1.0	0.5–4.4
2	20–40	1.0–1.5	4.4–6.9
3	40–60	1.5–2.2	6.9–10.0
4	60–80	2.2–3.1	10.0–17.6
5	80–90	3.1–3.9	17.6–30.1
6	90–95	3.9–4.6	30.1–44.2
7	95–98	4.6–5.3	44.2–62.1
8	98–100	5.3–8.5	62.1–143.3

Fig. 2a shows the averaged raindrop size distribution over the study period for the stratiform and convective rains. The raindrop size distribution for stratiform and convective rain is distinctive with the mean values of Dm (stratiform: 1.35 mm and convective: 1.69 mm) and $\log_{10}N_w$ (stratiform: 2.66 m^{-3} mm^{-1} and convective: 3.01 m^{-3} mm^{-1}). This implies that the average diameter and the number concentration are higher for convective rainfall than stratiform rain.

We further characterize DSD for different percentiles bins of rain rate (hereafter referred to as rain rate classes) to illustrate its variability for stratiform and convection rain. Table 1 summarizes percentile bins considered in the analysis and corresponding stratiform and convective rain rate ranges for each rain rate class. Fig. 2b and c show the average DSD as a function of rain rate classes for stratiform rain and convective rain, respectively. Since the rain rate ranges for stratiform rain and convective rain are different, the identical rain rate bins are not feasible. The stratiform DSD shows a peak at smaller raindrop size (< 1 mm) throughout the rain rate classes, and raindrop size increases with increasing rain rate over the entire size range. The convective DSD demonstrated a shift in the mode diameter with increasing rain rate, but the number concentration of small-sized rain drops decreased significantly with increasing rain rate.

Table 2 summarizes the number of samples, mass-weighted mean diameter, rain rate, and normalized intercept parameter for rain rate classes of stratiform and convective rain. The mass-weighted mean diameter is up to 1.5 times in convective rain (2.80 mm) as compared to stratiform rain (1.74 mm) in the higher rain rate classes. The sustained increase in $\log_{10}N_w$ indicated the growing number concentration of rain droplets, with bigger droplets at higher rain rate in convective rain. Fig. 3 presents the association between rain rate classes and calculated gamma parameters from the DSD. For all rain rate classes, D_m and $\log_{10}N_w$ values remained higher for convective rain compared to stratiform rain, as the convective rain contains higher number concentrations of medium to large size raindrops (Fig. 3a and b). The convective rain shows a rapid increase in D_m from small to medium-sized droplets with the rain rate, and the changes in stratiform were much lesser. Positive values of μ for both stratiform and convective rain indicates the concave downwards shape of DSD in the monsoon season (Fig. 3c). The overall higher value of μ in convective rainfall as compared to stratiform shows that the convective DSD is more skewed towards the right side (i.e., a higher concentration of larger droplets). The smaller values of Λ in the convective regime indicate a broader DSD that extends towards the larger drop size in the spectrum (Fig. 3d). The shape and slope parameters across the rain rate classes implies a wider raindrop size spectrum for convective rain than the stratiform rain.

Fig. 4 shows the association between D_m and $\log_{10}N_w$ for stratiform

Table 2

Averaged values of mass-weighted mean diameter (D_m), rain rate (R), and normalized intercept parameter ($\log_{10}N_w$) for stratiform rain (SR) and convective rain (CR) for each rain rate class.

Rain rate class	Quartile range	Stratiform rain				Convective rain			
		# Samples	D_m (mm)	R (mm/h)	$\log_{10}N_w$ (m^{-3} mm^{-1})	# Samples	D_m (mm)	R (mm/h)	$\log_{10}N_w$ (m^{-3} mm^{-1})
1	0–20	2072	1.1	0.79	2.59	852	1.28	2.66	2.84
2	20–40	2072	1.23	1.26	2.63	852	1.47	5.63	3.00
3	40–60	2072	1.34	1.81	2.66	852	1.58	8.34	3.06
4	60–80	2072	1.47	2.60	2.68	852	1.76	13.17	3.09
5	80–90	1036	1.58	3.47	2.70	426	2.16	22.48	3.02
6	90–95	518	1.65	4.24	2.72	213	2.48	35.77	3.01
7	95–98	311	1.69	4.92	2.75	128	2.64	52.07	3.08
8	98–100	206	1.74	5.96	2.79	84	2.80	76.35	3.15

and convective rain at Pune and previous studies. The stratiform rain and convective rain clusters are distinctive in the D_m - $\log_{10}N_w$ space. Bringi et al. (2003) showed that the normalized intercept parameter ($\log_{10}N_w$) and median volume diameter for convective rainfall derived from different (D_m) disdrometers were clustered into maritime and continental rain in the $\log_{10}N_w$ - D_m space. Similar segregation is visible between stratiform and convective rainfall from various sites. Chen et al. (2013) and Wen et al. (2016) reported the values from Nanjing, China during the Meiyu (June-August) season of 2009–11, and 2014–15, respectively. Seela et al. (2018) reported over Taiwan during the summer rainfall from 2005 to 14. The convective points from Nanjing and Taiwan are clustered around the maritime convective box of Bringi et al. (2003), as they are coastal sites in China Sea. Das et al. (2017) classified rain over Mahabaleshwar during the monsoon season of 2012–2015. The points from Mahabaleshwar stands out in the space since it is a high altitude site in the Western Ghats that receives orographically forced rainfall (Konwar et al., 2014). Lavanya et al. (2019) averaged the $\log_{10}N_w$ and D_m for all the rainfall during monsoon (2007–2015) over the coastal site of Thumba, Trivandrum, and the values lie in between other coastal stratiform and convective values in terms of D_m and have similar $\log_{10}N_w$. While the D_m at Pune is comparable to all the studies above for both stratiform and convection rain, the normalized DSD scaling parameter was smallest compared to the studies mentioned above. The location of the study and Mahabaleshwar (Konwar et al., 2014) both experience marine air masses during the monsoon, but Pune is on the leeward side of the Western Ghats,

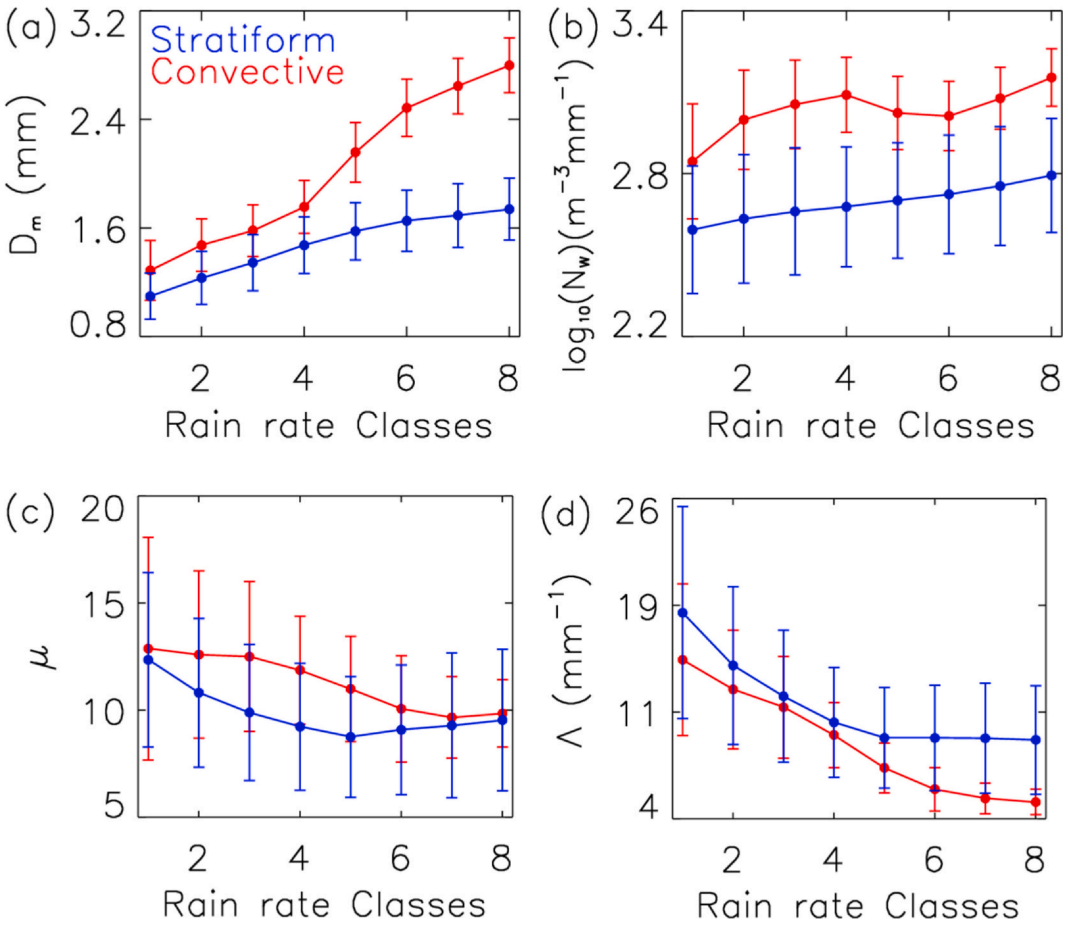

Fig. 3. Association between rain rate classes and calculated gamma parameters from the DSD. (a) mass-weighted mean diameter, (b) normalized DSD scaling parameter, (c) shape parameter and (d) slope parameter.

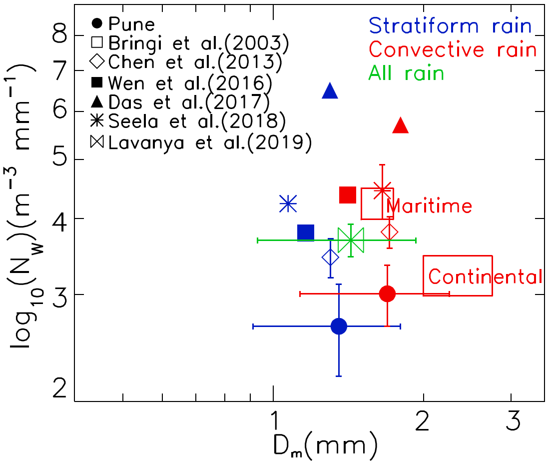

Fig. 4. The normalized DSD scaling parameter ($\log_{10}N_w$) versus mass-weighted mean diameter (D_m) for stratiform rain (blue color), convective rain (red color) and all rain (green color) regimes for this study (solid dot) and previous studies such as Bringi et al. (2003) (open square box), Chen et al. (2013) (open diamond), Wen et al. (2016) (filled square), Das et al. (2017) (filled upward triangle), Seela et al. (2018) (asterisk) and Lavanya et al. (2019) (open bowtie).

whereas Mahabaleshwar is on the windward side of the Western Ghats. This probably explains why the Mahabaleshwar site has a higher number of droplet number concentrations and bigger hydrometeors compared to Pune, which further suggests the influence of the orography on the DSD.

3.2. DSD response to cloud microphysical properties and meteorological conditions

The seasonal variation in the DSD has been associated with seasonal changes in cloud properties (Chakravarty et al., 2013; Lavanya et al., 2019; Seela et al., 2018). Within a season, both stratiform and convective rain regimes have different rain forming processes, and it is important to identify the instantaneous response of the rain DSD to the variation in cloud microphysical properties and meteorological conditions. Table 3 summarizes the low and high percentile values of CER, CDNC, CAPE and vertical wind shear (WS) for stratiform and convective rain regimes. The response of stratiform DSD to the CER is inverse to that of convective DSD (Fig. 5a). Low CER resulted in a narrower DSD (thin blue line connected by plus symbols) with a higher number concentration of small-sized raindrops ($<$ 1 mm) compared to high CER DSD (thick blue solid line) for stratiform rain. The high CER condition resulted in a higher concentration of medium-sized raindrops (1–3 mm) than low CER DSD in stratiform rain. In the case of convective rain, the response of DSD between low and high CER is opposite and only visible for large diameter droplets ($>$ 3 mm). The variation in the DSD at low and high CDNC also showed similar responses to that of CER. The low CDNC condition resulted in a higher concentration of medium and large-sized droplets in convective DSD compared to high CDNC.

Table 3
Summary of cloud microphysical properties and meteorological parameters at low and high percentiles for stratiform and convective rain. Low and high values indicate 33rd and 66th percentile values, respectively.

	Stratiform		Convective	
	Low	High	Low	High
CER (μm)	21.79	28.92	20.93	25.77
CDNC (cm^{-3})	45.18	68.93	41.65	73.62
CAPE (J/kg)	28.49	116.52	18.49	213.26
Wind Shear (s^{-1})	1.90	8.09	3.04	9.50

The high CAPE values indicate pseudo adiabatically rising air parcel, usually associated with taller thick clouds, and low WS aids such vertical extent of the cloud system and intensifies rainfall. The DSD response difference between low and high values of CAPE in stratiform rain was insignificant throughout the drop size spectrum except for a small increase for low CAPE conditions in small raindrops. But the variation is pronounced in convective rainfall, where high CAPE condition gives way to increased concentration of larger raindrops (Fig. 5c). Low WS, resulted in a higher concentration of medium and large droplets in both rain regimes. This impact is more visible in convective rain regimes (Fig. 5d).

4. Discussion

Previous studies segregated rain rates using absolute values to characterize DSD and gamma parameters (Chakravarty and Raj, 2013; Lavanya et al., 2019; Seela et al., 2018; Sreekanth et al., 2019). The rain rate classes based on absolute values result in a different number of samples in each class bin, and the range of class intervals will change with the type of rainfall, season, and location. Therefore, the equivalent percentile bin size, which yields the same number of samples in each rain rate class (Tables 1 and 2), was adopted. The equal number of samples in each rain rate class leads to the robust association between rain rate and gamma parameters in stratiform and convective regimes. In stratiform rainfall, the DSD has an increase in the concentration of raindrops in all sizes with the rain rate classes, whereas, in convective rain, the DSD curve skews towards the larger drop sizes with a decrease in small raindrops (Fig. 2a and b). The gamma parameters in Fig. 3a–d characterize the variation in DSD with rain rate classes. The overall higher values of D_m and $\log_{10}N_w$ in convective rain throughout the rain rate classes highlight the larger average raindrop size and number concentration of drops. The lower values of Λ and higher values of μ in the convective rain shows that the DSD is broader and skewed towards larger drop size. This variation in gamma parameters with respect to rain rate classes is attributed to the difference in the formation mechanism of stratiform and convective rain. Active cumulus or cumulonimbus clouds produce convective rain, and nimbostratus clouds produce stratiform rains (Houze, 2014). The major difference in these clouds being the updraft velocity in the convectively active clouds, which help the raindrops to grow to a medium to a large size before falling as precipitation.

Several studies over India have focused on the inter- and intra-seasonal variation of the DSD and linked it to the seasonally averaged cloud microphysical properties and dynamical processes (Chakravarty and Raj, 2013; Chakravarty et al., 2013; Das et al., 2017; Konwar et al., 2014; Lavanya et al., 2019). The mass-weighted mean diameter at Pune is comparable to previous studies in India and elsewhere (Bringi et al., 2003; Chen et al., 2013; Das et al., 2017; Lavanya et al., 2019; Seela et al., 2018; Wen et al., 2016), but the DSD scaling parameter is surprisingly smallest for both stratiform and convective rain at Pune compared to previous studies. Das et al. (2017) found that Mahabaleshwar, which is on the windward side of the Western Ghats, receives about 89% of shallow-convective rain, with the highest DSD scaling parameter. The location of Pune on the leeward side of the Western Ghats explains the dominance of smaller to medium-sized droplets. A previous study also showed that the breakup and collision-coalescence processes of large raindrops amplifies the number concentration of medium-sized drops over Pune (Konwar et al., 2014). They further suggested that orographically forced updrafts triggered collision-coalescence processes in the dynamically forced cloud over Mahabaleshwar. The inter-seasonal comparison of the DSD showed that the monsoon season has a higher number of smaller size raindrops as compared to pre-monsoon and post-monsoon, along with higher CER values (Chakravarty and Raj, 2013; Lavanya et al., 2019), corroborated by our findings. The high CER is the result of aerosol-induced cloud-

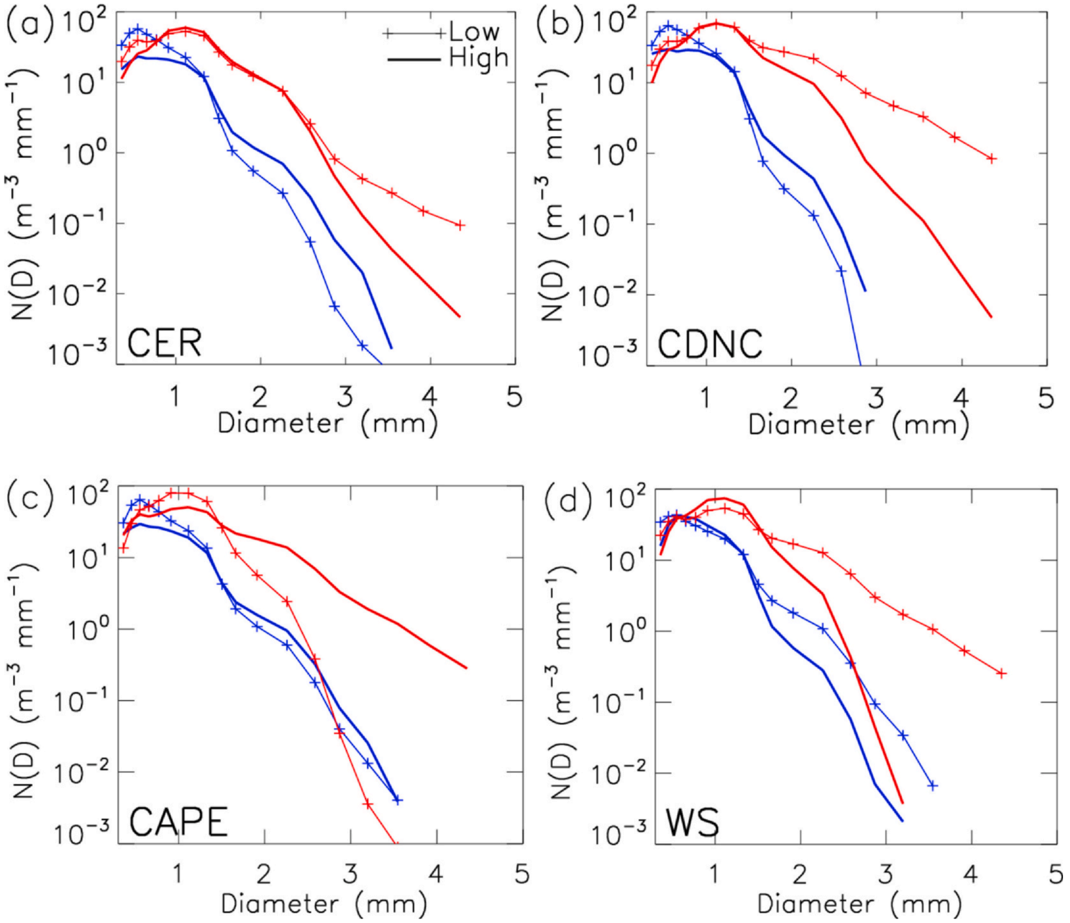

Fig. 5. The variation in the stratiform rain (blue color) and convective rain (red color) DSD with respect to low and high quartile values of (a) cloud effective radius, (b) cloud droplet number concentration, (c) convective available potential energy and (d) wind shear.

invigoration effect over Indian summer monsoon region, creating large size ice hydrometeors which result in the formation of larger raindrops as they leave the cloud base (Koren and Feingold, 2011; Sarangi et al., 2018; Sarangi et al., 2017). Our findings suggest that the narrower size distribution for high CER regime is due to the breakup of large size raindrops during the descent. Konwar et al. (2014) has shown that the break up of large raindrops leads to an increase in the concentration of midsize drops over Pune.

The observations made at Gadanki (southeastern peninsular India) also showed a prevalence of more number of smaller raindrops in the monsoon season (Rao et al., 2009). The aerosols can increase the number of cloud droplets and decrease the droplet size for a given cloud water content (Albrecht, 1989). But the increased moisture in the monsoon season aids in the growth of cloud drops (Chakravarty and Raj, 2013).

Higher CAPE values are an indicator of stronger convection, and the resulting stronger updrafts can lift up rain droplets that have fall velocity less than the draft velocity and only larger droplets reach the ground (Kollias et al., 2001). The smaller rain droplets are lifted higher up and remain in-cloud for a longer time helping in the growth process through collision and coalescence. The advection of cloud water to higher levels increases the efficiency of riming and forms large ice hydrometeors, which melts and falls as large droplets at the ground (Andreae et al., 2004; Rosenfeld et al., 2008; Sarangi et al., 2017). The monsoon circulation is characterized by strong vertical wind shear due to the presence of a low-level jet stream and a tropical easterly jet-stream (TEJ) (Joseph and Sijikumar, 2004). The presence of a low-level jet stream is associated with a higher vertical wind upto 4 km, resulting in enhanced convection (Joshi et al., 2006; Ruchith et al., 2016). The enhanced convection thus alter the DSD during the monsoon season. The convective and stratiform rains react differently to the cloud microphysical properties as the rain formation processes are different for stratiform and convective rains.

5. Conclusions

In this study, we characterized raindrop size distributions for stratiform and convective rain regimes during the Indian summer monsoon season (June through October 2013–2015). We further qualitatively analyzed the DSD response to cloud microphysical properties and meteorological conditions for stratiform and convection rain regimes. Overall, the stratiform rainfall was more frequent than convective rainfall, but the derived rain rate was much higher for convective rain compared to stratiform rain. The stratiform rain and convective rain clusters were distinctive in the $\log_{10}N_w$ - D_m space, with the smallest normalized DSD scaling parameter at Pune as compared to previous studies over this region and elsewhere. The response of DSD to the cloud microphysical properties such as cloud effective radius and cloud droplet number concentrations was different between stratiform and convective rain regimes. We found a wider DSD with a higher concentration of larger droplets for stratiform as opposed to the narrower distribution with smaller-sized rain droplets in convective rain at high cloud effective radius conditions. The narrower DSD at high cloud effective radius condition suggests the breakup of larger raindrops during its descent. The cloud droplet number concentrations were derived to understand the aerosol impact on the cloud and thus on the raindrop spectrum. The higher cloud droplet number concentration resulted in a broader DSD in the stratiform rain regime and the opposite for convective rain regime. The higher moisture and stronger ascent in the monsoon season help in the growth of raindrops even at high cloud droplet number concentrations. The response of convective DSD was much larger and was more prominent in the medium to larger-sized droplets. Lower wind shear and higher convective available potential energy further promoted the concentration of larger droplets in convective rain due to stronger updrafts in such conditions. Our findings suggest that the improved understanding of such instantaneous responses, especially on the convective rain DSD, could help in the short-term prediction of heavy rainfall events that are becoming frequent in the warming anthropogenic scenario.

CRediT authorship contribution statement

Abin Thomas: Methodology, Software, Visualization, Validation, Writing- Original draft preparation, Writng - review & editing. **Vijay P. Kanawade:** Conceptualization, Methodology, Formal Analysis, Writing- Original draft preparation, Writing- Reviewing and Editing, Supervision. **Kaustav Chakravarty:** Formal analysis, Software, Validation, Data curation, Visualization, Project administration, Funding acquisition. **Atul K. Srivastava:** Project administration, Resources, Writing- Reviewing and Editing

Declaration of Competing Interest

The authors declare that they have no known competing financial interests or personal relationships that could have appeared to influence the work reported in this paper.

Acknowledgment

VPK would like to thank University Grants Commission, Government of India, for UGC Start-Up Grant [Ref. No. F.4-5(230-FRP/2015/BSR)]. AT was supported by University Grants Commission Junior Research Fellowship. The authors acknowledge Director, Indian Institute of Tropical Meteorology, Ministry of Earth Sciences, India to support this study.

Disdrometer raindrop size distribution is archived at doi:10.17632/n3j6x74nb3.2 and KC may be contacted for any questions.

ERA-5 meteorological dataset is publicly available at https://cds.climate.copernicus.eu/cdsapp#!/home

MODIS cloud level 2 collection 6.1 is publicly available from LAADS DAAC at https://ladsweb.modaps.eosdis.nasa.gov/missions-and-measurements/science-domain/cloud

References

Albrecht, B.A., 1989. Aerosols, cloud microphysics, and fractional cloudiness. Science 245https://doi.org/10.1126/science.245.4923.1227. 1227–1130.

Anagnostou, E.N., Kummerow, C., 1997. Stratiform and convective classification of rainfall using SSM/I 85-Ghz brightness temperature observations. J. Atmos. Ocean. Technol. 14, 570–575. https://doi.org/10.1175/1520-0426(1997)014<0570:SACCOR>2.0.CO;2.

Andreae, M.O., Rosenfeld, D., Artaxo, P., Costa, A.A., Frank, G.P., Longo, K.M., Silva-Dias, M.A.F., 2004. Smoking rain clouds over the Amazon. Science 303, 1337–1342. https://doi.org/10.1126/science.1092779.

Baum, B.A., Menzel, W.P., Frey, R.A., Tobin, D.C., Holz, R.E., Ackerman, S.A., Heidinger, A.K., Yang, P., 2012. MODIS cloud-top property refinements for collection 6. J. Appl. Meteorol. Climatol. 41, 1145–1163. https://doi.org/10.1175/JAMC-D-11-0203.1.

Bringi, V.N., Seliga, T.A., Cooper, W.A., 1984. Analysis of aircraft hydrometeor spectra and differential reflectivity (ZDR) radar measurements during the Cooperative Convective Precipitation Experiment. Radio Sci. 19, 157–167. https://doi.org/10.1029/RS019i001p00157.

Bringi, V.N., Chandrasekar, V., Hubbert, J., Gorgucci, E., Randeu, W.L., Schoenhuber, M., 2003. Raindrop size distribution in different climatic regimes from disdrometer and dual-polarized radar analysis. J. Atmos. Sci. 60, 354–365. https://doi.org/10.1175/1520-0469(2003)060<0354:RSDIDC>2.0.CO;2.

Bruintjes, R.T., 1999. A review of cloud seeding experiments to enhance precipitation and some new prospects. Bull. Amer. Meteor. Soc. 80, 805–820. https://doi.org/10.1175/1520-0477(1999)080<0805:AROCSE>2.0.CO;2.

Chakravarty, K., Raj, E.P., 2013. Raindrop size distributions and their association with characteristics of clouds and precipitation during monsoon and post-monsoon periods over a tropical Indian station. Atmos. Res. 124, 181–189. https://doi.org/10.1016/j.atmosres.2013.01.005.

Chakravarty, K., Raj, E.P., Bhattacharya, A., Maitra, A., 2013. Microphysical characteristics of clouds and precipitation during pre-monsoon and monsoon period over a tropical Indian station. J. Atmos. Sol.-Terr. Phys. 94, 28–33. https://doi.org/10.1016/j.jastp.2012.12.016.

Chen, B., Yang, J., Pu, J., 2013. Statistical characteristics of raindrop size distribution in the meiyu season observed in eastern China. *J. Meteor*. Soc. Japan. Ser. II 91, 215–227. https://doi.org/10.2151/jmsj.2013-208.

Das, S., Maitra, A., 2018. Characterization of tropical precipitation using drop size distribution and rain rate-radar reflectivity relation. Theor. Appl. Climatol. 132, 275–286. https://doi.org/10.1007/s00704-017-2073-1.

Das, S.K., Konwar, M., Chakravarty, K., Deshpande, S.M., 2017. Raindrop size distribution of different cloud types over the Western Ghats using simultaneous measurements from micro-rain radar and disdrometer. Atmos. Res. 186, 72–82. https://doi.org/10.1016/j.atmosres.2016.11.003.

Dee, D.P., Uppala, S.M., Simmons, A.J., Berrisford, P., Poli, P., Kobayashi, S., et al., 2011. The ERA-interim reanalysis: Configuration and performance of the data assimilation system. Q. J. R. Meteorol. Soc. 137, 553–597. https://doi.org/10.1002/qj.828.

Dolan, B., Fuchs, B., Rutledge, S.A., Barnes, E.A., Thompson, E.J., 2018. Primary modes of global drop size distributions. J. Atmos. Sci. 75, 1453–1476. https://doi.org/10.1175/JAS-D-17-0242.1.

Dzotsi, K.A., Matyas, C.J., Jones, J.W., Baigorria, G., Hoogenboom, G., 2014. Understanding high resolution space-time variability of rainfall in Southwest Georgia, United States. Int. J. Climatol. 34, 3188–3203. https://doi.org/10.1002/joc.3904.

Freud, E., Rosenfeld, D., Kulkarni, J.R., 2011. Resolving both entrainment-mixing and number of activated CCN in deep convective clouds. Atmos. Chem. Phys. 11, 12887–12900. https://doi.org/10.5194/acp-11-12887-2011.

Gadgil, A., Dhorde, A., 2005. Temperature trends in twentieth century at Pune, India. Atmos. Environ. 39, 6550–6556. https://doi.org/10.1016/j.atmosenv.2005.07.032.

Goddard, J.W.F., Cherry, S.M., 1984. The ability of dual-polarization radar (copolar linear) to predict rainfall rate and microwave attenuation. Radio Sci. 19, 201–208. https://doi.org/10.1029/RS019i001p00201.

Hersbach, H., Dee, D., 2016. ERA5 reanalysis is in production. ECMWF Newslett. 147. https://www.ecmwf.int/en/newsletter/147/news/era5-reanalysis-production.

Houze, R.A., 2014. Nimbostratus and the separation of convective and stratiform precipitation. In: Houze, R.A. (Ed.), International Geophysics. Academic Press, pp. 141–163. https://doi.org/10.1016/B978-0-12-374266-7.00006-8.

Joseph, P.V., Sijikumar, S., 2004. Intraseasonal variability of the low-level jet stream of the Asian summer monsoon. J. Clim. 17, 1449–1458. https://doi.org/10.1175/1520-0442(2004)017<1449:IVOTLJ>2.0.CO;2.

Joshi, R., Singh, N., Deshpande, S., Damle, S., Pant, G., 2006. UHF wind profiler observations of monsoon low level jet over Pune. Indian J. Radio Space Phys. 35, 349–359. http://nopr.niscair.res.in/handle/123456789/3915.

Joss, J., Waldvogel, A., 1967. Ein spektrograph für niederschlagstropfen mit automatischer auswertung. Pure Appl. Geophys. 68, 240–246. https://doi.org/10.1007/BF00874898.

Kirankumar, N.V.P., Rao, T.N., Radhakrishna, B., Rao, D.N., 2008. Statistical characteristics of raindrop size distribution in southwest monsoon season. J. Appl. Meteorol. Climatol. 47, 576–590. https://doi.org/10.1175/2007JAMC1610.1.

Kollias, P., Albrecht, B.A., Marks Jr., F.D., 2001. Raindrop sorting induced by vertical drafts in convective clouds. Geophys. Res. Lett. 28, 2787–2790. https://doi.org/10.1029/2001GL013131.

Konwar, M., Das, S.K., Deshpande, S.M., Chakravarty, K., Goswami, B.N., 2014. Microphysics of clouds and rain over the Western Ghat. J. Geophys. Res. Atmos. 119, 6140–6159. https://doi.org/10.1002/2014JD021606.

Koren, I., Feingold, G., 2011. Aerosol–cloud–precipitation system as a predator-prey problem. Proc. Natl. Acad. Sci. U. S. A. 108, 12227–12232. https://doi.org/10.1073/pnas.1101777108.

Kulmala, M., Kontkanen, J., Junninen, H., Lehtipalo, K., Manninen, H.E., Nieminen, T., et al., 2013. Direct observations of atmospheric aerosol nucleation. Science 339, 943–946. https://doi.org/10.1126/science.1227385.

Lavanya, S., Kirankumar, N.V.P., Aneesh, S., Subrahmanyam, K.V., Sijikumar, S., 2019. Seasonal variation of raindrop size distribution over a coastal station Thumba: a quantitative analysis. Atmos. Res. 229, 86–99. https://doi.org/10.1016/j.atmosres.2019.06.004.

Maguire II, W.B., Avery, S.K., 1994. Retrieval of raindrop size distributions using two doppler wind profilers: Model sensitivity testing. J. Appl. Meteorol. 33, 1623–1635. https://doi.org/10.1175/1520-0450(1994)033<1623:RORSDU>2.0.CO;2.

Marzano, F.S., Cimini, D., Montopoli, M., 2010. Investigating precipitation microphysics using ground-based microwave remote sensors and disdrometer data. Atmos. Res. 97, 583–600. https://doi.org/10.1016/j.atmosres.2010.03.019.

Niu, S., Jia, X., Sang, J., Liu, X., Lu, C., Liu, Y., 2010. Distributions of raindrop sizes and fall velocities in a semi-arid plateau climate: Convective versus stratiform rains. J. Appl. Meteorol. Climatol. 49, 632–645. https://doi.org/10.1175/2009JAMC2208.1.

Platnick, S., Meyer, K.G., King, M.D., Wind, G., Amarasinghe, N., Marchant, B., et al., 2017. The MODIS cloud optical and microphysical products: Collection 6 updates and examples from TERRA and AQUA. IEEE Trans. Geosci. Remote Sens. 55, 502–525. https://doi.org/10.1109/TGRS.2016.2610522.

Radhakrishna, B., Satheesh, S.K., Rao, T.N., Saikranthi, K., Sunilkumar, K., 2016. Assessment of DSDs of GPM-DPR with ground-based disdrometer at seasonal scale over Gadanki. India. J. Geophys. Res. Atmos. 12, 11792–11802. https://doi.org/10.1002/2015JD024628.

Rao, T.N., Radhakrishna, B., Nakamura, K., Rao, P.N., 2009. Differences in raindrop size distribution from southwest monsoon to northeast monsoon at Gadanki. Q. J. R. Meteorol. Soc. 135, 1630–1637. https://doi.org/10.1002/qj.432.

Rosenfeld, D., Ulbrich, C.W., 2003. Cloud microphysical properties, processes, and rainfall estimation opportunities. In: Wakimoto, R.M., Srivastava, R. (Eds.), Radar and Atmospheric Science: a Collection of Essays in Honor of David Atlas. American Meteorological Society, Boston, MA, pp. 237–258. https://doi.org/10.1007/978-1-878220-36-3_10.

Rosenfeld, D., Lohmann, U., Raga, G., O'Dowd, C., Kulmala, M., Sandro, F., Reissell, A., Andreae, M., 2008. Flood or drought: how do aerosols affect precipitation? Science 321, 1309–13013. https://doi.org/10.1126/science.1160606.

Ruchith, R.D., Deshpande, S.M., Raj, E.P., 2016. UHF wind profiler observations of monsoon low-level jet (MLLJ) and its association with rainfall over a tropical Indian station. Atmosfera 29, 1–9 Doi:10.20937/ATM.2016.29.01.01.

Sarangi, C., Tripathi, S.N., Kanawade, V.P., Koren, I., Pai, D.S., 2017. Investigation of the aerosol–cloud–rainfall association over the Indian summer monsoon region. Atmos. Chem. Phys. 17, 5185–5204. https://doi.org/10.5194/acp-17-5185-2017.

Sarangi, C., Kanawade, V.P., Tripathi, S.N., Thomas, A., Ganguly, D., 2018. Aerosol-induced intensification of cooling effect of clouds during Indian summer monsoon. Nat. Commun. 9, 3754. https://doi.org/10.1038/s41467-018-06015-5.

Sato, T., Doji, H., Iwai, H., Kimura, I., Fukao, S., Yamamoto, M., Tsuda, T., Kato, S., 1990. Computer processing for deriving drop-size distributions and vertical air velocities from VHF doppler radar spectra. Radio Sci. 25, 961–973. https://doi.org/10.1029/RS025i005p00961.

Saud, T., Dey, S., Das, S., Dutta, S., 2016. A satellite-based 13-year climatology of net cloud radiative forcing over the Indian monsoon region. Atmos. Res. 182, 76–86. https://doi.org/10.1016/j.atmosres.2016.07.017.

Sauvageot, H., Lacaux, J.-P., 1995. The shape of averaged drop size distributions. J. Atmos. Sci. 52, 1070–1083. https://doi.org/10.1175/1520-0469(1995)052<1070:TSOADS>2.0.CO;2.

Seela, B.K., Janapati, J., Lin, P., Wang, P.K., Lee, M., 2018. Raindrop size distribution characteristics of summer and winter season rainfall over North Taiwan. J. Geophys. Res. Atmos. 123, 11602–11624. https://doi.org/10.1029/2018JD028307.

Singh, N., Ranade, A., 2010. The wet and dry spells across India during 1951–2007. J. Hydrometeorol. 11, 26–45. https://doi.org/10.1175/2009JHM1161.1.

Sreekanth, T.S., Varikoden, H., Sukumar, N., Mohan Kumar, G., 2017. Microphysical characteristics of rainfall during different seasons over a coastal tropical station using disdrometer. Hydrol. Process. 31, 2556–2565. https://doi.org/10.1002/hyp.11202.

Sreekanth, T.S., Varikoden, H., Mohan Kumar, G., Resmi, E.A., 2019. Microphysical features of rain and rain events during different seasons over a tropical mountain location using an optical disdrometer. Sci. Rep. 9, 19083. https://doi.org/10.1038/s41598-019-55583-z.

Szczodrak, M., Austin, P.H., Krummel, P.B., 2001. Variability of optical depth and effective radius in marine stratocumulus clouds. J. Atmos. Sci. 58, 2912–2926. https://doi.org/10.1175/1520-0469(2001)058<2912:VOODAE>2.0.CO;2.

Tokay, A., Short, D.A., 1996. Evidence from tropical raindrop spectra of the origin of rain from stratiform versus convective clouds. J. Appl. Meteorol. Climatol. 35, 355–371. https://doi.org/10.1175/1520-0450(1996)035<0355:EFTRSO>2.0.CO;2.

Ulbrich, C.W., 1983. Natural variations in the analytical form of the raindrop size distribution. J. Appl. Meteorol. 22, 1764–1775. https://doi.org/10.1175/1520-0450(1983)022<1764:NVITAF>2.0.CO;2.

Ulbrich, C.W., Atlas, D., 2007. Microphysics of raindrop size spectra: Tropical continental and maritime storms. J. Appl. Meteorol. Climatol. 46, 1777–1791. https://doi.org/10.1175/2007JAMC1649.1.

Wen, L., Zhao, K., Zhang, G., Xue, M., Zhou, B., Liu, S., et al., 2016. Statistical characteristics of raindrop size distributions observed in East China during the asian summer monsoon season using 2-D video disdrometer and micro rain radar data. J. Geophys. Res. Atmos. 121, 2265–2282. https://doi.org/10.1002/2015JD024160.

Yang, Y., Chen, X., Qi, Y., 2013. Classification of convective/stratiform echoes in radar reflectivity observations using a fuzzy logic algorithm. J. Geophys. Res. Atmos. 118, 1896–1905. https://doi.org/10.1002/jgrd.50214.

Zhang, R., 2010. Getting to the critical nucleus of aerosol formation. Science 328, 1366–1367. https://doi.org/10.1126/science.1189732.

Zhang, G., Vivekanandan, J., Brandes, E.A., Meneghini, R., Kozu, T., 2003. The shape–slope relation in observed gamma raindrop size distributions: Statistical error or useful information? J. Atmos. Ocean. Technol. 20, 1106–1119. https://doi.org/10.1175/1520-0426(2003)020<1106:TSRIOG>2.0.CO;2.

Zhang, G., Sun, J., Brandes, E.A., 2006. Improving parameterization of rain microphysics with disdrometer and radar observations. J. Atmos. Sci. 63, 1273–1290. https://doi.org/10.1175/JAS3680.1.

Zhu, Y., Rosenfeld, D., Li, Z., 2018. Under what conditions can we trust retrieved cloud drop concentrations in broken marine stratocumulus? J. Geophys. Res. Atmos. 123, 8754–8767. https://doi.org/10.1029/2017JD028083.